Physical analysis of the swirling wake of a porous disc : application to wind turbines

Ernesto Fuentes Noriega

UNIVERSITÉ D'ORLÉANS

ÉCOLE DOCTORALE
ÉNERGIE, MATÉRIAUX, SCIENCES DE LA TERRE ET DE L'UNIVERS

Laboratoire PRISME

THÈSE présentée par

Ernesto FUENTES NORIEGA

soutenue le : 19 Mars 2024

pour obtenir le grade de : **Docteur de l'Université d'Orléans**

Discipline/ Spécialité : Mécanique des fluides

Physical analysis of the swirling wake of a porous disc: application to wind turbines

Analyse physique du sillage tournant d'un disque poreux : application aux éoliennes

THÈSE dirigée par :

M. MAZELLIER Nicolas	Professeur, Université d'Orléans

RAPPORTEURS :

M. BUXTON Oliver	Reader, Imperial College London
M. VASSILICOS J. Christos	Directeur de Recherche, CNRS

JURY :

Mme AUBRUN-SANCHES Sandrine	Professeure, Ecole Centrale de Nantes Présidente du jury
M. BENARD Pierre	Maître de conférences, INSA Rouen Normandie
M. BUXTON Oliver	Reader, Imperial College London
M. MAZELLIER Nicolas	Professeur, Université d'Orléans
M. PINON Grégory	Professeur, Université Le Havre Normandie
M. RAIBAUDO Cédric	Maître de conférences, Université d'Orléans
M. VASSILICOS J. Christos	Directeur de Recherche, CNRS
Mme WEBER Régine	Maître de conférences, Université d'Orléans

A smooth sea never made a skilled sailor
— Franklin D. Roosevelt

To Mom and Dad.

Remerciements

Alors que j'écris ce dernier fragment, je suis saisi par une réalisation profonde. Il y a eu d'innombrables moments où je me suis retrouvé à fixer une page blanche, tandis qu'une vague déferlante d'idées et de mots se déchaînait dans mon esprit. Maintenant, alors que je réfléchis, plusieurs noms et souvenirs précieux se déploient devant moi, comme une partition musicale qui défile dans ma tête. Mon cœur est rempli de désir de reconnaître chacun, de transmettre la profondeur de ma gratitude dans ces lignes. C'est une tâche impossible, essayer de distiller une telle concentration d'émotions et d'expériences en simples mots. Je ne peux m'empêcher de craindre d'omettre involontairement certains des individus remarquables qui ont été mes piliers durant ce voyage de défis et d'apprentissage. Si votre nom n'est pas mentionné, sachez que ce n'est pas par manque d'appréciation. Mes plus profonds remerciements s'étendent à tous ceux qui ont fait partie de mon voyage, de manière grande ou petite.

Avant tout, ma plus profonde gratitude va aux membres du jury pour leur examen approfondi de cette thèse. Leurs questions, commentaires précieux et leurs discussions captivantes ont considérablement rehaussé la qualité de ce travail. Merci à J. Christos Vassilicos et à Oliver Buxton pour avoir rapporté la thèse. Je ne peux pas exprimer à quel point je me sens honoré que vous ayez lu ce travail et fourni votre critique constructive. Ma plus sincère appréciation va également à Sandrine Aubrun, présidente du jury, qui a guidé avec expertise la soutenance de thèse. Je suis profondément reconnaissant pour votre présence et le temps que vous avez investi dans ce moment crucial de ma carrière académique. Ma gratitude s'étend également à Grégory Pinon et Pierre Bénard, pour leur examen minutieux de mon travail et les questions qu'ils ont posées. Vos contributions ont enrichi mon parcours académique, et pour cela, je suis profondément reconnaissant. Rencontrer de tels scientifiques remarquables a été incroyablement inspirant, me servant de rappel quotidien de la beauté sans limites et intemporelle de la science.

Et maintenant, je voudrais remercier les personnes qui ont été cruciales dans la réalisation de cette thèse. Monsieur Professeur Nicolas Mazellier, les mots ne peuvent pas exprimer à quel point je suis reconnaissant pour ton mentorat, ton soutien inébranlable et pour ton aide inestimable tout au long de ces trois dernières années. Il est clair que ce travail n'aurait pas été possible sans toi. Au-delà de ta remarquable prouesse scientifique, c'est ton caractère que je respecte profondément - ta gentillesse, patience et humour ont créé un environnement idéal pour ma croissance personnelle et académique, me permettant de naviguer les défis et obstacles inévitables de toute carrière. Je suis incroyablement fier de t'avoir eu comme directeur de thèse et je m'efforce d'être un jour un aussi bon professeur que tu l'es. Je dois également une dette de gratitude à toute l'équipe du département d'écoulements et systèmes aérodynamiques (ESA) du Laboratoire PRISME. À Cédric, Régine, Azeddine Kourta - merci pour votre soutien et vos retours. En particulier, Stéphane Loyer, ton soutien dans la soufflerie était indispens-

able. Je suis inspiré par ton expertise et espère un jour égaler ta compétence dans la construction de montages expérimentaux. Pierre-Yves Passaggia, ta volonté d'explorer des idées inédites et de m'enseigner les subtilités de la PIV, ainsi que ton approche pour affronter les problèmes de front, sont grandement appréciées. Merci à tous pour vos contributions, vos conseils et pour les innombrables opportunités d'apprentissage que vous m'avez fournies.

À mes chers amis du laboratoire, vous savez combien je vous suis reconnaissant, à chacun d'entre vous. Depuis le tout début et maintenant que je termine ce chapitre de ma vie, vous m'avez véritablement fait sentir que je faisais partie d'une équipe. Je suis honoré de vous considérer non seulement comme des collègues, mais aussi comme de amis : Wassim, Roshan, Noura, Marin, Mathieu, Gaétan, Mylène, Ahmed, Enzo, Khaled, Sofia, Olfa, Laila, Léo, Abdel, Willy, Alfredo, Aurélien, Amaury, Alex, Jack. Je vous souhaite le meilleur dans la vie.

Je souhaite maintenant étendre ma gratitude à mes amis, toutes les personnes incroyables que j'ai croisées jusqu'à maintenant. C'est un défi de nommer chacun qui occupe une place spéciale dans mon cœur, mais je vais essayer. À mon meilleur ami et frère, Mateo Jordan, ta présence dans ma vie témoigne du fait que la distance s'efface devant la véritable amitié. Puis, aux premiers amis que j'ai faits à mon arrivée à Orléans : Gigi, Gui, Fernando, Vivi, Francisco, Nora, Silvia, Ale, Angie, Yudy, Raul, Mathieu ; merci. Je me suis senti chez moi dès la première minute grâce à vous. Aussi, un immense merci à ma MILPA, ma famille latino ici en France : Ximena, Tandy, Thibaut, Ignacio (nachito), Ana, Gigi, Bruno, Elo, Clem, Alfredito, Vane, Elise, Augusto, Jorge, Kari, Selene, Euge. Pour ceux que j'ai involontairement oubliés, acceptez mes sincères excuses.

À ma famille bien-aimée, qui me manque terriblement chaque jour, mon cœur déborde d'amour pour vous. Cette thèse est dédiée à mon père, Luis Fernando Fuentes Durán, et à ma mère, Sonia Noriega Saavedra de Fuentes, dont l'amour et les orientations m'ont façonné. Je ne pourrai jamais exprimer pleinement mon amour et ma fierté d'être votre fils. À ma chère s œur, Sofia Elena Fuentes, partager la vie avec toi a été l'une de mes plus grandes joies. Et à mes grands frères, Dennis Rada et Steve Bravo, vos caractères exemplaires ont enrichi notre famille et apporté joie et fierté. Hannah, ta patience et ton amour ont été un phare pendant ces temps difficiles, et je suis reconnaissant pour chaque souvenir que nous avons partagé/construit avec Haku. Ma famille française, Pascal, Anne et Émile Boisaubert, merci de m'avoir accueilli à bras ouverts et de partager votre joie.

Enfin, j'exprime ma gratitude à ma patrie, la Bolivie, et à ma seconde maison, la France, pour m'avoir accueilli avec leurs cultures riches et leurs opportunités. Et à vous, cher lecteur, alors que vous plongez dans ce manuscrit, je vous remercie de vous joindre à moi dans ce voyage tourbillonnant.

Acknowledgements

As I write this final piece of this manuscript, I'm struck by a profound realisation. There were countless moments I found myself staring at a blank page, as a tumult of ideas and words **swirled** in my mind. Now, as I reflect, several names and treasured memories unfurl before me, like a music sheet running through my head. My heart is filled with the desire to acknowledge each one, to encapsulate the depth of my gratitude within these lines. It's an impossible task, attempting to distil such a concentration of emotions and experiences into mere words. I can't help but worry I might inadvertently overlook some of the remarkable individuals who have been my pillars during this journey of challenges and growth. If your name is not mentioned, please know it's not for lack of appreciation. My deepest thanks extends to all who have been part of my journey, in ways both big and small.

First and foremost, my deepest gratitude goes to the esteemed members of the jury for their thorough review of this thesis. Their insightful questions, valuable comments, and engaging discussions have significantly elevated the quality of this work. Thank you J. Christos Vassilicos and Oliver Buxton for reviewing the thesis. I cannot express how honoured I feel for having you read through this work and providing your constructive criticism. My sincerest appreciation also goes to Sandrine Aubrun, the esteemed madam president of the jury, who expertly guided the defence and honoured me with the distinction of Doctor in Fluid Mechanics. I am deeply grateful for your presence and the time you invested in this critical moment of my academic career. My gratitude extends to Grégory Pinon and Pierre Bénard as well, for their meticulous examination of my work and the perceptive questions they posed. Your contributions have enriched my academic journey, and for that, I am profoundly thankful. Meeting such remarkable scientists and great people has been incredibly inspiring, serving as a daily reminder of the boundless and timeless beauty of science.

And now I would like to thank the people who have been critical in bringing this thesis to fruition. Professor Nicolas Mazellier, words cannot express how thankful I am for your mentorship, unwavering support and for your invaluable help throughout the years. It is clear that this work would not have been possible without you. Beyond your remarkable scientific prowess, it is your character that I deeply respect - your kindness, patience, and humour have created an ideal environment for my personal and academic growth, enabling me to navigate the inevitable challenges and obstacles of any career. I am incredibly proud to have had you as a director and I aim at being as good as a Professor as you are. I also owe a debt of gratitude to the entire team in the Aerodynamics Department (ESA) at the PRISME Laboratory. To Cédric, Régine, Azeddine Kourta - thank you for your support and feedback. In particular, Stéphane Loyer, your support in the wind tunnel was indispensable. I am inspired by your expertise and hope to one day match your skill in constructing experimental setups. Pierre-Yves Passaggia, your willingness to delve into uncharted ideas and teach me the

intricacies of PIV, as well as your approach to tackling problems head-on, are greatly appreciated. Thank you all for your contributions, guidance, and for the countless learning opportunities you've provided.

To my dear friends at the lab, you know how grateful I am towards each and every one of you. From the very start and now as I finish this chapter in my life, you have made me truly feel like I am part of a team. I am honoured to consider you not just as colleagues, but dear friends: Wassim, Roshan, Noura, Marin, Mathieu, Gaétan, Mylène, Ahmed, Enzo, Khaled, Sofia, Olfa, Laila, Léo, Abdel, Willy, Alfredo, Aurélien, Amaury, Alex, Jack. I wish you the very best in life.

I would like now to extend my gratitude to my friends, all the amazing people that I have crossed paths until now. It is challenging to enumerate everyone who holds a special place in my heart, yet I feel compelled to try. To my best friend and brother, Mateo Jordan, your presence in my life stands as a testament to the fact that distance fades in the face of true friendship. Then to the first friends that I made when I came to Orléans: Gigi, Gui, Fernando, Vivi, Francisco, Nora, Silvia, Ale, Angie, Yudy, Raul, Mathieu; thank you. I felt at home from the minute I got here thanks to you. Also an enormous thank you to my MILPA, my latino family here in France: Ximena, Tandy, Thibaut, Ignacio (nachito), Ana, Gigi, Bruno, Elo, Clem, Alfredito, Vane, Elise, Augusto, Jorge, Kari, Selene, Euge. To those I've inadvertently missed, accept my sincere apologies.

To my beloved family, whom I miss dearly every day, my heart overflows with love for you. This thesis is dedicated to my father, Luis Fernando Fuentes Durán, and to my mother, Sonia Noriega Saavedra de Fuentes, whose love and guidance have shaped me. I could never fully express my love and pride in being your son. To my dear sister, Sofia Elena Fuentes, sharing life with you has been one of my greatest joys. And to my big brothers, Dennis Rada and Steve Bravo, your exemplary characters have enriched our family and brought joy and pride. Hannah, your patience and love have been a beacon during these challenging times, and I'm grateful for every core memory we've shared/built along with Haku. My French family, Pascal, Anne, and Emile Boisaubert, thank you for welcoming me with open arms and sharing your joy.

Finally, I express my gratitude to my homeland, Bolivia, and my second home, France, for embracing me with their rich cultures and endless opportunities. And to you, dear reader, as you dive into this manuscript, I extend my thanks for joining me on this swirling journey.

Physical analysis of the swirling wake of a porous disc: application to wind turbines

Abstract

Wind energy stands out as a capital component of the renewable energy portfolio and has accordingly shown an exponential growth in recent years. Due to the limited regions with high wind energy potential, wind turbines are usually clustered in wind farms, whose power output will be impacted by wake interactions. Therefore, predicting the wake's evolution is of critical importance. To this end, fundamental studies are required to bring a comprehensive understanding of the underlying physics of wind turbine wakes. Porous discs are popular devices used to mimic the wake of wind turbines at the laboratory scale. So far, porous discs have been designed by adjusting a single physical parameter, its porosity, with the aim to match the velocity deficit of a target wind turbine. However, this simplistic approach excludes a key feature of wind turbine wakes : swirl. The present work tackles this issue by investigating in depth the role of swirl on the development of a wake generated by a porous disc. To do so, extensive wind tunnel experiments were conducted to measure the wake of a porous disc modified to passively incorporate swirl. It is found that swirl is a key ingredient to achieve self-similarity of the wake deficit in the intermediate wake region and matches very well the data reported in the literature of wind turbines. Based on non-equilibrium similarity theory, a novel scaling law for the decay of swirl is derived and shows very good agreement with the collected data. Finally, the turbulent entrainment at the turbulent/non-turbulent interface (TNTI) is analysed using highly resolved PIV data. An improved uniform momentum zones-based detection technique is developed to accurately detect the TNTI, whose fractal dimension appears to be unaffected by swirl. However, our results emphasise that swirl increases both the mean entrainment and the TNTI tortuosity. Altogether, these observations reveal the need to incorporate swirl to the actuator disc model to faithfully reproduce the wake of a wind turbine, both experimentally and numerically.

Analyse physique du sillage tournant d'un disque poreux : application aux éoliennes

Résumé

La production d'énergie éolienne, élément fondamental du portefeuille d'énergies renouvelables, a connu une croissance exponentielle ces dernières années. À cause de la limitation des sites dits à fort potentiel éolien, les turbines sont généralement regroupées dans des parcs éoliens, dont la production d'énergie est entravée par les interactions entre sillages. Par conséquent, prédire l'évolution du sillage éolien est d'une importance cruciale. À cette fin, des études fondamentales sont nécessaires pour apporter une compréhension fine de la physique sous-jacente des sillages d'éoliennes. Les disques poreux sont des dispositifs populaires utilisés pour imiter le sillage des éoliennes à l'échelle du laboratoire. Jusqu'à présent, les disques poreux ont été conçus en ajustant un seul paramètre physique, leur porosité, dans le but de reproduire le déficit de vitesse d'une éolienne cible. Cependant, cette approche simpliste exclut une caractéristique clé des sillages éoliens : le taux de rotation (*swirl*). Ce travail aborde cette problématique en étudiant en profondeur le rôle du taux de rotation sur le développement d'un sillage généré par un disque poreux. Pour ce faire, des expériences en soufflerie ont été menées pour mesurer le sillage d'un disque poreux modifié de telle sorte à intégrer passivement un taux de rotation. Il s'avère que le taux de rotation est un ingrédient clé pour atteindre l'auto-similarité du déficit de vitesse dans la région intermédiaire du sillage et correspond très bien aux données rapportées dans la littérature sur les éoliennes. Sur la base de la théorie de la turbulence hors-équilibre, une nouvelle loi d'échelle pour la décroissance du taux de rotation est dérivée et montre une très bonne concordance avec les données collectées. Enfin, l'entraînement turbulent à l'interface turbulent/non-turbulent (TNTI) est analysé en utilisant des données PIV hautement résolues. Une technique de détection améliorée basée sur les zones de quantité de mouvement uniforme est développée pour détecter avec précision la TNTI, dont la dimension fractale ne semble pas être modifiée par la rotation. Cependant, nos résultats soulignent que le taux de rotation augmente à la fois l'entraînement moyen et la tortuosité de la TNTI. Ces observations révèlent la nécessité d'incorporer désormais le taux de rotation dans le modèle de disque actuateur pour reproduire fidèlement le sillage d'une éolienne, aussi bien sur le plan expérimental que numerique.

Contents

1

Introduction and state of the art

Contents

This chapter sets the scope of this work in the thematic of wind energy and provides an overview of the current state of the art regarding wind turbine wakes. First, the global energy crisis is briefly discussed as well as the relevance of wind energy in the renewable energy portfolio. Subsequently, attention is turned to the intricacies of the wind farm layout optimisation problem, emphasising the critical role of wake modelling. Afterwards, the wind turbine wake is presented in detail and the different aerodynamic phenomena occurring in this specific flow are reviewed. To follow up, the actuator disc concept is introduced through the use of porous discs, strategically employed to simplify wind tunnel experiments. The main limitations of the porous disc model are elucidated with a focus on the generated wake and its main differences with wind turbine wakes. Finally, the knowledge gaps are clearly stated and the manuscript content is outlined with the objectives and our positioning in the problem.

1.1 Context: Climate change and the grand energy challenge

Climate change is one of the most significant global challenges that modern civilisation has to face today, and its impacts are becoming increasingly severe (Pörtner et al., 2022). As shown in the famous "hockey stick graph" of Mann et al. (1999) (figure 1.1), there is an undeniable anthropogenic forcing in global temperature trends since the industrial revolution (1760 - 1840). To tackle this major challenge, nations across the world gathered in 2015 and agreed to do everything in their power to reach carbon neutrality by 2050 (Schleussner et al., 2016). This historic gathering, known as the Paris Agreement, set a symbolic threshold to limit the global temperature increase to below 2°C. In a recent report (Pörtner et al., 2022), the IPCC[1] reaffirmed the pressing nature of this issue and emphasised the severe repercussions that would ensue if nations neglect to take decisive action.

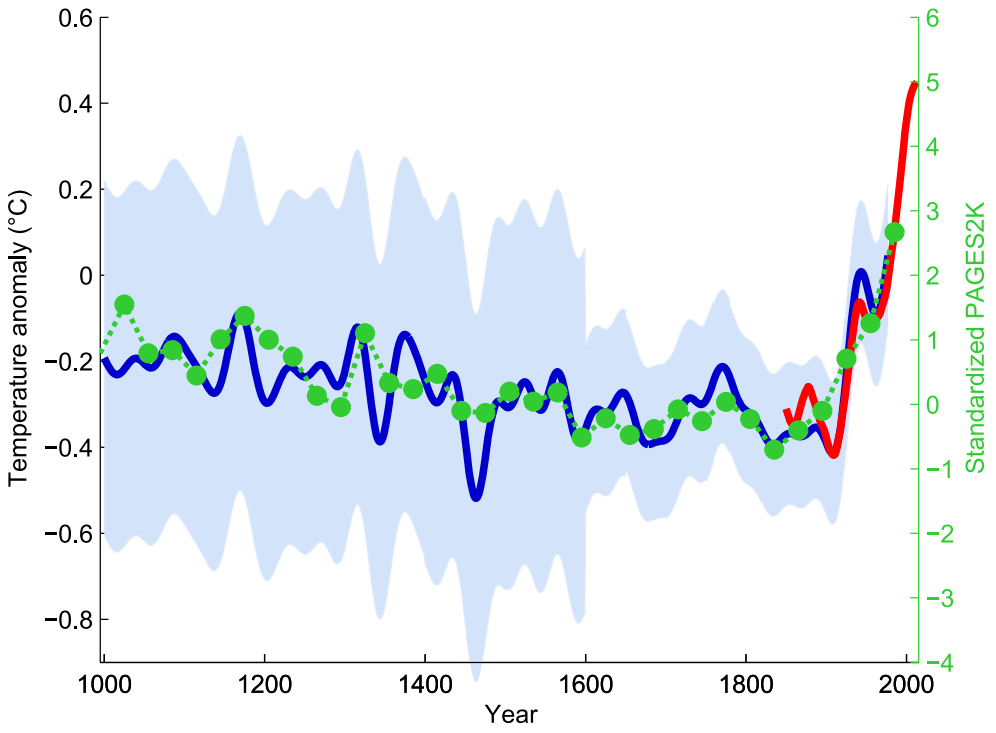

Figure 1.1: The original northern hemisphere temperature anomaly hockey stick graph of Mann et al. (1999) which provided compelling evidence of man-made influences on temperature trends. Smoothed curves shown in blue with its uncertainty range in light blue. Green dots : 30-year global average. Red curve: measured global mean temperature, according to HadCRUT4[2]data set from 1850 to 2013.

[1]Intergovernmental Panel on Climate Change

[2]Hadley Centre/Climatic Research Unit Temperature.

1.1.1 The energy transition challenge: from fossil fuels to renewable sources

In the framework of combating climate change, the critical role of renewable energies is of the utmost importance. The energy consumption has rapidly increased in the last century due to the social and economic development of an ever-growing society. Figure 1.2 shows the global primary energy consumption by source since the start of World War II. This graph takes into account all types of energy consumption (electricity generation, heat sources, mechanical energy) and highlights the swift surge in energy consumption but most importantly the strong dependency on fossil fuels.

Relying heavily on fossil fuels for energy poses a myriad of perilous consequences that extend beyond environmental concerns. The combustion of fossil fuels, such as coal, oil, and natural gas, releases substantial amounts of greenhouse gases into the atmosphere, contributing significantly to climate change (Olivier et al., 2012). This not only results in rising global temperatures, as famously discussed in Mann et al. (1999), but also leads to more frequent extreme weather events, sea level rise, and disruptions to ecosystems (Hardy, 2003). Moreover, the extraction and transportation of fossil fuels are associated with environmental degradation, including habitat destruction and water pollution (Butt et al., 2013). Beyond environmental implications, dependence on fossil fuels also subjects economies to geopolitical vulnerabilities and price fluctuations (Tol, 2009). On top of everything, the health impacts of air pollution from burning fossil fuels, with its links to respiratory diseases and premature deaths (Sommer, 2016), reaffirm the urgency of transitioning towards cleaner, renewable energy sources to safeguard both the planet and human well-being.

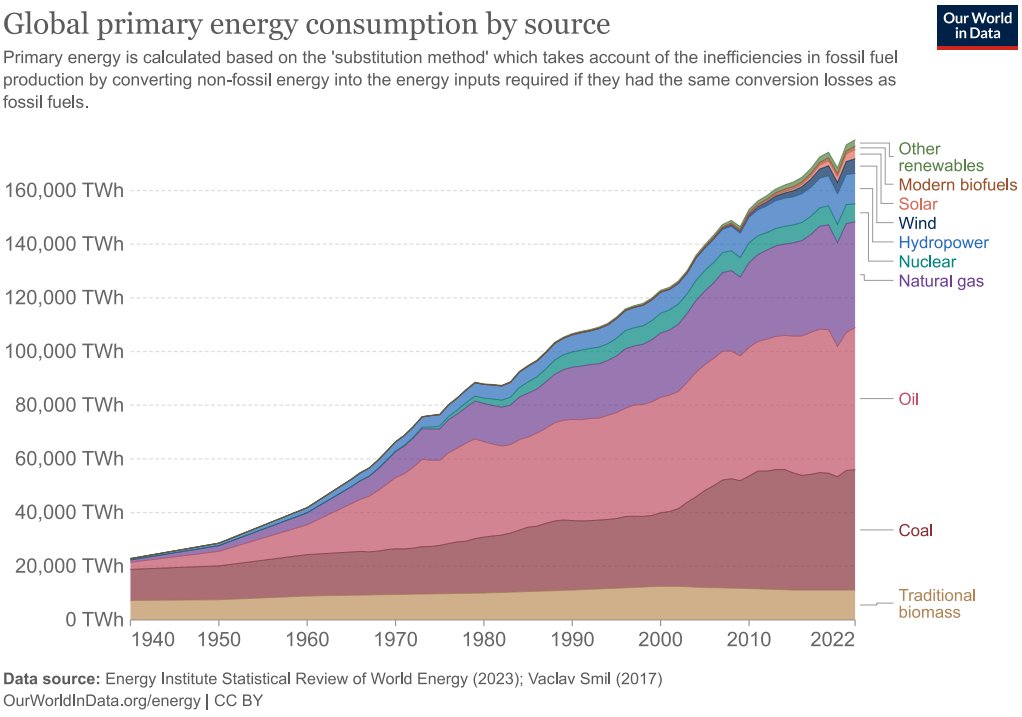

Figure 1.2: Global primary energy consumption evolution by source from 1940 to 2020. Taken from Ritchie et al. (2020).

1.1.2 Electricity mix evolution: slow and steady progress

Following Dincer (2000), renewable energy sources are sustainable, naturally occurring resources that can be harnessed to generate power without risking their depletion. Some examples include solar energy, which captures sunlight using photovoltaic cells (or thermal systems); hydroelectricity, which converts the energy of flowing water into electricity; geothermal energy, biomass, and wind energy, generated by harnessing the kinetic energy of wind with the use of wind turbines. These sources offer an environmentally friendly alternative to conventional energy production, emitting minimal or no greenhouse gases and mitigating the negative impacts associated with fossil fuel combustion. The development and widespread adoption of renewable energy technologies play a central role when meeting the net zero goal discussed in the Paris agreement (Schleussner et al., 2016). Figure 1.3 shows the global electricity mix evolution from 2011 to 2021, a key aspect highlighted in the REN21 (2022) global status report, with a particular emphasis on the increasing proportion of renewable electricity. Over the course of this decade, there has been a noteworthy 8% rise in the share of renewables, driven by substantial growth in the installed power capacity of both solar and wind energy. Additionally, there has been a decline of 6% in the share of fossil fuels and a 10% reduction in nuclear power. These trends underscore a global shift towards reducing reliance on fossil fuels and nuclear energy, accompanied by significant investments in renewable sources.

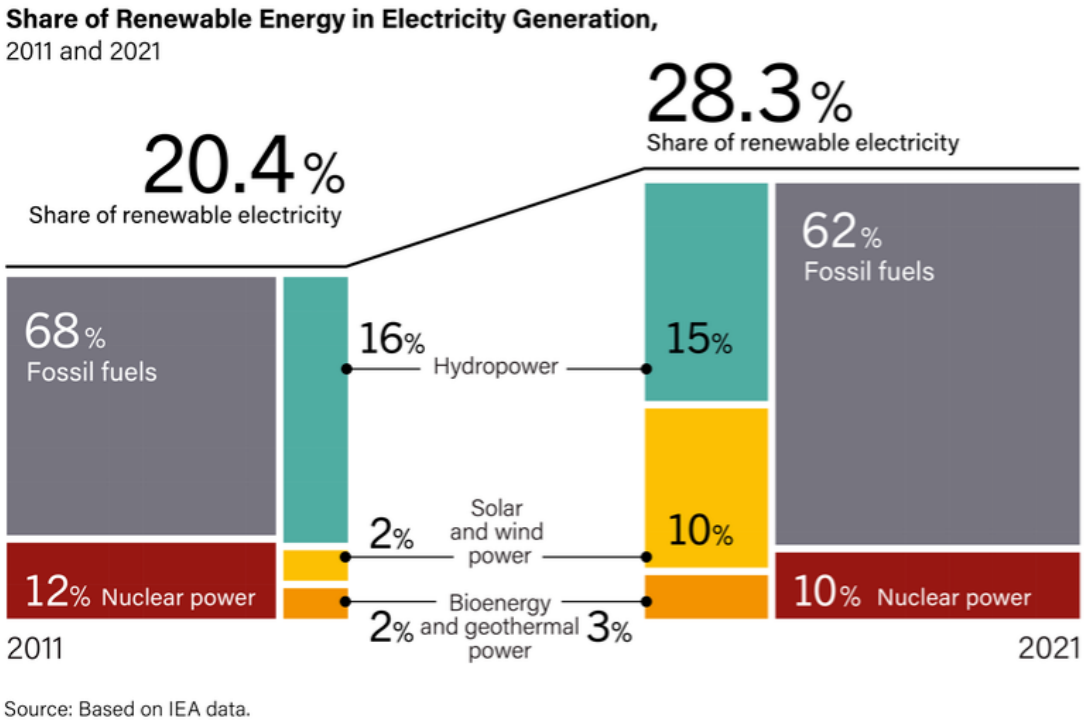

Figure 1.3: Global electricity mix evolution from 2011 to 2021 showing recent progress in the energy transition global project. Taken from the REN21 (2022) global status report.

1.2 Wind Energy

1.2.1 The untapped potential of wind energy

In recent decades, wind energy has emerged as a highly promising renewable source, earning increased attention and popularity due to its many benefits and largely untapped potential. A compelling evidence to this advancement lies in the remarkable growth of the wind energy sector following the Paris Agreement (2015). Figure 1.4 illustrates this surge, revealing a staggering 176% increase in the installed wind capacity in both onshore and offshore wind farms from 2015 to 2023. This trend reveals the remarkable growth of this particular energy sector with the aim to reach above 2750 GW in the total installed capacity by the year 2030.

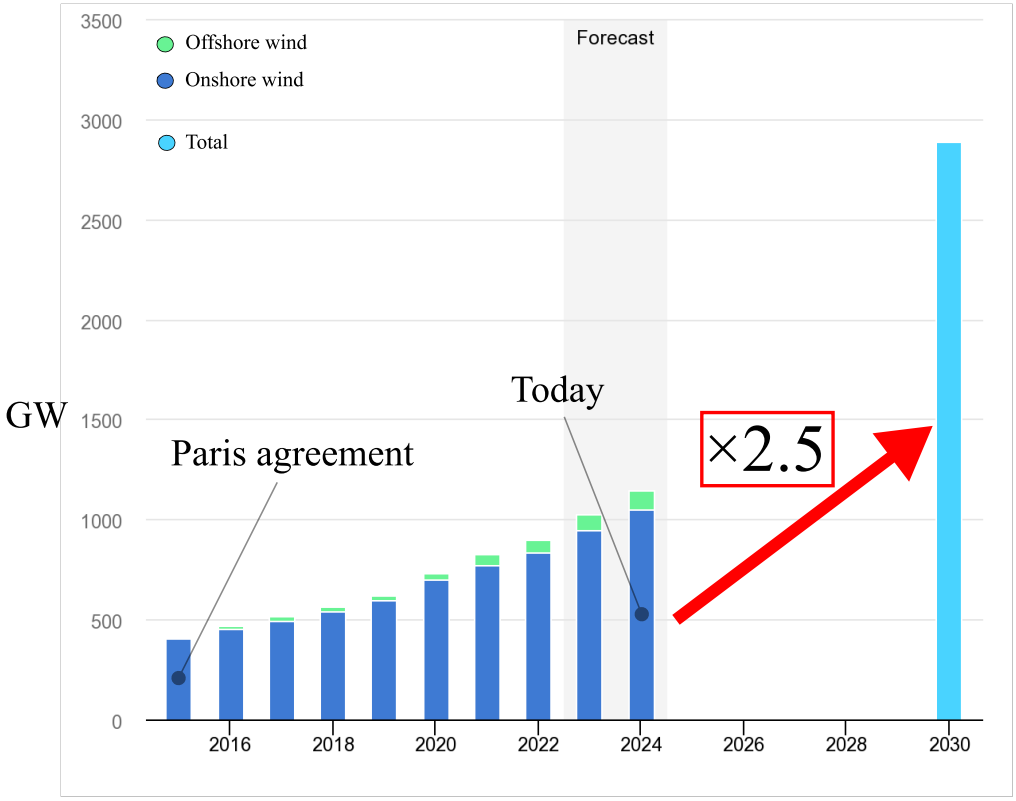

Figure 1.4: Wind power capacity evolution since the Paris agreement and forecast to reach the 2030 goal in the net zero scenario. Adapted from the renewable energy market update reported by the IEA (2023)[3].

The numbers vary from country to country but Europe has shown an exemplary growth in terms of wind farm installations (Soares-Ramos et al., 2020). In France, according to the ministry of energy transition ("*Ministère de la transition énergétique*"), there are currently four main large-scale wind energy projects: *Saint Nazaire* (480 MW), a 78 km^2 offshore wind farm of 80 wind turbines put in service in 2022; *Saint-Brieuc* (496 MW) a 75 km^2 offshore wind farm of 62 wind turbines expected to start generating clean energy in 2023; *Courseulles-sur-mer* (448 MW) and *Fécamp* (497 MW), both offshore wind farms expected to be put in service between 2024 and 2025. Future projects like "*Centre Manche 1 & 2*" in Dunkirk (2031-2032), also show that wind energy has a

[3]International Energy Agency. Market report updated on June 2023.

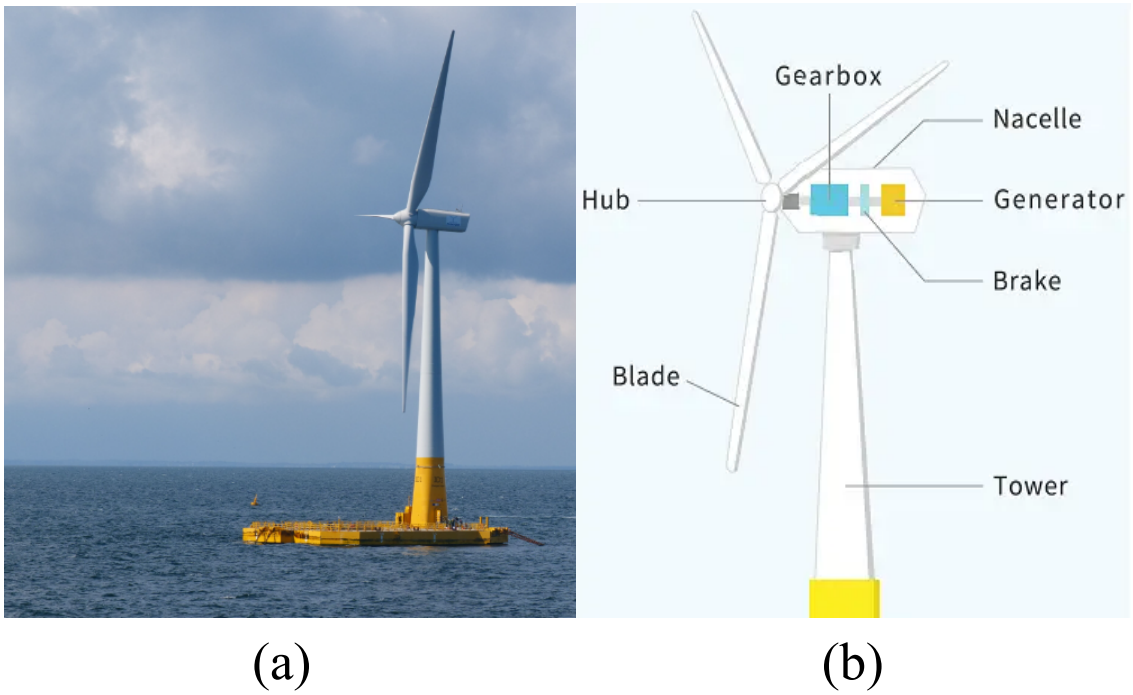

Figure 1.5: (a) Photograph of the FLOATGEN 2MW wind turbine: the first offshore floating wind turbine installed in France and (b) a diagram showing the main components of a HAWT. Photo credits: *Ecole Centrale de Nantes*. Diagram credits: "Your electrical guide".

promising and exciting future with increasingly larger installations ($\sim 1GW$). In light of the rapid growth in this sector, it is of capital importance to tackle the scientific problems that arise in these wind farms. In fact, a comprehensive examination of the involved physics (aero-servo-elasticity, wake aerodynamics, turbulence, structural resistance) and complexities that may emerge becomes essential to ensure the efficiency, reliability, and sustainability of these wind energy installations.

1.2.2 Wind turbines working principle

Wind turbines are structures engineered to harness the kinetic energy of wind and transform it into electricity. Wind turbines come in various sizes, from small-scale models suitable for residential use to massive industrial installations. Nowadays there are two main types of wind turbines: vertical axis wind turbines (VAWTs) and horizontal axis wind turbines (HAWTs). VAWTs are less frequently installed in large wind farms and are out of the scope of this work which focuses on HAWTs. Following figure 1.5, the most common configuration for a HAWT is a tall cylindrical tower with three rotor blades. The rotor is connected to a shaft connected to a generator, producing electrical power. The pitch of the blades and TSR[4] are then adjusted to optimise the power output of the generator. This parameter is defined as:

$$TSR = \frac{\Omega R}{U_\infty}, \tag{1.2.1}$$

where Ω is the rotational speed of the rotor, R is the radius of the rotor and U_∞ is the

[4]Tip Speed Ratio.

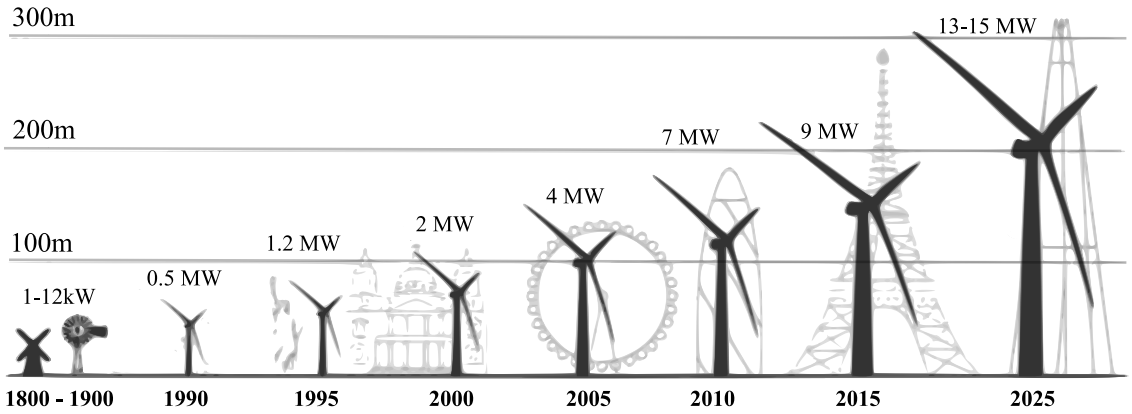

Figure 1.6: Time evolution of the size and power capacity of HAWTs compared to different landmarks. Adapted from Pisanò (2019).

velocity of the incoming wind. This parameter is not restricted to wind turbines only since it is an industrial control parameter relevant for a whole class of rotating bodies immersed in a fluid: wind turbines, propellers and helicopters for instance. The higher the TSR, the higher the effective blockage of the rotor with respect to the incoming flow. The reader is referred to the Wind Energy Handbook of Burton et al. (2011) for a comprehensive look on wind turbine working principles and operation.

Since the dawn of wind energy (early 19^{th} century) wind turbines have grown in size and in number to answer the evidenced escalating energy demands and to elevate the contribution of renewable energy sources to the overall energy mix. Over the years, wind turbines have undergone significant advancements in technology, design, size and efficiency, reflecting the ongoing commitment to harnessing the power of the wind as a sustainable source of electricity. As shown in figure 1.6, the rotors are getting bigger in size along with their individual power output. This trend is explained by the fact that larger rotor blades collect more energy and taller towers reach higher altitudes in the ABL where more energetic winds can be found. This means that every year, bigger, better and many more wind turbines are being built and put in service. Nevertheless, as discussed in the following section, the ascent in size and quantity brings with it a corresponding escalation in challenges and limitations.

1.2.3 Wind energy's limitations

First and foremost, the available power which can be extracted by a HAWT is directly proportional to the cube of the incoming wind speed (Burton et al., 2011). The efficiency of a wind turbine is characterised by the power coefficient, a dimensionless parameter defined as:

$$C_{pwr} = \frac{\mathcal{P}}{\frac{1}{2}\rho U_\infty^3 A}, \tag{1.2.2}$$

where $\mathcal{P}$ is the rotor power, ρ the air density and A the area swept by the rotor. An important limit to HAWTs is the theoretical Betz limit, historically derived by Betz (1919) which caps the extracted power to 59% of the available wind power. Furthermore, due to the limited regions of the world with strong uninterrupted wind, HAWTs are usually clustered together in wind farms. Figure 1.7 shows an example of such wind farms: the Horns Rev 1 wind farm located in the North Sea near the Danish

Figure 1.7: Photography of the Horns Rev 1 wind farm. Photography taken by C. Steiness for Vattenfall. Taken from Hasager et al. (2013).

coastline. Organising the HAWTs in such a manner is a good way to minimise installations, operation and maintenance costs. However, this configuration comes at the cost of diminished power output and performance for each turbine (Porté-Agel, 2019). The reason behind this is that all turbines, except those positioned at the forefront of the wind farm, will experience partial or complete immersion in the wake generated by the upstream wind turbines.

As summarised in Vinnes (2023), the typical spacing between farms ranges from 5 to 10 rotor diameters. Therefore, the downstream turbines will have less available momentum compared to their pairs at the front which are exposed to the (mostly) undisturbed atmospheric boundary layer (ABL), reducing their power output (Barthelmie and Jensen, 2010; Porté-Agel, 2019). To give a few numbers, Adaramola and Krogstad (2011) found in their experiments that a HAWT directly downstream of another would suffer losses up to 45% in the maximum power coefficient. Moreover, higher turbulence intensity of the HAWT wakes increases the mechanical loads on the downstream turbines whose gearbox wears quicker (Thomsen and Sørensen, 1999). Furthermore, the total blockage of the wind farm itself is now becoming a problem as wind farms become larger. Instead of flowing around each wind turbine, the flow reacts to the wind farm as a whole and circumvents it, leading to a decreased power output (Bleeg et al., 2018). Altogether, these investigations underscore the importance of furthering the scientific understanding of wind farm flows using field measurements, wind tunnel experiments, analytical models and numerical simulations (Porté-Agel, 2019).

1.3 The wind turbine wake

As outlined in the comprehensive review conducted by Porté-Agel (2019) regarding wind farm flows, the wind energy problem encompasses a large list of scales (see figure 1.8) that evolve from the smallest wind turbine airfoil scales, to the large wind farm scales which are reaching planetary wave-like scales and even locally affecting the weather (Barrie and Kirk-Davidoff, 2010). The wind farm, interacts with the ABL which has properties of its own like stratification and instabilities (Porté-Agel et al., 2011). As wind farms span an increasingly larger area, they act as a canopy and are

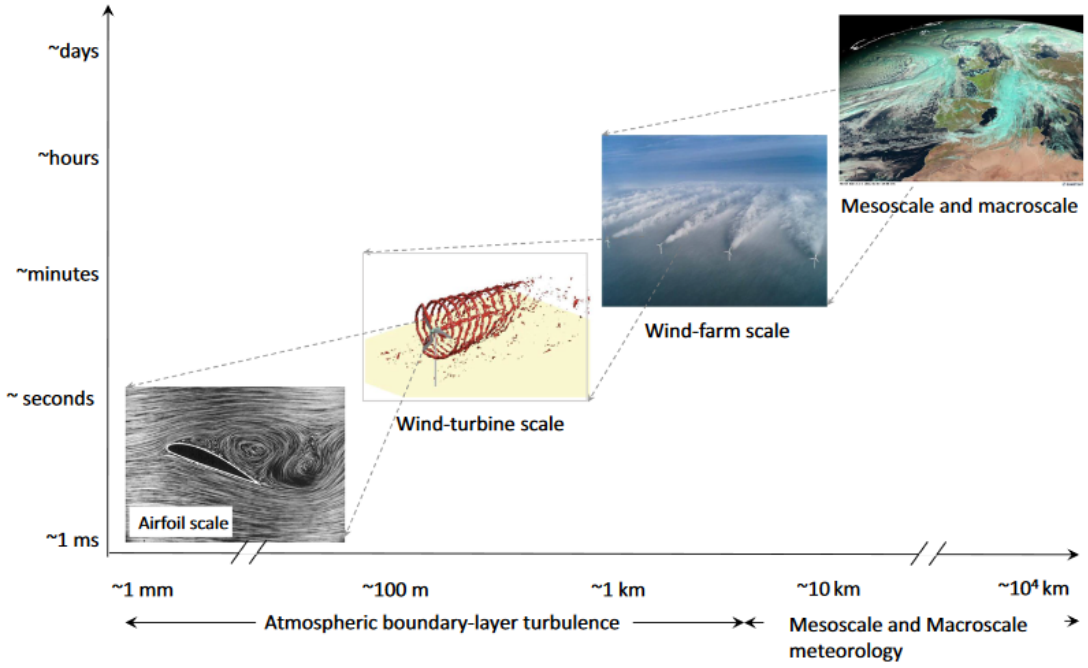

Figure 1.8: Schematic showing the wide range of flow scales relevant to wind energy. From the turbine blade scale to the planetary scale. Taken from Porté-Agel (2019).

seen as roughness elements by the ABL. In addition, the wind farm itself has a particular flow inside as the wind turbines will be positioned in arrays or in staggered formation depending on the employed layout strategy. To illustrate this point, an example of an LES[5] study of the mean flow around a wind farm are shown in figure 1.9. The colormap shows the normalised mean streamwise velocity of two wind farm flows with either an aligned or a staggered distribution, respectively. As discussed in Wu and Porté-Agel (2013), depending on the chosen layout and separation distances, the wakes will interact differently thereby altering the wind farm power output (Troldborg et al., 2011; Spera, 1994). To understand how wakes interact with each other in a wind farm configuration, the wake itself has to be fully characterised and the underlying key parameters have to be determined. Therefore, the focus of this work is on the development of the wake of a single wind turbine.

Many wind turbine and wind farm investigations jump straight to the more sophisticated concepts like meandering, yaw control, wake steering, wind farm optimisation while obviating the main attraction: the wake itself. As shown in figure 1.10 the fundamental fluid mechanics element making up the wind farm problem is the wake of the wind turbine. This brings us to the first question to be asked: what is a wake? According to the Oxford dictionary it is "the track left on the water's surface by a ship". However, a more general definition can be given from a fluid mechanics standpoint. Actually, many answers can be given to that fundamental question from different fluid mechanics perspectives (stability, similarity, inviscid theory, rarefied flows). A more accurate definition of a wake could be: the region of disturbed flow that forms downstream of an object in relative motion to an ambient fluid in which it is immersed. The wake has been studied since the dawn of science (Aristotle, Euclid, Galileo), throughout the years (Da Vinci, Marriott, Huygens, Cayley) until modern times where it has become a canonical problem of fluid mechanics and turbulent flows (Pope, 2000).

[5]Large Eddy Simulations.

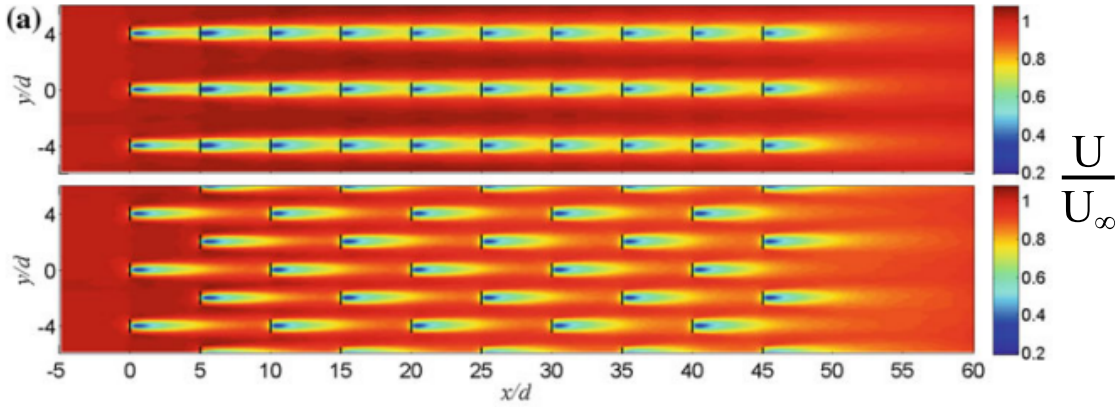

Figure 1.9: LES contours of the normalised mean streamwise velocity U/U_∞ of the flow inside a wind farm in aligned (top) and staggered (bottom) formations, respectively. Taken from Wu and Porté-Agel (2013).

The turbulent wake in particular has constituted the basis of a myriad of fundamental analyses which aimed at explaining the wake development in the downstream direction (Champagne, 1978; Johansson et al., 2003; Redford et al., 2012). In fact, the turbulent wake is one of the main free-shear type of flows, along with jets and mixing layers. As presented in figure 1.10 the immersed body extracts momentum from the surrounding flow and, in the case of a HAWT, converts it into electrical power. Note that propellers perform the exact inverse operation by adding momentum to the flow through the rotation of their blades (Wald, 2006). In that case, the exerted force is thrust instead of drag. In this context, predicting how the wake evolves in the downstream direction is the crux of wind farm problems. This is in fact a part of a broader fluid mechanics challenge, which involves identifying the scaling laws or a family of scaling laws that govern the recovery and the expansion of wakes in general. Achieving this needs the precise definition of key parameters associated with the wake. Figure 1.10 shows these main parameters emphasised in momentum theory (Tennekes and Lumley, 1972) which are the drag coefficient of the body C_D, the velocity deficit $\Delta U = (U_\infty - U)$ and a characteristic length scale of the flow δ. In particular, C_D is defined as:

$$C_D = \frac{F_D}{\frac{1}{2}\rho U_\infty^2 A}, \tag{1.3.1}$$

where F_D is the drag force experienced by the body. The wake is (mostly) characterised by its velocity deficit ΔU and its characteristic length scale δ. Following Tennekes and Lumley (1972), the conservation law linking the body drag to the wake is given by:

$$\boxed{C_D = \int U^* \Delta U^* dA^*}, \tag{1.3.2}$$

where ΔU^* is the mean streamwise velocity deficit normalised by the free-stream velocity U_∞. The characteristic length scale δ is then usually associated to the integral wake's width defined as:

$$\delta^2(x) = \frac{1}{U_s(x)} \int_0^\infty (U_\infty - U) r dr, \tag{1.3.3}$$

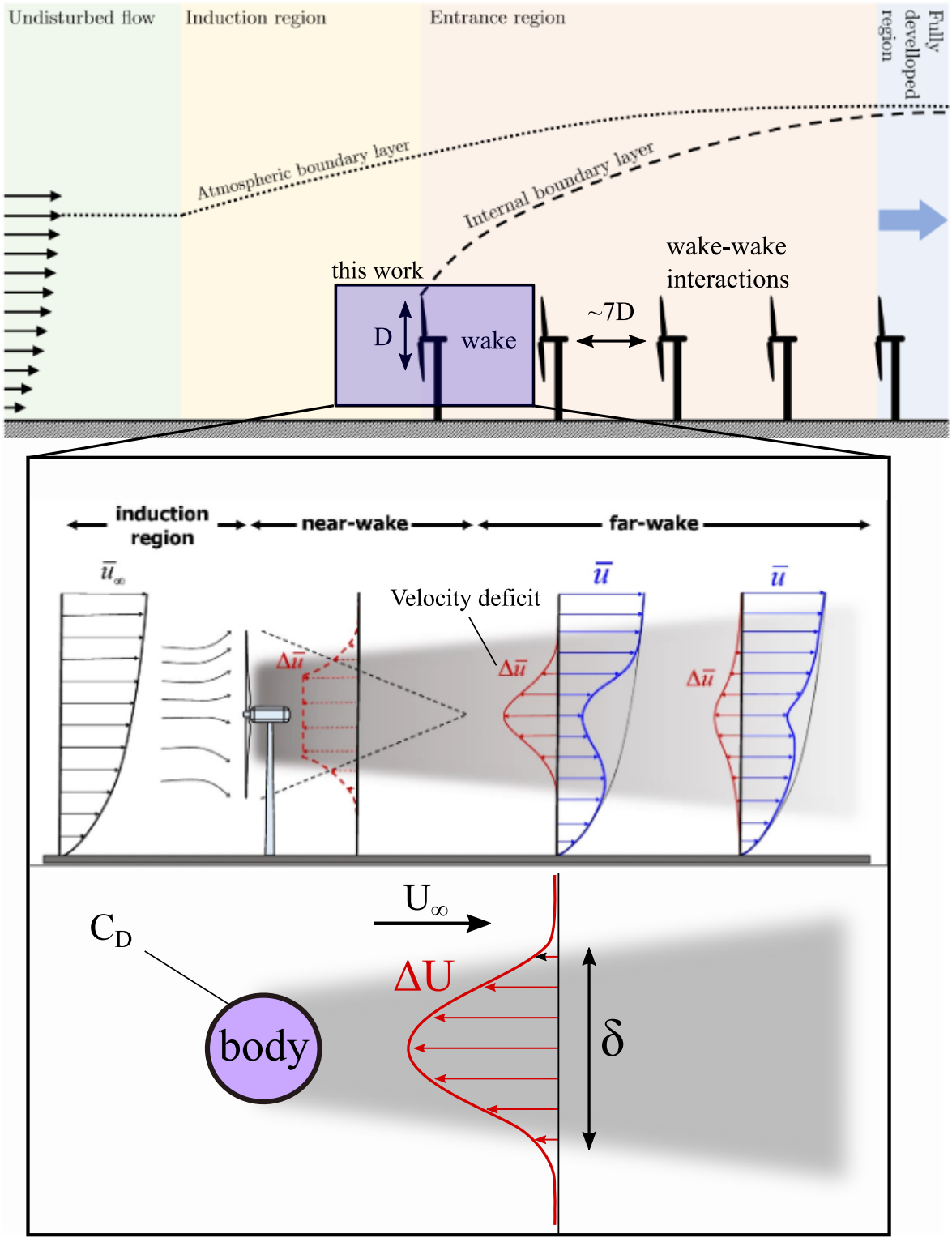

Figure 1.10: Schematic illustrating the wind farm problem and its intricacies. A wind farm is depicted as well as the mean wake of a wind turbine and the mean wake of a shapeless body. Adapted from Vinnes (2023) and Porté-Agel (2019).

where $U_s(x) = U_\infty - U(x, r = 0)$ is the centreline velocity deficit and r is the radial coordinate. The wake's recovery is related to the evolution of the velocity deficit which decays with the downstream distance (Townsend, 1976) and the wake expansion is related to the downstream increase of δ in accordance to the fundamental law (1.3.2). In wind energy terminology, we refer to thrust rather than drag, but for the sake of clarity and consistency, only drag will be used in the remainder of the manuscript. In any case, equation (1.3.2) poses the wake problem and underscores the importance of modelling ΔU and predicting its downstream evolution along with the characteristic length scale δ. There is a fundamental analytical prediction found in equilibrium similarity theory (Townsend, 1976) which stipulates that $\delta \sim x^{1/3}$ and $\Delta U \sim x^{-2/3}$ but is based on strong hypotheses about turbulence. This particular point is addressed in the next chapter. In any event, the straightforward characteristic of equation (1.3.2) is what motivated the scientific community of wind energy to investigate the mean flow velocity deficit distribution in the far field of HAWT wakes using field measurements (Barthelmie et al., 2006; Iungo et al., 2013; Käsler et al., 2010); laboratory wind tunnel experiments (Chamorro and Porté-Agel, 2010; Aubrun, 2013; Aubrun et al., 2019; Wu and Porté-Agel, 2012; Camp and Cal, 2016; Vinnes et al., 2022; Helvig et al., 2021; Howland et al., 2016; Lignarolo et al., 2016b) and numerical simulations (Wu and Porté-Agel, 2013; Bénard et al., 2018) to quote a few noteworthy investigations. Equation (1.3.2) not only set the scope of experimental measurements and simulations on the mean flow distribution but also served as the foundation for numerous analytical models addressing wind turbine wakes, a subject that will be explored in the next section.

1.4 Analytical wake modelling

As discussed in earlier sections, wind farm layout planning and wind farm optimisation require the knowledge of wake flows and their prediction to test several scenarios and configurations. However, as shown in figure 1.8, the sheer range of scales involved in wind farm flows is so colossal that performing precise simulations like LES and DNS[6] of full wind farms is practically impossible. Even with current HPC[7] calculations becoming more and more capable, high-fidelity simulation of a wind farm still requires a number of CPU hours incompatible with the industrial needs (Porté-Agel, 2019). This type of optimisation process at the industrial scale therefore relies on simple and computationally inexpensive wake models.

There are mainly two types of analytical wake models: empirical models and physical models. Empirical models are usually the simplest and solely rely on the fitting of experimental and numerical data assuming a simple mathematical function for the mean flow distribution (Högström et al., 1988; Magnusson and Smedman, 1999; Baker and Walker, 1984). These models rely on strong fluid mechanics assumptions regarding wakes, and while they can be optimised for specific cases or wind farm configurations, their adaptability to evolving scenarios or diverse layouts is frequently limited.

On the other hand, analytical models stand on physical grounds and are derived from the governing equations of motion. By nature, they are inherently more capable at capturing the intricate physics of wind turbine wakes. As discussed in Bastankhah and Porté-Agel (2014); Porté-Agel (2019) there is a myriad of different studies which

[6]Direct Numerical Simulations.

[7]High Performance Computation

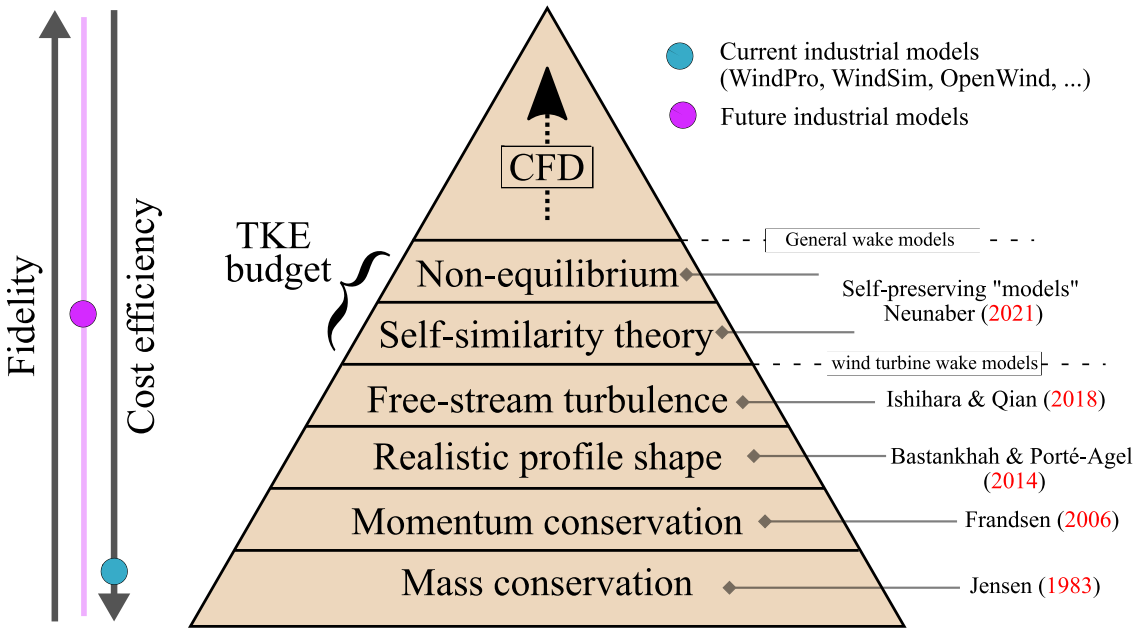

Figure 1.11: Schematic showing some of the existing analytical wake models and the physical laws in which they are based on. CFD: Computational Fluid Dynamics.

have proposed different analytical models like Jensen (1983); Frandsen et al. (2006); Bastankhah and Porté-Agel (2014); Ishihara et al. (2004). The reader is referred to the recent comprehensive review of these models found in Kaldellis et al. (2021). In particular, Jensen (1983) derived the pioneering wake model based on mass conservation which is currently used in most commercial software to predict wind farm power outputs (e.g., WAsP, WindPRO, WindSim, OpenWind).

Figure 1.11 presents the analytical models which have shown consistent improvements and have added more physical elements to their structure. To give a brief overview of two of the main models: the so-called Jensen model (Jensen, 1983) is obtained by performing a mass budget over a control volume directly downwind of the wind turbine (Tennekes and Lumley, 1972). The Jensen model then assumes a top-hat shape for the distribution of the normalised mean velocity deficit ΔU^*. Following Jensen (1983) the velocity deficit model is given by:

$$\Delta U^* = \frac{1 - \sqrt{1 - C_D}}{(1 + 2k_t x/D)^2}, \tag{1.4.1}$$

where x is the streamwise direction, D is the rotor diameter and $k_t =$ is the wake growth rate. There is a significant scatter in the values found for k_t (Göçmen et al., 2016) since it depends on many other flow properties filtered by the model. In any case, this model is based on the assumption that the wake expands linearly $\sim x$. In later years, Frandsen et al. (2006) improved upon the Jensen (1983) model to account for momentum conservation using the same top-hat shape for the velocity deficit distribution to yield:

$$\Delta U^* = \frac{1}{2}\left(1 - \sqrt{1 - \frac{2C_D}{A + k_t x/D}}\right), \tag{1.4.2}$$

where A is defined as:

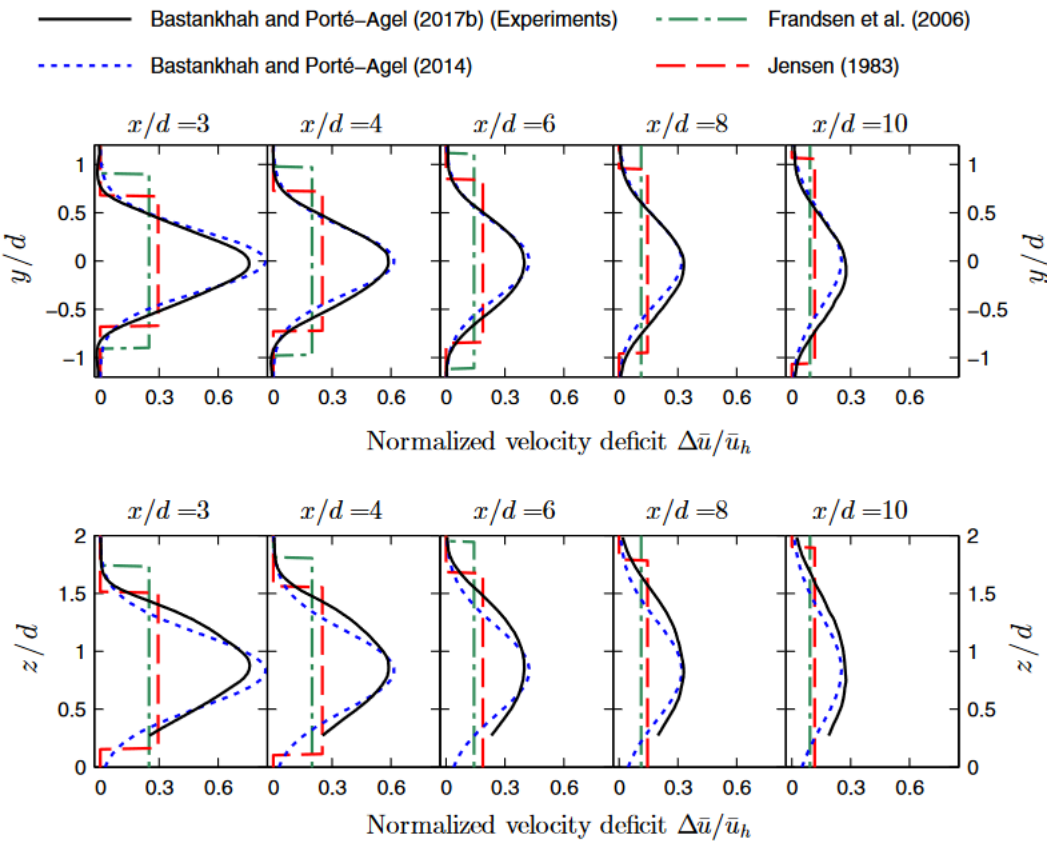

Figure 1.12: Comparison of the Jensen (1983), Frandsen et al. (2006) and Bastankhah and Porté-Agel (2014) models and experimental data points (Bastankhah and Porté-Agel, 2017). Lateral and vertical profiles of the mean streamwise velocity deficit normalised by the velocity at hub level at different streamwise locations are shown. Taken from Porté-Agel (2019).

$$A = \frac{1+\sqrt{1-C_D}}{2\sqrt{1-C_D}}. \tag{1.4.3}$$

In this model, the wake growth is yet again based on an assumption, this time as $\sim x^{1/2}$. Both of these models assume a top-hat distribution for ΔU^* which were shown to underestimate the velocity deficit at the wake centre and overestimate it at the edges of the wake (Bastankhah and Porté-Agel, 2014). Since the power coefficient of the wind turbine is proportional to the cube of velocity (equation 1.2.2), these slight deviations can result in large errors when computing the available power for the HAWT. Furthermore, no physical analysis is given as to the chosen expansion rate of the wake. A fairly recent model was derived in Bastankhah and Porté-Agel (2014) which has become a very popular model due to its accuracy (Kaldellis et al., 2021) and consistency (see figure 1.12). Bastankhah and Porté-Agel (2014) showed that a self-similar Gaussian distribution captures the real velocity profiles in the wake of a wind turbine with reasonable deviations. In this model ΔU^* is given by:

$$\Delta U^* = C(x)\exp\left(-\frac{r^2}{2\sigma^2}\right), \tag{1.4.4}$$

where $C(x)$ is the maximum velocity deficit at each streamwise location and σ is the gaussian standard deviation. More details on this particular model can be found in

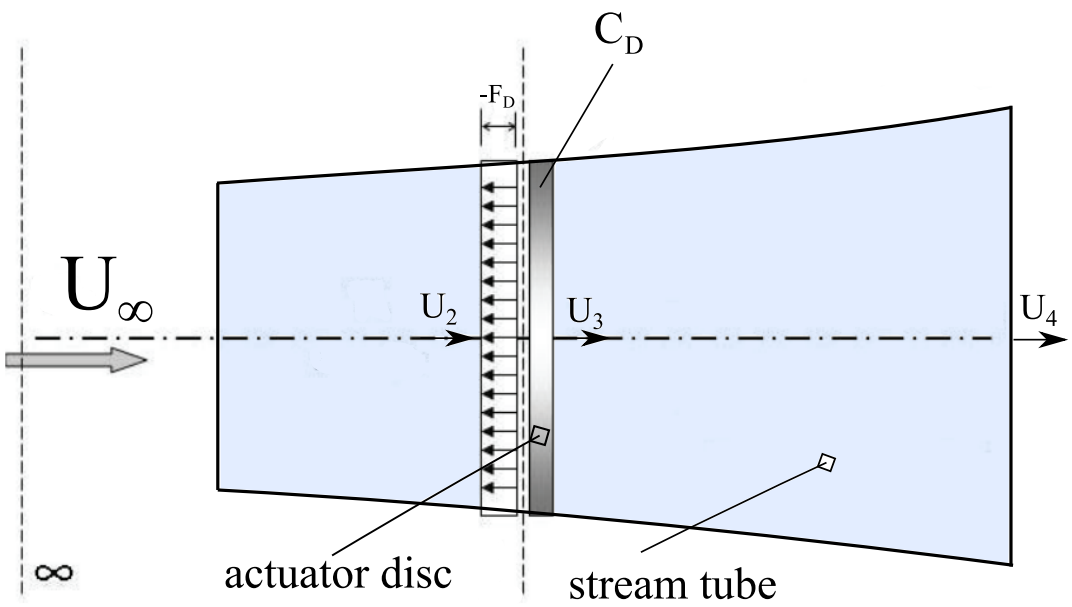

Figure 1.13: Schematic of the actuator disc concept exerting a force $-F_D$ distributed uniformly over the area swept by a HAWT rotor resulting in a drag coefficient C_D. Adapted from Crasto et al. (2012).

Bastankhah and Porté-Agel (2017) as it has proven to be one of the most accurate models to date. However, this model assumes a linear expansion rate as the Jensen (1983) model without a physical explanation. However, this study highlighted the need for further fundamental studies regarding the wake growth. The author mentioned the $\sim x^{1/3}$ growth rate predicted by equilibrium similarity theory (Tennekes and Lumley, 1972) but did not elaborate further as the data did not collapse with this prediction. A crucial shared characteristic among all these models is the omission of detailed representations of a wind turbine such as a rotor with blades, a nacelle, hub, tower etc. Such intricate features are typically reserved for the more costly and realistic numerical simulations. Instead, the rotor is represented as an actuator disc which exerts an equivalent force to the control volume in the momentum budget that yields a wake comparable to the wind turbine wake.

1.5 The actuator disc concept: a wind turbine surrogate

1.5.1 The actuator disc model

The actuator disc (AD) concept is represented in figure 1.13. While only briefly outlined here, a thorough and comprehensive description of this widely known model can be found in the seminal work of Manwell et al. (2010). First, a control volume is delineated by the stream tube, encompassing the AD. The control volume is defined with an inlet positioned in the undisturbed inflow and an outlet situated downstream of the AD. Subsequently, the wind turbine rotor is conceptualised as an AD: an idealised disc with an equivalent swept area as the rotor, characterised by no thickness but enforcing a pressure drop across it. The AD model is based on several assumptions: the flow is steady, homogeneous, and incompressible; frictional drag is disregarded; there is no

rotation of the wake; and static pressure remains consistent across the control volume. In any case, this model is not only the basis for the aforementioned analytical models but has been extensively used as a digital surrogate in numerical simulations with acceptable accuracy (Stevens and Meneveau, 2016; Allaerts and Meyers, 2018).

1.5.2 The porous disc equivalent

One would think that the most straightforward way to study the wake of a wind turbine in the wind tunnel would be to make a small lab-scale rotating wind turbine. However, as pointed out in the seminal work of Sforza et al. (1981), modelling actual rotors that reproduce the range of power and drag coefficients at the correct TSR was not achievable without fundamentally altering the flow properties. In recent years, some rotating models have been developed and used in wind tunnels studies like the ones proposed in Bottasso et al. (2014); Campagnolo et al. (2016); Lignarolo et al. (2016b) or Berger et al. (2018); Camp and Cal (2016). Nevertheless, as highlighted in Canet et al. (2021), these models are not only costly but also fall short in accurately capturing the dynamics of a true-to-scale wind turbine. This inadequacy comes from the necessity for the model to rotate at significantly higher TSR to attain kinematic similarity, leading to a wake that deviates substantially from the actual flow. Recognising these limitations, Sforza et al. (1981) proposed an alternative based on the pioneering research on porous plates by Castro (1971): the porous disc, a physical equivalent of the actuator disc model. In fact, as discussed in Sforza et al. (1981) and shown in equation (1.3.2), the main factor in wake development is the drag coefficient, which has to be adequately modelled to mimic the wake of a wind turbine.

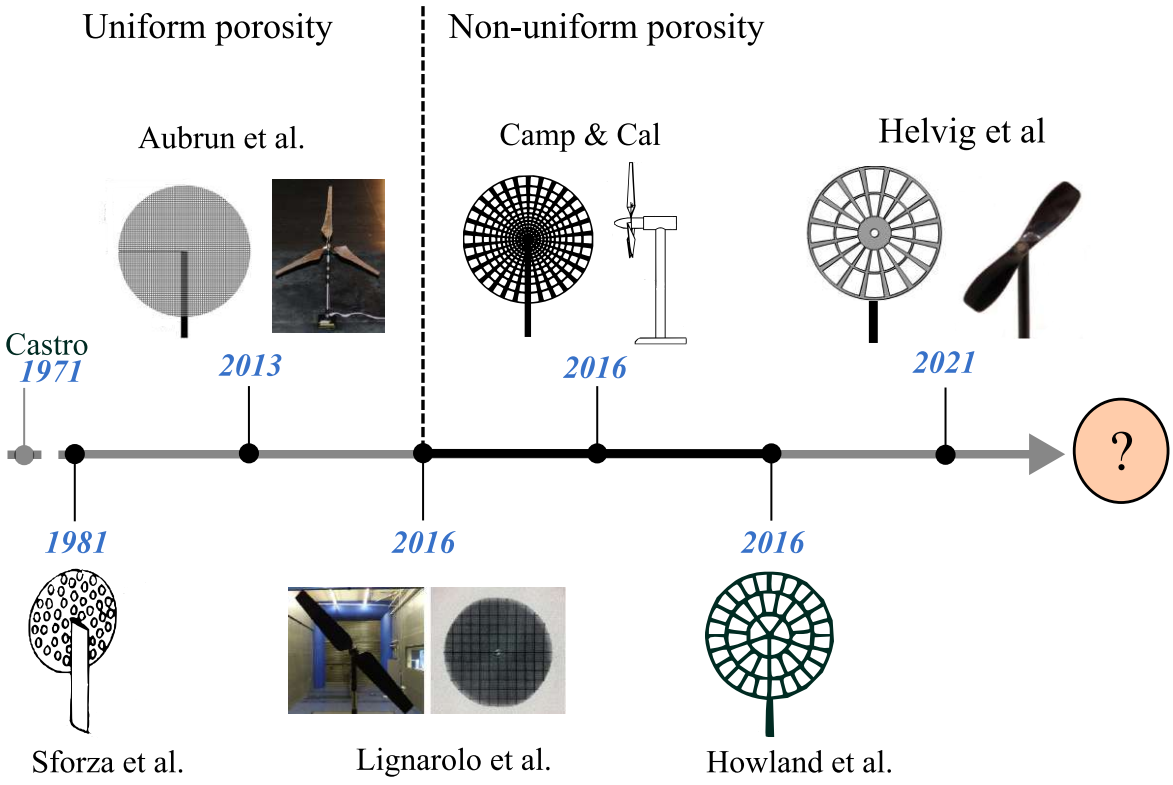

Figure 1.14: Chronology of the porous disc used as a wind turbine surrogate for wind tunnel experiments and corresponding references.

Ever since, the porous disc model has shown an evolution throughout the years which

is illustrated in figure 1.14. The first porous disc models were introduced by Sforza et al. (1981) and by Aubrun (2013) with a uniform porosity distribution. In particular, swirl was historically omitted from porous discs since the work of Sforza et al. (1981) who stated:

> "*since wake rotation is not considered to be one of the more important features of the re-energization of a wind turbine wake, it is felt that the thrust (drag) may be produced by an appropriate stationary model that has the correct geometric shape, permits flow-through, and allows an appropriate C_D variation. Such model characteristics can be provided by a porous disk...*" - Sforza et al. (1981)

This statement is indeed corroborated by equation (1.3.2) which shows that C_D has no asymptotic dependency on swirl whatsoever and is solely related to the mean velocity deficit. This is what set the main design process of porous discs (figure 1.14) and the aforementioned analytical models. In recent years, a non-uniform porosity was considered in Howland et al. (2016); Camp and Cal (2016) and in Helvig et al. (2021) to better represent the probability of presence of the rotor blades. Recently, Travis et al. (2022) and Öztürk et al. (2023) used the model proposed in Camp and Cal (2016) as wind turbine surrogates to study the effects of inertial particles in the wake and the effect of external turbulence, respectively. Despite a clear evolution towards a more complex design with the aim to better represent the blades of a wind turbine, the design process is still based on a single parameter: the porosity. In fact, porosity is a straightforward parameter to tune the drag coefficient of the porous disc without altering its global dimensions.

Recently, Aubrun et al. (2019) and Vinnes (2023) performed a detailed comparison of both types of porosity distribution in different facilities. The authors found some differences between the models and from test to test due to the changes in the initial conditions but collapsed reasonably well if enough distance was given for the wake to reach a self-preserving state. This emphasises the universality of axisymmetric wakes and their sensitivity to initial conditions underscored in Bevilaqua and Lykoudis (1978). In particular, Aubrun et al. (2019) showed that the wake of a porous disc could suffer a downwash effect depending on the experimental set-up which hindered the comparison between measurements. In fact, all of the porous disc models in current literature were designed with the aim to match the drag coefficient and dimensions of a target wind turbine and found a reasonably accurate collapse at around 3-5 rotor diameters from the object depending on the study. The authors then concluded that the best model was simply the one which showed self-similar collapse faster. However, according to equation (1.3.2), all porous discs with the same drag coefficient should generate a wake which evolves to the same universal asymptotic state. A more relevant way to reformulate these questions would be: What sets the virtual origin of the self-preserving wake? How fast is the asymptotic self-preserving state reached and what are the mechanisms that determine the rate at which it is reached? Some elements to answer this line of questioning are available in the work of Lavoie et al. (2007), Shiri et al. (2008) and Mazellier and Vassilicos (2010). These studies recognised the significance of initial conditions in influencing the virtual origin of the flow and eventually affecting the mechanisms described as "internal readjustments" by George (1989), which enable the flow to achieve complete self-preservation.

It is this questioning which motivated this work and the proposal of a novel porous disc.

1.6 Positioning of this work

1.6.1 The wind turbine wake: a multi-scale and multi-physics problem

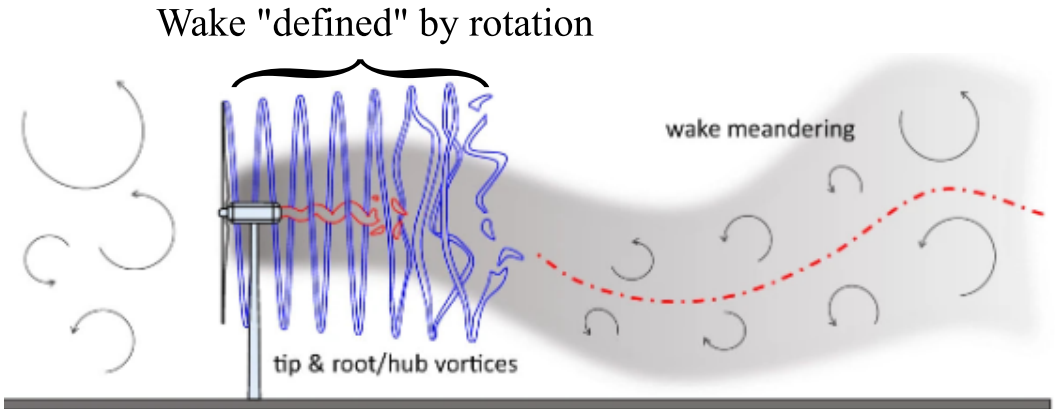

(a) Adapted from Porté-Agel (2019).

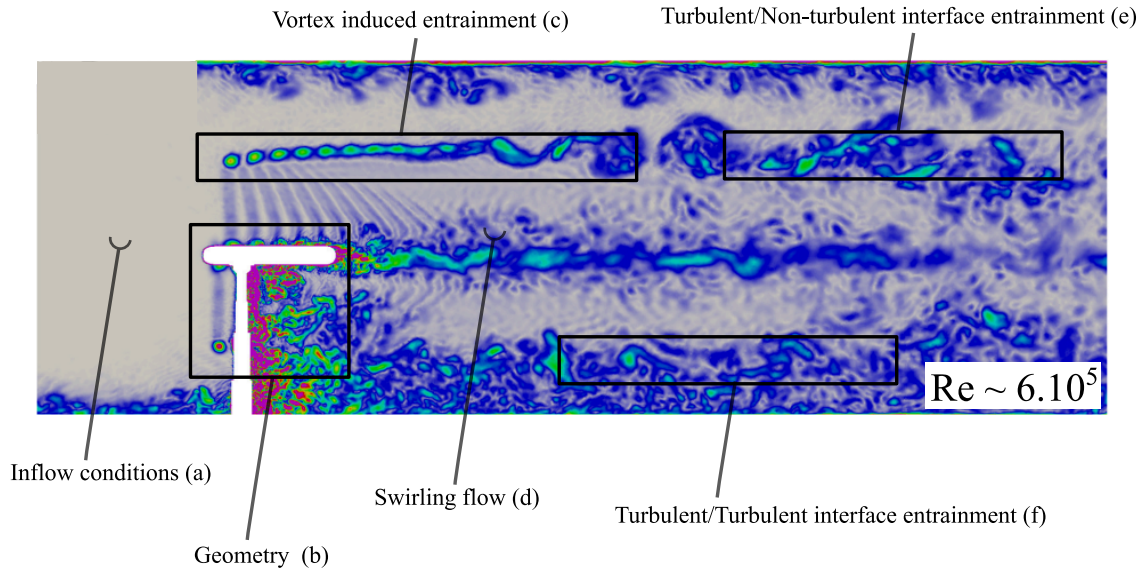

(b)

Figure 1.15: Schematic diagram showing (a) an instantaneous HAWT wake and (b) the different physical processes involved in the wake of a HAWT. LES flow visualisation taken from Bénard et al. (2018), showing iso-contours of the norm of vorticity.

Contrary to the averaged view shown in figure 1.10, the wind turbine wake is a complex multi-scale and multi-physics turbulent free shear flow as illustrated in figure 1.15. The wake has been typically divided into two main regions: the near wake and the far wake (Vermeer et al., 2003; Porté-Agel, 2019). As the name implies, these regions are characterised by their distance to the wake generator, whose geometrical properties and motions set the initial conditions of the flow. However, if one explores the body of research on wakes, there is no precise definition based on physical arguments to delimit these two regions. Recent literature on wind turbine wakes suggests that the transition to the far wake occurs when the individual wakes of the nacelle, tower, and blades cease to be distinguishable from the main flow (Crespo et al., 1999). At this

point, global parameters such as drag and power coefficient are believed to govern the entire flow. Nevertheless, this view is too simplistic as it is acknowledged that the initial wake conditions carry information throughout the turbulent flow's life, shaping the mechanisms that lead to asymptotic states (Bevilaqua and Lykoudis, 1971; Lavoie et al., 2007). This emphasis on initial conditions doesn't diminish the importance of global parameters; instead, these parameters define the asymptotic state and the primary transport mechanisms (Townsend, 1976). To comprehensively predict wake development, both the global parameters and the finer details of initial conditions must be taken into account. A remarkable finding was recently pointed out in the work of Neunaber et al. (2021), where similarity theory was applied to field measurements of wind turbine wakes. The authors concluded that the general wake models which derived from a few robust turbulence assumptions (self-preservation, far wake approximation) improve the wind turbine wake modelling, especially by adding an additional parameter to the models: a virtual origin.

To emphasise the complexity of the wind turbine wake, some physical processes featuring this flow are shown in figure 1.15. (a) the inflow conditions are set by the ABL and change in particular the external turbulence level which has shown to have a significant influence on the wake of bluff bodies (Bearman and Morel, 1983). In the case of wind turbines, the interactions with the large scale turbulent eddies in the ABL may lead to wake meandering, which adds a layer to the dynamics of the wake (Larsen et al., 2008; Espana et al., 2011). Furthermore, (b) the complex geometry of wind turbines (nacelle, tower, hub) make it a multi-scale wake generator which were studied in Bénard et al. (2018); Stevens et al. (2018); Foti et al. (2019) for instance. (c) The wake itself is characterised by coherent structures such as tip and root vortices which evolve in the downstream direction and breakdown (Okulov et al., 2014; Sherry et al., 2013). Recent studies of other separated flows (ramps) such as Berk et al. (2017); Stella et al. (2018) and the seminal study of Gerrard (1966), revealed that this type of structures play a crucial role in the entrainment mechanisms which are the reason wakes expand and recover (Turner, 1986; Bisset et al., 2002). Following up on entrainment, the wind turbine wake has at least one characteristic interface (e)-(f) where the turbulent rotational wake meets the free-stream (Bisset et al., 2002). Many studies have focused on the transfer of mass, momentum and energy of this particular interface in all types of flow because this is where entrainment takes place (da Silva et al., 2014; Stella et al., 2017; Westerweel et al., 2009; Kankanwadi and Buxton, 2022). Finally, (d) the rotation of the blades will generate a non-null azimuthal velocity component of the flow which makes the wake of the wind turbine a swirling flow (Alekseenko et al., 1999; Dufresne, 2013) with specific properties. Altogether, these physical processes show the intricacies and particularities of the wind turbine wake and yet the strong similarities with mechanisms found in other types of turbulent flows.

1.6.2 Limitations of the actuator/porous disc model

Evidently, all the distinct features of the wind turbine wake cannot be reproduced by a simple porous disc. For example the tip and root vortices cannot be reproduced by the porous disc. What is more, the typical matched drag coefficients make it so the porosity values of the discs are far above the porosity threshold of 30% evidenced by Crasto et al. (2012), below which vortex shedding is suppressed due to air bleed. This limitation was one of the main results of the study carried out in Lignarolo et al. (2016b) and in Helvig et al. (2021) which used a uniform porosity disc and a non-uniform porosity

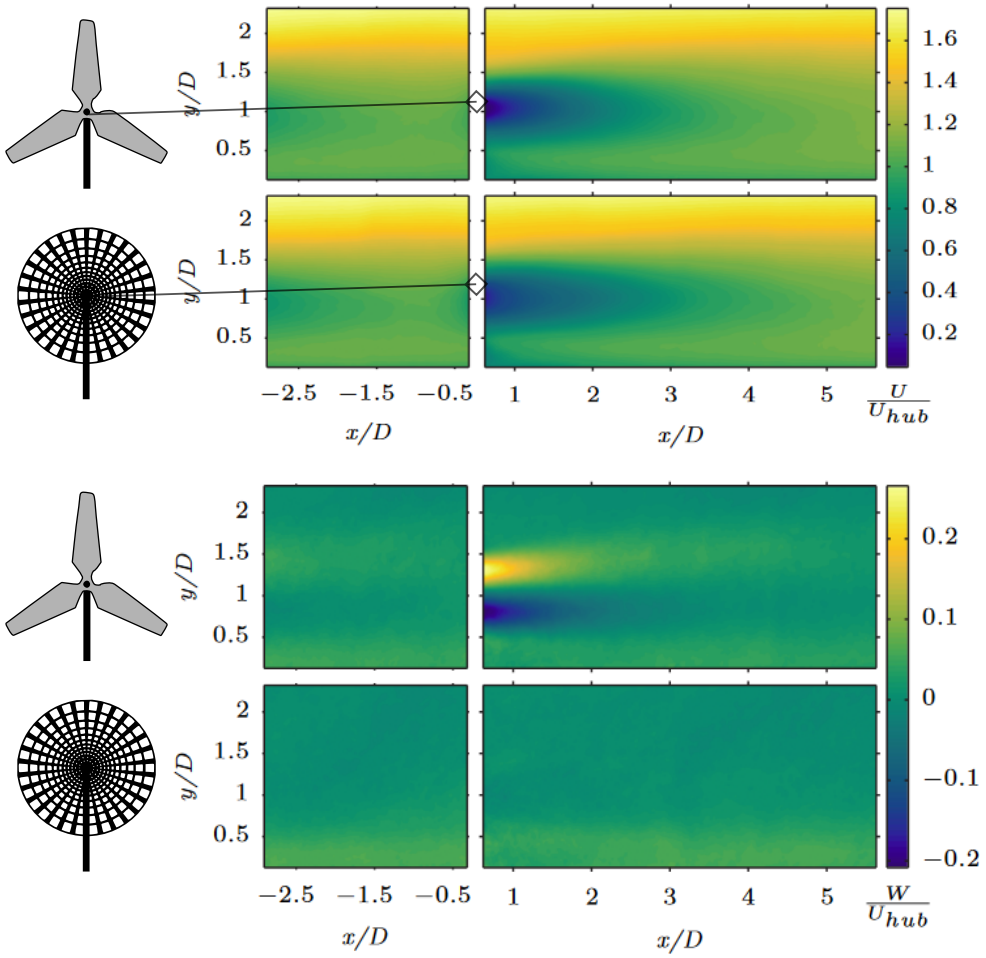

Figure 1.16: Normalised mean streamwise U/U_{hub} (top) and swirling W/U_{hub} (bottom) velocity fields comparison between a three-bladed rotor and a porous disc with matched dimensions and drag coefficient. Adapted from Camp and Cal (2016).

disc, respectively. Furthermore, Foti et al. (2019), Stevens et al. (2018) and Bénard et al. (2018) showed the importance of the geometric properties of the wake such as the tower, the hub and the nacelle, which are currently absent in the porous disc test rigs found in literature. As discussed in Foti et al. (2019), this has a noticeable effect on the wind farm output as per the numerical simulations result and emphasises the importance of geometric accuracy of the set-up. Furthermore, Stevens et al. (2018) emphasised that adding the nacelle and the mast to the geometry of the actuator disc model greatly increased the accuracy of the LES results and showed better collapse with the experimental data of Chamorro and Porté-Agel (2010); Chamorro and Porte-Agel (2011).

Finally, Camp and Cal (2016) highlighted that one of the most important initial conditions of a wind turbine wake was missing from the porous disc model: the swirling motion. The authors investigated the different streamwise evolution of all the physical quantities relevant to mass, momentum and energy conservation in the near to intermediate wake $X/D \leq 6$ for a rotating model and a non-uniform porous disc. As shown in figure 1.16, their results revealed that all the physical quantities were well approximated by the porous disc model except for swirl W, which is naturally absent in the case of the porous disc model, especially in the near wake ($X/D \leq 3.5$). Beyond $X/D \geq 3.5$ however, the differences between the porous disc model and the rotating

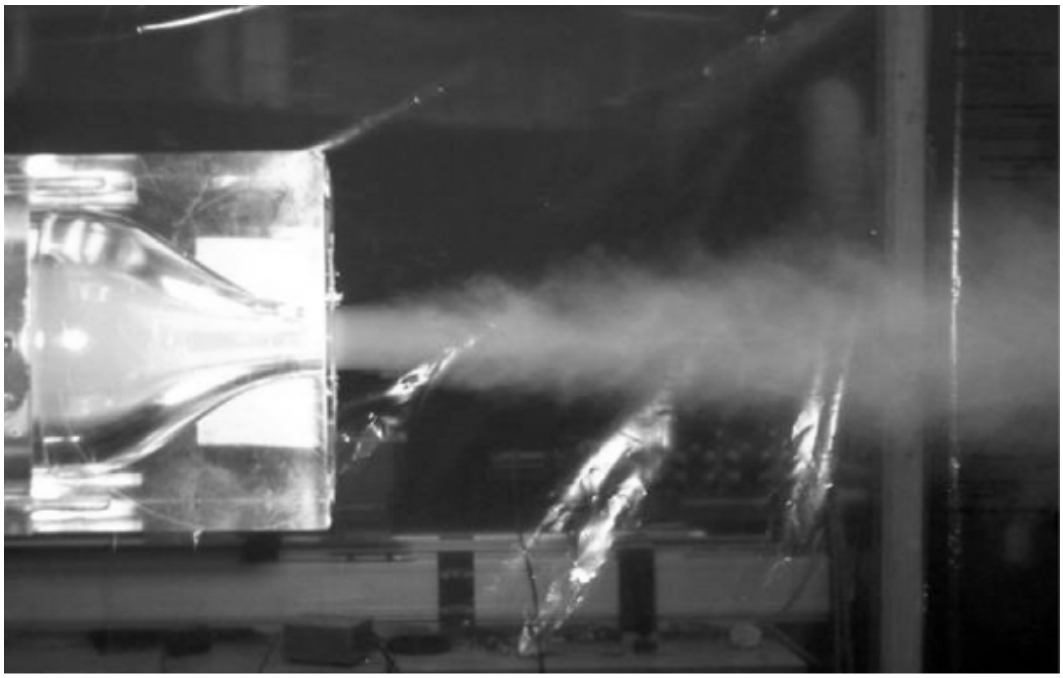

Figure 1.17: Photograph of the swirling jet nozzle and exit flow using smoke visualisation. Taken from Shiri et al. (2008).

disc faded in terms of mean flow. Nevertheless, one can not ignore that swirl is the most distinguishable feature of the wind turbine wake which sets its initial conditions and were already shown to have an impact on the development of other flows.

1.6.3 Objective of this thesis: addressing the role of swirl

Following Bevilaqua and Lykoudis (1971), Lavoie et al. (2007) and Mazellier and Vassilicos (2008, 2010) it is known that the initial conditions of turbulent flows are not erased by turbulence and their signature is preserved in the physical processes of the flow. Their signature is in fact preserved even when these flows have reached a self-preserving state (George, 1989). In this framework, the rotation is a feature shaping the initial conditions of the wake of a HAWT which has already shown to have a critical importance on the topology of the flow (Alekseenko et al., 1999). For example, swirl plays a stabilising role when applied to a turbulent flame (Masri et al., 2004) or to turbulence subjected to Coriolis force (Moisy et al., 2011). Another important finding emphasising the effect of swirl was established by Shiri et al. (2008) where the far field of a swirling jet (see figure 1.17) was compared to its non-swirling counterpart (at iso-thrust). In this work, it was found that even if both jets attained the same far field asymptotic state, swirl shifted the virtual origin of the flow and accelerated the "initial spread", hinting at an enhanced entrainment caused by swirl. Altogether, these limitations underscore the need to improve the actuator disc model by taking into account the angular momentum of the wake.

Actually, Professor Joukowsky (1912) had already pointed out the relevance of angular momentum in screw vortex systems like propellers, helicopters and wind turbines (see figure 1.18). Joukowsky (1912)'s historic paper on vortex theory is not easy to find but his work was recently underscored in the review paper of Okulov et al. (2015). The authors pointed out that following the theories put forth by Joukowsky (1912),

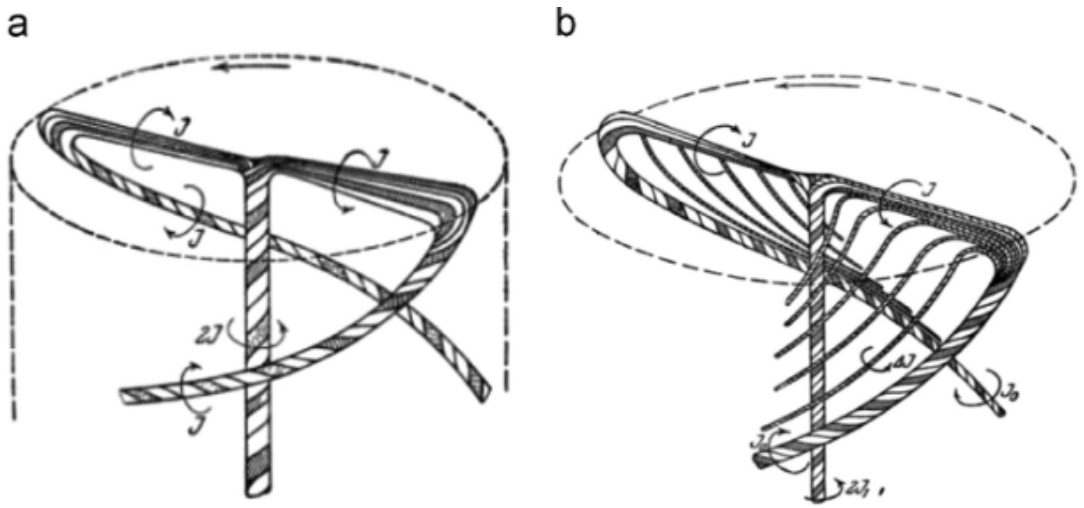

Figure 1.18: The original diagrams of screw vortex system with circulation distributions by (a) Joukowsky (1912) and (b) Vetchinkin (1913). Taken from the review paper of Okulov et al. (2015) on the rotor theories of Professor Joukowsky.

Professor Georgy Bothezat (1917) showed that including the azimuthal component to the actuator disc concept greatly improved its accuracy. All of these elements motivated this work and positioned the investigation topic within the wind energy problematic and turbulent wake studies.

Based on these elements, while swirl is a key parameter in the wake of a wind turbine, it is currently omitted in the porous disc design. The core objective of this study is therefore to include this missing ingredient in the wake of the actuator disc. The goal of this phd is threefold: (i) Introducing swirl into an experimental porous disc set-up, (ii) Modelling the effect of swirl on the wake development in the streamwise direction, and (iii) Identifying the physical mechanism at the origin of initial wake development. Consequently, the outline of the manuscript is as follows:

Chapter 2: The theoretical background for the swirling wake analysis. In this chapter the governing equations of motion for swirling wakes are derived and the relevant hypothesis are discussed. The role of swirl in the governing equations and conservation laws is underscored and a similarity scaling analysis is carried out. In particular, the added degree of freedom brought by swirl is discussed and non-equilibrium turbulence is used to derive a novel scaling law for swirl decay.

Chapter 3: Experimental set-up. In this chapter the porous disc design process is discussed in detail with a particular focus on the methodology used to passively add swirl. Subsequently, the experimental apparatus is presented as well as the measurement techniques employed to measure the wake. The experimental set up and subsequent measurement campaigns were designed to measure the physical quantities featuring the equations derived in chapter 2. Finally, the redundancy of some velocity measurements were leveraged to estimate the uncertainties and corroborate each other.

Chapter 4: Effect of a swirling motion on the wake properties of a porous disc. In this chapter the generated mean flow is described and the effects of the swirling motion are assessed. Particular attention is given to axisymmetry

and self-similarity where the scaling laws derived in chapter 2 are sought. The sensitivity of the mean wake to swirl and porosity is eventually assessed.

Chapter 5: On the entrainment mechanisms of the swirling wake of a porous disc. This chapter completes the main findings of chapter 4 and focuses on the mechanisms responsible for the development: entrainment. The effect of swirl on mean entrainment is studied and an accurate detection of the turbulent/non-turbulent interface allows us to assess the geometric properties of this interface.

A conclusion is drawn at the end of the manuscript with regards to the obtained results and a number of perspectives that were elucidated during this thesis are given.

Résumé en français: Introduction et état de l'art

Ce chapitre introduit le contexte écologique et industriel de cette étude ainsi que les problématiques scientifiques liées aux sillages éoliens. Le long du chapitre, les références clés sont utilisées pour établir l'état de l'art autour des sillages turbulents tournants appliqués aux sillages éoliens.

Le chapitre débute en replaçant le contexte global des initiatives déployées depuis 2015 pour décarboner le secteur énergétique. Des chiffres clés soulignent une volonté mondiale de multiplier le nombre de parcs éoliens et d'accroître leur envergure. Cette démarche s'inscrit dans une amélioration continue de cette technologie en vue d'atteindre les objectifs de neutralité carbone d'ici 2050. En raison des coûts de maintenance et d'exploitation, les éoliennes sont regroupées au sein de parcs éoliens, généralement espacées d'environ 7 diamètres de rotor D. Cette disposition engendre des interactions complexes, où les éoliennes situées en aval se trouvent partiellement ou complètement exposées au sillage turbulent de celles positionnées en amont. Ces interactions de sillage sont responsables de pertes énergétiques significatives et entraînent une hausse des coûts d'entretien des installations. Cela est dû au fait que le sillage d'une éolienne est caractérisée par un déficit de vitesse ΔU et d'une plus grande intensité turbulente, engendrant une fatigue aérodynamique plus élevée. Dans ce cadre, l'étude du sillage proche d'une éolienne est d'une importance capitale. Ce chapitre souligne notamment que cette étude fait partie d'une problématique plus large sur le développement des sillages turbulents auto-similaires et les lois d'échelles qui les régissent.

Ce qui distingue le sillage turbulent d'une éolienne des autres types de sillage est l'aspect tournant de celui-ci. La rotation des pâles confère une quantité de mouvement angulaire au sillage, ajoutant ainsi un nouveau degré de liberté. La modélisation précise et peu coûteuse de ces quantités et de leur évolution le long de la direction du sillage constitue le point névralgique pour répondre aux défis industriels. Cette démarche de modélisation s'impose du fait que les mesures expérimentales *in situ* et les simulations de haute fidélité (LES) demeurent encore incompatibles avec les impératifs industriels. Cela est dû au caractère multi-échelles et multi-physiques du sillage éolien.

À l'échelle du laboratoire, des disques poreux ont été employés comme substituts simples et économiques pour reproduire, aussi fidèlement que possible, un sillage éolien (Sforza et al., 1981; Aubrun, 2013; Camp and Cal, 2016). Ce dispositif est l'équivalent physique du modèle théorique du disque actuateur (*"actuator disc"*), où l'éolienne est remplacée par un disque virtuel d'épaisseur infinitésimale appliquant une force de poussée équivalente à la traînée de l'éolienne (Crasto et al., 2012). Conformément à la conservation de la quantité de mouvement linéaire (éq. 1.3.2), des travaux tels que ceux menés par Sforza et al. (1981) et Aubrun (2013) ont démontré qu'un objet poreux de dimensions similaires et de coefficient de traînée C_D identique, reproduit un sillage équivalent à celui d'une éolienne. Le coefficient de traînée peut donc être directement choisi via l'ajustement d'un seul paramètre: la porosité β. Au fil des années, différentes équipes ont proposé des améliorations de ce disque poreux en définissant divers types de porosité afin de représenter au mieux les conditions initiales d'un véritable sillage éolien. Cependant, jusqu'à présent, le sillage ainsi généré, ne contenait pas la condition initiale la plus caractéristique du sillage éolien : la composante de vitesse azimutale ou "swirl" (Camp and Cal, 2016).

L'objectif de cette étude est donc d'introduire cet élément manquant dans le modèle de disque poreux/actuateur et ensuite de caractériser expérimentalement le sillage généré.

Le chapitre finit avec une annonce de plan visant à structurer le manuscrit de la façon suivante:

Chapitre 2: Fondements théoriques de l'analyse du sillage tournant. Dans ce chapitre sont dérivées les équations fondamentales du mouvement pour les sillages avec rotation, en introduisant les hypothèses pertinentes. Le rôle du swirl dans les équations et lois de conservation est souligné, avec une analyse d'échelle de similitude. Une attention particulière est accordée au degré de liberté supplémentaire ajoutée par la conservation de quantité de mouvement angulaire. Utilisant le paradigme de la turbulence hors équilibre, une nouvelle loi d'échelle pour la décroissance du swirl est dérivée.

Chapitre 3: Dispositif expérimental. Ce chapitre détaille la conception du disque poreux, en mettant l'accent sur la méthodologie d'ajout passif de swirl. Ensuite, le banc expérimental est présenté ainsi que les techniques de mesure utilisées pour caractériser le sillage. La configuration expérimentale et les campagnes de mesure ont été conçues pour évaluer les grandeurs physiques présentées dans le chapitre 2. Enfin, la redondance de certaines mesures de vitesse est exploitée pour estimer les incertitudes et les corroborer mutuellement.

Chapitre 4: Effet du swirl sur les propriétés du sillage tournant d'un disque poreux. Ce chapitre décrit l'écoulement moyen généré et évalue les effets du swirl. Une attention particulière est portée à l'axisymétrie et à l'auto-similarité, où les lois d'échelle dérivées au chapitre 2 sont évaluées. La sensibilité du sillage moyen au taux de rotation injecté et à la porosité sont finalement discutés.

Chapitre 5: Les mécanismes d'entraînement du sillage tournant d'un disque poreux. Ce chapitre complète les principales conclusions du chapitre 4 et se concentre sur les mécanismes responsables du développement du sillage : l'entraînement. L'effet du swirl sur l'entraînement moyen est étudié, et une détection précise de l'interface turbulente/non turbulente permet d'évaluer les propriétés géométriques de cette interface.

Une conclusion est tirée à la fin du manuscrit concernant les résultats obtenus, et plusieurs perspectives dégagées au cours de cette thèse sont présentées.

2

Theoretical background for the swirling wake analysis

Contents

As explained in Porté-Agel (2019), the (physics based) analytical models used to predict the evolution of a wind turbine wake are all based on conservation laws (mass, momentum, energy). It is the case of the well-known Jensen (1983) model, based on mass conservation and other, more sophisticated models, like the ones proposed in Frandsen et al. (2006); Bastankhah and Porté-Agel (2014); Ishihara and Qian (2018). It is expected that the addition of a swirling motion will alter the balance of these conservation laws. The effect of an additional angular momentum on the wake needs then to be analysed with the proper theoretical tools.

This chapter aims at establishing the theoretical framework of a turbulent swirling axisymmetric wake applied here for the swirling wake of the porous disc. The governing equations of motion are introduced first, with the details on the hypotheses considered and the relevant simplifications made. Secondly, a derivation of the Reynolds-Averaged Navier-Stokes (RANS) equations is written to express the governing equations of the mean flow of an axisymmetric wake. Similarity scalings are also defined from these conservation laws. The classical equilibrium turbulence similarity analysis is fully explained before using non-equilibrium turbulence in order to propose a novel scaling law for swirl decay.

All the equations and derivations presented here are rewritten based on previous theoretical analysis on shear flows with swirl like jets (Shiri, 2010) and wakes (Dufresne, 2013; Holmes and Naughton, 2022). However, to the author's knowledge, the non-equilibrium similarity scalings have never been applied to the swirling wake of an actuator disc to date.

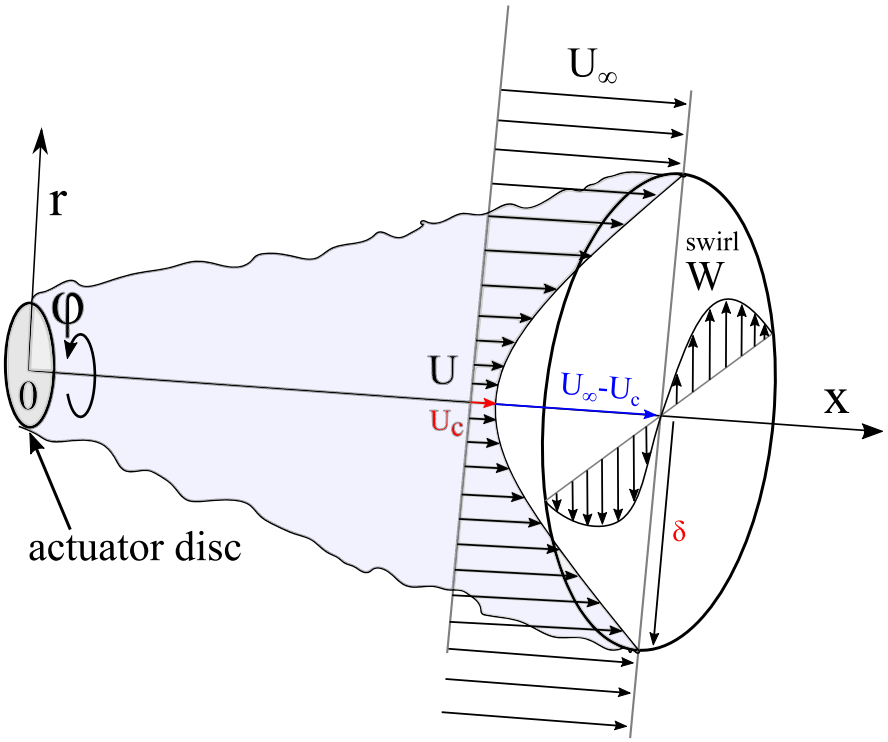

Figure 2.1: Schematic of an axisymmetric swirling wake generated by an actuator disc in the cylindrical coordinates (x,r,ϕ). The origin is set at the centre of the actuator disc. U and W are the mean axial and azimuthal velocity components, respectively. U_∞ is the streamwise undisturbed free-stream velocity, U_c is the wake streamwise centreline velocity, and δ is the wake width.

2.1 Governing equations of motion

The natural coordinates system appropriate to study the problem of an axisymmetric swirling wake is the cylindrical system (x, r, ϕ), which corresponds to the streamwise direction, the radial direction and the azimuthal direction, respectively. The coordinates system is presented in figure 2.1 along with a representation of the swirling wake of an actuator disc. In the following, $\widetilde{U}$ denotes the streamwise velocity, $\widetilde{V}$ the radial velocity, $\widetilde{W}$ the azimuthal velocity or "swirl" and $\widetilde{P}$ the static pressure. The $(\widetilde{\circ})$ symbol represents a raw random variable. The instantaneous physical quantities in this study will be expressed according to the Reynolds decomposition, as the sum of a mean (uppercase) component and a fluctuating (lowercase) component as follows:

$$\begin{cases} \tilde{U}(x,r,\phi,t) &= U(x,r,\phi) + u(x,r,\phi,t) \quad (x) \\ \tilde{V}(x,r,\phi,t) &= V(x,r,\phi) + v(x,r,\phi,t) \quad (r) \\ \tilde{W}(x,r,\phi,t) &= W(x,r,\phi) + w(x,r,\phi,t) \quad (\phi) \\ \tilde{P}(x,r,\phi,t) &= P(x,r,\phi) + p(x,r,\phi,t) \end{cases} \tag{2.1.1}$$

where $(U,V,W) = (\overline{\widetilde{U}}, \overline{\widetilde{V}}, \overline{\widetilde{W}})$, with the $(\overline{\circ})$ symbol denoting an average operator.

Here, air is considered to be a constant-property Newtonian fluid of density ρ and kinematic viscosity ν. The equations which govern the axisymmetric swirling wake are the Navier-Stokes (NS) equations which can be readily found in many fluid mechanics

textbooks such as in Batchelor (1967) or Pope (2000). The full derivation of the NS equations is available in these references as only a simplified version with the relevant approximations is presented here. In this study, the classical hypotheses are made regarding high-Reynolds turbulent flows in air (Anderson, 2011). The viscous term is neglected and the fluid's density is treated as a constant due to the incompressibility hypothesis, which is valid for low Mach number flows. In this framework, the Reynolds averaged Navier-Stokes equations (RANS) read as follows:

The mean continuity equation:

$$\frac{\partial U}{\partial x} + \frac{1}{r}\frac{\partial (rV)}{\partial r} + \frac{1}{r}\frac{\partial W}{\partial \phi} = 0, \tag{2.1.2}$$

and the mean momentum transport equations along the x, r and ϕ directions, respectively read:

$$\frac{\partial U}{\partial t} + U\frac{\partial U}{\partial x} + V\frac{\partial U}{\partial r} + \frac{W}{r}\frac{\partial U}{\partial \phi} = -\frac{1}{\rho}\frac{\partial P}{\partial x} - \frac{\partial \overline{u^2}}{\partial x} - \frac{\partial \overline{uv}}{\partial r} - \frac{1}{r}\frac{\partial \overline{uw}}{\partial \phi} - \frac{\overline{uv}}{r}, \tag{2.1.3}$$

$$\frac{\partial V}{\partial t} + U\frac{\partial V}{\partial x} + V\frac{\partial V}{\partial r} + \frac{W}{r}\frac{\partial V}{\partial \phi} - \frac{W^2}{r} = -\frac{1}{\rho}\frac{\partial P}{\partial r} - \frac{\partial \overline{uv}}{\partial x} - \frac{\partial \overline{v^2}}{\partial r} - \frac{1}{r}\frac{\partial \overline{vw}}{\partial \phi} + \frac{\overline{w^2} - \overline{v^2}}{r}, \tag{2.1.4}$$

$$\frac{\partial W}{\partial t} + U\frac{\partial W}{\partial x} + V\frac{\partial W}{\partial r} + \frac{W}{r}\frac{\partial W}{\partial \phi} + \frac{VW}{r} = -\frac{1}{\rho r}\frac{\partial P}{\partial \phi} - \frac{\partial \overline{uw}}{\partial x} - \frac{\partial \overline{vw}}{\partial r} - \frac{1}{r}\frac{\partial \overline{w^2}}{\partial \phi} - 2\frac{\overline{vw}}{r}. \tag{2.1.5}$$

Furthermore, the turbulent kinetic energy ($k = \frac{1}{2}[\overline{u^2} + \overline{v^2} + \overline{w^2}]$) transport equation reads:

$$\begin{aligned}
&\frac{\partial k}{\partial t} + U\frac{\partial k}{\partial x} + V\frac{\partial k}{\partial r} + \frac{W}{r}\frac{\partial k}{\partial \phi} - W\frac{\overline{vw}}{r} + V\frac{\overline{w^2}}{r} = \\
&-\frac{1}{\rho}\left(\frac{\partial \overline{pu}}{\partial x} + \frac{1}{r}\frac{\partial (r\overline{pv})}{\partial r} + \frac{1}{r}\frac{\partial \overline{pw}}{\partial \phi}\right) - \left(\frac{\partial \overline{uk}}{\partial x} + \frac{1}{r}\frac{\partial (r\overline{vk})}{\partial r} + \frac{1}{r}\frac{\partial \overline{wk}}{\partial \phi}\right) - \\
&\left(\overline{u^2}\frac{\partial U}{\partial x} + \overline{uv}\frac{\partial U}{\partial r} + \frac{\overline{uw}}{r}\frac{\partial U}{\partial \phi} + \overline{uv}\frac{\partial V}{\partial x} + \overline{v^2}\frac{\partial V}{\partial r} + \frac{\overline{vw}}{r}\frac{\partial V}{\partial \phi} + \overline{uw}\frac{\partial W}{\partial x} + \overline{vw}\frac{\partial W}{\partial r} + \frac{\overline{w^2}}{r}\frac{\partial W}{\partial \phi}\right) \\
&- \epsilon,
\end{aligned} \tag{2.1.6}$$

where ϵ is the turbulent dissipation rate.

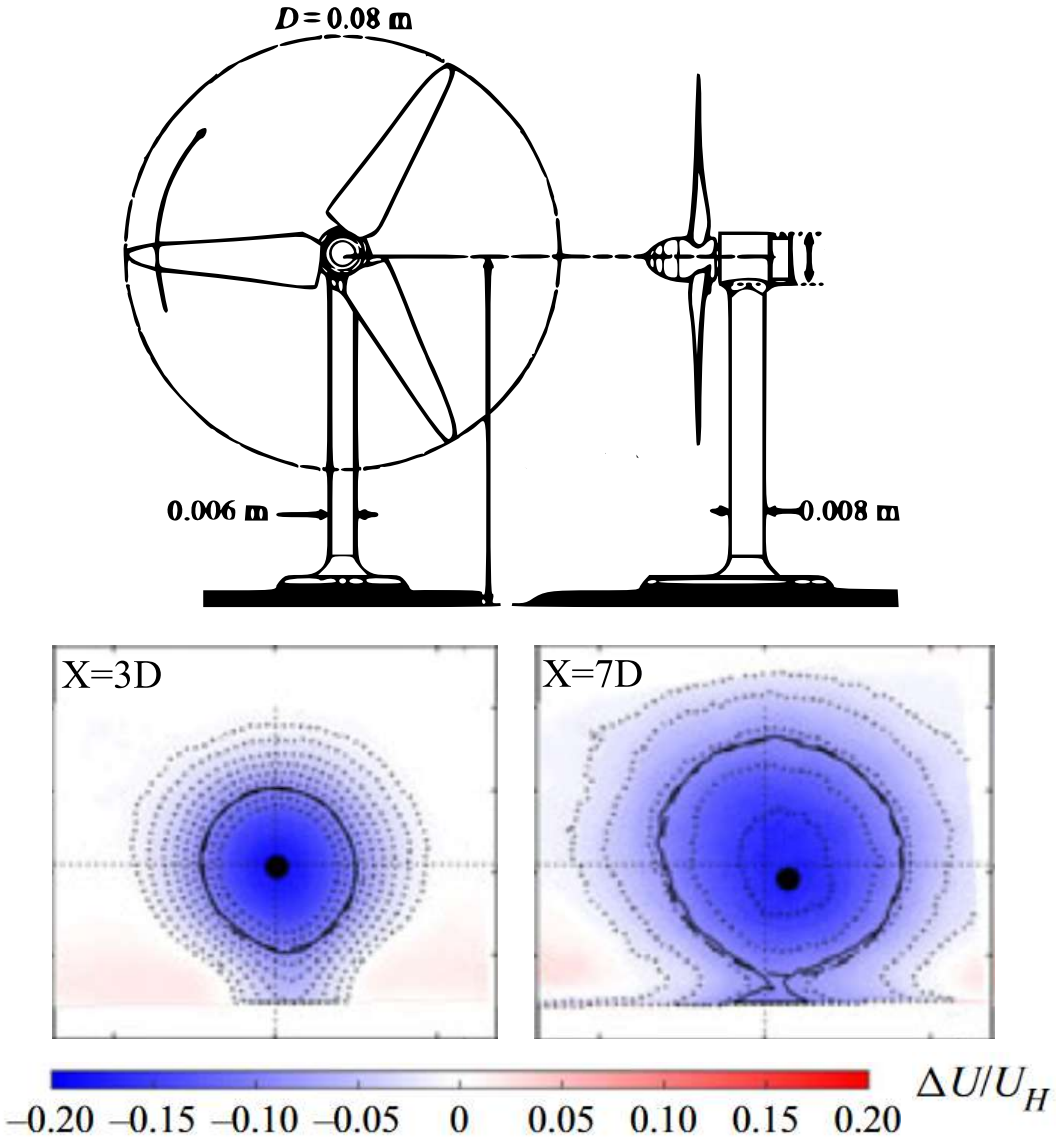

Figure 2.2: Velocity deficit contours normalised by the hub-height mean velocity U_H of a rotating wind turbine at $X = 3D$ and $X = 7D$. Taken from Bossuyt et al. (2021).

2.1.1 Relevant simplifications of the governing equations

These equations govern the motion of a swirling wake but can be simplified using the relevant hypotheses. In this study, since the swirling motion is generated in a passive manner (see chapter 3), the mean flow is steady, which means that all time derivatives in the RANS equations are null ($\partial/\partial t \equiv 0$). Moreover, the axisymmetric hypothesis can be made for the wake of a wind turbine despite the cylindrical mast holding the rotor in place, as detailed in Vermeer et al. (2003). The same is true for lab-scale wind turbines as evidenced in the work of Chamorro and Porté-Agel (2010) and more recently in Bossuyt et al. (2021).

Figure 2.2 shows the mean wake of a rotating wind turbine at two different streamwise locations with a fitted ellipse. As detailed in Bossuyt et al. (2021) and shown in figure 2.2, the wake has a roughly circular shape in the near to intermediate wake. More generally speaking, as shown in the work of Nedic (2013) and in Lignarolo et al.

(2016b), any porous disc or fractal plate held in place by a thin cylindrical mast has a roughly axisymmetric wake. Based on these findings, the axisymmetric hypothesis will be invoked in this study and later checked (see chapter 3). Therefore, for an axisymmetric wake, the azimuthal derivatives in the RANS equations are identically zero ($\partial/\partial\phi \equiv 0$).

Lastly, as discussed in Shiri (2010) and Dufresne (2013), the thin shear layer approximation can be invoked for the axisymmetric flows since this type of shear flow exhibits much greater spatial gradients in the radial (r) direction than in the axial (x) direction (i.e $\partial/\partial r \gg \partial/\partial x$). This assumption is well supported by the measurements reported in chapter 3.

Given these hypotheses, the RANS equations for the mean flow of a swirling axisymmetric wake reduce to:

The mean continuity equation:

$$\frac{\partial U}{\partial x} + \frac{1}{r}\frac{\partial (rV)}{\partial r} = 0, \tag{2.1.7}$$

and the reduced mean momentum transport equations:

$$U\frac{\partial U}{\partial x} + V\frac{\partial U}{\partial r} = -\frac{1}{\rho}\frac{\partial P}{\partial x} - \frac{\partial \overline{uv}}{\partial r} - \frac{\overline{uv}}{r}, \qquad (x) \tag{2.1.8}$$

$$U\frac{\partial V}{\partial x} + V\frac{\partial V}{\partial r} - \frac{W^2}{r} = -\frac{1}{\rho}\frac{\partial P}{\partial r} - \frac{\partial \overline{v}^2}{\partial r} + \frac{\overline{w^2} - \overline{v^2}}{r}, \qquad (r) \tag{2.1.9}$$

$$U\frac{\partial W}{\partial x} + V\frac{\partial W}{\partial r} + \frac{VW}{r} = -\frac{\partial \overline{vw}}{\partial r} - 2\frac{\overline{vw}}{r}. \qquad (\phi) \tag{2.1.10}$$

Furthermore, with these simplifications the reduced TKE equation becomes:

$$\underbrace{U\frac{\partial k}{\partial x} + V\frac{\partial k}{\partial r}}_{\mathcal{C}} = \underbrace{-\frac{1}{\rho}\left(\frac{\partial \overline{pu}}{\partial x} + \frac{1}{r}\frac{\partial (r\overline{pv})}{\partial r}\right)}_{\Phi} \underbrace{-\frac{1}{2}\left(\frac{\partial \overline{uk}}{\partial x} + \frac{1}{r}\frac{\partial (r\overline{vk})}{\partial r}\right)}_{\mathcal{T}} \tag{2.1.11}$$

$$\underbrace{-\left(\overline{u^2}\frac{\partial U}{\partial x} + \overline{uv}\frac{\partial U}{\partial r} + \overline{uv}\frac{\partial V}{\partial x} + \overline{v^2}\frac{\partial V}{\partial r} + \overline{uw}\frac{\partial W}{\partial x} + \overline{vw}\frac{\partial W}{\partial r} + W\frac{\overline{vw}}{r}\right)}_{\mathcal{P}} - \epsilon,$$

where a balance between energy terms can be outlined. The mean flow convection of TKE $\mathcal{C}$ is balanced by the energy transport contribution of pressure Φ, turbulence $\mathcal{T}$, the TKE production $\mathcal{P}$ and dissipation ϵ.

2.1.2 On the pressure term and the role of swirl

Equation (2.1.9) can be further simplified using an order of magnitude analysis, as detailed in Shiri (2010) and in Dufresne (2013), to obtain an expression for the radial pressure gradient $\partial P/\partial r$.

Order of magnitude analysis

An order of magnitude analysis is conducted in the following paragraph to obtain leading order terms in equation (2.1.9). As detailed in the work of Shiri (2010), this analysis is carried out by associating characteristic scales to each term in the momentum transport equations. This analysis is akin to the classical scaling of the governing equations in boundary layer problems described in detail in the work of Schlichting and Kestin (1961), for example.

In this framework, a scale for the streamwise velocity is defined as:

$$U \sim U_s, \tag{2.1.12}$$

where the similarity symbol "$\sim$" denotes similar order of magnitude between terms. In the same manner, the following scales are defined for the mean radial velocity V and for the mean swirling velocity W, respectively:

$$V \sim V_s, \tag{2.1.13}$$

$$W \sim W_s. \tag{2.1.14}$$

As for the Reynolds stress terms, a unique scale $\overline{u_s^2}$ is defined for the normal and for the shear stress terms such as:

$$\overline{u^2} \sim \overline{v^2} \sim \overline{w^2} \sim \overline{uv} \sim \overline{u_s^2}. \tag{2.1.15}$$

Following Shiri (2010), pressure will have its own scale such as:

$$P \sim \Phi. \tag{2.1.16}$$

Furthermore, length scales are also defined in the streamwise and radial directions and their corresponding gradients such as:

$$x \sim L, \tag{2.1.17}$$

$$r \sim \delta, \tag{2.1.18}$$

and

$$\partial/\partial x \sim 1/L, \tag{2.1.19}$$

$$\partial/\partial r \sim 1/\delta. \tag{2.1.20}$$

As stated in Shiri (2010), the highly three-dimensional nature of turbulent flows makes them difficult to model. In the case of the near wake of a porous disc, very few assumptions can be deemed reasonable. However, the following boundary layer-type approximation can be made to establish compelling phenomena:

$$1/\delta \gg 1/L \quad \text{or} \quad \delta \ll L. \tag{2.1.21}$$

Substituting the defined order of magnitude scalings (2.1.12) - (2.1.20) in the continuity equation (2.1.7) gives:

$$\frac{U_s}{L} + \frac{1}{\cancel{\phi}}\frac{\cancel{\phi} V_s}{\delta} \sim 0, \tag{2.1.22}$$

which immediately yields:

$$V_s \sim U_s\left(\frac{\delta}{L}\right). \tag{2.1.23}$$

Equation (2.1.23) already contains information about the differences in magnitude between the streamwise velocity and the radial velocity. In fact, using the thin shear layer approximation, the factor ($\delta/L \ll 1$) will cause U_s to be an order of magnitude above V_s.

The order of magnitude analysis can be also applied to the radial momentum transport equation (2.1.9) and reads:

$$U_s\frac{V_s}{L} + V_s\frac{V_s}{\delta} - \frac{W_s^2}{\delta} \sim \Phi + \frac{\overline{u_s^2}}{\delta} + \frac{\overline{u_s^2}}{\delta}. \tag{2.1.24}$$

Substituting V_s in equation (2.1.24) using equation (2.1.23) yields:

$$U_s^2\frac{\delta}{L^2} + U_s^2\frac{\delta}{L^2} - \frac{W_s^2}{\delta} \sim \Phi + \frac{\overline{u_s^2}}{\delta} + \frac{\overline{u_s^2}}{\delta}. \tag{2.1.25}$$

Equation (2.1.25) is then multiplied by δ/U_s^2 to obtain:

$$\underbrace{\left(\frac{\delta}{L}\right)^2}_{\ll 1} + \underbrace{\left(\frac{\delta}{L}\right)^2}_{\ll 1} - \left(\frac{W_s}{U_s}\right)^2 \sim \frac{\delta\Phi}{U_s^2} + \frac{\overline{u_s^2}}{U_s^2} + \frac{\overline{u_s^2}}{U_s^2} \tag{2.1.26}$$

Invoking the thin shear layer approximation, the first two terms in equation (2.1.26) are clearly small compared to the rest given that $\delta/L \ll 1$. As for the rest of the terms, no more simplifications can be performed without the need of stronger assumptions. This order of magnitude analysis further simplifies equation (2.1.9) and yields the first order approximation of the radial momentum transport equation found in George (1989); Shiri (2010); Dufresne (2013) and reads:

$$-\frac{W^2}{r} = -\frac{1}{\rho}\frac{\partial P}{\partial r} - \frac{\partial \overline{v}^2}{\partial r} + \frac{\overline{w^2} - \overline{v^2}}{r}. \tag{2.1.27}$$

Axisymmetric pressure field expression

Equation (2.1.27) can be rearranged and written as:

$$\frac{1}{\rho}\frac{\partial P}{\partial r} = \frac{W^2}{r} - \frac{\partial \overline{v^2}}{\partial r} + \frac{\overline{w^2} - \overline{v^2}}{r}, \tag{2.1.28}$$

where the radial pressure gradient is balanced by swirl and turbulence. Equation (2.1.28) can be integrated with respect to r to yield:

$$\frac{1}{\rho}[P(x,r) - P(x,r=\infty)] = -\int_r^\infty \frac{W^2 + (\overline{w^2} - \overline{v^2})}{r'} dr' + \int_r^\infty \frac{\partial \overline{v^2}}{\partial r} dr'. \tag{2.1.29}$$

It immediately follows:

$$P(x,r) - P_\infty(x) = -\rho \int_r^\infty \frac{W^2 + (\overline{w^2} - \overline{v^2})}{r'} dr' - \overline{v^2}, \tag{2.1.30}$$

where $P_\infty(x)$ is the free-stream static pressure. For nearly isotropic turbulence the approximation $\overline{w^2} \approx \overline{v^2}$ can be made and equation (2.1.30) reduces to:

$$P(x,r) - P_\infty(x) = -\rho \underbrace{\int_r^\infty \frac{W^2}{r'} dr'}_{\text{Swirl}} - \overbrace{\overline{v^2}}^{\text{Turbulence}}, \tag{2.1.31}$$

which shows that, for non-swirling axisymmetric wakes, to a first approximation, pressure is essentially driven by the radial normal Reynolds stress $-\overline{v^2}$ as famously proposed by Lee and Smith (1987) and in Antonia and Rajagopalan (1990). Regardless of isotropy, recent studies concerning bluff body wakes, like the work of Shanmughan et al. (2020), have shown that the persisting coherent structures in the wake dramatically increase the $-\overline{v^2}$ term and therefore drives the pressure distribution. In the near wake however, large scale isotropy is very unlikely and equation (2.1.31) is only shown to highlight the effect of swirl on the pressure distribution and will not be used in the following.

In the case of this study (and porous discs investigations in general), the porosity of the disc is above the threshold evidenced by Castro (1971) where large coherent structures start to develop. In fact, the air bleed through the pores of the disc reduce the mean shear which mitigates the production of turbulence and the formation of coherent structures. Furthermore, the term $\overline{w^2}$ shows considerable discrepancies with $\overline{v^2}$ and $\overline{u^2}$ especially in the near field ($X \leq 4D$). These arguments lead to the consideration of the full pressure equation (2.1.30) in the following without considering the flow nearly isotropic. In any case, equation (2.1.30) emphasises that the addition of a mean swirling motion will increase the mean pressure drop across the actuator disc. Moreover, if the swirling motion term is higher than the turbulence term (which is likely the case in the near wake), swirl is expected to govern the pressure distribution.

With this direct expression for the pressure field, the streamwise pressure gradient in equation (2.1.8) can be easily computed by differentiating equation (2.1.30) with respect to x to yield:

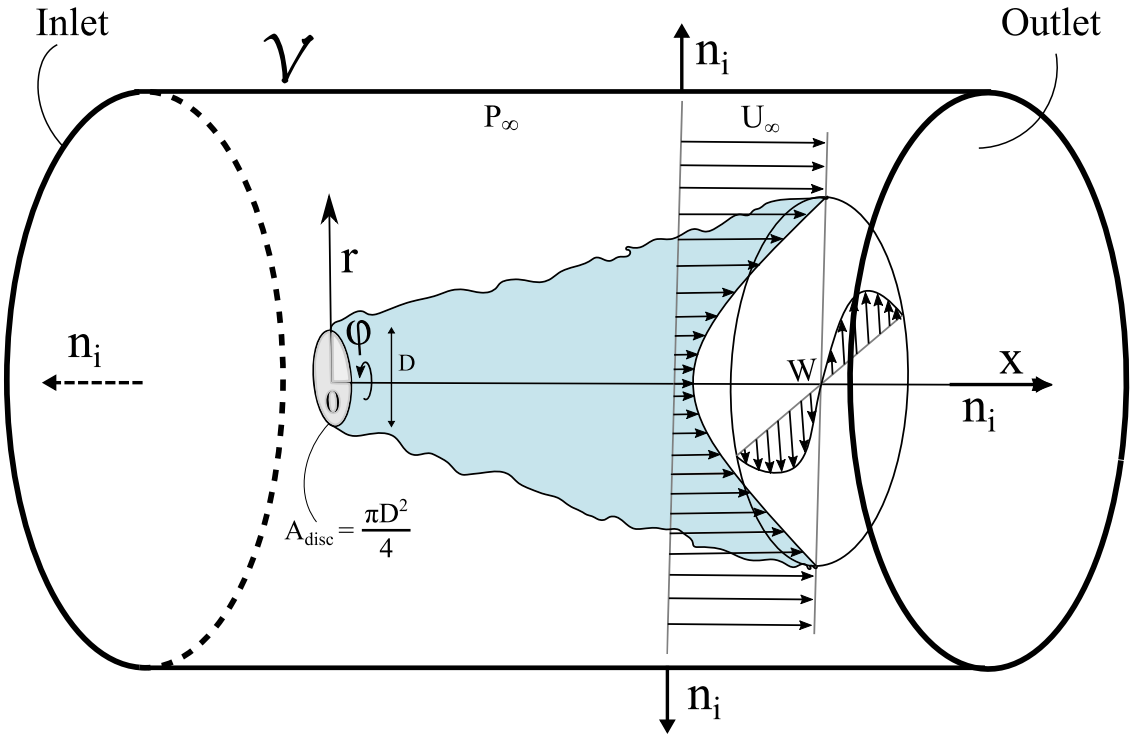

Figure 2.3: Schematic of a control volume $\mathcal{V}$ containing the actuator disc in cylindrical coordinates. The outbound vectors normal to the surface $\mathcal{S}$ are noted n_i

$$\frac{1}{\rho}\frac{\partial P(x,r)}{\partial x} = \frac{1}{\rho}\frac{dP_\infty(x)}{dx} - \frac{\partial}{\partial x}\left(\int_r^\infty \frac{W^2 + (\overline{w^2} - \overline{v^2})}{r'}dr'\right) - \frac{\partial \overline{v^2}}{\partial x}. \tag{2.1.32}$$

For experimental conditions with relatively high blockage (above 10%), there is a non-null streamwise pressure gradient in the free-stream. However, as detailed in further chapters, it was verified that the test rig had a very small blockage (below 3%) and that the free-stream had indeed a near-zero pressure gradient. Therefore, equation (2.1.32) yields:

$$\boxed{\frac{1}{\rho}\frac{\partial P(x,r)}{\partial x} = -\frac{\partial}{\partial x}\left(\int_r^\infty \frac{W^2 + (\overline{w^2} - \overline{v^2})}{r'}dr'\right) - \frac{\partial \overline{v^2}}{\partial x}}. \tag{2.1.33}$$

2.2 Mean momentum budgets

To analytically estimate the loads and torque acting on the wind turbine, in particular the drag and the angular momentum, a mean momentum budget is carried out. To perform the momentum budget, the local governing equations (2.2.1) and (2.1.10) are integrated over a control volume $\mathcal{V}$ depicted in figure 2.3. This control volume is defined containing the actuator disc which acts as a body force to account for drag F_D and angular momentum G_0. As shown in figure 2.3 this control volume is a cylinder of volume $\mathcal{V}$ delimited by a closed surface $\mathcal{S}$.

With the explicit expression for the streamwise pressure gradient (2.1.33) the streamwise mean momentum transport equation (2.1.8) can be written as:

$$\rho U\frac{\partial U}{\partial x}+\rho V\frac{\partial U}{\partial r}=-\frac{\rho}{r}\frac{\partial(r\overline{uv})}{\partial r}+\rho\frac{\partial}{\partial x}\left\{\overline{v^2}-\overline{u^2}+\int_r^\infty\frac{W^2+(\overline{w^2}-\overline{v^2})}{r'}dr'\right\} \quad (2.2.1)$$

2.2.1 Streamwise mean momentum budget: the drag force

Using the axisymmetry hypothesis (Shiri, 2010), the integration of equation (2.2.1) over a cylinder of infinitesimal thickness yields:

$$2\pi\frac{d}{dx}\left[\int_0^\infty\left(\rho U^2+\rho\overline{u^2}-\rho\overline{v^2}\right)rdr-\int_0^\infty\left(\rho\int_r^\infty\frac{W^2+(\overline{w^2}-\overline{v^2})}{r'}dr'\right)rdr\right]=0. \quad (2.2.2)$$

The last term in equation (2.2.2) is integrated by parts to yield:

$$2\pi\frac{d}{dx}\left[\int_0^\infty\left(\rho U^2+\rho\overline{u^2}-\rho\frac{W^2}{2}-\rho\frac{\overline{w^2}+\overline{v^2}}{2}\right)rdr\right]=0. \quad (2.2.3)$$

Finally, equation (2.2.3) is integrated in the streamwise direction from the inlet of the control volume to its outlet to obtain:

$$F_D=2\pi\left[\underbrace{\int_0^\infty\rho U_\infty^2rdr}_{\text{Inlet}}-\underbrace{\int_0^\infty\left(\rho U^2+\rho\overline{u^2}-\rho\frac{W^2}{2}-\rho\frac{\overline{w^2}+\overline{v^2}}{2}\right)rdr}_{\text{Outlet}}\right], \quad (2.2.4)$$

where F_D is the net drag force imparted on the actuator disc which acts as a body force since the control volume encompasses the AD. The experimental conditions were carefully put in place to have a uniform inflow velocity, hence the inlet term containing only the free-stream momentum transport.

To go further, the continuity equation is used to couple both integrals in equation (2.2.4). Integrating the continuity equation (2.1.7) over $\mathcal{V}$ yields:

$$2\pi\underbrace{\int_0^\infty\rho U_\infty rdr}_{\text{Inlet}}=2\pi\underbrace{\int_0^\infty\rho Urdr}_{\text{Outlet}}. \quad (2.2.5)$$

Equation (2.2.5) is then used with equation (2.2.4) to obtain:

$$F_D=2\pi\int_0^\infty\rho U\Delta Urdr-2\pi\int_0^\infty\rho\left[\overline{u^2}-\frac{\overline{w^2}+\overline{v^2}}{2}\right]rdr+2\pi\int_0^\infty\rho\frac{W^2}{2}rdr, \quad (2.2.6)$$

where ΔU is the mean streamwise velocity deficit in the wake defined as:

$$\Delta U=U_\infty-U. \quad (2.2.7)$$

Finally, equation (2.2.6) can be normalised with the help of the dimensionless drag coefficient C_D to yield the dimensionless streamwise momentum conservation law:

$$C_D = 16\left[\underbrace{\int_0^\infty U^*\Delta U^* r^* dr^*}_{\text{Velocity deficit}} - \underbrace{\int_0^\infty \left[\overline{u^2}^* - \frac{\overline{w^2}^* + \overline{v^2}^*}{2}\right] r^* dr^*}_{\text{Turbulence/Anisotropy}} + \underbrace{\int_0^\infty \left[\frac{{W^*}^2}{2}\right] r^* dr^*}_{\text{Swirl}}\right], \tag{2.2.8}$$

where the drag coefficient C_D is defined as:

$$C_D = \frac{F_D}{\frac{1}{2}\rho U_\infty^2 A}, \tag{2.2.9}$$

where $A = \pi(D/2)^2$ is the frontal area of the actuator disc. The $(\circ^*)$ superscript denotes dimensionless quantities normalised using the undisturbed free-stream velocity U_∞ and D as characteristic scales for velocities and length, respectively.

The axial momentum conservation equation (2.2.8) shows that the drag coefficient has three main contributors. Namely: the mean velocity deficit flowrate, turbulence and the mean swirling velocity terms, respectively. Therefore, following Steiros and Hultmark (2018), since swirl increases the pressure drop across the actuator disc, swirl is expected to increase the drag coefficient as ${W^*}^2/2$. However, the near wake is characterised by a strong velocity deficit, which makes the swirling velocity term an order of magnitude below the velocity deficit term. Furthermore, the turbulence contribution is in fact an anisotropy term since it compares all three Reynolds normal stresses. For a nearly isotropic wake $\overline{u^2} \approx \overline{v^2} \approx \overline{w^2}$ and therefore the contribution of turbulence to drag would be null. However, in reality the near wake is characterised by strong anisotropy with particularly high $\overline{u^2}$ values (Antonia and Rajagopalan, 1990). These considerations suggest that the drag force of a porous disc is mainly driven by the velocity deficit and that the swirling velocity has a contribution of roughly the same order as turbulence.

2.2.2 Azimuthal mean momentum budget: angular momentum conservation

One distinguishing feature of the swirling wake over the classical axisymmetric wake is the presence of an additional conservation law: the conservation of angular momentum. This law is obtained by integrating the azimuthal mean momentum transport equation (2.1.10) which is recalled below for readability:

$$\rho U\frac{\partial W}{\partial x} + \rho V\frac{\partial W}{\partial r} + \rho\frac{VW}{r} \;=\; -\rho\frac{\partial \overline{vw}}{\partial r} - 2\rho\frac{\overline{vw}}{r} - \left\{\rho\frac{\partial \overline{uw}}{\partial x}\right\}. \tag{2.2.10}$$

Here, the term in curly brackets in equation (2.2.10) was kept this time to remain faithful to the original work of Shiri (2010) and Dufresne (2013) but is negligible compared to the rest. The derivation of the angular momentum conservation law is detailed in the following. First, the left-hand side of equation (2.2.10) can be manipulated to yield:

$$\rho U\frac{\partial W}{\partial x}+\rho V\frac{\partial W}{\partial r}+\rho\frac{VW}{r} \;=\; \rho\left[\frac{\partial UW}{\partial x}+\frac{\partial VW}{\partial r}+\frac{VW}{r}-W\frac{\partial U}{\partial x}-W\frac{\partial V}{\partial r}\right]. \quad (2.2.11)$$

The $\partial U/\partial x$ term can be replaced using the continuity equation (2.1.7) to obtain:

$$\rho U\frac{\partial W}{\partial x}+\rho V\frac{\partial W}{\partial r}+\rho\frac{VW}{r} \;=\; \rho\left[\frac{\partial UW}{\partial x}+\frac{\partial VW}{\partial r}+2\frac{VW}{r}\right]. \quad (2.2.12)$$

Equation (2.2.12) is then multiplied by r and integrated over a cylinder of infinitesimal thickness to obtain:

$$2\pi\rho\int_0^\infty\left[\frac{\partial UW}{\partial x}+\frac{\partial VW}{\partial r}+2\frac{VW}{r}\right]r^2dr \;=2\pi\rho\int_0^\infty\left[\frac{\partial UW}{\partial x}\right]r^2dr+2\pi\rho\int_0^\infty\frac{\partial r^2VW}{\partial r}dr,$$

$$=2\pi\rho\frac{d}{dx}\int_0^\infty UWr^2dr+2\pi\rho\cancel{\left[r^2VW\right]_0^\infty}, \quad (2.2.13)$$

$$=2\pi\rho\frac{d}{dx}\int_0^\infty UWr^2dr, \quad (2.2.14)$$

where the last term in equation (2.2.13) is null since radial and azimuthal velocities collapse at infinity. Similarly, the right hand side of equation (2.2.10) is integrated to yield:

$$-2\pi\rho\int_0^\infty\frac{\partial\overline{uw}}{\partial x}r^2dr-2\pi\rho\int_0^\infty\frac{\partial r^2\overline{vw}}{\partial r}dr= \;-2\pi\rho\frac{d}{dx}\int_0^\infty\overline{uw}r^2dr-2\pi\rho\cancel{\left[r^2\overline{vw}\right]_0^\infty},$$

$$=\;-2\pi\rho\frac{d}{dx}\int_0^\infty\overline{uw}r^2dr. \quad (2.2.15)$$

Combining equations (2.2.14) and (2.2.15) yields the integration of the azimuthal momentum transport equation (2.2.10) over a cylinder of infinitesimal thickness:

$$2\pi\rho\frac{d}{dx}\int_0^\infty(UW+\{\overline{uw}\})r^2dr. \quad (2.2.16)$$

Finally, integrating equation (2.2.16) from the inlet to the outlet of $\mathcal{V}$ yields the angular momentum conservation law:

$$G_0=2\pi\rho\int_0^\infty(UW+\{\overline{uw}\})r^2dr, \quad (2.2.17)$$

where $G_0 = \text{const.}$ is the source value of the angular momentum conferred to the wake by the actuator disc. A dimensionless version of equation (2.2.17) can be defined with the following normalisation:

$$G_0^* = \frac{G_0}{\frac{1}{8}\rho U_\infty^2 \pi D^3} = 16 \int_0^\infty (U^* W^* + \{\overline{uw}^*\}) r^{*^2} dr^*. \tag{2.2.18}$$

Equation (2.2.18) is the dimensionless angular momentum conservation law which governs how swirl will evolve as the wake develops. In the next section, the far wake approximation will be clearly stated and its implications of the conservation laws will be given.

2.2.3 Far wake approximations

The far wake approximation considers, as the name implies, the far field of the wake where some further simplifications to the governing equations (2.1.8) - (2.1.10), (2.2.8) and (2.2.18) can be made. By far, the most important assumption is that the mean streamwise convective velocity is assimilated to the free-stream velocity U_∞. As shown in the seminal work of George (1989) and later discussed in the work of Dufresne (2013), this scaling is unique to the turbulent wake which differs from the scalings in other shear flows like boundary layers or turbulent jets (Schlichting and Kestin, 1961; Shiri, 2010). Furthermore, the far wake approximation entails a control volume $\mathcal{V}_\infty$ long enough in the streamwise direction so that the pressure term and the turbulence term in equation (2.2.8) can be neglected (Townsend, 1976). With these approximations and following George (1989), the conservation of streamwise momentum for a swirling wake simply becomes:

$$C_D = 16 \int_0^\infty [U_\infty^* \Delta U^*] r^* dr^*, \tag{2.2.19}$$

which states that the drag coefficient of the actuator disc is directly related to the velocity deficit ΔU^*. This far wake conservation law is the physical ground for the various well known analytical wake models like the one proposed by Frandsen et al. (2006), Bastankhah and Porté-Agel (2014), or Ishihara and Qian (2018) to name a few. Despite considering a swirling axisymmetric wake, swirl plays no part in the axial conservation law (2.2.19) with the far wake approximations. This means that in the far wake, both non-swirling and swirling axisymmetric wakes are asymptotically identical in terms of drag. This result was also shown for the far field of swirling and non-swirling jets in the work of Shiri (2010).

This fundamental result is the reason why the swirling motion (and turbulence) was historically omitted from the analytical modelling of wind turbine wakes (Porté-Agel, 2019). The most popular analytical models like the models proposed in Jensen (1983), Frandsen et al. (2006) or Bastankhah and Porté-Agel (2014) focused on modelling the streamwise evolution of the mean velocity deficit. Between these models, different coefficients were proposed with different mathematical functions to describe the shape of the velocity deficit. Accordingly, porous discs surrogates were designed throughout the years focusing only in reproducing the same velocity deficit and drag of a target wind turbine (Sforza et al., 1981; Aubrun, 2013; Aubrun et al., 2019; Lignarolo et al., 2016b; Vinnes et al., 2022; Helvig et al., 2021; Camp and Cal, 2016; Öztürk et al., 2023; Howland et al., 2016). Naturally, following the influential work of Castro (1971), porosity was the main tuning parameter.

In the same manner, the far field approximation of the angular momentum conservation (2.2.18) yields:

$$G_0^* = 16 \int_0^\infty [U_\infty^* W^*] r^{*^2} dr^*. \tag{2.2.20}$$

Equation (2.2.20) governs how the mean swirling motion will evolve in the streamwise direction. Swirl will decay rapidly with the streamwise distance as shown in Dufresne (2013) and in Shiri (2010). To conserve angular momentum, swirl will spread over a larger area. In general, both balance equations (2.2.19) and (2.2.20) will govern the far wake evolution of the mean swirling wake. Conversely, the mean velocity deficit is absent from the angular momentum conservation. This suggests that the far wake is a region of the flow where the angular momentum is decoupled from the streamwise momentum.

The studied flow is not necessarily under ideal far wake conditions, given that the assessed distances are relatively close to the wake generator ($X/D \geq 2$). Nevertheless, these approximations enable us to establish compelling phenomena associated with swirl and extend far wake notions to a more intermediate region of the flow. In particular, these approximations facilitate the application of similarity theory, incorporating an additional constraint in the form of the conservation of mean angular momentum, thereby enriching the framework of similarity analysis.

2.3 Similarity analysis and scaling laws

The similarity analysis consists in seeking self-similar solutions for the flow properties (velocity deficit, wake width, swirl, Reynolds stresses ...) which have to satisfy the conservation laws listed in the previous section. These conservation laws act as the "similarity constraints", as stated by George (1989), which condition the scaling laws for the wake properties. In particular, the characteristic scales $S_i(x)$ for shear flows have power law dependencies on the streamwise variable x such as $S_i(x) \sim x^{\beta_i}$ (Pope, 2000). The similarity analysis gives analytical values for the exponents β_i. In the following section, the similarity analysis for the turbulent axisymmetric swirling wake will be discussed in detail as well as the different closures used during the analysis.

In order to establish similarity, self-preserving solutions are considered for the mean streamwise velocity, Reynolds stresses (R_{ij}), turbulent kinetic energy (k) transport terms in equation (1.1.11) and dissipation (George, 1989; Dairay et al., 2015). For example, the following self-preserving solution for the velocity deficit ΔU is defined:

$$\Delta U = U_\infty - U(x, r) = U_s(x) f(\eta), \tag{2.3.1}$$

where $U_s(x)$ is a characteristic velocity deficit scale and $f(\eta)$ is the corresponding similarity function. Following Pope (2000)'s work, the U_s scale in equation (2.3.1) is defined as the centreline velocity deficit which in most cases corresponds exactly to the maximum velocity deficit. Therefore, the following properties regarding equation (2.3.1) are established:

$$U_s(x) = U_\infty - U(x, 0) \quad \text{and} \quad f(0) = 1. \tag{2.3.2}$$

Similarity theory states that $f(\eta)$ is an invariant with respect to the streamwise distance by definition. In this framework, η is the normalised radial distance in the wake such

that $\eta = r/\delta$, where δ is a characteristic length scale of the flow. Usually, δ is chosen as either the wake's half width (Pope, 2000) or the wake's integral scale (George, 1989; Nedic, 2013; Dairay et al., 2015). Both of these cases however, naturally relate δ to the velocity deficit. In this work, no universality on the length scale δ is assumed and it is hypothesised to depend on the similarity constraints used during the similarity analysis.

In the same manner as equation (2.3.1), the following self-preserving functions are considered for the other physical quantities involved in the governing equations.

$$R_{ij}(x,r) = R_s(x)g_{ij}(\eta), \tag{2.3.3}$$

$$k(x,r) = K_s(x)\kappa(\eta), \tag{2.3.4}$$

$$\left(\frac{\overline{pv}}{\rho} - \frac{1}{2}\overline{vk^2}\right) = T_s(x)t(\eta), \tag{2.3.5}$$

$$\epsilon(x,r) = D_s(x)e(\eta). \tag{2.3.6}$$

In addition to these classical (George, 1989; Redford et al., 2012) self-similar functions, a self-preserving solution is also considered for the mean swirling velocity $W(x,r)$ (Shiri et al., 2008; Dufresne, 2013) such as:

$$W(x,r) = W_s(x)h(\eta). \tag{2.3.7}$$

As was shown in the work of Townsend (1976) and George (1989) on self-preserving turbulent flows, the energy equation and the momentum conservation equations do not suffice to obtain scaling laws for the flow properties. To demonstrate this, the self-similar solutions are substituted in governing equations (2.1.8) and in the TKE equation (1.1.12) using the far field approximations to yield:

$$\left[\frac{\delta}{U_s}\frac{dU_s}{dx}\right]f - \left[\frac{d\delta}{dx}\right]\eta f' = -\left[\frac{R_s}{U_\infty U_s}\right]\frac{1}{\eta}\frac{d}{d\eta}(\eta g_{12}), \tag{2.3.8}$$

and

$$\left[\frac{\delta}{K_s}\frac{dK_s}{dx}\right]\kappa - \left[\frac{d\delta}{dx}\right]\eta\kappa' = -\left[\frac{R_s}{K_s}\left(\frac{U_s}{U_\infty}\right)\right]g_{12}f' + \left[\frac{T_s}{K_s U_\infty}\right]t - \left[\frac{D_s\delta}{K_s U_\infty}\right]e, \tag{2.3.9}$$

where all the x-dependent terms are enclosed in square brackets. Self-preservation requires that all these terms have the same x-dependency. Therefore, from equation (2.3.8):

$$\frac{d\delta}{dx} \sim \frac{\delta}{U_s}\frac{dU_s}{dx} \tag{2.3.10}$$

and

$$\frac{d\delta}{dx} \sim \frac{R_s}{U_\infty U_s}. \tag{2.3.11}$$

For the TKE equation, self-preservation requires:

$$\frac{d\delta}{dx} \sim \frac{\delta}{K_s}\frac{dK_s}{dx}, \tag{2.3.12}$$

$$\frac{d\delta}{dx} \sim \frac{R_s}{K_s}\frac{U_s}{U_\infty}, \tag{2.3.13}$$

$$\frac{d\delta}{dx} \sim \frac{T_s}{K_s U_\infty}, \tag{2.3.14}$$

and

$$\frac{d\delta}{dx} \sim \frac{D_s\delta}{K_s U_\infty}, \tag{2.3.15}$$

From equations (2.3.11) and (2.3.13) it can be shown that:

$$K_s \sim U_s^2, \tag{2.3.16}$$

which simplifies the similarity relation (2.3.9) and yields the self-preservation condition:

$$\frac{d\delta}{dx} \sim \frac{R_s}{U_s U_\infty} \sim \frac{T_s}{U_s^2 U_\infty} \sim \frac{D_s\delta}{U_s^2 U_\infty}. \tag{2.3.17}$$

At this point in the similarity analysis, there is the need for *ad hoc* assumptions for the scale function of other terms in the energy equation and in particular for the dissipation ϵ to proceed further. In particular, two cases for the scaling of dissipation were historically proposed in the seminal work of George (1989) depending on the Reynolds number (Tennekes and Lumley, 1972). In this work, only the high-Reynolds number case will be discussed but the reader is referred to the work of George (1989) and Johansson et al. (2003) for more information on the low-Reynolds number case.

The choice for the scaling function for dissipation is based on fundamental considerations regarding the sate of turbulence in the flow (Batchelor, 1953; George, 1989; Nedic, 2013; Dairay et al., 2015).

2.3.1 Generalised scaling laws

For over a decade, an extensive body of research has produced a considerable amount of evidence, encompassing both experimental and numerical simulations. This evidence consistently relates the dissipation coefficient, denoted as C_ϵ, to a combined dependence on a local and a global Reynolds number (Seoud and Vassilicos, 2007; Mazellier and Vassilicos, 2008; Nedic, 2013; Laizet et al., 2013; Nagata et al., 2013; Vassilicos, 2015; Dairay et al., 2015; Nagata et al., 2017). Notably, contrary to the predictions of equilibrium turbulence in the Kolmogorov (1941) sense, C_ϵ is not a constant; instead, it scales proportionally to the ratio of a global Reynolds number Re_G to a local Reynolds number Re_l, such as:

$$C_\epsilon \sim \frac{Re_G^m}{Re_l^n}. \tag{2.3.18}$$

where $Re_G = Re_D = (U_\infty D/\nu)$ and $Re_l = (U_s\delta)/\nu$. The exponents n and m will depend on the assumptions made on the turbulence dissipation scaling. From equation (2.3.18) a general dissipation scaling law can be written as detailed in Nedic (2013) which reads:

$$D_s \sim \frac{Re_G^m}{Re_L^n} \cdot \frac{U_s^3}{\delta}, \tag{2.3.19}$$

which after some manipulation yields:

$$\boxed{D_s \sim \left(\frac{U_\infty D}{\nu}\right)^m \cdot \frac{U_s^{(3-n)}\nu^n}{\delta^{(n+1)}}}. \tag{2.3.20}$$

Without making additional assumptions, the generalised dissipation scaling (2.3.20) can be used in combination with the similarity condition (2.3.17) to yield:

$$\frac{d\delta}{dx} \sim \frac{U_\infty^{(m-1)} D^m}{\nu^m} \cdot \frac{U_s^{(1-n)}\nu^n}{\delta^n}, \tag{2.3.21}$$

which is obtained without the need of any similarity constraint imposed by the conservation laws. At this point in the analysis, either a similarity constraint has to be used to proceed further or an assumption has to be made regarding turbulence (Nedic, 2013; Vassilicos, 2015).

2.3.2 An additional degree of freedom in the similarity analysis: conservation of mean angular momentum

As detailed in Nedic (2013) and later in Dairay et al. (2015), when applying similarity theory to a turbulent axisymmetric wake without swirl, there is only one main similarity constraint coming from the conservation of streamwise momentum (2.2.19). Injecting self-similar solutions to this law yields:

$$F_D = 2\pi\rho\big[U_\infty U_s \delta^2\big] \int_0^\infty f\eta d\eta = 2\pi\rho U_\infty^2 \theta^2 = \text{const.} \tag{2.3.22}$$

where θ is the momentum thickness and is defined as:

$$\theta^2 = \frac{1}{U_\infty^2} \int_0^\infty U_\infty (U_\infty - U) r dr. \tag{2.3.23}$$

From equation (2.3.22), it follows that:

$$\frac{U_s}{U_\infty} \sim \left(\frac{\delta}{\theta}\right)^{-2}, \tag{2.3.24}$$

which links the intensity of the mean velocity deficit to a characteristic length scale of the wake. However, in the case of a swirling wake, the similarity analysis is not as straightforward. The conservation of angular momentum in fact adds a degree of freedom to the analysis and therefore constitutes an extra similarity constraint. This constraint is obtained by writing the conservation of angular momentum (2.2.20) with a self-similar swirl (2.3.7) and yields:

$$G_0 = 2\pi\rho U_\infty [W_s \delta^3] \int_0^\infty h\eta^2 d\eta = \text{const.} \tag{2.3.25}$$

From equation (2.3.25), it follows:

$$W_s \sim \delta^{-3}, \tag{2.3.26}$$

which links the intensity of mean swirl to a characteristic length scale of the wake. From equations (2.3.24) and (2.3.26) it is clear that there are now two parameters that can prescribe the development of the wake and set its characteristic length scale. In fact, this was already pointed out in the historic work of Reynolds (1962) who stated:

> *"The asymptotic forms for swirling wakes and jets are determined not only by their net linear momentum but also by their net angular momentum. With this parameter added, it is possible to define two scale lengths and two scale velocities. No longer is there a clear prescription of the variation of width and intensity. Instead, the similarity condition takes the form of an unprescribed functional relationship between two non-dimensional parameters, one characterizing the linear momentum, the other the angular momentum"* -Reynolds (1962)

In the influential contribution of Reynolds (1962), the author delineated two primary asymptotic conditions wherein either linear or angular momentum governs the development of the swirling wake. Although the author refrained from assigning a specific term to the "functional relationship" linking these parameters, the classification of the two principal scenarios was characterised by the ratio of streamwise momentum to angular momentum. This non-dimensional parameter was precisely defined as follows:

$$\frac{F_D \mathcal{L}}{G_0} = \frac{1}{\hat{S}}, \tag{2.3.27}$$

where $\mathcal{L}$ is a global scale of the flow which in our case can be associated to the diameter D of the rotor/actuator disc. In later years, pioneering work on swirling flows like Gupta et al. (1984) and Alekseenko et al. (1999) reported on the importance of this ratio and defined the swirl number $\hat{S}$. The two limiting cases considered by Reynolds (1962) were: $\hat{S} \gg 1$ and $\hat{S} \ll 1$.

The $\hat{S} \gg 1$ case corresponds to a wake where the swirling component dominates the flow and the angular momentum is sufficient to characterise the development of the wake. It is improbable that this high swirl number condition is applicable to the current study, given that wind turbine wakes typically exhibit moderate swirl numbers (Holmes and Naughton, 2022). Such conditions are more reminiscent of wakes behind self-propelled bodies or propellers with a pronounced swirling component (Alekseenko et al., 1999). In this case however, the characteristic length scale δ would be solely related to W_s by equation (2.3.26) and the following scaling laws would be obtained:

$$\frac{\delta}{\theta} \sim \left(\frac{x}{\theta}\right)^{1/4}, \tag{2.3.28}$$

and

$$\frac{W_s}{U_\infty} \sim \left(\frac{x}{\theta}\right)^{-3/4}. \tag{2.3.29}$$

Conversely, in the second case where $\hat{S} \ll 1$, the wake development is fully controlled by the conservation of streamwise momentum (2.3.22) and the classical scalings for axisymmetric wakes are obtained (Townsend, 1976). An important conclusion in the work of Reynolds (1962) was that, at the current time:

> "*Similarity arguments give no further definite information about the variation of the scales when* $F_D\mathcal{L}/G_0 \sim \mathcal{O}(1)$" - Reynolds (1962)

which means that at that moment, the case $\hat{S} = \mathcal{O}(1)$ did not produce clear scaling laws since some relations were missing from the similarity analysis. However, with the body of research regarding non-equilibrium turbulence (Mazellier and Vassilicos, 2008; Nedic, 2013; Vassilicos, 2015), these "arguments" are now at our disposal to further similarity theory of swirling wakes in the case where $\hat{S} = \mathcal{O}(1)$. As will be shown in chapter 4, the order of magnitude of $\hat{S}$ in wind turbine wakes and in our study is around $\hat{S} = [0.2 - 0.3]$ which corresponds to the $\hat{S} = \mathcal{O}(1)$ case.

2.3.3 Equilibrium vs. non-equilibrium turbulence

The consequences of considering equilibrium turbulence or non-equilibrium turbulence in the similarity analysis of swirling wakes will be discussed in the following. If $n = m = 0$ is imposed in the generalised dissipation scaling equation (2.3.20), the classical equilibrium scaling law for dissipation is obtained which reads:

$$C_\epsilon = \text{const.} \quad \text{and} \quad D_s \sim \frac{U_s^3}{\delta}. \tag{2.3.30}$$

If this dissipation model (2.3.30) is used in combination with the similarity condition (2.3.17) it can be shown that:

$$\frac{d\delta}{dx} \sim \frac{U_s}{U_\infty}, \tag{2.3.31}$$

which entails that the wake expansion rate is directly related to the velocity deficit. Within this equilibrium approximation, an additional condition becomes necessary to advance further. However, the similarity constraint involving both U_s and δ is the conservation of mean streamwise momentum (2.3.24). Using this constraint in conjunction with (2.3.31) yields the classical Townsend (1976) and George (1989) equilibrium scaling law:

$$\boxed{\frac{\delta}{\theta} \sim \left(\frac{x}{\theta}\right)^{1/3}}, \tag{2.3.32}$$

predicting a wake expansion as $x^{1/3}$. Interestingly, to obtain the similarity scaling law (2.3.32), the streamwise momentum balance had to be used. This constrains the nature of δ and relates it directly to the velocity deficit as explained in Pope (2000); George (1989); Johansson et al. (2003). This means that, for equilibrium turbulence the nature of the wake's characteristic length δ is related to the velocity deficit (Nedic, 2013). In the words of Reynolds (1962), the approximation $\hat{S} \ll 1$ was implicitly applied by the use of equilibrium turbulence in far wake conditions.

From equations (2.3.32) and (2.3.24) it immediately follows that:

$$\boxed{\frac{U_s}{U_\infty} \sim \left(\frac{x}{\theta}\right)^{-2/3}}, \tag{2.3.33}$$

which predicts a wake recovery as $x^{-2/3}$. Direct numerical simulations (DNS) of the axisymmetric wake of a disc reported in Johansson et al. (2003), showed that these far wake equilibrium scaling laws held true over a wide range of distances $100 \leq x/\theta \leq 600$ for high Reynolds numbers (see figure 2.4). Other studies (Redford et al., 2012; Cannon et al., 1993) have also observed these equilibrium scaling laws for other types of bluff bodies (with and without porosity) over a similar x range.

Recent studies like that of Shiri (2010) and Dufresne (2013) have extended these equilibrium scalings to the swirling component of swirling shear flows (jets and wakes). In particular Dufresne (2013) extended the equilibrium scalings to the swirling wake of a wind turbine. Using the angular momentum similarity constraint (2.3.26) with (2.3.32), the equilibrium scaling law for swirl decay is obtained (Dufresne, 2013):

$$\boxed{\frac{W_s}{U_\infty} \sim \left(\frac{x}{\theta}\right)^{-1}}, \tag{2.3.34}$$

which predicts a x^{-1} decay for the swirling velocity component of the axisymmetric wake (Wosnik and Dufresne, 2013). From equations (2.3.33) and (2.3.34), a scaling law linking the velocity deficit recovery with swirl decay can be obtained and reads:

$$\boxed{\frac{W_s}{U_\infty} \sim \left(\frac{U_s}{U_\infty}\right)^{3/2}}. \tag{2.3.35}$$

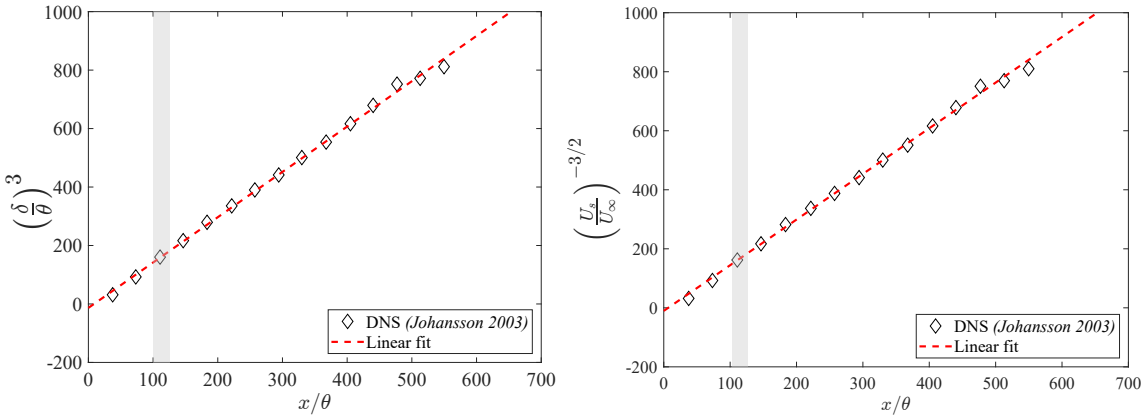

(a) (b)

Figure 2.4: DNS data of the axisymmetric wake of a disc showing the streamwise evolution of (a) the wake width and (b) the velocity deficit with equilibrium scalings. Shaded areas show the near wake limit where non-equilibrium is expected. Taken from Johansson et al. (2003).

The studies reported in Wosnik and Dufresne (2013) established that swirl decay, in the near field and intermediate field of a wind turbine, was not well predicted by the equilibrium scaling law (2.3.34), as evidenced by figure (2.5a). The authors argued that tip vortices "complicated the swirl" and prevented the decay rate to set. Interestingly, the equilibrium law, linking the swirl decay rate with the velocity deficit (2.3.35), exhibited better data collapse at distances around $X/D = 6$ (figure 2.5b).

Holmes and Naughton (2022) studied the axisymmetric swirling wake of a rotating porous disc at different rotating speeds. The authors argued that the equilibrium scaling laws predicted the swirl decay rate only for $X/\theta > 20$, after an "initial adjustment region" in the near to intermediate field. In other words, Wosnik and Dufresne (2013) as well as Holmes and Naughton (2022) evidenced that equilibrium turbulence is not found in the near to intermediate wakes of wind turbines and a rotating surrogate. In fact, this region of the wake is characterised by strong non-homogeneity and anisotropy, where equilibrium is highly unlikely (Dairay et al., 2015). This means that the equilibrium turbulence hypothesis ($C_\epsilon = \text{const.}$) is not an appropriate candidate to study the swirling wake properties in the intermediate field of a swirling turbulent wake.

In the following therefore, the non-equilibrium turbulence approach to the similarity analysis will be given and, for the first time, this approach will be extended to the swirling wake. Assuming $n = m = 1$ in equation (2.3.20), following Vassilicos (2015); Dairay et al. (2015), gives the non-equilibrium dissipation scaling and reads:

$$D_s \sim \frac{U_\infty U_s^2}{\delta}\left(\frac{D}{\delta}\right). \tag{2.3.36}$$

Furthermore, the non-equilibrium scalings in equation (2.3.21) yield:

$$\frac{d\delta}{dx} \sim \frac{D}{\delta}, \tag{2.3.37}$$

which entails that the wake expansion rate is not related to either W_s or U_s but rather is entirely related to the unprescribed characteristic length scale δ. After some manipulation, equation (2.3.37) yields:

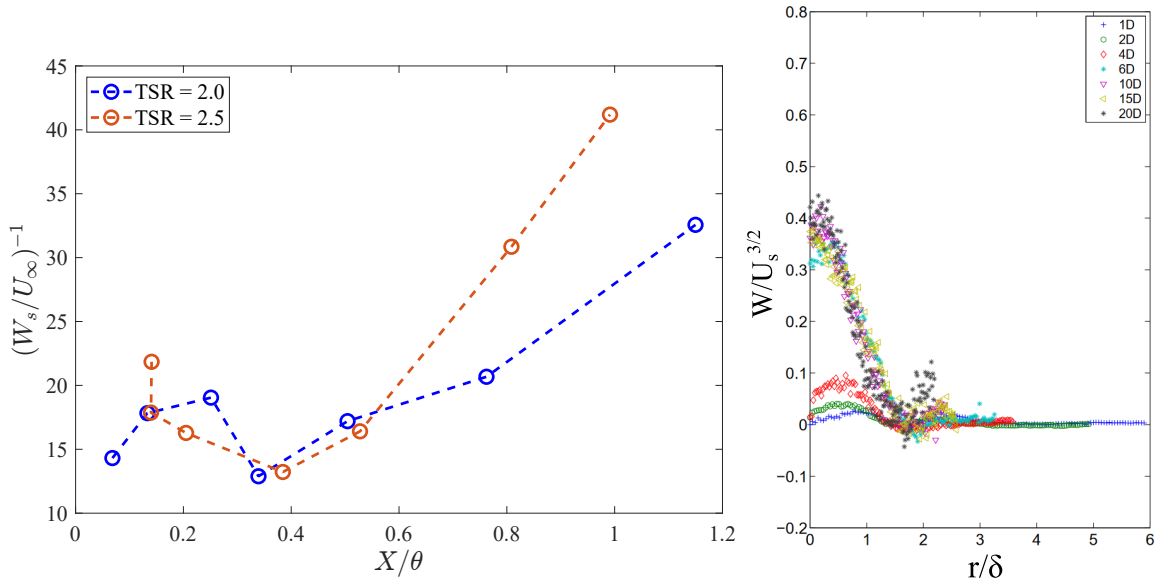

(a) (b)

Figure 2.5: Hot-wire data for the wake of a rotating wind turbine at different tip-to-speed ratios (TSR) with equilibrium scaling laws for (a) the swirl decay rate and (b) the swirl scaling with $U_s^{3/2}$. Taken from Wosnik and Dufresne (2013).

$$\boxed{\frac{\delta}{\theta} \sim \left(\frac{x}{\theta}\right)^{\frac{1}{2}} \left(\frac{\theta}{D}\right)^{-\frac{1}{2}}}, \tag{2.3.38}$$

where no extra similarity constraints were needed to obtain equation (2.3.38). This means that, with a non-equilibrium approach, the nature of the length scale δ is not yet set to any mechanism (velocity deficit, turbulence, swirl, ...). Therefore, the length scale δ will be purely related to the mechanism which sets the level of dissipation in the turbulent wake. There is no trivial solution to the question of what mechanism sets the level of dissipation in turbulent flows, as was stated by Tennekes and Lumley (1972). However, for a swirling axisymmetric wake, the main mechanism could be either swirl or the velocity deficit, since these equations are decoupled using the far field approximations.

It will be shown in the next chapters that swirl sets the initial conditions of the wake expansion and recovery. It is therefore argued that the length scale δ will be related to swirl ($\delta = \delta_{swirl}$), where δ_{swirl} is defined as a characteristic length scale of swirl. Equation (2.3.38) therefore predicts a swirl spreading as $x^{1/2}$. Since both the swirling and non-swirling wakes evolve towards the exact same asymptotic state, the governing mechanism might shift to the velocity deficit distribution. At this point however, the similarity scalings will also predict a wake growth as $x^{1/2}$. In fact, as shown in figure 2.6, where data from the work of Chamorro and Porté-Agel (2010) was taken. If δ is assumed to be related to the velocity deficit, no trend is clear for δ in the near to intermediate wake. As the streamwise distance increases however, a trend becomes clear and is well approximated by a $\delta \sim x^{1/2}$ non-equilibrium law.

The non-equilibrium scaling laws can be then extended to the conservation of angular momentum and swirl. From equations (2.3.38) and (2.3.26), a novel scaling law can be obtained for swirl decay such as:

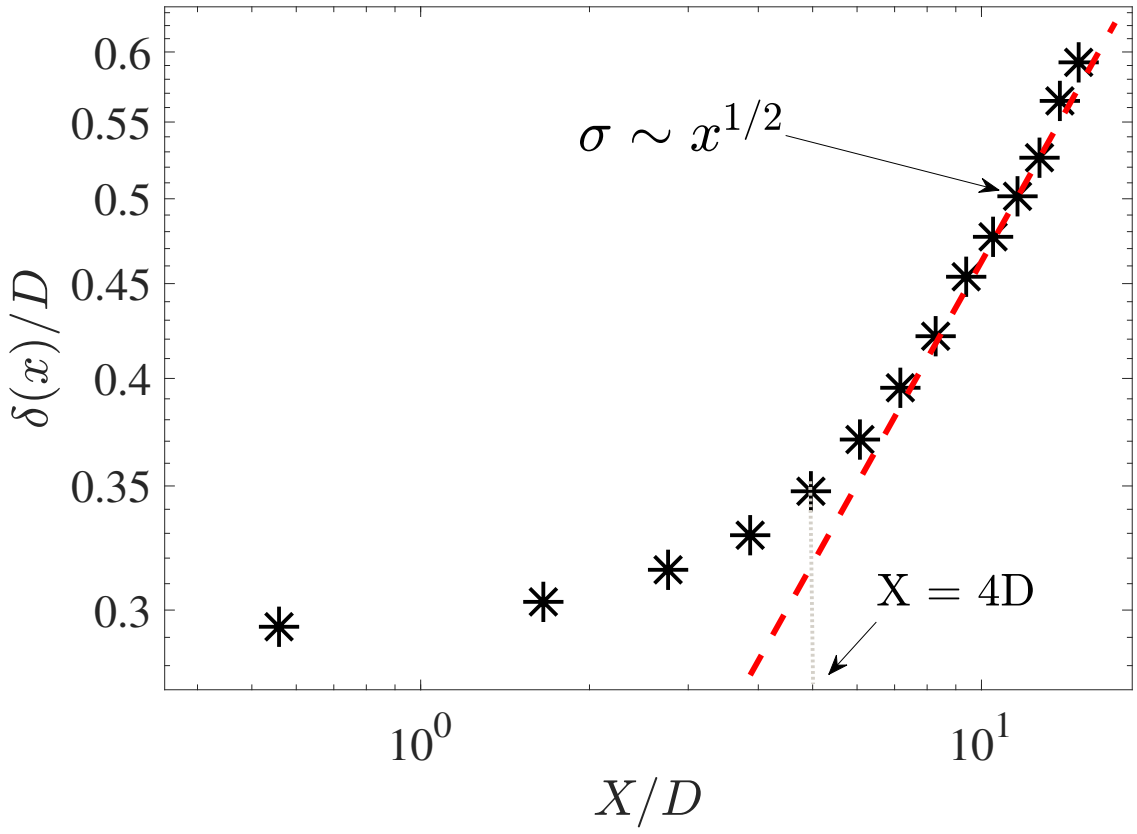

Figure 2.6: Wake width streamwise evolution of a lab-scale wind turbine. Adapted from Bastankhah and Porté-Agel (2014) where the displayed data comes from the work of Chamorro and Porté-Agel (2010).

$$\boxed{\frac{W_s}{U_\infty} \sim \left(\frac{x}{\theta}\right)^{-3/2}\left(\frac{\theta}{D}\right)^{3/2}}, \tag{2.3.39}$$

which predicts a swirl decay with $x^{-3/2}$. From equations (2.3.38) and (2.2.19) the non-equilibrium scaling law for U_s is obtained and reads:

$$\boxed{\frac{U_s}{U_\infty} \sim \left(\frac{x}{\theta}\right)^{-1}\left(\frac{\theta}{D}\right)}, \tag{2.3.40}$$

which predicts a wake recovery as x^{-1}. Using equations (2.3.40) and (2.3.39) yields:

$$\boxed{\frac{W_s}{U_\infty} \sim \left(\frac{U_s}{U_\infty}\right)^{3/2}}, \tag{2.3.41}$$

which is the same scaling law link as the one predicted by the equilibrium turbulence approach. This result explains in part why this scaling was shown to hold true for a variety of cases and over longer distances (Dufresne, 2013; Holmes and Naughton, 2022). This could prove most useful when predicting wake recovery, since this power law remains true regardless of the turbulence state (in equilibrium or not). Furthermore, measuring the swirling velocity could then suffice to predict how the wake would recover. This opens the door for other wake modelling approaches which consider swirl

Turbulence state	D_s	(δ/θ)	(U_s/U_∞)	(W_s/U_∞)	(W_s) vs. (U_s)
Equilibrium $(n = m = 0)$	$\sim \frac{U_s^3}{\delta}$	$\sim \left(\frac{x}{\theta}\right)^{1/3}$	$\sim \left(\frac{x}{\theta}\right)^{-2/3}$	$\sim \left(\frac{x}{\theta}\right)^{-1}$	$\frac{W_s}{U_\infty} \sim \left(\frac{U_s}{U_\infty}\right)^{3/2}$
Non-equilibrium $(n = m = 1)$	$\sim \frac{U_\infty U_s^2}{\delta}\left(\frac{D}{\delta}\right)$	$\sim \left(\frac{x}{\theta}\right)^{1/2}$	$\sim \left(\frac{x}{\theta}\right)^{-1}$	$\sim \left(\frac{x}{\theta}\right)^{-3/2}$	$\frac{W_s}{U_\infty} \sim \left(\frac{U_s}{U_\infty}\right)^{3/2}$

TABLE 2.1: Summary of the similarity scaling laws of the wake properties predicted by equilibrium and non-equilibrium turbulence.

and its impact on the wake properties. The different scaling laws stemming from the similarity analysis are summarised in table 2.1.

2.4 Concluding remarks

This theoretical examination of the turbulent wake produced by an actuator disc with added swirl has unveiled intriguing phenomena concerning the evolution of the wake and the distinctions between swirling and non-swirling wakes. The analysis demonstrated that, in the distant wake scenarios, both swirling and non-swirling wakes converge toward a common asymptotic state where drag is solely dictated by the velocity deficit. The effect of swirl is shown to be mainly located in the pressure term. Additionally, these approximations revealed a decoupling of both conservation laws: mean angular momentum and mean streamwise momentum conservation. This result suggested that additional length and velocity scales of the flow could be introduced in the problem thus enriching the framework of similarity theory as discussed by Reynolds (1962). In particular, it was shown that the conservation of angular momentum adds an extra constraint to the similarity analysis where two scales coexist and can potentially drive the development of the wake depending on the swirl number dimensionless parameter $\hat{S}$.

In the case of equilibrium turbulence, the application of the streamwise momentum conservation constraint becomes necessary for deriving scaling laws for the wake, thereby establishing a connection between length scales and velocity deficit. This perspective implicitly assumes that angular momentum is negligible compared to streamwise momentum which is likely not the case in the near to intermediate wake. On the other hand, it was revealed that non-equilibrium turbulence does not require an additional condition to produce a scaling laws for the evolution of the characteristic length scale δ. Consequently, non-equilibrium similarity avoids making assumptions about the swirl number, allowing both angular momentum and streamwise momentum to govern the wake development. This scenario leads to the identification of alternative scaling laws supported by recent literature. Additionally, employing non-equilibrium similarity theory, a novel scaling law for swirl decay is proposed, expressed as $W_s/U_\infty \sim (x/\theta)^{-3/2}$.

These findings naturally give rise to scientific questions that will be addressed, either partially or comprehensively, in the subsequent chapters:

Chapter 3: How can we add swirl to the porous disc?

Chapters 4 & 5: Which scalings are found in the generated wake?

Chapter 5: Were the fundamental mechanisms or scales of wake development (entrainment) changed by swirl?

In this study, leveraging the substantial experimental and theoretical expertise, as well as the advanced facilities at the PRISME laboratory, conducting an experimental analysis of the swirling wake was the natural decision. Accordingly, the incorporation of swirl into the porous disc model becomes imperative. Therefore, the following chapter presents the innovative design of the porous disc, now enhanced with swirl, and provides a comprehensive description of the experimental setup.

Résumé en français: Fondements théoriques de l'analyse du sillage tournant

Ce chapitre se consacre à une analyse théorique approfondie du sillage turbulent tournant, mettant particulièrement l'accent sur l'analyse par similarité. Bien que des cadres théoriques aient été établis précédemment pour les jets turbulents tournants (Shiri, 2010) ainsi que pour les sillages (George, 1989; Pope, 2000; Dufresne, 2013), ce chapitre va au-delà en dérivant une nouvelle loi d'échelle pour la décroissance d'amplitude du taux de rotation dans le sillage. De plus, une discussion détaillée sur l'effet du swirl sur cette analyse est présentée dans le cadre d'une turbulence en équilibre et hors équilibre au sens de Kolmogorov (1941).

Au début du chapitre, les principales équations de mouvement sont présentées dans leur forme RANS (Reynolds Averaged Navier Stokes). Le fluide est considéré comme incompressible, l'écoulement moyen est considéré comme stationnaire et les termes visqueux des équations de quantité de mouvement sont négligés. Ensuite, les hypothèses clés sont discutées afin de simplifier les équations générales. En particulier, l'hypothèse d'axisymmetrie est invoquée en s'appuyant sur des résultats d'études antérieures faites à ce sujet et appliquées à des éoliennes et à des sillages au sens large (Vermeer et al., 2003; Chamorro and Porté-Agel, 2010; Bossuyt et al., 2021; Nedic, 2013). De plus, l'approximation de couche de cisaillement mince est utilisée pour le sillage moyen tel que montré dans les travaux de Shiri et al. (2008). Ces hypothèses permettent d'écrire les équations RANS simplifiées relatives à notre cas. A l'aide d'un bilan de quantité de mouvement, les lois de conservations qui régissent cet écoulement sont établies : la conservation de quantité de mouvement linéaire et angulaire. Ces deux lois de conservation sont liées via le nombre de swirl $\hat{S}$ (Reynolds, 1962; Gupta et al., 1984). Jusqu'à présent, les cas asymptotiques $\hat{S} \ll 1$ et $\hat{S} \gg 1$ ont été traités et des lois d'échelle ont été proposées (Reynolds, 1962; Townsend, 1976; George, 1989; Johansson et al., 2003; Nedic, 2013). Cependant, le cas $\hat{S} = (\mathcal{O})1$ n'a pas encore été traité et sera l'objet de cette étude. D'après la littérature scientifique des éoliennes d'échelle réelle (Holmes and Naughton, 2022), les nombres de swirl sont d'environ $\hat{S} = [0.2 - 0.4]$, les plaçant dans le cas $\hat{S} = (\mathcal{O})1$.

L'analyse du sillage tournant à montré que, dans l'approximation du sillage lointain ("*far wake*"), le sillage tournant et non-tournant sont identiques en termes de quantité de mouvement linéaire. Même si les distances examinées dans le sillage du disque poreux sont relativement faibles (de deux à sept diamètres de disque), les approximations de sillage lointain nous permettent d'asseoir des phénoménologies liées au swirl et son influence sur les lois d'échelle. En particulier, l'ajout de la loi de conservation de quantité de mouvement angulaire enrichi le cadre de l'analyse de similarité du sillage établie par Townsend (1976) et George (1989).

En seconde partie du chapitre, une analyse de similarité (George, 1989; Pope, 2000) est appliquée au cas du sillage tournant afin d'établir les lois d'échelle pilotant son développement. Le développement du sillage tournant est caractérisé par une récupération, une expansion et une évolution du swirl. En effet, l'originalité de cette étude réside dans l'introduction du swirl, multipliant ainsi le nombre d'échelles caractéristiques du sillage. Une vitesse caractéristique de swirl W_s et une longueur caractéristique de swirl δ_{swirl} sont ajoutées à l'analyse de similarité, soulevant la question du choix de la longueur caractéristique qui guide l'évolution auto-similaire du sillage. Grâce à cette analyse, des lois d'échelle sont dérivées à la fois dans le cadre de la cascade de tur-

bulence classique (Kolmogorov, 1941), dans lequel le taux de dissipation de l'énergie cinétique turbulente est en équilibre avec le flux inter-échelles, et du paradigme dans lequel la dissipation est hors équilibre (Vassilicos, 2015). Pour la première fois, l'analyse d'auto-similarité dans le cadre de la turbulence hors équilibre est appliquée au cas du sillage tournant. De cette analyse, une nouvelle loi d'échelle de décroissance du swirl est proposée (éq. 2.3.39). En effet, l'analyse de similarité avec une turbulence en équilibre, associe la longueur caractéristique δ au déficit de vitesse et donc suppose que $\hat{S} \ll 1$. Cependant, l'analyse avec une turbulence hors-équilibre, n'associe cette longueur caractéristique à aucune "contrainte de similarité" au sens de George (1989). Ce degré de liberté permet au sillage d'être décrit par une échelle liée au swirl ou au déficit de vitesse le long de son épanouissement. Dans cette étude, nous supposons que l'échelle caractéristique qui pilote cet écoulement est liée au swirl (δ_{swirl}). Ces réflexions suscitent les interrogations scientifiques suivantes, auxquelles nous apporterons des réponses tout au long de ce manuscrit :

Chapitre 3 : Comment peut-on ajouter un taux de rotation (swirl) dans le sillage d'un disque poreux ?

Chapitre 4 & 5 : Quelles lois d'échelles trouve-t-on dans le sillage généré ?

Chapitre 5 : Les mécanismes fondamentaux liés à l'entraînement ont-ils été modifiés par l'ajout de swirl ?

Dans cette étude, en tirant parti de l'expertise expérimentale et des installations avancées du laboratoire PRISME, une analyse expérimentale du sillage turbulent avec swirl s'est imposée comme une démarche naturelle. En conséquence, l'incorporation du swirl dans le modèle de disque poreux devient impérative. Le chapitre suivant présente donc la conception innovante du disque poreux, désormais enrichi avec une composante azimutale de vitesse, et fournit une description complète du dispositif expérimental.

3

Experimental set-up: test rig design and measurement techniques

Contents

The experiments presented in this chapter were performed at the PRISME Laboratory (*Laboratoire Pluridisciplinaire de Recherche, Ingénierie des Systèmes, Mécanique et Energétique*). The objective of this chapter is to describe the porous disc design process to passively include swirl and the experimental campaigns that were carried out to measure the generated wakes. The methodology for the design of the porous disc will be first presented, then the wind tunnel properties and eventually the metrology used to characterise the wake with the added swirling motion.

Part A

Experimental apparatus

3.1 Geometry and design of the porous discs with swirl

This section focuses on providing a detailed description of the porous disc design process used as a wind turbine surrogate. The key characteristics of the porous disc are highlighted with particular attention given to the chosen technique to passively add swirl.

3.1.1 Geometrical characteristics of the porous discs

The main geometrical parameters and dimensions of the porous discs used in this study are shown in figure 3.1. The design of the porous disc was inspired from the one proposed in Helvig et al. (2021). In the present study, the porous discs have a diameter and a thickness of $D = 100$ mm and $e = 5$ mm, respectively. Each porous disc has a central solid disc of 25 mm in diameter with a 6 mm hole in the middle. From this solid disc, 16 trapezoidal blades make up the body of the disc along with an inner rim of 61 mm in diameter and 1.5 mm in width. The outer rim of the porous disc is 2 mm wide.

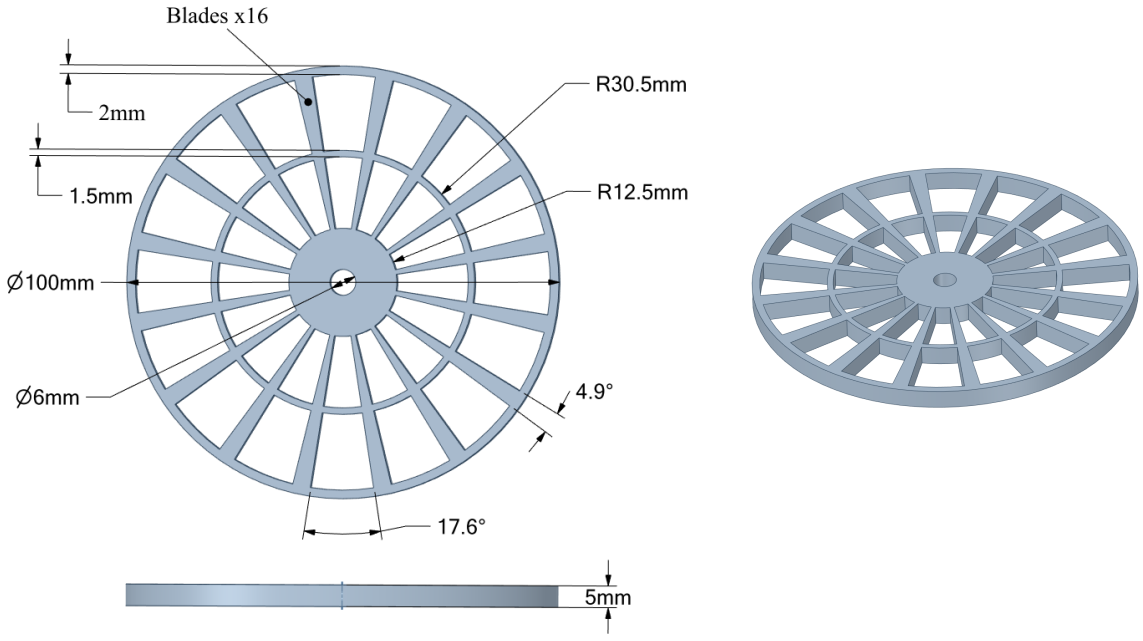

(a) (b)

Figure 3.1: Non-uniform porous disc (a) global parameters (front and side view) and (b) isometric view

Following Camp and Cal (2016) and Helvig et al. (2021), the number of blades and their size are the main factors which can be adjusted to obtain the desired porosity, noted β. As discussed in the previous chapter, porosity is an important parameter for these type of studies since it will determine the drag coefficient of the surrogate model (Castro, 1971; Sforza et al., 1981; Aubrun, 2013). It is defined as:

$$\beta = \frac{A_h}{A}, \tag{3.1.1}$$

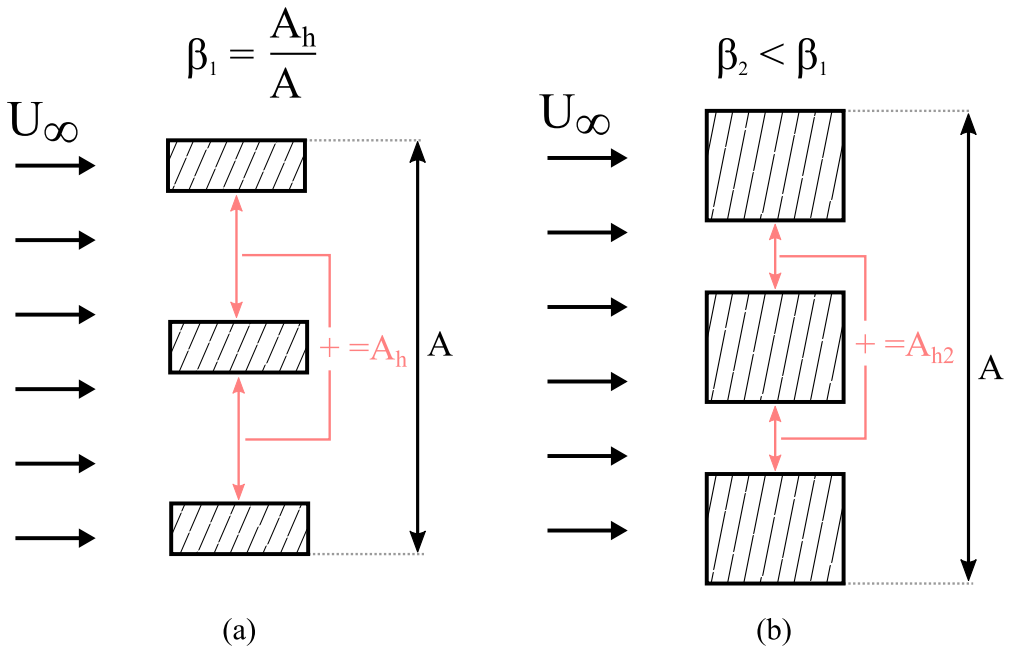

Figure 3.2: Schematic diagram of three consecutive blades of the porous disc and the calculation of porosity β. The diagram shows an unfolded view of two examples with different porosity values (a) and (b).

where A_h is the empty area of the trapezoidal holes and A is the total area of the disc defined as $A = \pi(D/2)^2$. Figure 3.2 shows an unfolded view of the porous disc used in this study with an example of two distinct porosity values β_1 and β_2. Here, the porosity has a non-uniform distribution and a reference value of $\beta = 65\%$, matching exactly the porosity of the disc studied in Helvig et al. (2021).

The porous discs were designed with a commercial 3D design software ANSYS^{TM} SpaceClaim and printed in Polylactic acid (PLA) using a Cura^{TM} Ultimaker 3 Extended printer. The precision of the 3D printer is 0.1 mm and the chosen infill is 80% (5h of printing time per disc approximately). This fabrication method allowed us to precisely set the value of β using equation (3.1.1) by simple extrusion of the blades (figure 3.2).

3.1.2 Passive swirl generation

As was mentioned in the introduction (§1.6.2), a notable limitation of the existing porous disc design is the absence of a swirling component, a key feature among the initial conditions of a wind turbine wake. This section tackles this primary challenge by presenting a method aimed at reintroducing the swirling motion to the wake of a stationary porous disc model. Ideally, this method should accomplish the desired effect without making substantial alterations to the disc's original design and blockage.

To the author's knowledge, only one other study proposed to re-introduce the swirling component to the wake of a porous disc. In the wind tunnel study depicted in figure 3.3, Holmes and Naughton (2022) designed a porous disc test rig capable of generating a swirling wake with the help of an integrated DC[1] motor. The experimental apparatus in question used metallic wires to suspend the test rig at the middle of the test section and the motor was housed in a streamlined nose cone. The motor rotated the porous disc

[1]Direct Current

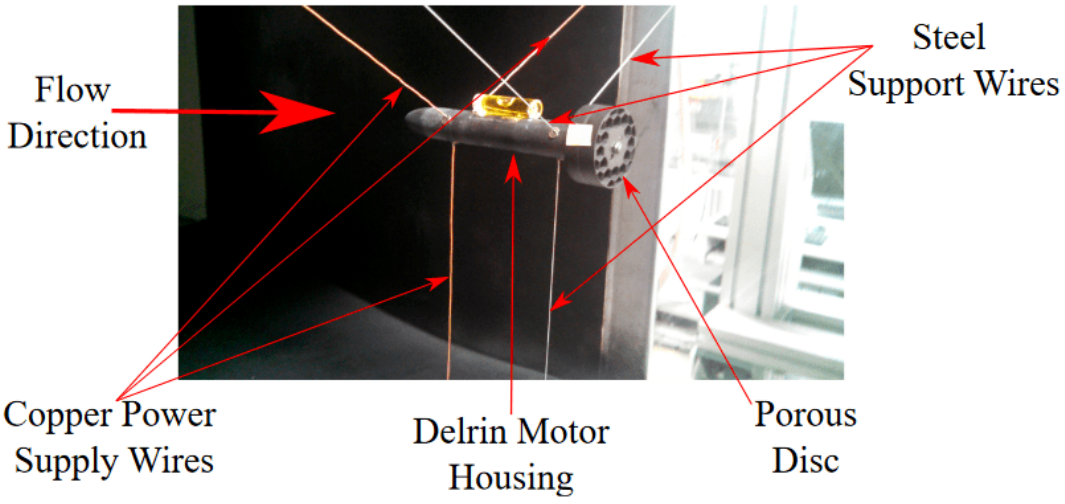

Figure 3.3: Experimental set-up of the porous disc generating a swirling wake used in the work of Holmes and Naughton (2022).

at an adjustable constant speed thereby generating a swirling wake. The advantages of this approach were that the use of wires enhanced the axisymmetry of the generated wake. Also, the use of the motor granted the ability to directly adjust the rotation speed of the disc, which grants the ability to control the value of the injected angular momentum G_0 with minimal blockage alteration (iso-porosity).

Nevertheless, a significant drawback of this approach is evident, as the dimensions of the nose cone closely match those of the porous disc. The boundary layers forming along the walls of the nose cone will have a significant influence on the inflow of the porous disc, introducing a notable geometric disparity with a HAWT. Additionally, the substantial increase in the technical complexity of the test rig, when compared to a stationary porous disc, does not warrant the use of a rotating porous disc. As discussed in the introduction (§1.6), lab-scale models of HAWTs, as demonstrated in the work of Chamorro and Porté-Agel (2010); Bottasso et al. (2014); Campagnolo et al. (2016), have successfully generated a swirling wake with features more akin to those of an actual HAWT. Hence, it is concluded that this approach did not fulfil the primary objective of a porous disc model, which is to simplify wind tunnel experiments of wind turbine wakes (Aubrun, 2013). Other approaches could be envisioned taking inspiration from other swirling flow studies like that of Shiri (2010), where a swirling jet was generated with azimuthally angled jets. One could imagine equipping a porous disc with azimuthally disposed actuators that confer angular momentum to the wake. However, these approaches involve, yet again, increasing the technical complexity of the set-up without mentioning the effect on drag of adding jets to the back of the disc.

With simplicity in mind, a modification of the porous disc blades was envisioned with the aim to azimuthally deflect the bleed air passing through the porous disc, thereby generating swirl. The employed methodology to modify the porous discs is shown in figure 3.4. The 16 trapezoidal blades that come out from the centre of the disc were pitched of an angle $\alpha > 0°$. Compared to the main direction of the incoming flow, the disc's blades will deflect the inflow direction and confer a net angular momentum G_0 to the wake without the need of active rotation. Figure 3.5 shows an unfolded view of the porous discs to showcase the passive generation of swirl. In fact, some predictions for the swirl intensity as a function of α can be made by invoking the inviscid flow

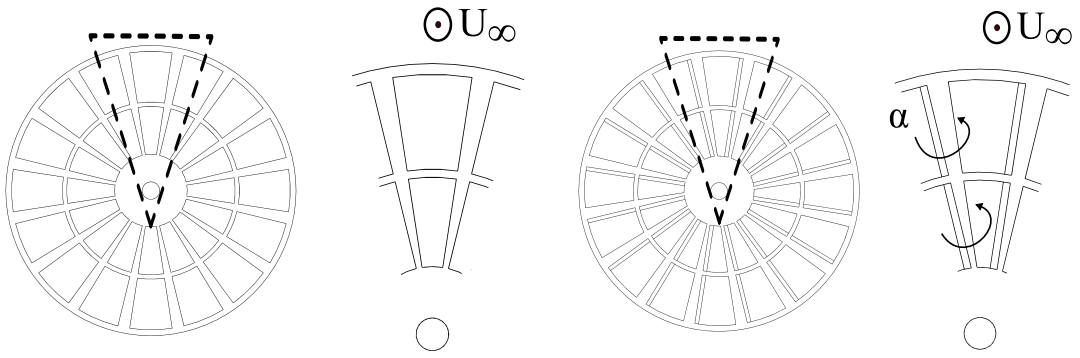

(a) (b)

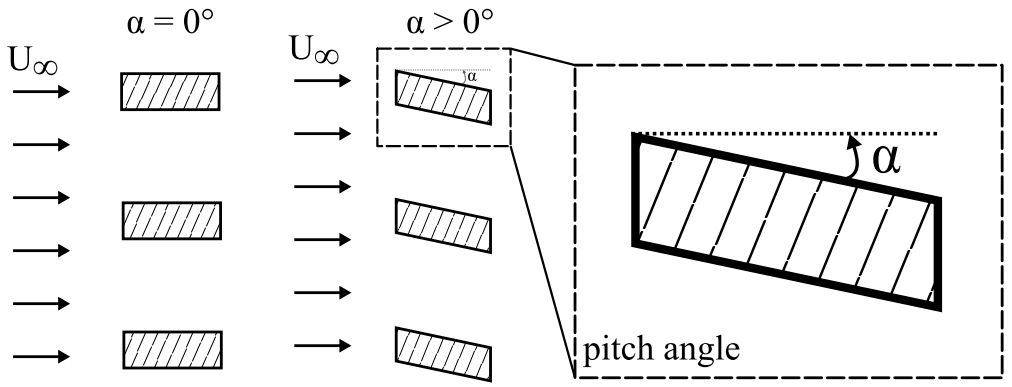

(c)

Figure 3.4: Modification of the porous discs to generate a swirling wake showing a frontal view of (a) the $\alpha = 0°$ reference case, (b) a frontal view of a porous disc with pitched blades ($\alpha > 0°$) and (c) an unfolded view of the modifications. The black dashed lines represent the borders of the zoomed-in area depicted on the right-hand side of the figures.

theory (Batchelor, 1967). As shown in figure 3.5, assimilating each individual blade as a thin flat plate inclined at an angle of attack α, the thin airfoil theory (Anderson, 2011; McCullough and Gault, 1949) predicts a lift coefficient of $C_L = 2\pi\alpha$, with α in radians. According to the Kutta-Joukowski theorem, for non-stalled blades, the lift coefficient can be expressed as a function of the circulation Γ such as $C_L = 2\Gamma/U_\infty we$, where w and e are the blade span and mean chord, respectively. Since the inclination of the blades is what induces the swirling motion, the circulation per unit span is intimately related to the swirling velocity such as $\Gamma \sim W_s \ell$ where, by definition ℓ is the typical extent of the contour integral on which the circulation is computed and W_s is the generated swirl intensity. It comes naturally that $\ell = \pi D/n$, where n is the number of blades of the porous disc. These relations relate the lift coefficient per unit span to the swirl generated such as:

$$C_L = \left(\frac{2\pi D}{U_\infty n w e}\right) W_s. \tag{3.1.2}$$

Therefore, $C_L \sim W_s/U_\infty$ according to potential flow theory. Coupling equation (3.1.2) with the thin airfoil theory yields:

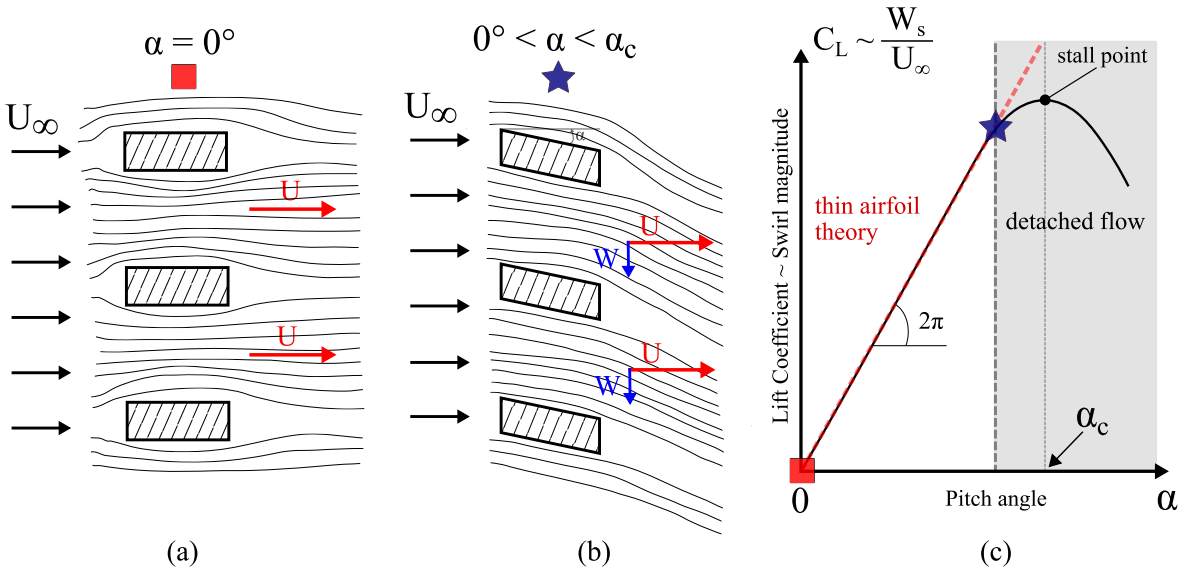

Figure 3.5: Schematic diagram of the pitch angle α on the blades of the porous disc to passively add swirl. The diagram shows an unfolded view of (a) blades with no pitch and (b) blades with a pitch angle below a threshold pitch angle α_c beyond which stall is expected. The conceptual graph (c) shows the thin airfoil theory predictions and the stall angle α_c where the flow is expected to detach and swirl generation starts decreasing.

$$\frac{W_s}{U_\infty} \sim \left(\frac{en}{D}\right)\alpha, \tag{3.1.3}$$

which predicts a linear increase of the swirl magnitude with respect to the pitch angle α such as $W_s/U_\infty = 0.8\alpha$. The slope of equation (3.1.3) sets the theoretical upper limit for the generation of swirl, at least until stall appears (figure 3.5). Due to finite size blade effects, non constant aspect ratio of the blades, and their surface finish (roughness induced by the additive manufacturing process), a deviation from this theoretical swirl magnitude slope is expected. In any case, following figure 3.4c, a pitch angle exists which achieves maximum swirl generation while keeping the flow attached.

An additional benefit of this approach is that, at these small to moderate angles of attack, the flow remains attached to the blades (figure 3.5a) thereby minimally changing the blockage and thus the drag coefficient (Anderson, 2011; Nakayama, 1988). In other words, with attached flow, the effective porosity of the disc is not modified ($\beta_{eff} = \beta$), which allows a parametric study of the pitch angle α at iso-porosity. However, there is a critical pitch angle α_c beyond which stall occurs and lift begins to drop. According to equation (3.1.2) the stalling of the blades would translate to a loss of swirl generation due to the separated flow in the suction sides of each blade thus decreasing the effective porosity as shown in figure 3.7. The value of α_c depends on the aspect ratio of the blade and other parameters, making it difficult to accurately predict. However, based on experimental data reported in the literature, a discernible range can be defined for flat plates with approximately comparable average aspect ratios, as highlighted by Anderson (2011); Mohebi et al. (2017); Shademan and Naghib-Lahouti (2020), this range is $\alpha_c \in [14° - 20°]$. In particular, the study by Nakayama (1988), relying on experimental data from Hikaru Ito, identified a critical stall angle of $\alpha_c = 15°$ for infinite thin flat plates.

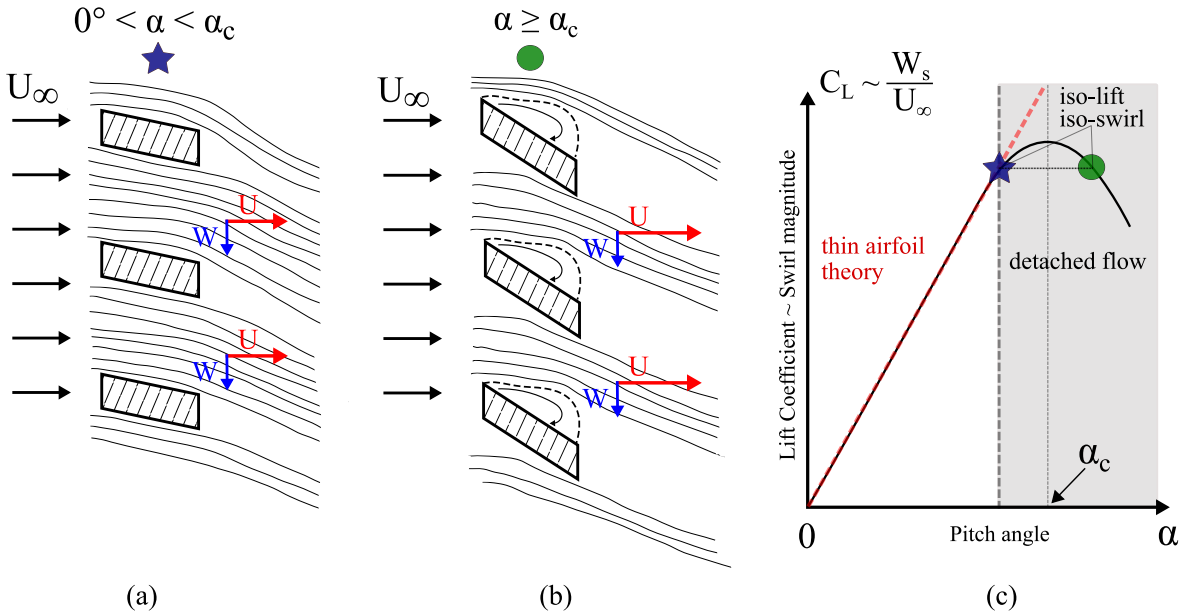

Figure 3.6: Schematic diagram in an unfolded view of a porous disc with (a) a pitch angle below the stall point, (b) with stalled blades but with iso-swirl generation as (a) and (c) a conceptual graph of the lift coefficient as a function of the pitch angle $C_L = f(\alpha)$.

At post-stall angles, the loss of lift is not sudden and it does not fall to zero. In fact as shown in figures 3.6b and 3.6c, the continuous loss of lift at post-stall pitch angles could be exploited to study the effect of a decreased porosity at iso-swirl. If this second key pitch angle is experimentally identified, it enables a distinct parametric investigation, permitting a comprehensive confrontation of both β and α. By adopting this methodology, the experimental study gains the ability to isolate the impacts of porosity (blockage) and swirl, providing insights into which initial condition holds dominance on the scaling laws, for instance (chapter 4).

As shown in figure 3.7b, stalled blades create a region of recirculating fluid in the suction side of the blades due to separation which is expected to decrease the effective porosity β'_{eff} and increase drag. To discern if the observed wake behaviour stems from swirl or from an increased effective blockage, additional porous discs were designed with the aim to match their porosity β'' to the effective porosity of the porous discs with post-stall pitched blades (see figure 3.7b and 3.7c). The methodology employed was to increase the thickness of the blades to match the projected surface area of the post-stall pitched blades. This approach came with a natural drawback in the sense where the equivalent porosity discs would have a decreased effective porosity β''_{eff} themselves due to the *vena contracta* effect (White, 1990). As specified in this work and references therein, the restricted area can reach up to 60% of the available space, thus decreasing β''_{eff}. Therefore, an increase in the drag coefficient for these equivalent porosity discs is also expected.

Since no references exist on these specific type of non-standard blades, several pitch angles are tested to determine the pitch angle with maximum swirl at iso-porosity and the pitch angle with iso-swirl with decreased porosity. Therefore, the tested pitch angles are $\alpha = [0°, 5°, 10°, 15°, 20°, 25°, 30°]$, and a more complete investigation will be performed on the angles $\alpha = [0°, 15°, 25°]$ for reasons explained later in chapter 4. The $\alpha = 0°$ case corresponds to the non-pitched porous disc used in Helvig et al. (2021) as

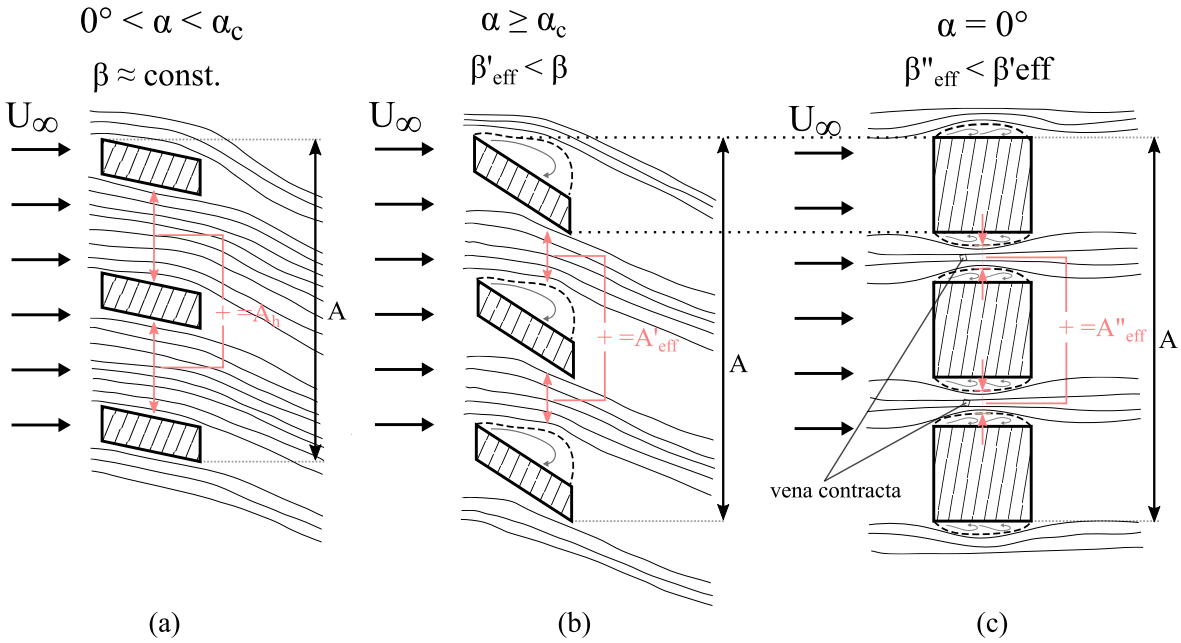

Figure 3.7: Schematic diagram of the increase in blockage due to stalled blades and the equivalent porosity discs. The schematic shows an unfolded view of a porous disc with (a) a pitch angle below the stall point, (b) a post-stall pitch angle and (c) a decreased porosity disc with thicker blades aiming to match the frontal surface area of (b).

they only differ in diameter.

3.2 The S2 wind tunnel

The following section describes the features of the wind tunnel used to generate the inflow for the studied porous discs. Moreover, the tests performed to ensure the quality of the inflow are presented along with the test rig used to position the porous discs in the wind tunnel.

3.2.1 Wind tunnel characteristics and operation

The experiments were conducted in the open-circuit, Eiffel-type, subsonic "S2" wind tunnel of the PRISME Laboratory and is presented in figure 3.8. The test section is 2 m long with a cross-sectional area of 0.50×0.50 m^2 with walls entirely made of Plexiglas to allow for optical access. The free-stream velocity U_∞ can reach 50 $m.s^{-1}$ with a precision of 0.2 $m.s^{-1}$. A honeycomb combined with fine mesh screens installed at the wind tunnel's inlet ensures that large turbulent structures from the natural environment are broken down before entering the test section. Near the inlet of the test section, the wind tunnel floor has a circular access point where different objects can be attached to an ATI^{TM} Mini40-E aerodynamic balance, sitting directly beneath such access point. A diffuser installed at the outlet of the test section collects and decelerates the flow before being diverted to the exhaust.

The flow is generated by the wind tunnel's fan, which is powered by a three-phase electric motor controlled by a manual potentiometer. A LED display shows an accurate

(a)

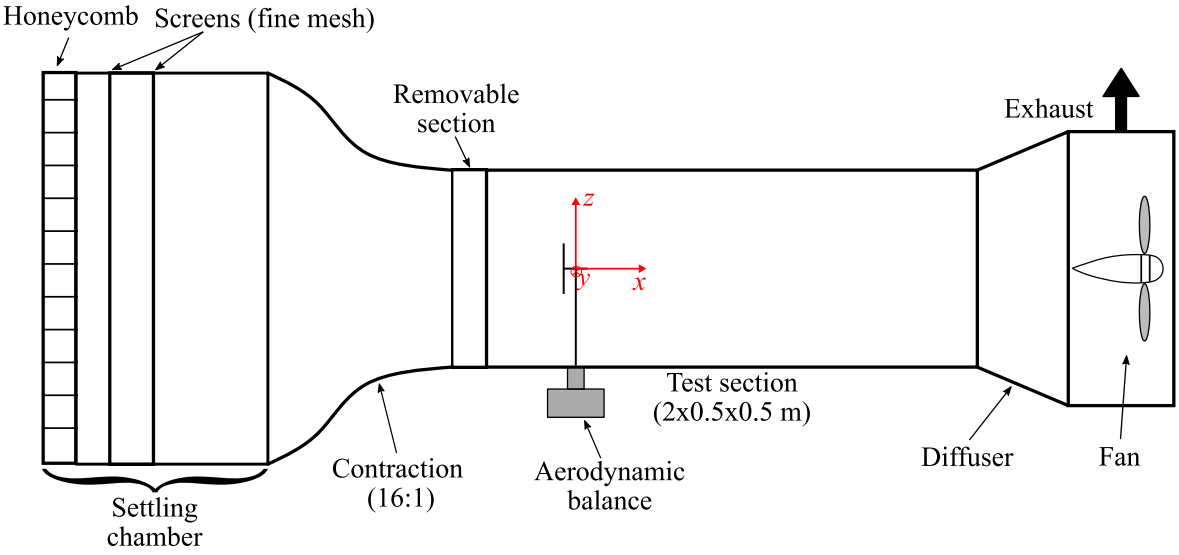

(b)

Figure 3.8: Depiction of the S2 wind tunnel showing (a) a side view picture and (b) a schematic diagram underscoring the main features of S2.

reading of the motor's RPM[2] that allow the operator to set a nominal value. The corresponding value of the flow velocity U_∞ at the inlet of the test section is determined by measuring the static pressure drop ΔP_{cc} across the convergent using an FC014 analog micromanometer and applying Bernoulli's principle to obtain:

$$\Delta P_{cc} = \frac{1}{2}\rho U_\infty^2 \tag{3.2.1}$$

$$\text{with} \quad \Delta P_{cc} = g\rho_w h_w, \tag{3.2.2}$$

where ρ and ρ_w are the density of air and of water, respectively, g is the gravitational acceleration and h_w is the corresponding water column height. The FC014 micromanometer directly provides readings of the product $\rho_w h_w$. It immediately follows:

$$U_\infty = \sqrt{\frac{2g(\rho_w h_w)}{\rho}}. \tag{3.2.3}$$

[2]Rotations Per Minute.

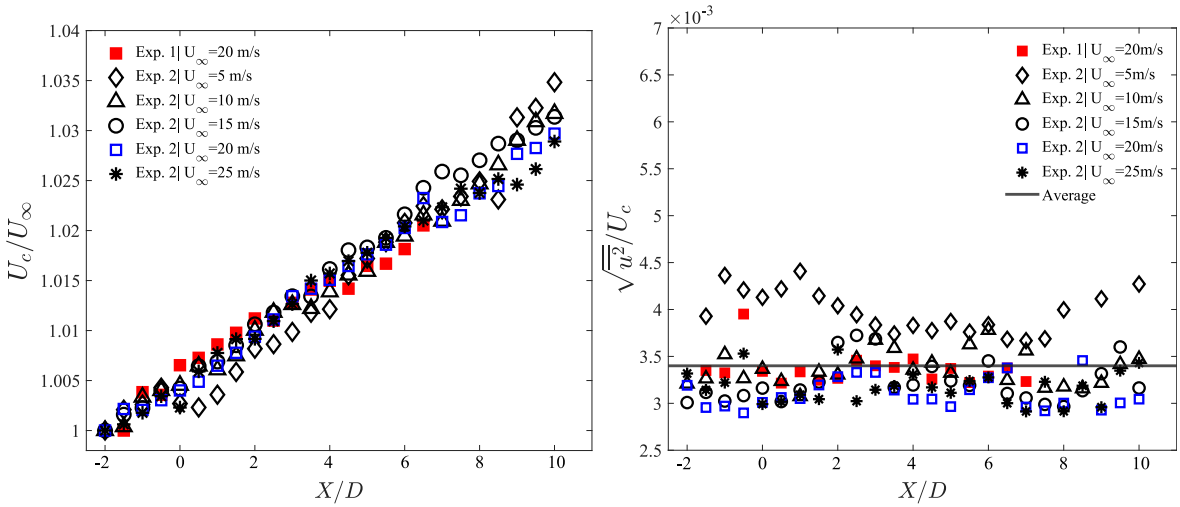

Figure 3.9: Centreline ($z = y = 0$) streamwise evolution of (a) the mean streamwise velocity $U_c(x)$ and of (b) the turbulence intensity $\sqrt{\overline{u^2}}/U_c$ for the empty test section.

The density of air ρ was calculated using accurate measurements of the ambient air temperature and pressure while the density of water $\rho_w = 998$ kg.m^{-3} is considered constant. The pressure readings have a relative uncertainty of 0.5% which corresponds to a relative uncertainty around 1% for U_∞.

3.2.2 Wind tunnel qualification

Before each experimental campaign, it is critical to assess the flow quality inside the test section. The key factors used to evaluate the flow quality are the homogeneity of the mean flow and turbulence level (Barlow et al., 1999). A qualification was performed before each main experimental campaign.

Hot-wire measurements were performed to characterise the wind tunnel test section without the test rig. A single component, Platinum-plated tungsten hot-wire probe (Dantec$^{\text{TM}}$, 55P11) was used here. The probe measured the streamwise velocity component at several different positions. The sampling frequency and time at each location are $f_{qual.} = 40$ kHz and $T_{qual.} = 10$ s, respectively. Centreline profiles and $y - z$ cross-sectional maps were chosen at different x-locations. The cross-sectional maps were set with $Z/D \in [-1.3, 1.3]$ and $Y/D \in [-1.3, 1.3]$ and a spatial resolution of $\Delta Y = \Delta Z = 0.1D$. The origin of the coordinate system coincides with the same origin as the experimental campaigns and the distances are normalised by the porous disc diameter D.

Figure 3.9 provides an assessment on the streamwise evolution of the free-stream properties in the middle of the test section. The mean streamwise centerline velocity $U_c(x)$ shows an acceleration of 0.2% for all tested inlet velocities $U_\infty \in [5, 10, 15, 20, 25]$ m.s^{-1}. This is consistent with the weak pressure gradient and the development of the boundary layers formation on the test section walls, which accelerates the flow by causing a fluid contraction. A total increase of 3% in free-stream velocity relative to its nominal value is observed and considered acceptable for the purpose of this work. The centreline streamwise turbulence intensity remains fairly uniform at an average of 0.34% and up to 0.45% for $U_\infty = 5$ m.s^{-1}.

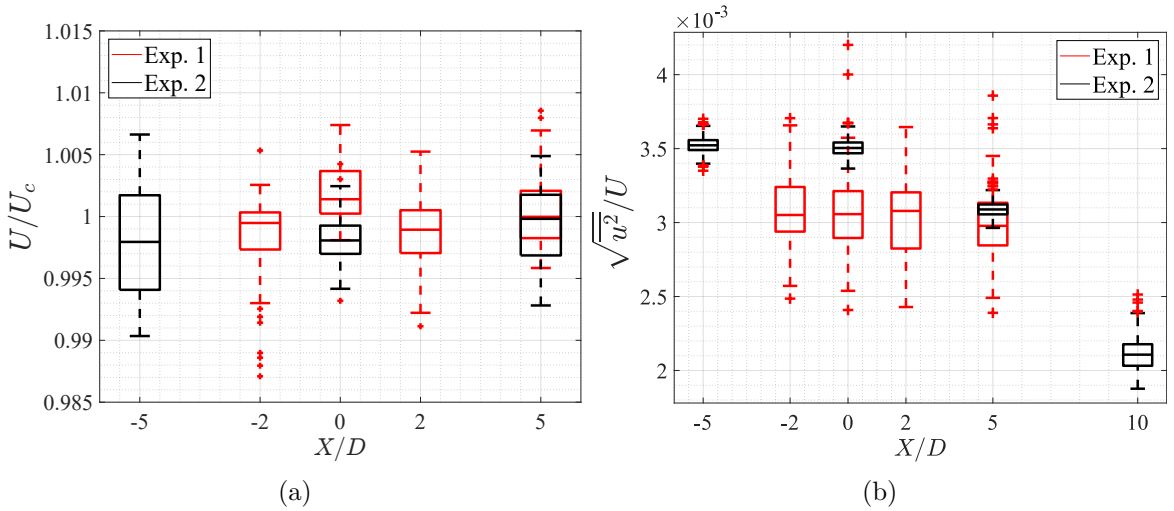

Figure 3.10: Cross-sectional spatial statistics at different streamwise locations of (a) the normalised mean streamwise velocity U/U_c and (b) the turbulence intensity $\sqrt{\overline{u^2}}/U$.

The cross-sectional spatial homogeneity is emphasised in figure 3.10 for a free-stream velocity of $U_\infty = 20$ m.s^{-1}. Similar analyses were performed for $U_\infty = [10 - 30]$ m.s^{-1} and the same conclusions were reached. For each x-position, box-plots summarise the statistics of the flow properties. The mean streamwise velocity (see figure 3.10a) shows an overall satisfactory homogeneity with variations contained within $\pm 1.5\%$ at maximum. The repeatability of the experiments was verified by reproducing twice the same conditions. For the second qualification, the spatial distribution of the turbulence intensity (figure 3.10b) shows a slight increase, particularly close to the test section's inlet where the removable section is installed (figure 3.8b). The turbulence levels in the test section show values around 0.31% for the first qualification and 0.35% for the second one. Furthermore, the distributions for the second experimental campaign are much tighter (smaller boxes), indicating that the background turbulence has become more homogeneous despite a slight increase in overall turbulence levels.

3.2.3 Test rig implementation and scaling factors

The implementation of the porous discs in the wind tunnel is depicted in figure 3.11. The discs are fixed on a T-shaped aluminium cylindrical rod with a diameter $d = 6$ mm representing the wind turbine nacelle and tower. The hub can be assimilated to the central solid disc where the disc is fixed to the rod (see figure 3.1). With this set-up, the porous discs were interchangeable without the need to remove the rod, ensuring that our data would not be affected by an eventual misalignment between experiments. The wind tunnel blockage ratio is approximately 2% (rod included) ensuring a relatively undisturbed wake.

The scaling factors of the test rig compared to a reference NREL 5MW offshore wind turbine are reported in table 3.1. The data relevant to the real-scale NREL wind turbine is taken from the comprehensive technical report of Jonkman et al. (2009) for this system. The tower and nacelle diameter correspond roughly to the aspect ratios found in the real-scale HAWT as well as the hub height. However, due to the porous disc design, the solid disc acting as the hub creates a significant local blockage at the centre of the porous disc. Evidently, Reynolds similarity is unattainable under these

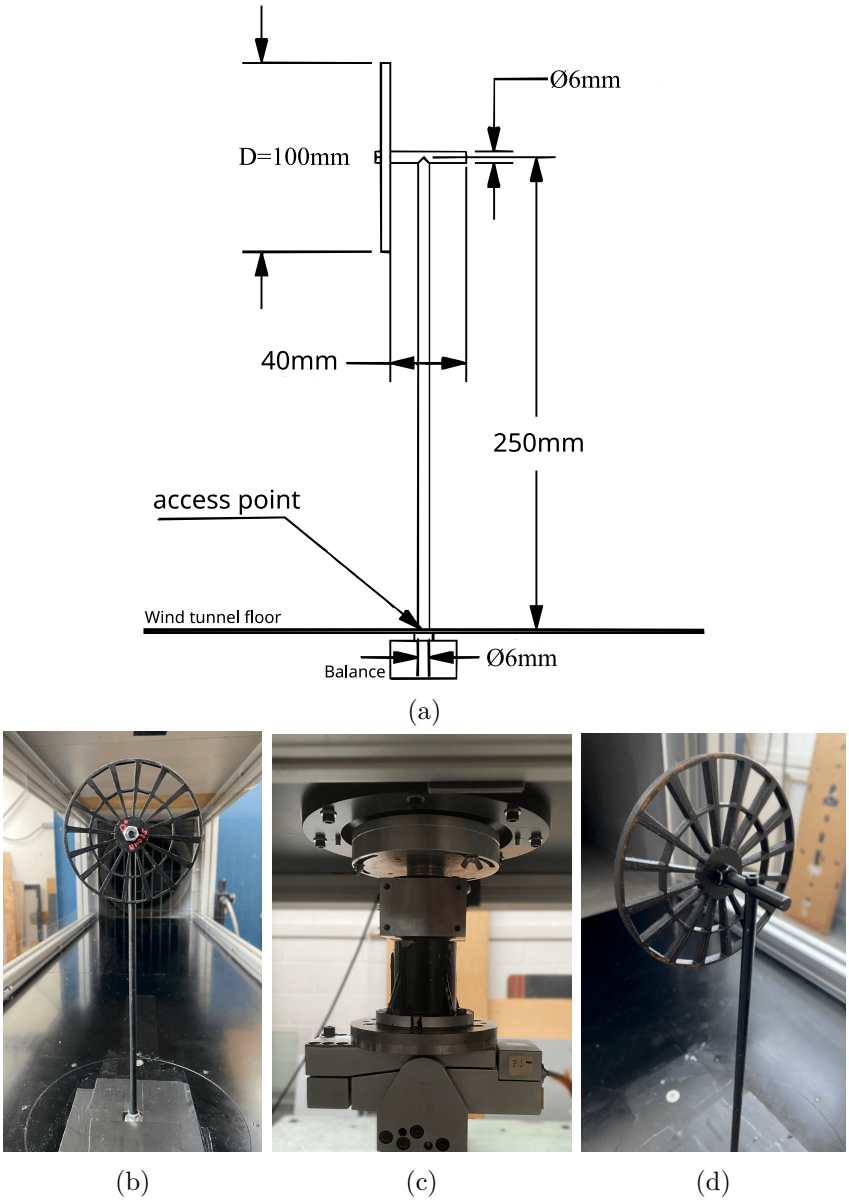

Figure 3.11: Test rig implementation on the test section showing (a) a schematic of the test rig attached to the (c) aerodynamic balance and (b) front and (d) back views of the set-up.

conditions, as the scale of the laboratory experiments conducted here does not allow for it. However, as shown in chapter 2, phenomenologies can still be established at high Reynolds numbers which is the case of this study. As mentioned in the introduction, the drag coefficient C_D of a wind turbine is mainly a function of the pitch of the blades and of the TSR (Ragheb, 2011; Stevens et al., 2018). As shown in Dufresne (2013), this dimensionless parameter will directly set the level of swirl in the wake of a a wind turbine. In terms of surrogacy, the porous disc has a straightforward equivalent to the thrust coefficient, which is the drag coefficient of the disc, as established by the seminal work of Aubrun (2013). When dealing with swirl however, only a rotating surrogate, like the porous disc studied in Holmes and Naughton (2022), has a direct swirl parameter to compare to the TSR, since the rotational speed of the disc is used to set the level of swirl. In this study, the porous disc is static and passively generates swirl through the pitching of the blades. Since defining a TSR, in a straightforward way,

Property	NREL 5MW	Test rig	Scaling factor (model/real)
Rotor diameter (m)	126	0.1	8×10^{-4}
Tower diameter	4%	6%	1.5
Hub diameter	2.5%	25%	10
Nacelle diameter	3%	6%	2
Hub height	71%	250%	3.5
Reynolds number range	25M - 96M[3]	50k-230k	$\sim 10^{-3}$
Inflow turbulence intensity	5%[4]	0.35%	0.07

TABLE 3.1: Summary of the scaling factors between a reference real-scale HAWT and the porous disc test rig of this work. All lengths are normalised by the rotor/disc diameter unless specified otherwise.

for a static object is meaningless, another common characteristic parameter related to swirl has to be considered from velocity measurements, like the swirl number $\hat{S}$ defined in chapter 2 (§2.3.2). Moreover, the turbulence intensities reproduced in this lab-scale scenario are not representative of the real case since the inflow is laminar. The focus of this work is the wake development of the porous disc, which warrants the deliberate generation of low turbulent inflow. However, this opens the door to a potential perspective of the investigation, which is to add external perturbations to the flow to match the turbulent ABL.

[3]Range calculated from the cut-in to the rated wind speeds.

[4]Lowest common value found in an offshore ABL (Schliffke, 2022).

Part B

Metrology and methodologies

3.3 Measurements objectives and protocol

As presented in the introduction (§1.6) and in chapter 2 (§2.2), the wind turbine wake is a multi-physics and multi-scales phenomenon, distinguished from the general turbulent wake by a swirling motion. The porous disc under examination is designed to induce such a swirling wake, following the methodology elaborated in part A. For ease of reference, the primary conservation laws governing the wake development in the downstream direction derived in chapter 2 are recalled below:

$$C_D = 16\left[\int_0^\infty U^*\Delta U^* r^* dr^* - \int_0^\infty \left[\overline{u^2}^* - \frac{\overline{w^2}^* + \overline{v^2}^*}{2}\right] r^* dr^* + \int_0^\infty \left[\frac{W^{*^2}}{2}\right] r^* dr^*\right], \tag{3.3.1}$$

$$G_0^* = \frac{G_0}{\frac{1}{8}\rho U_\infty^2 \pi D^3} = 16\int_0^\infty (U^* W^* + \overline{uw}^*) r^{*^2} dr^*. \tag{3.3.2}$$

These laws and the body of similarity theory naturally established the measurement protocols carried out in this thesis and the corresponding methodologies. From equation (3.3.1), the drag force of the porous disc has to be measured to obtain direct values of C_D (force balance). Furthermore, streamwise velocity measurements are warranted since the velocity deficit was shown to be pivotal to the wake's development. Moreover, equations (3.3.1) and (3.3.2) warrant the measurement of all three components of velocity to close the budgets and to accurately measure swirl. Furthermore, to determine which similarity scaling laws are found in the wake development, in particular for the swirl decay, three-components velocity measurements are needed at various streamwise locations. Figure 3.12 summarises the different measurements that were carried out throughout this investigation. On top of directly measuring the drag force, multiple complementary measurement techniques were considered to measure the velocity components at different key locations in the wake. As explained in further sections, each technique has advantages and drawbacks but their redundancy allowed us to estimate uncertainties, corroborate values and ensure the quality of the database.

Drag force measurements allowed us to skim the problem and locate the key pitch angles at which drag started to increase due to stall and to set other parameters of the experiments like the Reynolds number. Three Components Hot-Wire Anemometry (3CHWA) allowed us to start measuring the wake at different positions and pitch angles (exploratory phase) due to the relative simplicity of its set-up. Furthermore, it allowed us to characterise the main parameters of the flow like turbulence scales of the wakes. Finally, Particle Image Velocimetry (PIV) and Stereoscopic Particle Image Velocimetry (SPIV) provided velocity measurements of the wakes having near Taylor-scale spatial resolution in the streamwise plane ($Y = 0$) and in different spanwise planes. All in all, these complementary measurements provided us with the necessary elements to answer the questions established in the introduction.

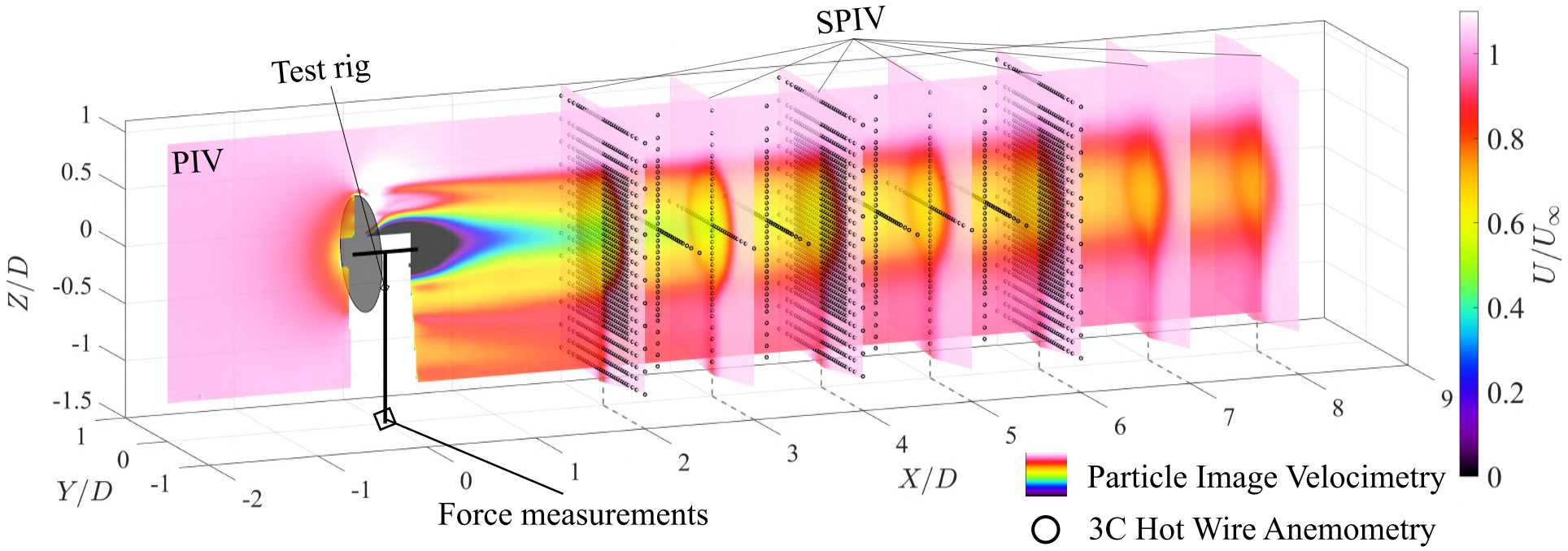

Figure 3.12: Metrology summary of the experimental measurements of the swirling wake of a porous disc. The colormap shows the normalised mean streamwise velocity of a swirling wake ($\alpha = 15°$) common to all velocity measurements carried out in this work.

3.4 Drag force measurements

In order to determine the drag coefficient C_D of each porous disc, an ATI^{TM} Mini40-E balance was used (see figure 3.11c). Placed directly beneath the S2 wind tunnel floor, this balance is capable of measuring force and torque components in all three directions (x, y, z) of space. This system is composed of a Force/Torque ±10 V transducer and a 16-bit DAQ[3] system. A standard metric SI-80-4 calibration was conducted, which resulted in a force along the streamwise direction (F_x) with a sensing range and a resolution of 80 N and 0.04 N, respectively. It was verified that all measured loads were at least an order of magnitude above the balance resolution and did not exceed the sensing range.

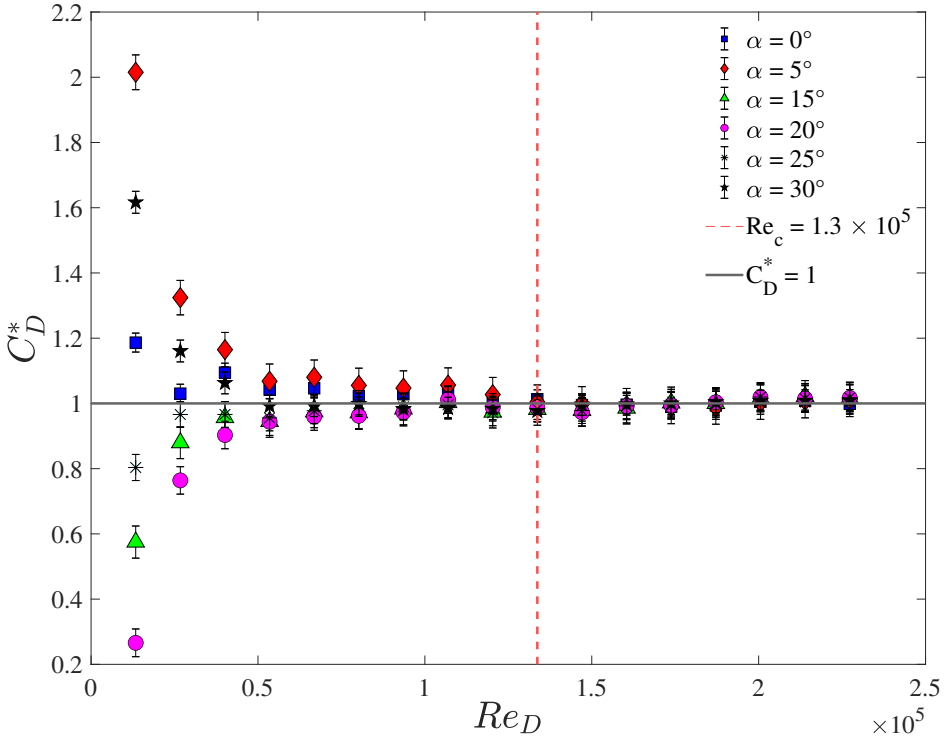

Figure 3.13: Normalised drag coefficient as a function of the global Reynolds number Re_D for porous discs with different pitch angles α. The reference drag used to normalise C_D is that obtained at $U_\infty = 20$ m.s^{-1} (red dashed line).

Since the entire test rig is attached to the Mini40-E attach point, the balance provides measurements of the test rig's total drag F_x^{TR}. To exclude the drag generated by the mast, not included in our definition of C_D, drag measurements of the T-shaped rod alone F_x^{rod} were performed and subtracted from the test rig's total drag. This method was also successfully used in the work of Helvig et al. (2021) and gives an estimation of the porous disc drag following $F_D = F_x^{TR} - F_x^{rod}$. The sampling frequency is $f_b = 1$ kHz and the measurement duration is $T_s = 180$ s. A moving average on 100 samples was used to filter the vibrations, resulting in an effective sampling frequency of $f_{eff} = 10$ Hz. The balance was tared between each measurement in order to correct for potential drift of the apparatus. The uncertainties were estimated using the calibration errors (±1.5% of the measured load) and the statistical errors. The statistical errors

[3]Data acquisition.

were determined using the standard deviation of the force signal. The uncertainties amounted to $\epsilon_{C_D} = 0.03$ on average.

The drag coefficient of the porous discs C_D depends on the Reynolds number up to a certain value (Helvig et al., 2021). Since Reynolds number similarity is not the purpose of this work, the measurements need to be carried out at a Reynolds number above this threshold. This threshold was evidenced using drag force measurements and is emphasised in figure 3.13. The drag coefficients were arbitrarily normalised by their value at $U_\infty = 20$ m.s^{-1}. For all porous discs, the drag coefficient becomes independant of the Reynolds number at round $Re_D \approx 10^5$. Therefore, a constant Reynolds number was set for the rest of the measurements at $Re_D = Re_c = 1.3 \times 10^5$, corresponding to a free-stream velocity of $U_\infty = 20$ m.s^{-1}.

3.5 Velocity measurements

As shown in figure (3.12), two main techniques were used to measure the velocity components in this thesis: 3CHWA and (S)PIV. First 3CHWA anemometry was used to measure all three components of velocity at several interest points and compute statistics of the flow. The streamwise component of velocity is obviously a key component following equation (3.3.1) and needs to be measured. However, measuring swirl requires the other two cartesian components since the swirling velocity is computed as:

$$\frac{W(x,r,\phi)}{U_\infty} = \frac{U_y(x,y,z)}{U_\infty}\sin(\phi) - \frac{U_z(x,y,z)}{U_\infty}\cos(\phi), \tag{3.5.1}$$

where $U_z(x,y,z)$ and $U_y(x,y,z)$ are the mean vertical and horizontal velocity components, respectively. The versatility and relative ease of installation made 3CHWA the preferred technique to provide initial measurements of the wake.

3.5.1 Three-components hot-wire anemometry

Hot-Wire Anemometry (HWA) is a highly sensitive fluid velocity measurement technique. The constant temperature version of this technique involves positioning a thin wire within a fluid flow and heating it up to a constant temperature using a CTA[4]. Following King (1914)'s law, the fluid's instantaneous velocity can be then calculated from the voltages delivered by the CTA. This technique offers several advantages, such as high accuracy, fast response time, low cost and easy implementation. However, it also requires careful calibration and manipulation due to its sensitivity to factors such as temperature, humidity, wire properties, and flow conditions (Comte-Bellot, 1976; Bruun, 1996).

The measurements were conducted using a Dantec Dynamics^{TM} Streamline CTA system with a Gold-Platinum-plated tungsten tri-axial wire probe (55P91) depicted in figure 3.14. The probe has three Gold-plated tungsten wires having a diameter of 5 μm, an individual wire sensing length of 1.2 mm leading to a spatial resolution of 3.2 mm which is of the order of the Taylor micro-scale $\lambda \in [2;4]$ mm (Sreenivasan et al., 1983; Mora et al., 2019). The wires are held in place by prongs which are positioned

[4]Constant Temperature Anemometer

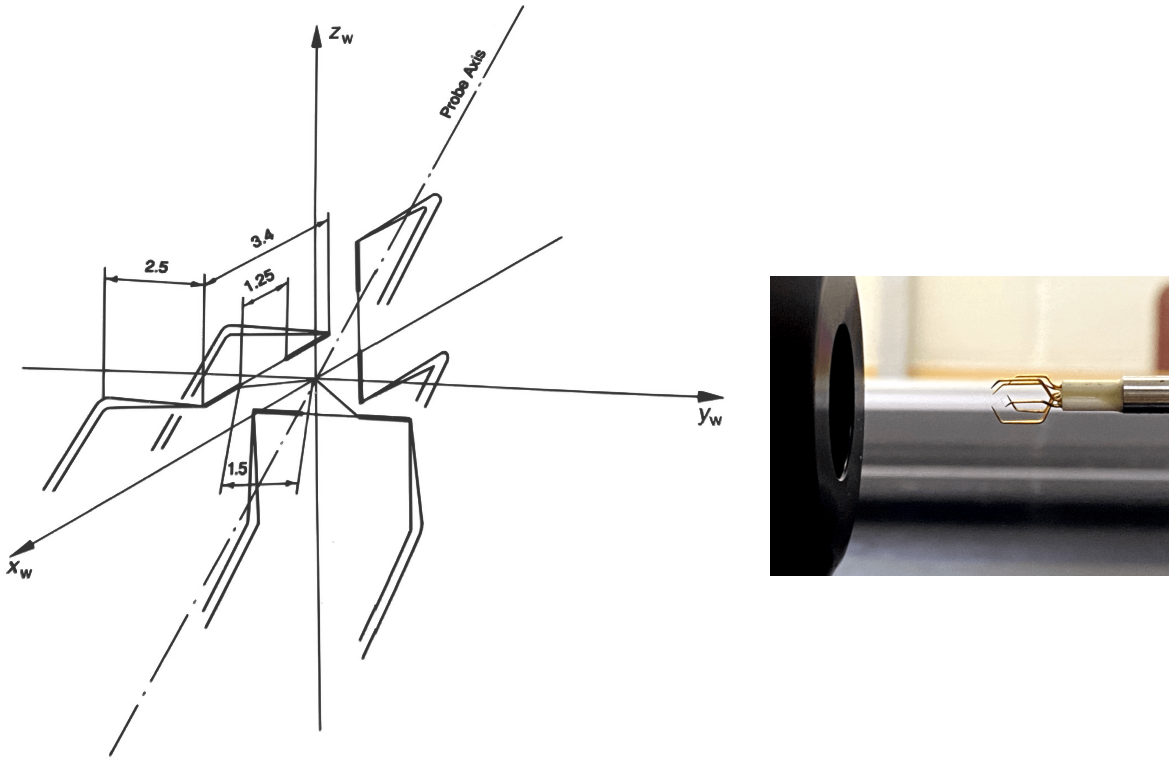

(a) (b)

Figure 3.14: Schematic diagram showing (a) the wire and prong configuration of the DANTEC 55P91 claw-type three-wire probe (taken from Bruun (1996)) and (b) The probe during the velocity calibration process. The dimensions are depicted in millimetres.

in a claw configuration to minimise the aerodynamic-interference effect. The wires are mutually orthogonal and are inclined of an angle $\alpha_w = 54.7°$ with respect to the probe axis (figure 3.14a).

Three-component HWA is based on the effective velocity concept which uses the linearisation functions of each individual wire and decomposes the effective velocity vector in a coordinate system aligned with each wire. The reader is referred to the work of Comte-Bellot (1976), Bruun (1996) and Chew et al. (1988) for a detailed review of the probe calibration process used here. In practice, as shown in figure 3.15 the 55P91 probe needs a velocity calibration and a directional calibration in order to obtain measurements of the three velocity components (U_x, U_y, U_z) in cartesian laboratory coordinates (x, y, z). To ensure minimal drift, a calibration was performed between each measurement set.

The velocity calibration was done by subjecting the probe to a set of known velocities $U_n \in [2; 60]$ m.s^{-1} using a dedicated calibration unit (see figures 3.14b and 3.15a). The corresponding temperature-corrected voltages are recorded, and velocity calibration coefficients are determined through fourth-order polynomial fits and compared to King's law. As for the directional calibration, the probe is then placed in a holder facing the calibration unit which permits the probe to be manually yawed with respect to the calibration unit inflow and rotated around its axis (see figure 3.15b). The calibration consists in varying the yaw and rotation angle of the probe which yields the calibration coefficients. This specific probe has a maximum yaw angle range of $[-30°; +30°]$ beyond which velocity measurements are erroneous.

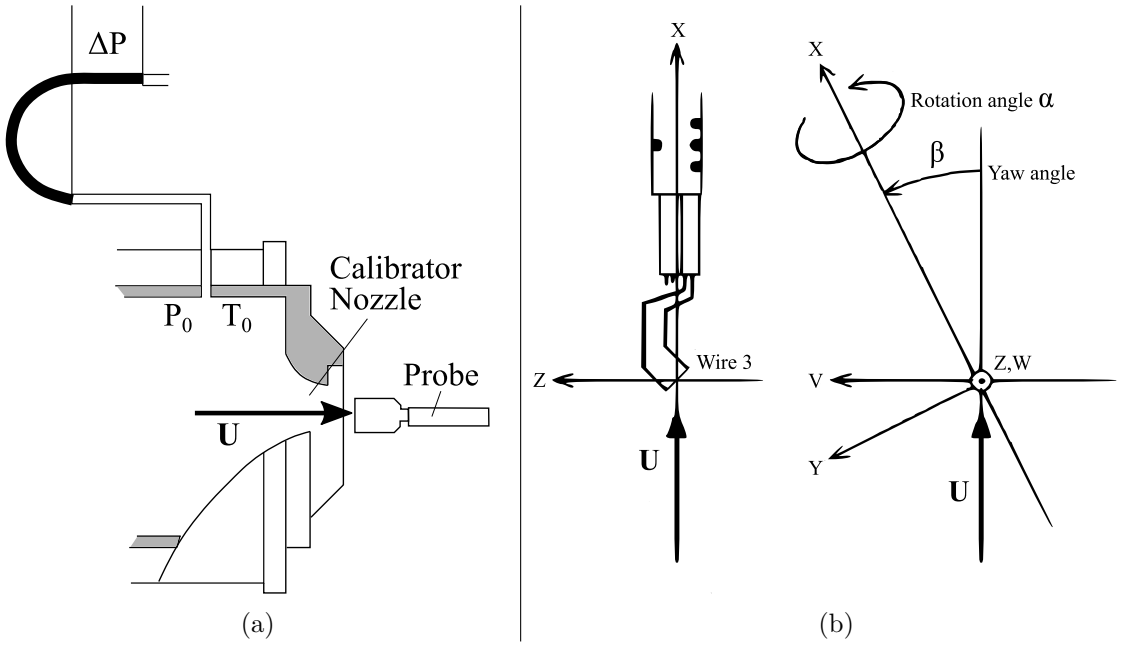

Figure 3.15: Schematic diagrams showing (a) the Calibration process of the 3CHWA probe and (b) geometric details of the probe. Taken from Finn (2002).

$\alpha(^\circ)$	0	5	10	15	20	25	30
$\mathcal{L}_{int}$ (mm)	16	15	16	17	23	28	30
λ (mm)	3	3	3	3	2	2	3
η (μm)	250	230	262	220	230	250	290
Re_λ	150	160	165	190	200	200	300
$\mathcal{T}_{int}$ (ms)	1.4	1.3	1.4	1.6	1.9	3.2	2.5

TABLE 3.2: Turbulence statistics in the centre of the wake of the different porous discs at $X = 6D$.

The HWA measurements allowed us to compute certain turbulence statistics and estimate the characteristic scales of the flow reported in table 3.2. Using methodologies discussed in Sreenivasan et al. (1983); Mora et al. (2019); Fuchs et al. (2021). The estimated scales are: $\mathcal{L}_{int}$ the integral length scale, λ the Taylor micro-scale, η the Kolmogorov length scale and $\mathcal{T}_{int} = \mathcal{L}_{int}/U$ the integral time scale. The local Reynolds number Re_λ is defined as:

$$Re_\lambda = \frac{\sqrt{\overline{u^2}}\lambda}{\nu}. \tag{3.5.2}$$

After a final verification, 3CHWA measurements were performed at different positions summarised in figure 3.16. Cross-sectional ($Y - Z$) planes were measured at three streamwise positions: $X = 2D$, $X = 4D$ and at $X = 6D$. The number of measurements points is $N_p = 1130$. The spatial resolution resolution is $\Delta y_{wake} = \Delta z_{wake} = 5$ mm ($\sim 2\lambda$) inside the wake and 10-20 mm ($\sim \mathcal{L}_{int}$) in the free stream (see figure 3.16b). Additional spanwise and vertical profiles were measured between $X = 2D$ and $X = 6D$

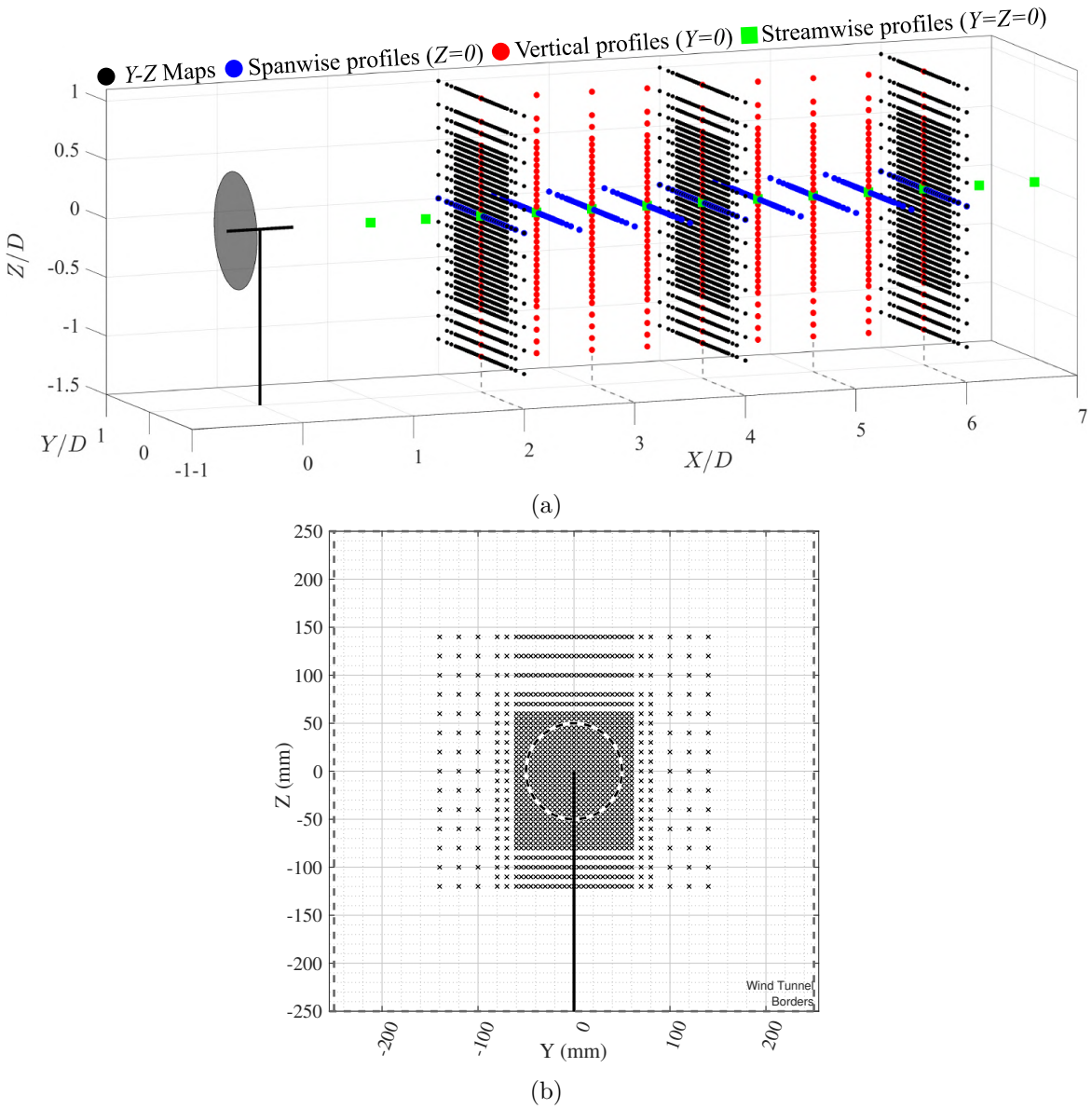

Figure 3.16: Summary of the 3CHWA measurements showing (a) the different measurement locations and traverses and (b) the distance (in mm) between each position at $X = \text{const}$. Dashed and solid black lines: edges of the test rig.

with a streamwise step of $\Delta_X = 0.5D$. The sampling frequency is $f_{HWA} = 40$ kHz for an acquisition time of $T_{HWA} = 2.5$ s ($\sim 10^3 \mathcal{T}_{int}$) at each location.

During the HWA measurements, the main uncertainty sources came from the inherent changes in the experimental conditions (temperature, humidity, pressure) and from the calibration of the hot-wire probe (Duffman, 1980; Bruun, 1996). The total uncertainty in the free-stream was below 0.5% and around 0.8-2% in the wake depending on the position of the probe with respect to the test rig. The temperature of the room was monitored throughout each experiment and was shown not to exceed a variation of more than 5% for all cases. The HWA uncertainties were estimated between experiments using the calibration unit and corroborated by redundant measurements. More information regarding uncertainties estimations and cross-technique corroboration is given in section 3.6

Following equations (3.3.1) and (3.3.2) and the HWA measurements, the spatial dis-

tribution of the streamwise velocity component and swirl had to be measured with a better spatial resolution and accuracy that what is achievable with HWA. Therefore, PIV and SPIV measurements were performed in the streamwise plane and at different spanwise planes.

3.5.2 Particle Image Velocimetry: principle and common experimental features

The principle and implementation of PIV is presented in this section. For each experimental campaign (PIV, SPIV) a different set-up was developed and will be described in the following.

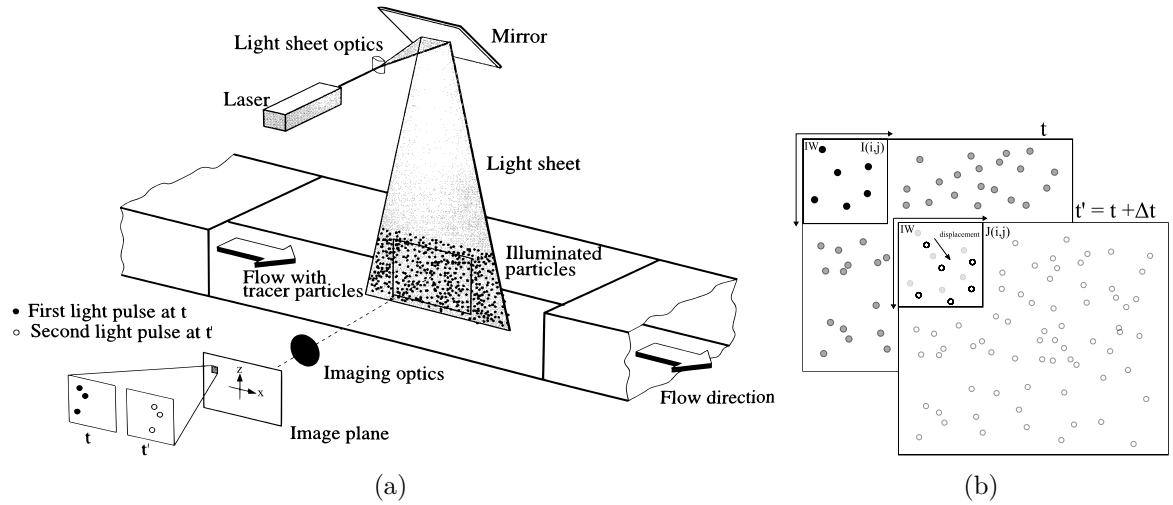

Figure 3.17: Particle Image Velocimetry principle depicting (a) a typical PIV set-up in a wind tunnel (taken from Raffel et al. (2007)) and (b) a schematic illustrating the cross-correlation PIV algorithm.

PIV is a laser based velocimetry technique which consists in illuminating a seeded flow and recording two snapshots t and t' taken at a very short time interval dt (figure 3.17). These snapshots effectively record the displacement $(\Delta x, \Delta y)$ of the tracer particles that moved due to the local velocity which can be obtained following:

$$U_x = \frac{\Delta x}{dt} \quad , \quad U_y = \frac{\Delta y}{dt}. \tag{3.5.3}$$

Each snapshot is divided into regular sub-regions called interrogation windows (IW) big enough to have particles in and small enough to have a uniform displacement. The cross-correlation between snapshots is then calculated for each pair of IW and velocity vectors are determined for each IW. The reader is referred to the comprehensive work of Raffel et al. (2007) regarding this technique. Here, the flow was seeded with olive oil droplets from a PIVTEC$^{\text{TM}}$ aerosol generator and had an average diameter of $d_p \approx 2-3$ μm. Olive oil droplets were chosen as tracers since they are non-reactive, non-toxic, scatter light appropriately and are sufficiently small in order to faithfully represent the fluid motion. To prove this last important point, the average Stokes number St was calculated following Kallio and Stock (1992); Vincent (2007); Hamdi et al. (2014) as:

$$St = \frac{\tau_p}{\tau_f} = \frac{\rho_p d_p^2 \mathcal{U}}{18\mu_f \mathcal{L}}. \tag{3.5.4}$$

Where $\tau_p = \rho_p d_p^2/18\mu_f$ is the relaxation time of the oil droplets and $\tau_f = \mathcal{L}/\mathcal{U}$ is a characteristic time scale of the flow. The quantities ρ_p, d_p and μ_f are the density of olive oil, the average particle diameter and the dynamic viscosity of air, respectively. Three main characteristic time scales of turbulent flows can be defined from integral, Taylor and Kolmogorov length and velocity scales, respectively. In this study, HWA allowed us to estimate these scales and a Stokes number range was calculated $St \in [1; 40] \times 10^{-3} \ll 1$ which confirms that the generated tracer particles will follow all scales of motions reliably (Bendicks et al., 2011).

In both the PIV and SPIV experimental campaigns, the recorded snapshots were analysed using a commercial PIV software (Davis 10.2, LaVision$^{\text{TM}}$). First, the background was subtracted from the image sets in order to filter out the residual reflections and improve the signal to noise ratio. After, a multi-pass cross-correlation method with 50% overlap was applied using an initial interrogation window (IW) size of 64×64 px^2 for the PIV measurements and 96×96 px^2 for the SPIV measurements. Then, a a final IW of 32×32 px^2 was chosen. A gaussian filter was used for sub-pixel interpolation and a median filter was applied in order to remove eventual spurious vectors.

3.5.3 Planar particle image velocimetry

Planar particle image velocimetry (PIV2d2c) was used to measure the wakes in a $x-z$ plane (see figure 3.18). This technique was used to get high resolution data of the mean streamwise velocity and the mean vertical velocity which corresponds exactly to the radial velocity in this configuration. In the streamwise direction, the region of interest is located between $X = -2D$ and $X = 8D$. This region is decomposed into 3 separate fields of view (FoV) labelled A, B and C, respectively. The dimensions of the individual FoVs are ($x \times z$) 4.2D$\times$ 2.6D and the full region reaches 10D $\times$ 2.6D. Between each FoV, there is an overlapping area of 25% (1D). The mean flow on the whole region of interest was obtained by stitching the mean velocity fields following a methodology described in section §3.5.4. A double pulse 400 mJ Nd:YAG laser system mounted on a vertical rail was used to illuminate the flow. The laser and optical system generated a laser sheet with an average thickness of 1.5 mm (figure 3.19).

The image sets were captured using an 11 megapixels LaVision$^{\text{TM}}$ LX-11M CCD[5] camera mounted on an optical rail parallel to the test section (see figure 3.20a). A ZEISS$^{\text{TM}}$ camera lens was used with focal length $f_0 = 85$ mm at infinity and was set at an aperture of $f_0/4$ for best results. For each FoV configuration (A, B, C), 2600 image pairs were recorded at a time interval of $dt = 55$ μs between snapshots. The sampling frequency was set at $f_{PIV} = 2.1$ Hz rate which corresponds to a total acquisition time of $T_{PIV} = 24$ minutes. The laser pulses and the frame recordings were synchronised using an external LaVision$^{\text{TM}}$ Programmable Timing Unit (PTU).

Each FoV required an individual calibration. The calibration was performed using a custom calibration plate with uniformly spaced dots that either completely or partially covered all three FoV (figure 3.20). The plate is 540 mm long and 420 mm tall and has a total of 560 dots (28×20) which are 4 mm in diameter and 19.45 mm apart.

[5]Charge-Coupled Device.

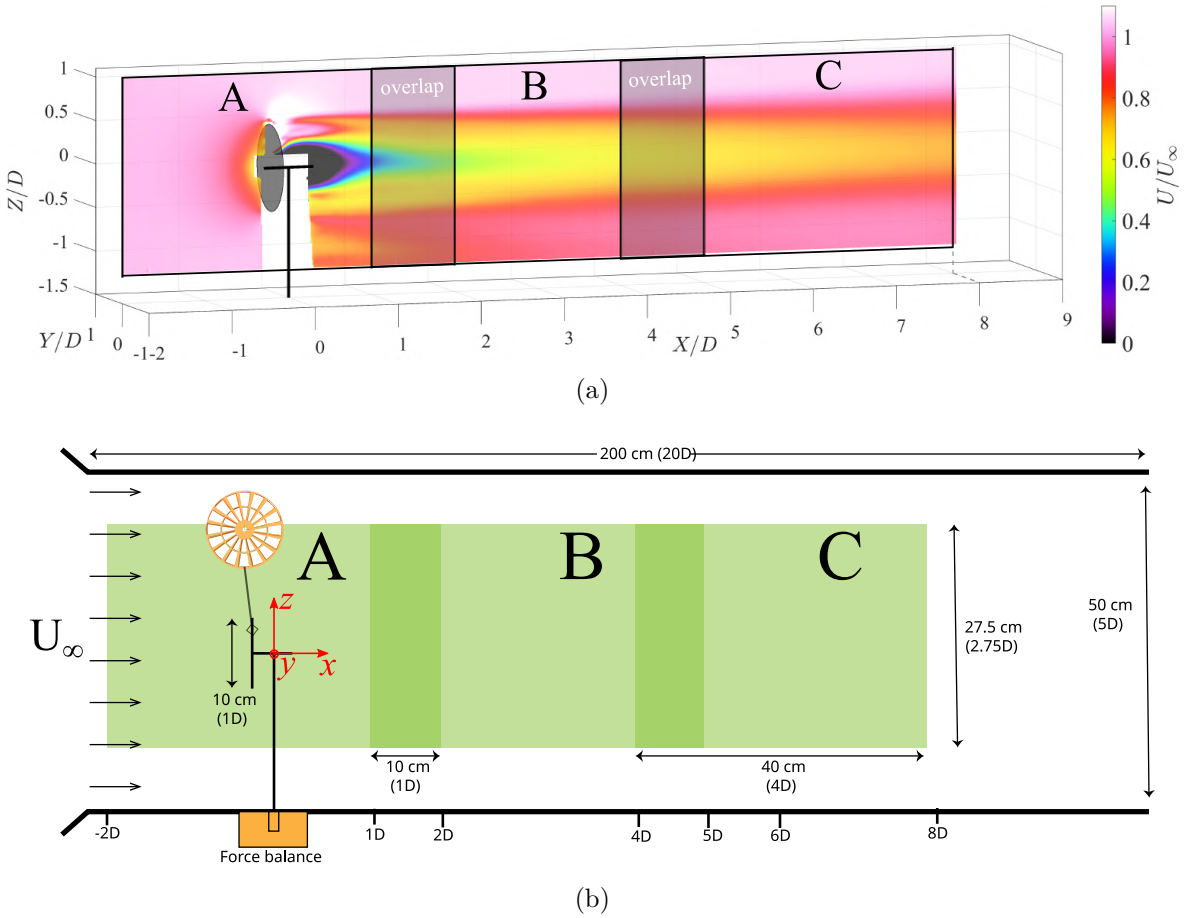

Figure 3.18: Summary of the PIV2d2c measurements showing (a) an example of a normalised mean streamwise velocity field and (b) a schematic diagram of the experimental set-up (not to scale). Green boxes: PIV FoVs.

The calibration plate was placed in the mid-span plane ($Y = 0$) of the test section next to the test rig. The resulting calibrations allowed each field of view to have a magnification factor (pixels to mm) and to correct optical aberrations (Raffel et al., 2007). The magnification factor had a constant value of $SF = 9.61$ pixels/mm for each calibration. Combined with the final IW size, the calculation algorithm yielded velocity vectors with a resolution of $\Delta_x^{\mathrm{PIV}} = \Delta_z^{\mathrm{PIV}} = 1.66$ mm which is of the order of the Taylor micro-scale λ and 10 times smaller than the integral length scale $\mathcal{L}_{int}$ (see table 3.2).

Uncertainties of the PIV measurements were calculated using correlation statistics, a method comprehensively studied in Wieneke (2015); Sciacchitano and Wieneke (2016) and applied here. This method estimates PIV uncertainties based on a pixel-wise statistical analysis that quantifies the contribution of each pixel to the shape of the correlation peak. In an ideal scenario where the particles between snapshots match perfectly, the correlation peak is symmetrical. However, the noise of a real measurement will deform the shape of the peak (or peaks in extreme noise scenarios) that will introduce error to the calculation of the displacement vector. The error quantification method resulted in a displacement uncertainty of $\epsilon_d \in [0.03; 0.08]$ px which fall within the order of magnitude of the 0.06 px value recommended in Raffel et al. (2007). As a side note, the error shoots up to values of $\epsilon_d \approx 0.15 - 0.20$ px very close to the test rig which is expected since strong 3D effects are present and increase the noise

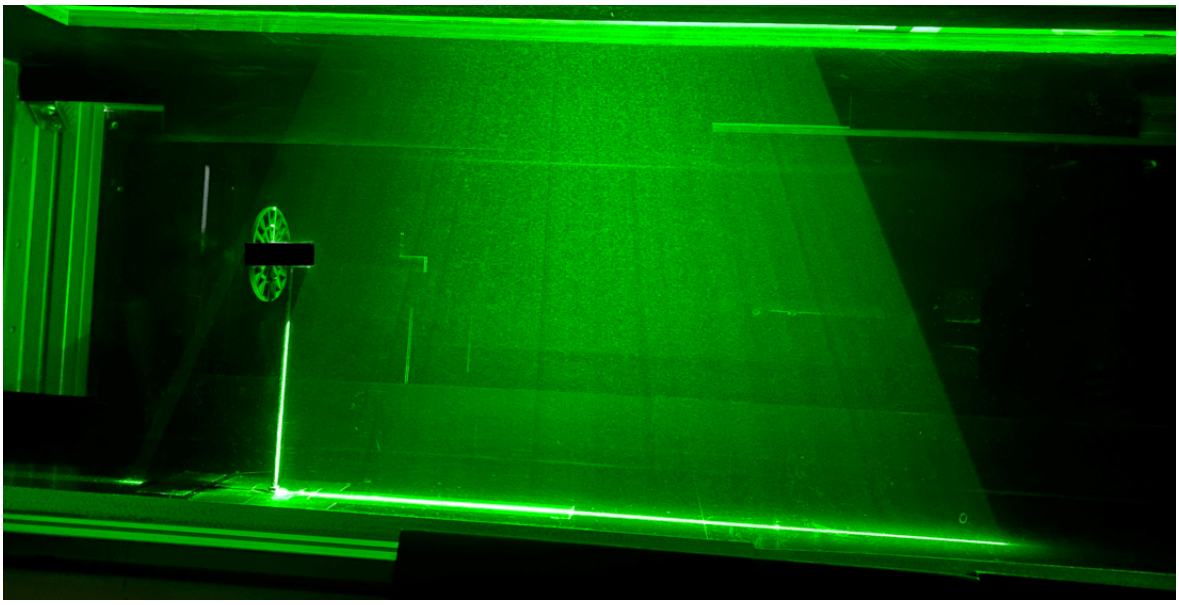

Figure 3.19: Picture of the laser sheet illuminating the streamwise ($Y = 0$) plane for a PIV2d2c measurement in a B FoV configuration.

due to out-of-plane motion. Moreover, the swirling cases will increase this out-of-plane motion by definition. This error was quantified and corresponds to an instantaneous velocity uncertainty of 0.8% and a mean uncertainty below 0.5% in the wake of the porous discs.

To verify if enough recordings were conducted to properly capture the flow properties, all velocity fields were subjected to statistical analysis. An example of such process is shown in figure 3.21 where a point was randomly selected in the approximate position of the shear layer of a measured wake. The normalised residuals were calculated for the flow variables appearing in equations (3.3.1) and (3.3.2) as a function of the number of snapshots used n_v. In particular, the 2D divergence was computed along with the available Reynolds stress terms. For example, the normalised residuals (NR) for the mean streamwise velocity are computed as:

$$\mathrm{NR}_U = \frac{U_{n_v+1} - U_{n_v}}{U_\infty} \tag{3.5.5}$$

As shown in figure 3.21, the flow statistics converged after around $n_V = 2000$. This process was repeated for different locations of the flow in zones A,B,C and for all tested porous discs thereby verifying the convergence of the PIV2d2c measurements.

3.5.4 Multi-FoV PIV mean vector field stitching method

To acquire the mean and standard deviation velocity fields throughout the entire ROI, the fields for each individual FoV were stitched together using a method suggested in Li et al. (2021a) and Vinnes et al. (2022). The stitching method is illustrated in figure 3.22 for the mean streamwise velocity field of an empty wind tunnel test section at $U_\infty = 20$ m.s^{-1} along with redundant HWA measurements for comparison purposes. The method consists in an iterative process that stitches the vector fields line per line. First, the overlap zones are trimmed to remove low quality vectors in the far edges of the fields. For each line (streamwise profiles) the best match is found and a weighted

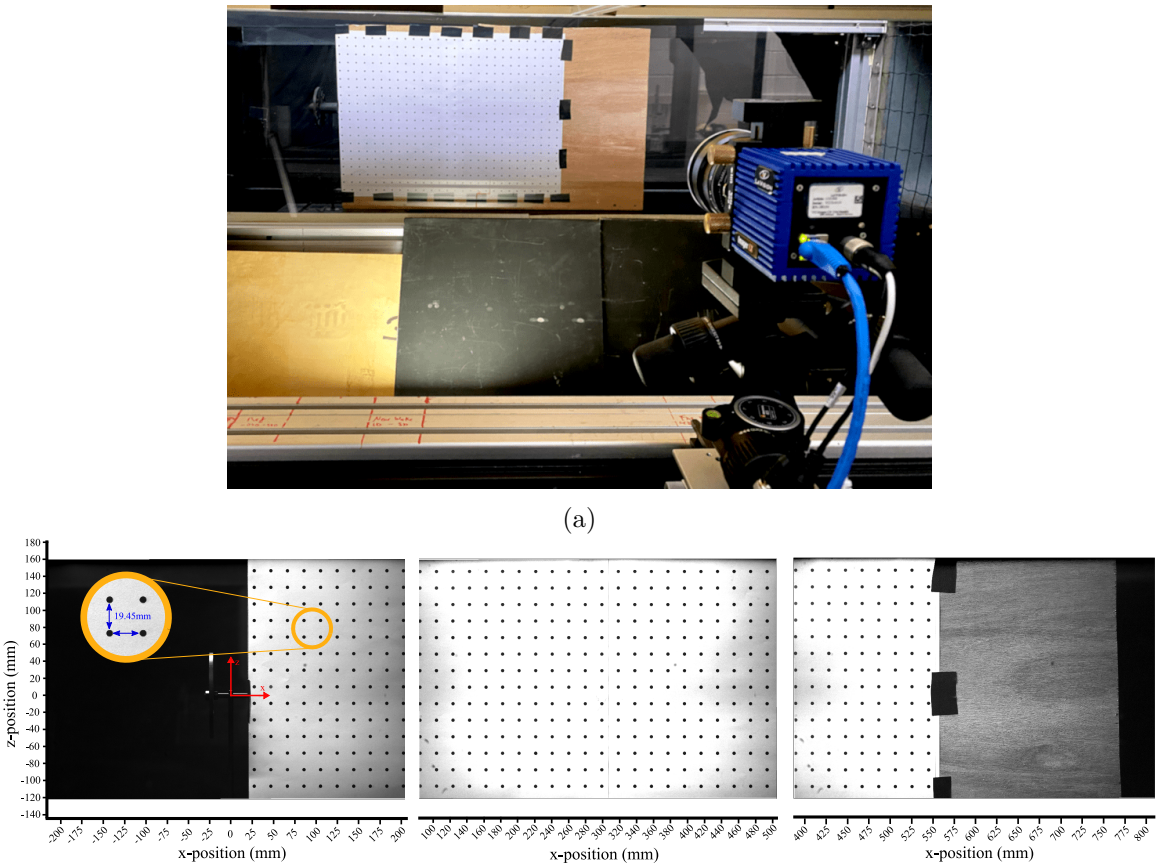

(a)

(b) Zone A (c) Zone B (d) Zone C

Figure 3.20: PIV2d2c calibration process depicting (a) the calibration set-up with the custom plate and (b-d) the three studied fields of view

average vector is computed in the overlap zones between fields. The weights in the average computation depend on the distance to the edge of the field, favouring vectors closer to the centre of the FoVs. As shown in figure 3.22 the stitched PIV data shows very good agreement with the HWA data and does not exhibit any discontinuities in the overlap zones. The highest discrepancy (0.6%) occurs at the end of the region of interest ($X = 8D$) where a mild noise increase is expected in the PIV2d2c data. In addition, both techniques corroborated a marginal rise in mean streamwise velocity, consistent with the findings observed during the wind tunnel qualification (§3.2.2). Furthermore, following the procedure detailed in Herpin et al. (2008), the uncertainty of the method was evaluated in the overlap regions. The estimated uncertainty was shown to remain below 0.6% U_∞ for all cases, which is of the order of the RMS velocities in the free-stream. More data cross-validation results can be found in section §3.6.

PIV2d2c allowed us to accurately measure the distribution of the mean streamwise and radial velocities. However, measuring the out-of-plane component, corresponding to swirl, was unfeasible in this configuration. In order to measure the swirling wake of the porous disc and characterise swirl (equation 3.3.2), measurements of all three velocity components across various spanwise planes were needed. To address this requirement, SPIV measurements were carried out.

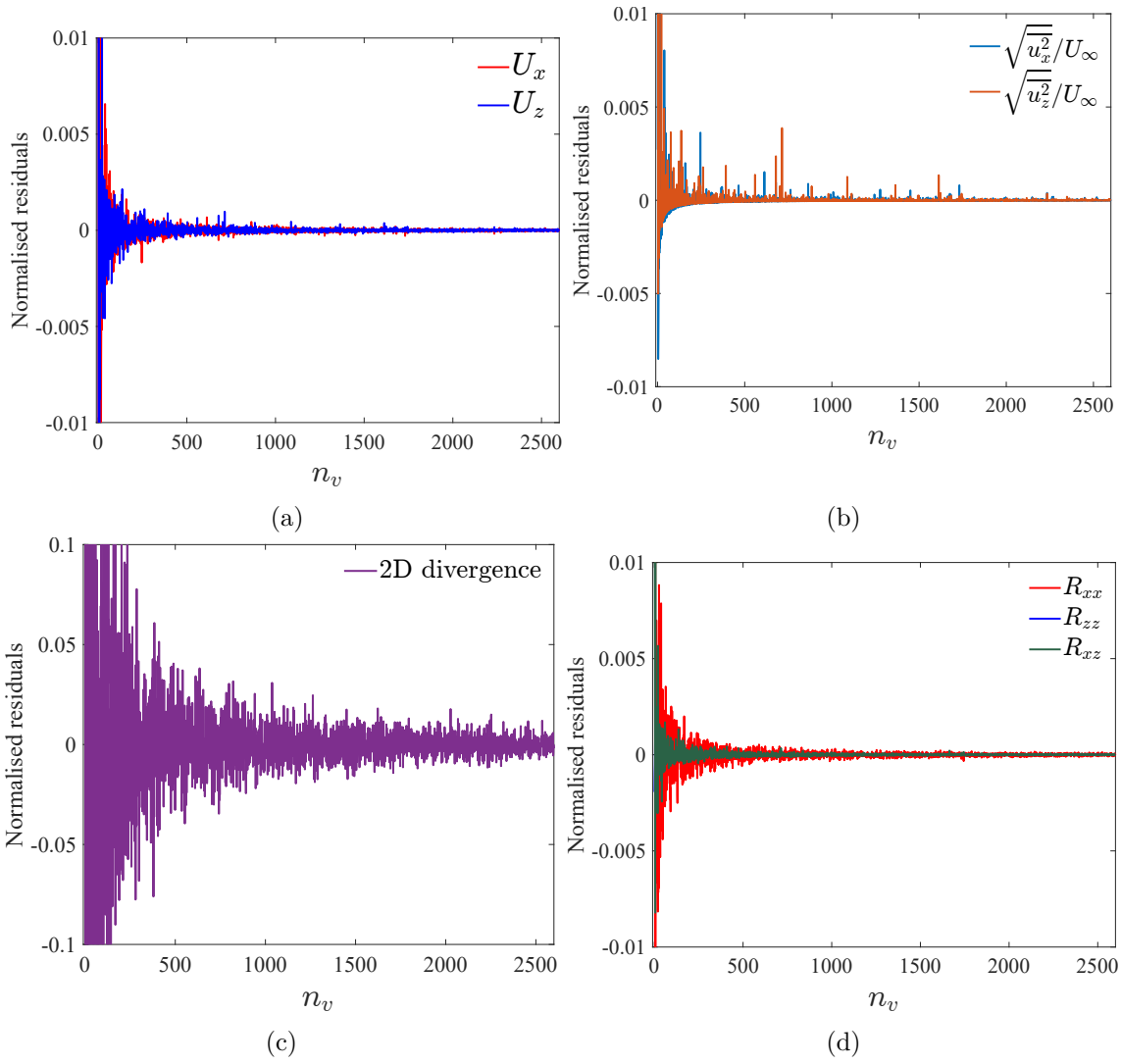

Figure 3.21: Example of a statistical convergence verification for the PIV2d2c measurements showing the computed normalised residuals for the (a) mean velocity, (b) the RMS velocity, (c) the 2D divergence and (d) the available Reynolds stress terms.

3.5.5 Stereoscopic Particle Image Velocimetry

The basic principle of SPIV is similar to the standard PIV presented previously. This technique requires the use of an additional camera to record the image sets from a different angle in order to reconstruct the third velocity component in a plane (2d3c). The SPIV experimental set-up is depicted in figure 3.23. The laser guiding arm (LGA) and cameras were attached to the wind tunnel's streamwise translation robot, which served as a common foundation. The LGA was securely attached to a vertical optical rail, mounted on a cantilevered structure equipped with a roller guide. This design allowed synchronised movement of the LGA with the camera system. A double pulse Nd:YAG laser was used to illuminate the seeded flow. The image sets were recorded using two 25 megapixels LaVision^{TM} MX-CXP-25M cameras equipped with planar ZEISS^{TM} lenses of 85 mm focal lengths. The MX-CXP-25M is a global-shutter camera with a CMOS[6] sensor and a CoaxPress CXP6 4-lane interface. The cameras were mounted on vertical optical rails parallel to the test section walls (backward-forward

[6]Complementary Metal-Oxide Semiconductor

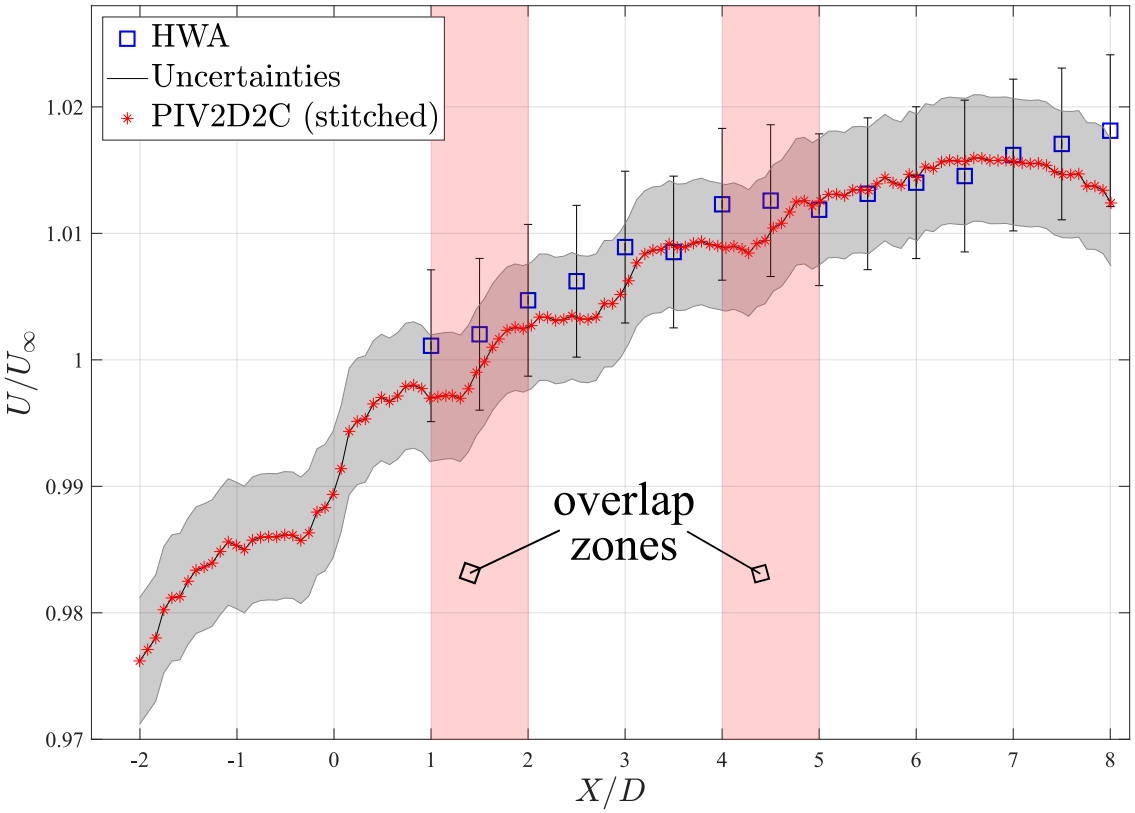

Figure 3.22: Normalised mean streamwise velocity centerline profiles showing redundant HWA measurements and stitched PIV data for an empty test section with a free-stream velocity of $U_\infty = 20$ m.s^{-1}.

scattering configuration) and were positioned at the same height and with a 90° angle between the camera viewing axes. This camera arrangement increases accuracy and minimises uncertainties (Raffel et al., 2007). Since the laser sheet, the lens and the image planes are not aligned, a Scheimpflug mount was installed between the lenses and the cameras and adjusted to obtain uniformly sharp images. The laser pulses and the camera recordings were synchronised with a high speed LaVision$^{\text{TM}}$ PTU device.

A SPIV calibration was performed between experiments using a two-level metallic calibration plate (LaVision$^{\text{TM}}$ 309-15) placed in the same planes as the laser sheet. The calibration plate is maintained perpendicular to the wind tunnel floor and at the desired height using a stand with an optical rail on top. The properties of the calibration of each camera and at each position showed very small discrepancies and confirmed that the set-up was symmetrical and sturdy. The standard deviation of the pinhole fit remained below 0.5 pixels for all calibrations. The scale factor is constant for all calibrations at $SF_{SPIV} = 21.9$ px/mm.

The SPIV measurements are summarised in figure 3.24 where an example of the obtained mean streamwise velocity fields is shown. Cross-sectional planes were measured at every disc diameter from $X = 2D$ to $X = 8D$. The region of interest at each $x-$location measures $2.4D \times 2.4D$ with a spatial resolution of $\Delta_y^{\text{SPIV}} = \Delta_z^{\text{SPIV}} = 0.76$ mm ($\sim \lambda/4$, $\sim 25\mathcal{L}_{int}$). For each configuration, 3000 image pairs were captured per camera, with a time interval of $dt = 23$ μs between snapshots. The sampling frequency was set at $f_{SPIV} = 30$ Hz corresponding to a total acquisition time of $T_{SPIV} = 100$ s.

The uncertainties for the SPIV measurements of the in-plane components were estimated using the same correlation statistics approach as described in section §3.5.3. The

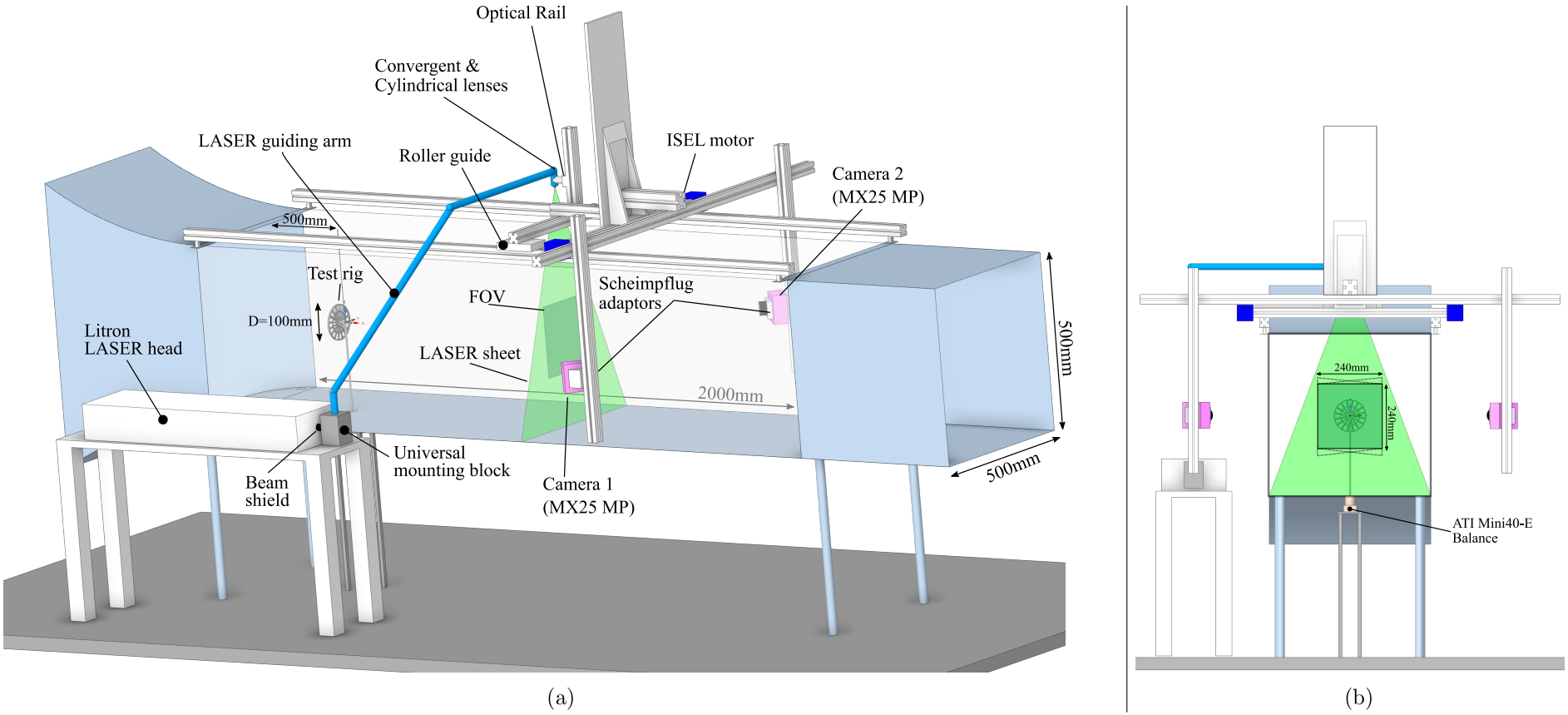

Figure 3.23: Stereoscopic image velocimetry experimental set-up showing a scaled schematic in (a) isometric view and (b) back view.

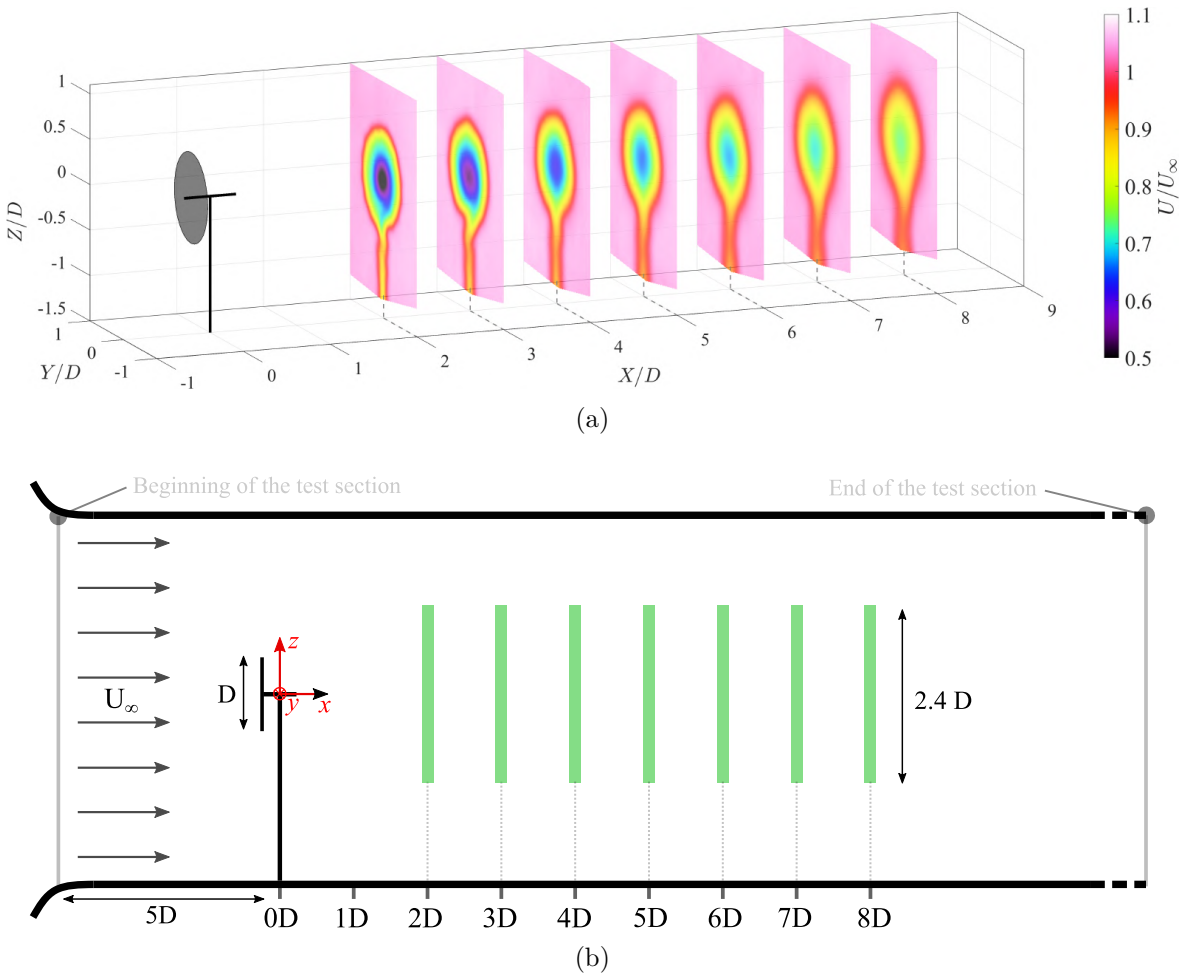

Figure 3.24: (a) Summary of the SPIV measurements and (b) a schematic diagram (not to scale) of the SPIV FoVs.

resulting uncertainties for the velocity components in every plane amounted to around 0.5%-1.2% for the instantaneous wakes and below 0.3% for the mean wakes. These uncertainties are very low compared to those of the 3CHWA technique and thereby achieve a more precise characterisation of swirl and radial velocities associated to entrainment (chapter 5). The SPIV measurements also underwent a statistical analysis to verify convergence. The results were identical to those presented in section §3.5.3.

3.6 Corroboration of the measurements and combined uncertainty estimation

Beyond individual uncertainty estimation specific to each technique, the redundancy of the velocimetry techniques was leveraged to cross-validate the data and estimate uncertainties. Moreover, for each technique, an empty wind tunnel test section measurement was performed serving as a test-case. This section presents some examples which helped ensure the quality of the database.

As explained earlier, the 3CHWA probe used here has a finite yaw angle (γ) calibration range $\gamma \in [-30°, +30°]$. If the measured velocity angle at a specific position exceeds this range, the HWA measurements are not accurate. To determine the minimum distance

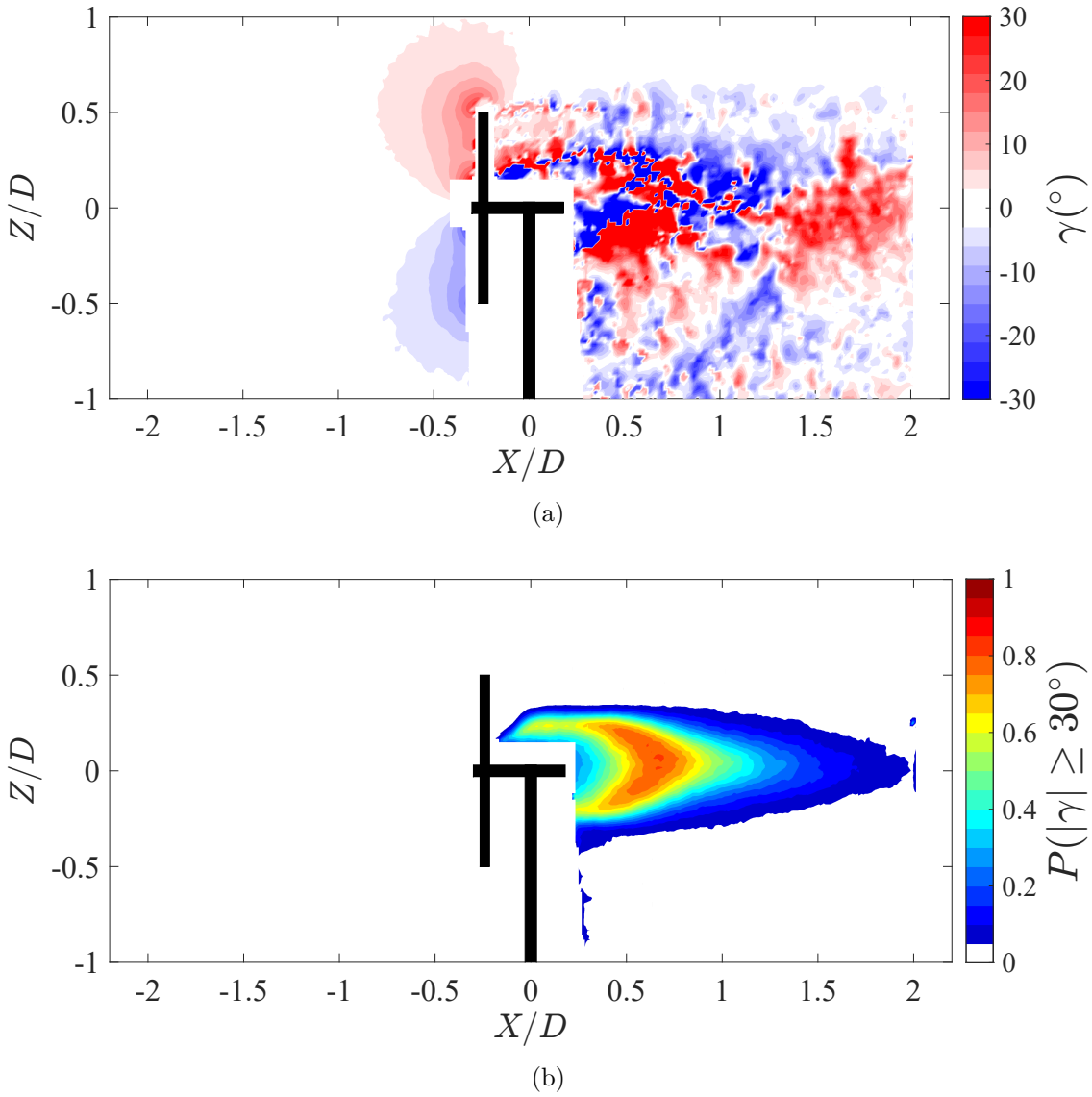

Figure 3.25: PIV2d2c zone A example of (a) the calculated velocity angles γ for an instantaneous PIV2d2c streamwise field to obtain (b) the 3HWA calibration range exceeding probability $P(|\gamma| \geq 30°)$.

necessary between the test rig and the probe, PIV2d2c velocity measurements were used to calculate the in-plane distribution of the yaw angle γ. To determine the zones where the probe was susceptible to find velocity vectors with angles exceeding the calibration range, a probability of exceeding this range ($P(|\gamma| \geq 30°)$) was defined and calculated for each case. An example of this process is presented in figure 3.25. As shown in figure 3.25a, close to the test rig where strong 3D effects are expected, the yaw angle exceeds the calibration range, especially at hub-height and for $X/D \leq 1$. However, the probability of exceeding the calibration range quickly falls to zero at $X = 2D$ (figure 3.25b). The results were almost identical for all the tested porous discs. This result explains the choices made in §3.5.1 regarding the measurement points distribution and provide an example of how velocimetry redundancy was leveraged in this work.

Redundant velocimetry techniques were especially useful to validate the mean fields stitching method presented in section 3.5.4. The method is illustrated in figure 3.26 for the mean streamwise velocity field of case $\alpha = 15°$. As shown in figure 3.26b, the mean streamwise velocity matches well between FoVs and between the PIV and the

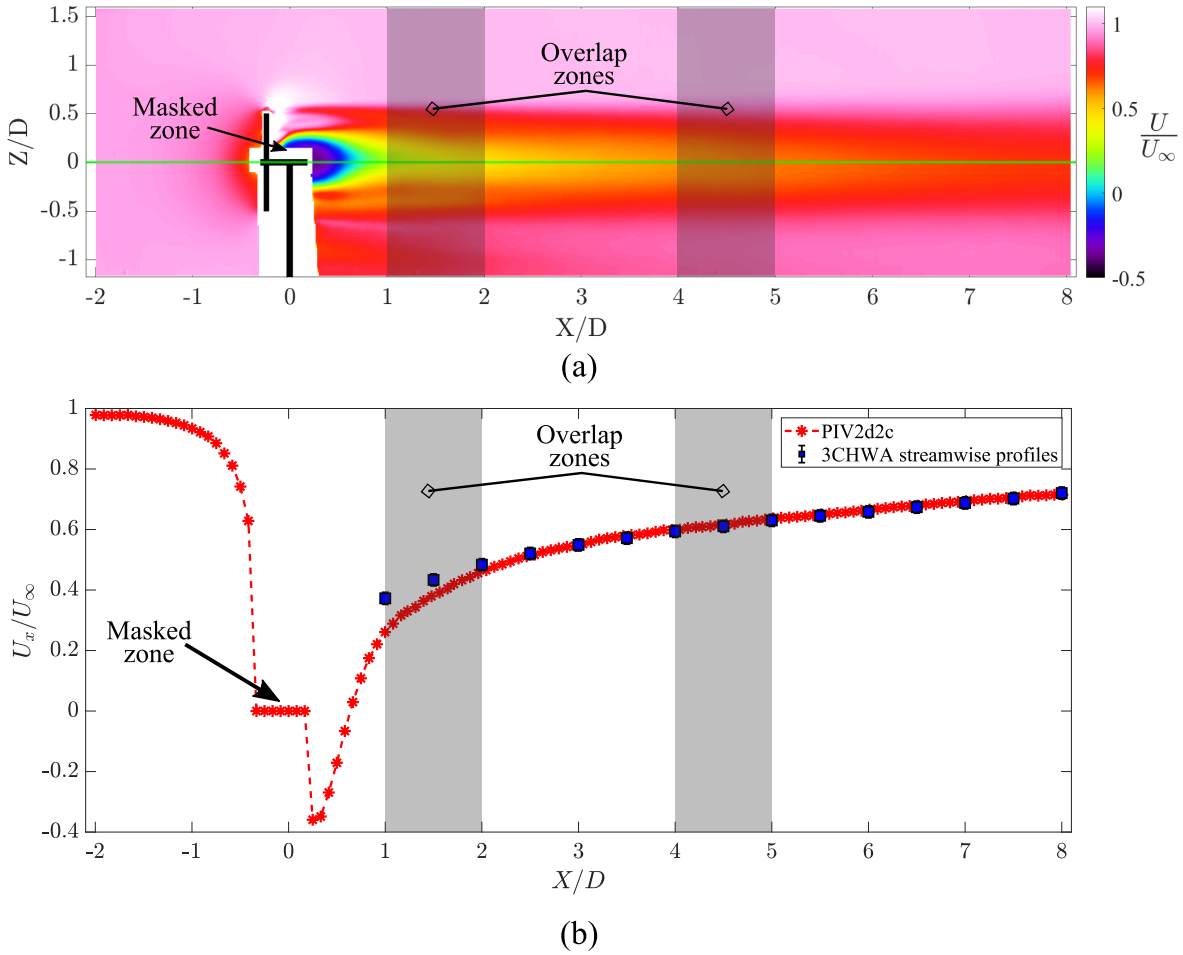

Figure 3.26: Example of the Multi-FoV PIV velocity fields stitching method showing (a) the streamwise velocity field from each FoV. The solid green line represents the centreline profile that is used to illustrate the method in (b). 3CHWA measurements are also plotted for corroboration. Black patched area : test rig outline.

HWA. A mild difference is observed at $X = 1D$, corresponding to the close proximity to the test rig where some back-flow is expected and the velocity vector angles exceed the 3CHWA calibration range (see figure 3.25b), thereby over-estimating the real streamwise velocity (Bruun, 1996). Figure 3.27 emphasises the corroboration of PIV2d2c and 3CHWA in the centreline profiles of vertical velocity and available RMS velocities. From figure 3.27a, it is clear that both techniques collapse fairly well except for a mild difference close to the test rig. Furthermore, as shown in figures 3.27b and 3.27c, the RMS velocities show very good agreement throughout the wake except for a slight underestimation of the vertical RMS velocity close to the test rig. This is most likely due to a small difference between the origins of both measurements. In any case, both methodologies show a good consistency with each other, serving to validate the 3CHWA measurements. This is particularly crucial given the susceptibility of 3CHWA measurements to calibration drifts, as explained in section 3.5.1. Moreover, spanwise profiles corroborating 3CHWA and SPIV at $X = 2D$ are reported in figure 3.28. Swirl is particularly difficult to measure at longer distances since its intensity is an order of magnitude below the streamwise component and it decays faster than the mean streamwise velocity deficit. These results however, allowed us to further estimate the uncertainties of each technique and validate the different campaigns.

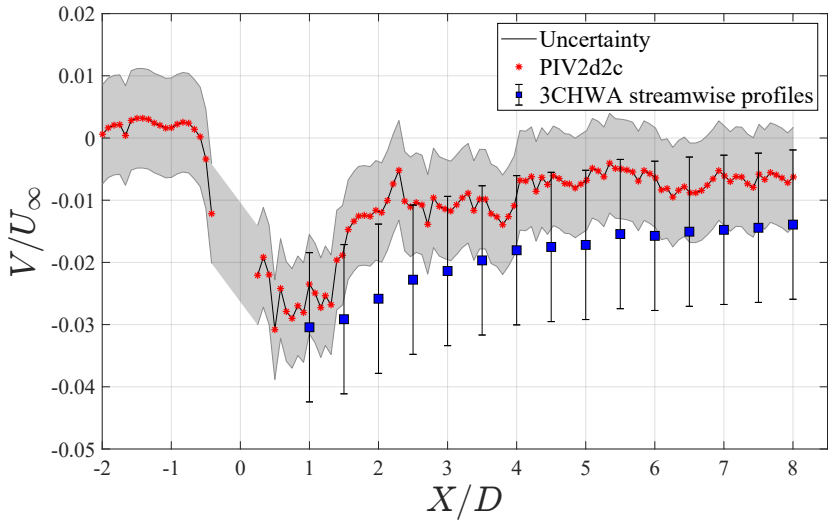

(a)

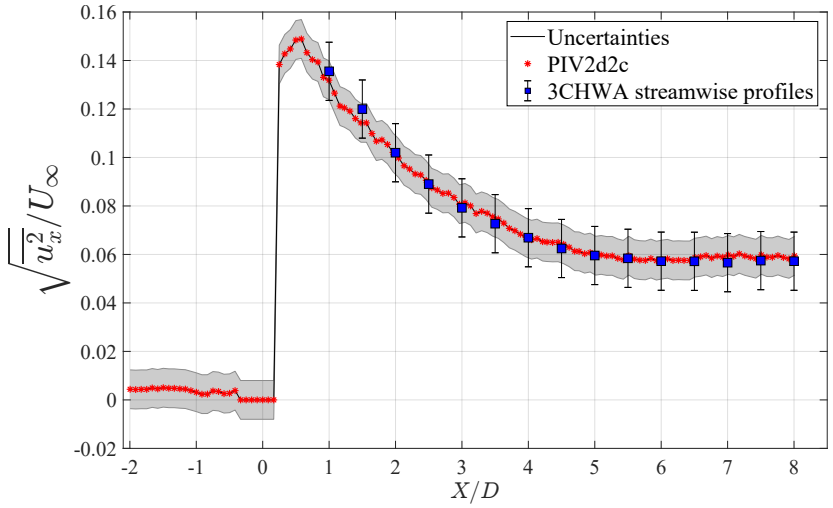

(b)

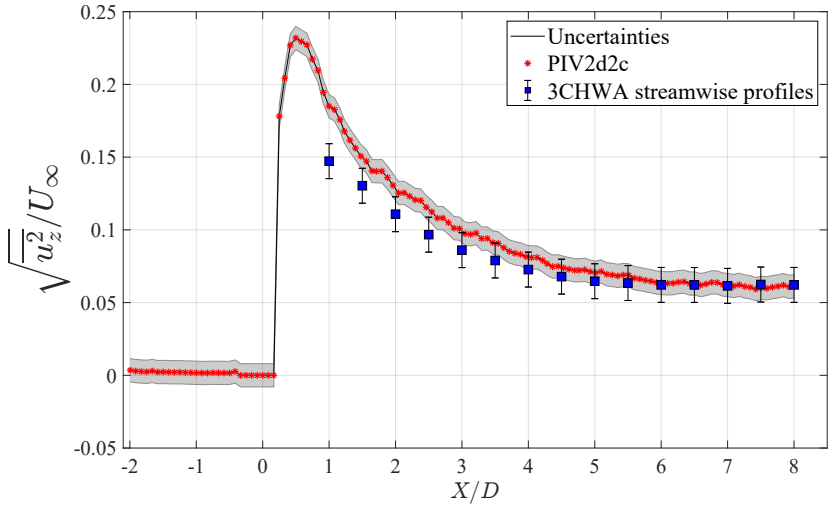

(c)

Figure 3.27: PIV2d2c and 3CHWA redundancy plots showing streamwise profiles (a) mean radial velocity component, (b) streamwise RMS velocity and (c) vertical RMS velocity.

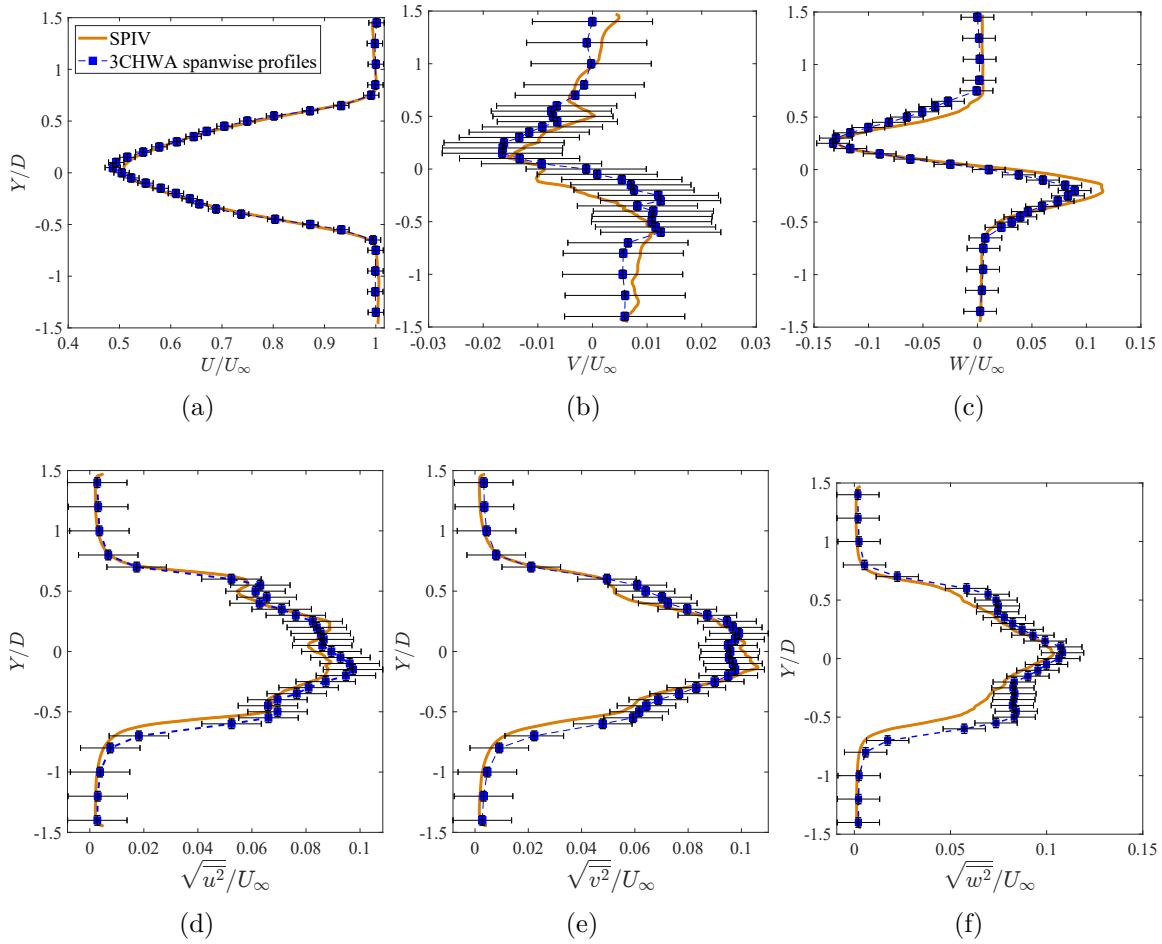

Figure 3.28: SPIV and 3CHWA redundancy plots showing lateral profiles of (a) mean streamwise velocity, (b) mean radial velocity, (c) mean swirl velocity, (d) streamwise RMS velocity, (e) radial RMS velocity and (f) swirl RMS velocity.

This chapter presented the experimental apparatus and the different measurement techniques relevant to this study and to the goals established in the introduction. Part A of this chapter discussed in detail the design process of the porous disc with particular attention given to the passive generation of swirl. Moreover, the experimental facilities were presented and some qualification results were shown. Part B gave a comprehensive look on the metrology and methodology used to measure the relevant terms that came from the theoretical foundation given in chapter 2. Each measurement technique and set-up was described underscoring their relevance to this work. Their redundancy was further leveraged to corroborate each other and estimate the uncertainties. These results give confidence that the measurements were conducted with the proper rigour, ensuring that the relevant physical quantities were accurately measured. The next chapter will characterise the introduced swirl and its effect on the development of the axisymmetric wake. Particular attention will be given to the characteristic scales of swirl and to the eventual scaling laws followed by the wake properties.

Résumé en français: Dispositif expérimental

Les expériences exposées dans ce chapitre ont été menées au sein du Laboratoire PRISME (Laboratoire Pluridisciplinaire de Recherche, Ingénierie des Systèmes, Mécanique et Énergétique). L'objectif premier de ce chapitre réside dans la description détaillée du processus de conception du disque poreux, élaboré de manière à intégrer passivement le swirl, ainsi que dans la description approfondie des campagnes expérimentales déployées pour mesurer les sillages générés. D'abord, la méthodologie de conception du disque poreux est exposée, englobant les considérations aérodynamiques et les choix conceptuels qui ont guidé le développement de ce substitut. Par la suite, une attention particulière est portée sur les propriétés de la soufflerie utilisée pour les campagnes expérimentales. Enfin, les techniques de mesure mises en place pour caractériser les sillages générés sont exposées en détail. Cette section du chapitre offre une vue d'ensemble des instruments et des protocoles expérimentaux, soulignant la robustesse de l'approche méthodologique adoptée pour obtenir une base de données fiable et complète.

La conception du disque poreux s'inspire de celle proposée par Helvig et al. (2021). Les paramètres globaux du disque poreux sont répertoriés sur la figure 3.1. La taille et le nombre de pâles sont ajustées pour obtenir la porosité souhaitée (Aubrun, 2013; Camp and Cal, 2016). La porosité (éq. 3.1.1) est un paramètre important pour ce type d'études puisqu'elle déterminera le coefficient de traînée du substitut. Dans un souci de simplicité, une modification des pales du disque poreux a été envisagée dans le but de dévier azimutalement l'air passant à travers le disque poreux, générant ainsi du swirl. Cette modification est illustrée sur la figure 3.4. Les 16 pales trapézoïdales qui sortent du centre du disque ont été calées d'un angle $\alpha > 0°$. Certaines prédictions concernant l'intensité de swirl en fonction de l'angle de calage peuvent être faites en invoquant la théorie des écoulements potentiels (Batchelor, 1953). Pour des petits angles de calage, l'écoulement autour de la pale est attaché et le swirl est généré sans modifier le blocage du disque. Pour des angles de calage au delà de l'angle de décrochage, la théorie inviscide n'est plus valable et l'amplitude de swirl diminue. Des disques pour des angles de calage $\alpha = [0, 5, 10, 15, 20, 25, 30]°$ ont été imprimés et testés. Une analyse plus approfondie est réalise pour les disques $\alpha = 15°$ et $\alpha = 25°$ pour des raisons expliquées dans le chapitre suivant.

Les expériences ont été réalisées dans la soufflerie subsonique "S2" de type Eiffel en circuit ouvert du laboratoire PRISME (voir 3.8). En amont de chaque campagne expérimentale, une qualification de la veine d'essai (Barlow et al., 1999) à été réalisée. Cette démarche vise à garantir l'homogénéité de l'écoulement incident et à évaluer le niveau d'intensité turbulente résiduel dans la veine, comme démontré dans les figures 3.9 et 3.10. L'intégration du disque poreux dans la soufflerie a été réalisée à l'aide d'un mât cylindrique en forme de "T", représentant la tour et la nacelle d'une éolienne, tel qu'illustré dans la figure 3.11. Ce dispositif a ensuite été fixé à une balance aérodynamique positionnée dans la partie inférieure de la veine d'essai. Pour établir une comparaison pertinente avec une éolienne de référence (NREL 5MW), des facteurs d'échelle significatifs sont présentés dans le tableau 3.1.

La seconde partie de ce chapitre présente le dispositif expérimental mis en place pour les campagnes d'essais. Les protocoles expérimentaux et les différentes techniques utilisées (fil chaud et vélocimétrie par images de particules) ont été mises en place pour mesurer les quantités identifiées dans le chapitre théorique précédent. D'après

l'équation (3.3.1), la force de traînée du disque poreux doit être mesurée pour obtenir des valeurs directes de C_D. En outre, les équations (3.3.1) et (3.3.2) justifient la mesure des trois composantes de vitesse. Pour déterminer les lois d'échelle de similarité que l'on trouve dans le développement du sillage, en particulier pour la décroissance du swirl, il est nécessaire de mesurer les trois composantes de la vitesse à différents endroits dans le sens de l'écoulement. La figure 3.12 synthétise les diverses mesures effectuées tout au long de cette étude. Chaque technique de mesure présente ses avantages et inconvénients propres, cependant, leur confrontation a permis d'estimer les incertitudes et de corroborer les valeurs obtenues. Les mesures de la force de traînée nous ont non seulement permis de cerner le problème et de localiser les angles de calage clés mais aussi de définir d'autres paramètres des expériences comme le nombre de Reynolds (figure 3.13). L'anémométrie à fil chaud trois composantes (3CHWA) nous a permis de commencer à mesurer le sillage à différentes positions et à différents angles de calage (phase exploratoire) grâce à la relative simplicité de son installation. En outre, elle nous a permis de caractériser les principaux paramètres de l'écoulement tels que les échelles de turbulence des sillages. Enfin, la vélocimétrie par image de particules (PIV) et la vélocimétrie stéréoscopique par image de particules (SPIV) ont permis de mesurer les composantes de vitesse avec une résolution spatiale proche de l'échelle de Taylor (λ) dans des plans orthogonaux au sens de l'écoulement ($Y = 0$).

Dans l'ensemble, ces mesures complémentaires ont fourni les éléments nécessaires pour répondre aux questions initialement soulevées dans l'introduction. Les différents dispositifs expérimentaux sont présentés sur les figures 3.16, 3.18 et 3.24. La dernière section de ce chapitre se focalise sur la corroboration de vélocimétrie et sur l'estimation des incertitudes. Par exemple, les données PIV ont servi pour détecter la distance minimale de placement du fil chaud trois composantes (figure 3.25). En effet, proche de l'objet, les effets 3D engendrent des angles d'attaque pour la sonde qui risquent de dépasser l'angle maximal d'étalonnage. Les mesures de vitesse redondantes (HWA et PIV) ont été particulièrement utiles pour valider la méthode de fusion des champs moyens présentée dans la section §3.5.4. Ces éléments donnent l'assurance que les mesures ont été effectuées avec la rigueur nécessaire, garantissant que les grandeurs physiques pertinentes ont été mesurées avec précision. La prochaine étape de ce travail consistera à caractériser le swirl ainsi que son impact sur le développement du sillage turbulent.

4

Effect of a swirling motion on the wake properties of a porous disc

Contents

The previous chapters have established the theoretical framework and the experimental methodology for studying the influence of a swirling motion on the turbulent axisymmetric wake of a porous disc. A momentum budget with the relevant hypotheses have yielded conservation laws which govern the flow. Similarity solutions were considered for the wake properties and extended to the conservation of angular momentum. In particular, a new scaling law was proposed for the swirl decay based in non-equilibrium turbulence following the works of Shiri et al. (2008), Mazellier and Vassilicos (2008, 2010), Nedic (2013), Dufresne (2013), Vassilicos (2015) and of Dairay et al. (2015).

This chapter aims at qualifying and quantifying the influence of the swirling motion on the properties of the mean wake and their streamwise evolution. The effect of pitched blades on drag is first examined. Then, the swirling motion is characterised globally. Moreover, the effect of swirl on the wake topology is assessed through a momentum budget and the distribution of pressure across the wake. In the last section, scaling laws of the self-preserving swirling wake are established and compared to the similarity theory predictions.

4.1 Introduction

As covered in earlier chapters, the key global parameter used to choose a porous disc surrogate as representative of a rotating wind turbine, is the drag coefficient C_D. This coefficient is tuned through the porosity β of the disc to match C_D to the thrust coefficient C_T of a target wind turbine (Sforza et al., 1981; Aubrun, 2013). This coefficient C_D is crucial as it is directly related to the axial momentum extracted from the flow. The streamwise momentum and angular momentum balances established in chapter 2, are the conservation laws which will mostly govern the structure of the wake and its streamwise evolution. For ease of reference, these fundamental equations are recalled below:

$$C_D = 16\left[\int_0^\infty U^*\Delta U^* r^* dr^* - \int_0^\infty \left[\overline{u^2}^* - \frac{\overline{w^2}^* + \overline{v^2}^*}{2}\right] r^* dr^* + \int_0^\infty \left[\frac{{W^*}^2}{2}\right] r^* dr^*\right] \tag{4.1.1}$$

and

$$G_0^* = 16\int_0^\infty (U^*W^* + \overline{uw}^*){r^*}^2 dr^*. \tag{4.1.2}$$

Additionally, the corresponding far wake versions of equations (4.1.1) and (4.1.2) are also recalled, respectively:

$$C_D = 16\int_0^\infty [U_\infty^*\Delta U^*] r^* dr^*, \tag{4.1.3}$$

$$G_0^* = 16\int_0^\infty [U_\infty^* W^*]{r^*}^2 dr^*. \tag{4.1.4}$$

Furthermore, the mean swirl and the azimuthal and radial normal Reynolds stress terms in equation (4.1.1) come from the pressure contribution to drag. As explained in chapter 2, the swirling motion is expected to essentially modify the pressure distribution across the wake, following the equation for the pressure coefficient:

$$C_p(r,x) = -\frac{1}{2}\int_r^\infty \frac{{W^*}^2 + (\overline{w^2}^* - \overline{v^2}^*)}{r'} dr' - \frac{\overline{v^2}^*}{2}, \tag{4.1.5}$$

with $C_P = (P - P_\infty)/\frac{1}{2}\rho U_\infty^2$, where P_∞ is the static pressure of the undisturbed free-stream. The key ingredient introduced in this investigation is the swirling velocity component in the wake of a novel porous disc. As explained in chapter 3 (§3.1.2), this component was passively added to the wake by pitching the blades of the disc of an angle α, aiming to deflect the bleed air passing through the disc. Using Kutta-Joukowsky's theorem and following thin airfoil theory, some predictions were given for the generation of swirl with this approach. In particular, it was predicted that the swirl magnitude would increase linearly with α without increasing the blockage (iso-porosity), at least until stall appears. Beyond the stall point ($\alpha \geq \alpha_c$), blockage is expected to increase due to the massive separation in the suction side of each blade, thereby increasing drag

and decreasing swirl. This last point can be exploited experimentally to find a post stall pitch angle α_s having a decreased effective porosity while maintaining the same swirl magnitude. To the author's knowledge, there are no prior investigations focused on porous discs equipped with pitched blades. It is thus necessary to determine these particular pitch angles experimentally. Consequently, the following two sections are dedicated to the determination of these pitch angles via drag measurements and the characterisation of swirl.

4.2 Drag coefficient of porous discs with pitched blades: two regimes

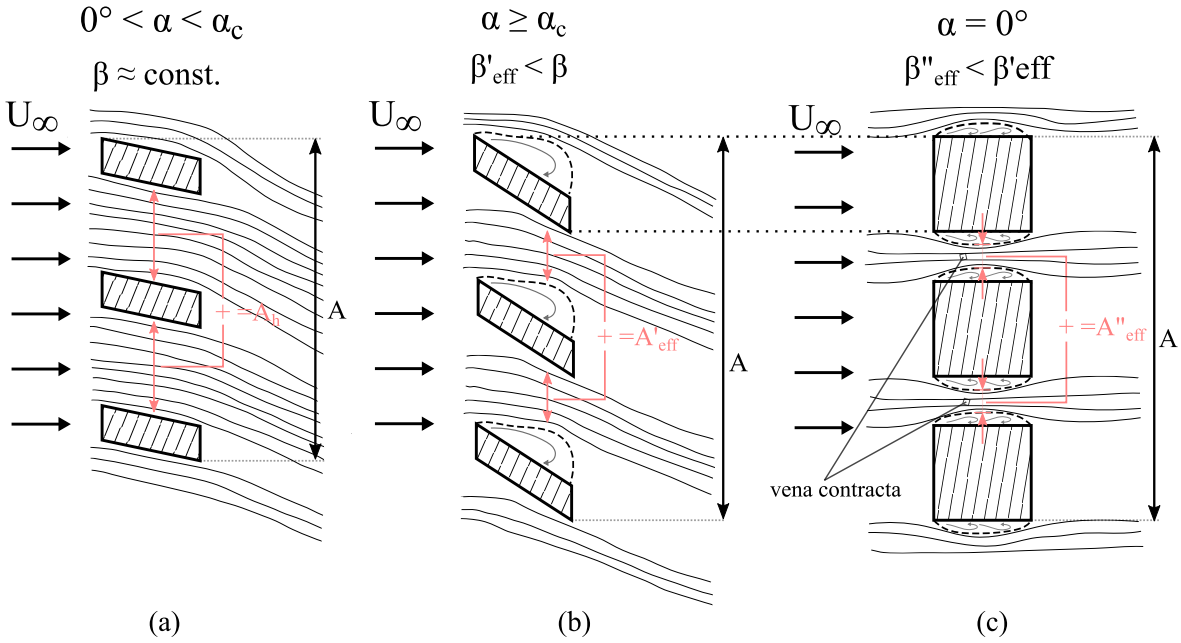

Figure 4.1: Schematic diagram of the increase in blockage due to stalled blades and the equivalent porosity discs. The schematic shows an unfolded view of a porous disc with (a) a pitch angle below the stall point, (b) a post-stall pitch angle and (c) a decreased porosity disc with thicker blades aiming to match the effective porosity of (b).

For porous bodies, the bleed air passing through the body decreases their drag coefficient by reducing the pressure drop across it (Castro, 1971; Steiros and Hultmark, 2018). As shown by Steiros and Hultmark (2018), the drag coefficient of a porous body is a function of the porosity β. As discussed in chapter 3, pitching the blades of the porous disc to generate swirl is expected to show two regimes: the attached flow regime and the stall regime. Figure 4.1 recalls the schematic diagram shown in chapter 3 (§3.1.2) emphasising these two regimes and their effect on effective porosity β_{eff}. In the attached flow regime (figure 4.1a), the Kutta condition of each blade is fulfilled and swirl is generated with no change in effective porosity. In the stall regime (figure 4.1b), the flow separation on the blades will create a sudden drop in effective porosity as blockage is increased, thereby increasing drag. To experimentally validate this prediction, two decreased porosity discs with same frontal area as their pitched counterparts were printed for cases $\alpha = 15°$ and $\alpha = 25°$ (figure 4.1c). Their porosity values are $\beta''_{15} = 55\%$ and $\beta''_{25} = 48\%$, respectively. Due to the *vena contracta* effect, a

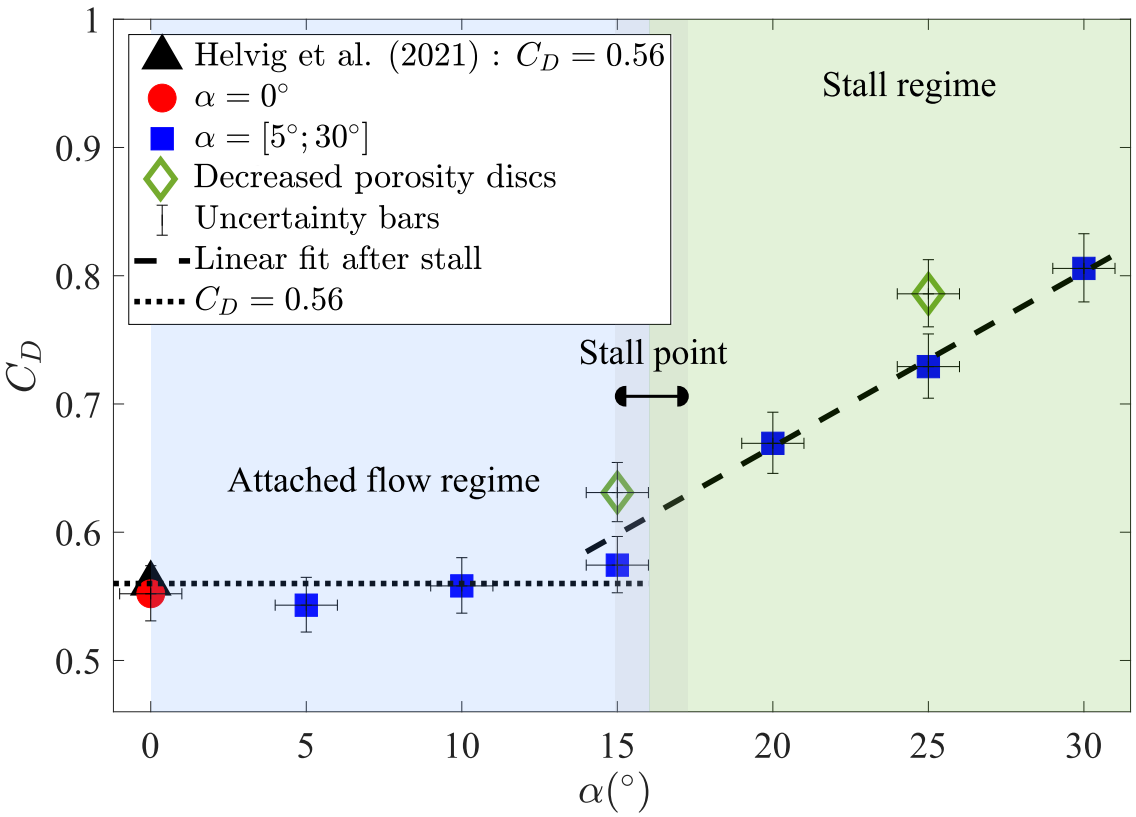

Figure 4.2: Measured drag coefficient C_D of the studied porous discs with different pitch angles α. Dotted black line: constant C_D before stall, dashed black line: linear trend after stall.

mild positive offset in drag relative to their stalled counterparts is expected (Chapter 3, §3.1.2).

The effect of the pitch angle α on the drag coefficient C_D of the porous discs is shown in figure 4.2. The present values are compared with that reported in Helvig et al. (2021), where the 65% porosity non-uniform porous disc corresponds almost exactly to the $\alpha = 0°$ case in this study. As previously explained, the drag coefficient appears to follow two different trends before and after $\alpha = 15°$. For pitch angles below $\alpha = 15°$, the drag coefficient remains constant with marginal deviations. Stall appears for $\alpha > 15°$ and induces a strong increase of the drag coefficient, which deviates significantly from the attached flow prediction. A linear fit such as $C_D = 0.78\alpha + 0.40$ (with α in radians) approximates fairly well the trend of the data. For this configuration, the stall point is therefore located around $\alpha_c \in [15°; 18°]$ [1] which is consistent with what can be found in flat plates research like in the work of Nakayama (1988), for example.

As predicted, the same slope is found between the decreased porosity discs (green diamonds), with a positive offset of 8-9% relative to their stalled counterparts. Based on momentum theory and potential flow, Steiros and Hultmark (2018) developed a mathematical model for the drag coefficient of porous plates as a function of β such as $C_D \sim (1/\beta^2)$ (see figure 4.3). Their comprehensive work encompassed a large spectrum of arbitrary porosity ranging from $\beta = 0$ (solid plate) to $\beta = 0.8$. As shown in figure 4.3, the porosity range examined in this thesis, is only a fraction of what was reported in Graham (1976) and Steiros and Hultmark (2018). In this

[1] Additional pitch angles would need to be tested to measure the exact value of the stall angle, but determining such angle was out of the scope of this work.

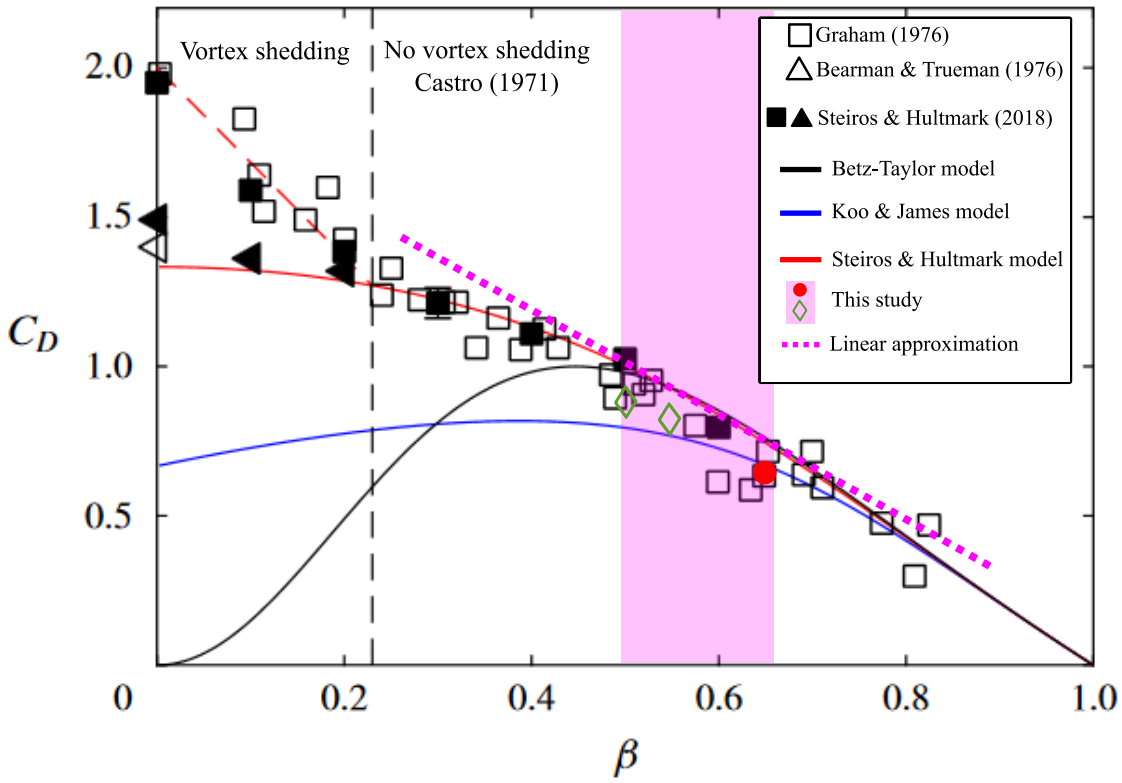

Figure 4.3: Drag coefficients of flat plates with arbitrary porosity as a function of β compared to the scope of this porous disc study. Adapted from Steiros and Hultmark (2018).

region ($\beta \in [0.5 - 0.65]$), the drag coefficient evolution as a function of porosity is well approximated by a linear asymptote, corroborating our results. In any event, the $\alpha = 15°$ case appears to be the porous disc having the highest value of α, while maintaining a constant blockage (maximum swirl generation at iso-porosity). The following section focuses on characterising swirl in the wake of the porous discs and the swirl magnitude evolution as a function of the pitch angle.

4.3 Characterisation of the swirling motion

4.3.1 Effect of the pitch angle on the generation of swirl

For a quantitative characterisation of swirl, spanwise profiles of W/U_∞ obtained for $\alpha = 25°$ are displayed in figure 4.4. In order to quantify swirl magnitude and its streamwise evolution, two characteristic scales are introduced: the peak-to-peak swirling velocity $W_s(x)$ and the swirling length $\delta_{swirl}(x)$, based on the spanwise distance between these two peaks. The way these two parameters are extracted from the profiles is illustrated in figures 4.4a and 4.4b for $X = 2D$ and $X = 6D$, respectively. At $X = 2D$, W_s/U_∞ reaches values of around 0.34, while it falls to around 0.12 at $X = 6D$. Meanwhile, δ_{swirl}/D increases from 0.65 at $X = 2D$ to 0.98 at $X = 6D$. This means that, in the streamwise direction, the swirl magnitude decreases but is spread over a larger area respecting the conservation of angular momentum (equation 4.1.4). Furthermore, the presence of the mast yields an asymmetry on the swirling velocity profiles which is prominent at $X = 2D$ but is damped as the wake evolves downstream.

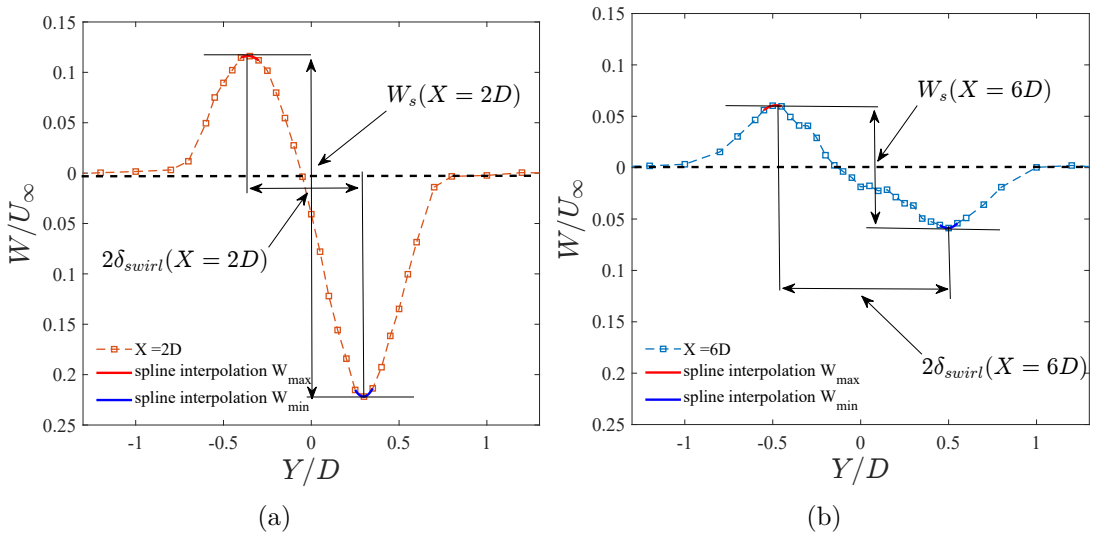

Figure 4.4: Definition of the peak-to-peak swirling velocity $W_s(x)/U_\infty$ and the swirling length $\delta_{swirl}(x)$ for the $\alpha = 25°$ case at (a) $X = 2D$ and at (b) $X = 6D$ (3CHWA).

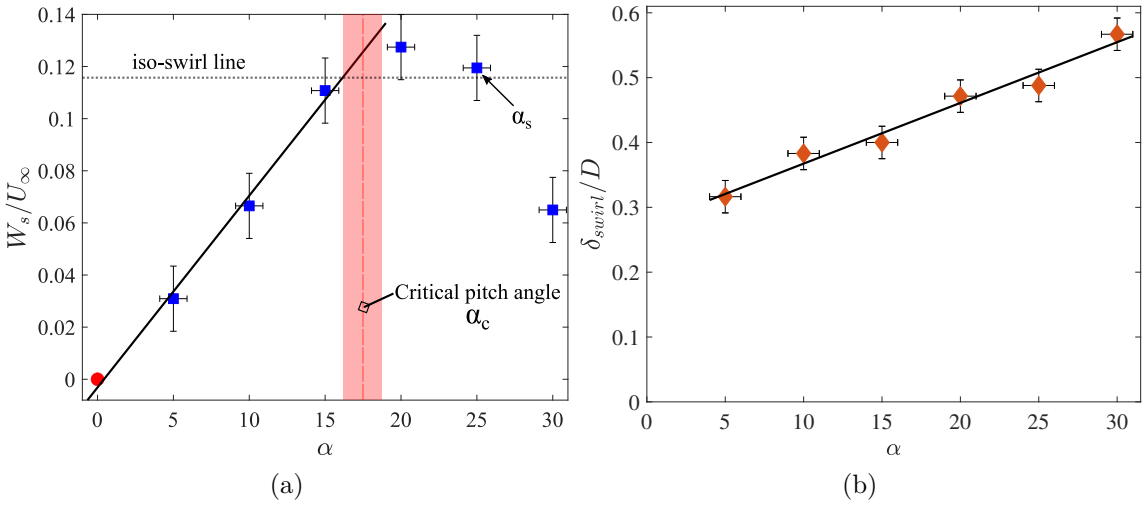

Figure 4.5: (a) Peak-to-peak swirling velocity W_s/U_∞ and (b) swirling length δ_{swirl}/D as a function of the pitch angle α evaluated at $X = 6D$.

The effect of the pitch angle on W_s and δ_{swirl} at $X = 6D$ is reported in figures 4.5a and 4.5b, respectively. The swirl magnitude W_s increases linearly with α as predicted in chapter 3, until $\alpha = 15°$. It was predicted that the swirl magnitude would increase with pitch such as $W_s/U_\infty = 0.8\alpha$ (with α in radians). However, the fitted law for the data (figure 4.5a) yields $W_s/U_\infty = 0.42\alpha$, a much lower value than the predicted slope. The discrepancies between the predicted and the fitted slopes are explained by neglecting finite-size blade effects, cross interaction between the blades as well as the geometry of the porous disc in general. Corroborating drag measurements, it appears that the critical pitch angle is $\alpha_c \in [16°; 18°]$, corresponding to what is reported for thin flat plates (Nakayama, 1988; Anderson, 2011; Mohebi et al., 2017; Shademan and Naghib-Lahouti, 2020). Beyond the critical angle α_c, the swirling velocity drops, due to stall (figure 4.6b). This phenomenon represents an intrinsic limitation to the production of swirl using this kind of modified porous disc. Nevertheless, the post-stall pitch angle $\alpha = 25°$ shows very similar values of swirl magnitude as the non-stalled case $\alpha = 15°$ (see figure 4.6c). Therefore, this particular pitch angle $\alpha_s = 25°$ (decreased porosity

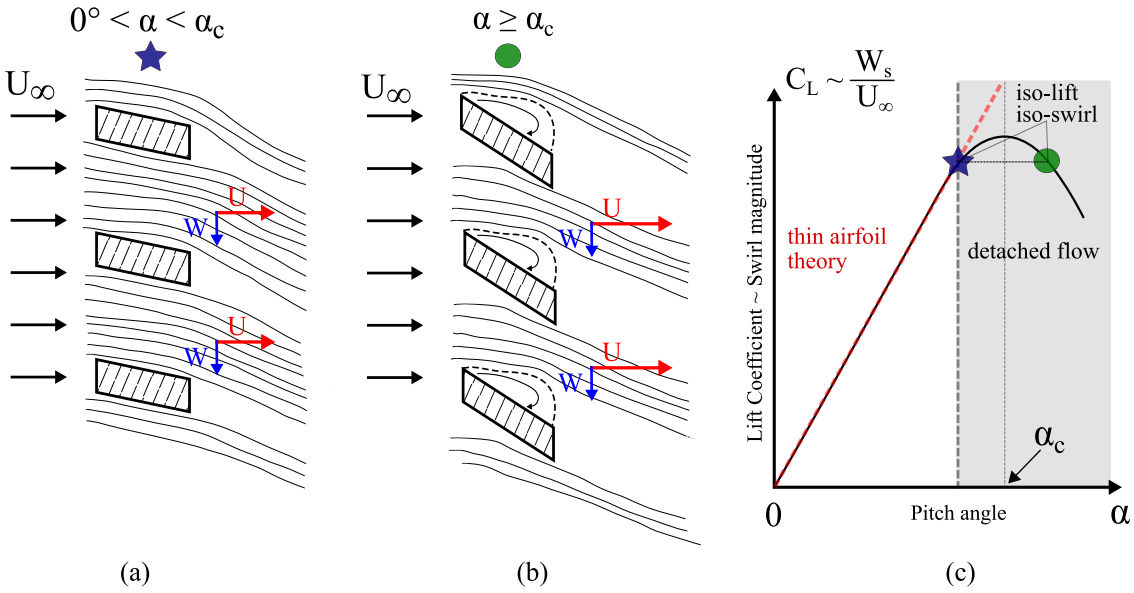

Figure 4.6: Schematic diagram in an unfolded view of a porous disc with (a) a pitch angle below the stall point, (b) with stalled blades but with iso-swirl generation as (a) and (c) a conceptual graph of $C_L = f(\alpha)$.

at iso-swirl) allows us to separate the parameters α and β thanks to stall. As shown in figure 4.5b, this behaviour is not observed on the evolution of δ_{swirl} with respect to α. The trend shows that the data is well approximated by a linear fit such as $\delta_{swirl}/D = 0.54\alpha + 0.27$ (with α in radians). Extrapolated to $\alpha = 0°$, the swirling length is non-null, corresponding to the position of the inner rim of the porous disc. This can also be interpreted as the existence of a virtual origin α_0 for the swirling length as a function of α such as $\delta_{swirl}/D = 0.54(\alpha - \alpha_0)$ where $\alpha_0 = -0.5$ rad or $\alpha_0 = -28.6°$.

It has been proved that the new disc design, proposed in this study, is an effective solution to passively generate a swirling motion in the wake of porous discs. Moreover, the α parameter appears to fully predict the swirling magnitude. In the following, the characteristic scales of swirl are calculated and compared to the existent literature.

4.3.2 Characteristic parameters of swirl: TSR vs. Swirl number

As explained in chapter 3 (§3.2.3), the TSR is not a straightforward comparison parameter to use as a swirl magnitude indicator for a static object. Nevertheless, as explained in Dufresne (2013), this parameter directly sets the magnitude of swirl for wind turbines. Therefore, to characterise the swirl introduced in the wake of the porous disc and compare it to wind turbine data, a different dimensionless parameter is examined: the swirl number. However, the literature of swirling flows reports various ways of defining such a parameter (Gupta et al., 1984; Alekseenko et al., 1999; Shiri, 2010; Dufresne, 2013; Holmes and Naughton, 2022). Furthermore, to the author's knowledge, there are very few studies which have reported on the swirl number of real wind turbines, let alone any established correlation between the TSR and the swirl number.

Following the theoretical breakthrough of Reynolds (1962) regarding swirling flows, a swirl number $\hat{S}$ can be defined as the ratio of angular momentum to axial momentum

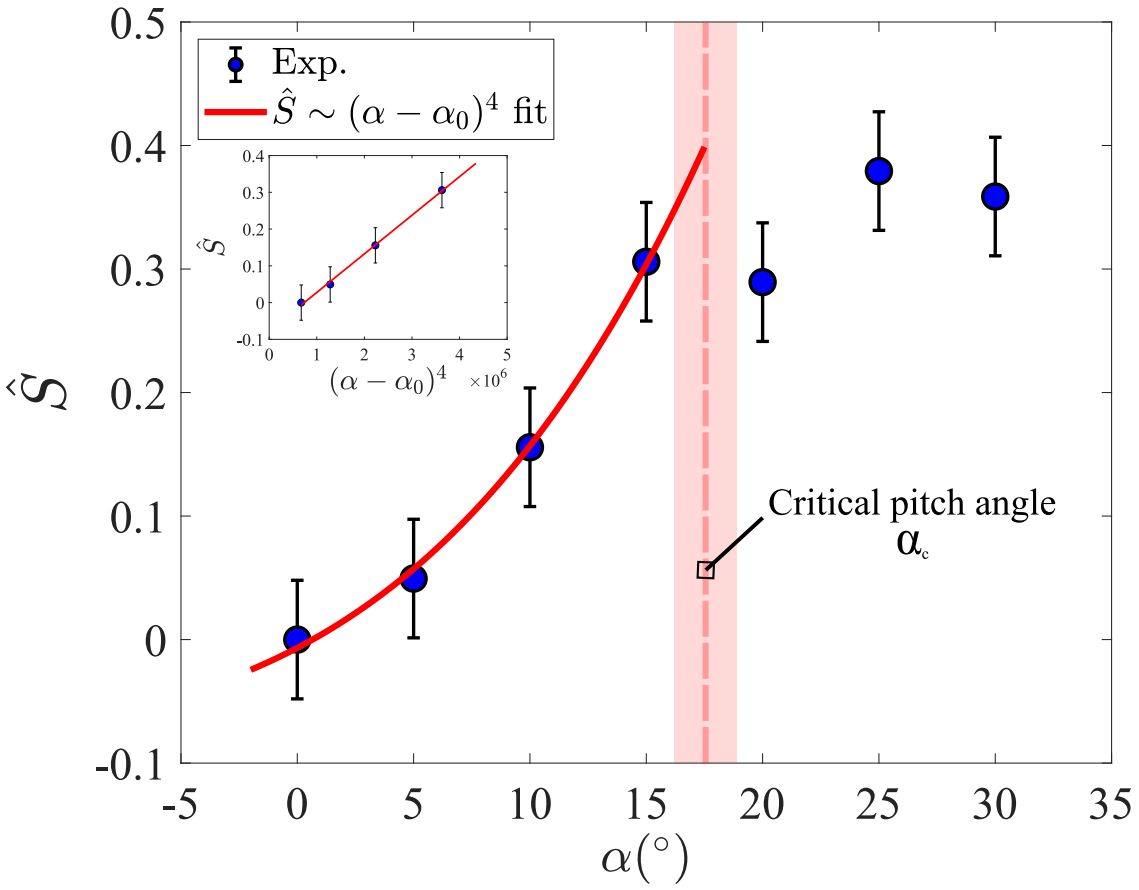

Figure 4.7: Momentum-based swirl number $\hat{S}$ estimation as a function of the pitch angle α measured at $X = 6D$. Red line: semi-empirical law from observations and thin airfoil theory giving $\hat{S} \sim (\alpha - \alpha_0)^4$.

flow rates such as:

$$\hat{S} = \frac{\int_0^\infty [UW + \overline{uw}] r^2 dr}{\int_0^\infty \left[U(U_\infty - U) + \frac{W^2}{2} - \overline{u^2} + \frac{\overline{w^2}+\overline{v^2}}{2} \right] r dr} \frac{1}{D} = \frac{G_0^*}{C_D}. \tag{4.3.1}$$

As discussed in Chapter 2 (§2.3.2), the term "swirl number" was not initially coined by Reynolds (1962). Instead, it was Gupta et al. (1984) who introduced both the terminology and notation for this parameter. Later, Alekseenko et al. (1999) underscored the importance of this parameter in shaping the structure of swirling flows. As detailed in Alekseenko et al. (1999), calculating $\hat{S}$ with equation (4.3.1), with an acceptable accuracy, is very challenging and therefore rarely estimated in wind turbine wakes or in swirling flows. For this reason, only rough estimates of $\hat{S}$ for wind turbines exist in current literature (Lee et al., 2020; Wosnik and Dufresne, 2013; Morris et al., 2016), giving values of swirl $\hat{S} \in [0, 0.4]$. This corresponds exactly to the $\hat{S} = \mathcal{O}(1)$ case mentioned in the perspectives of Reynolds (1962)'s work, where the interplay of both angular and streamwise momentum conservation govern the structure of the wake.

The effect of the pitch angle on the estimated swirl number $\hat{S}$ is emphasised in figure 4.7. Before the critical pitch angle α_c, the momentum swirl number increases with α until reaching a plateau when stall occurs. From thin airfoil theory and the results obtained for $\delta_{swirl} = f(\alpha)$ in section §1.3.1, a semi-empirical law can be discerned for the evolution of $\hat{S}$ as a function of pitch, at least until stall appears. Before stall, it

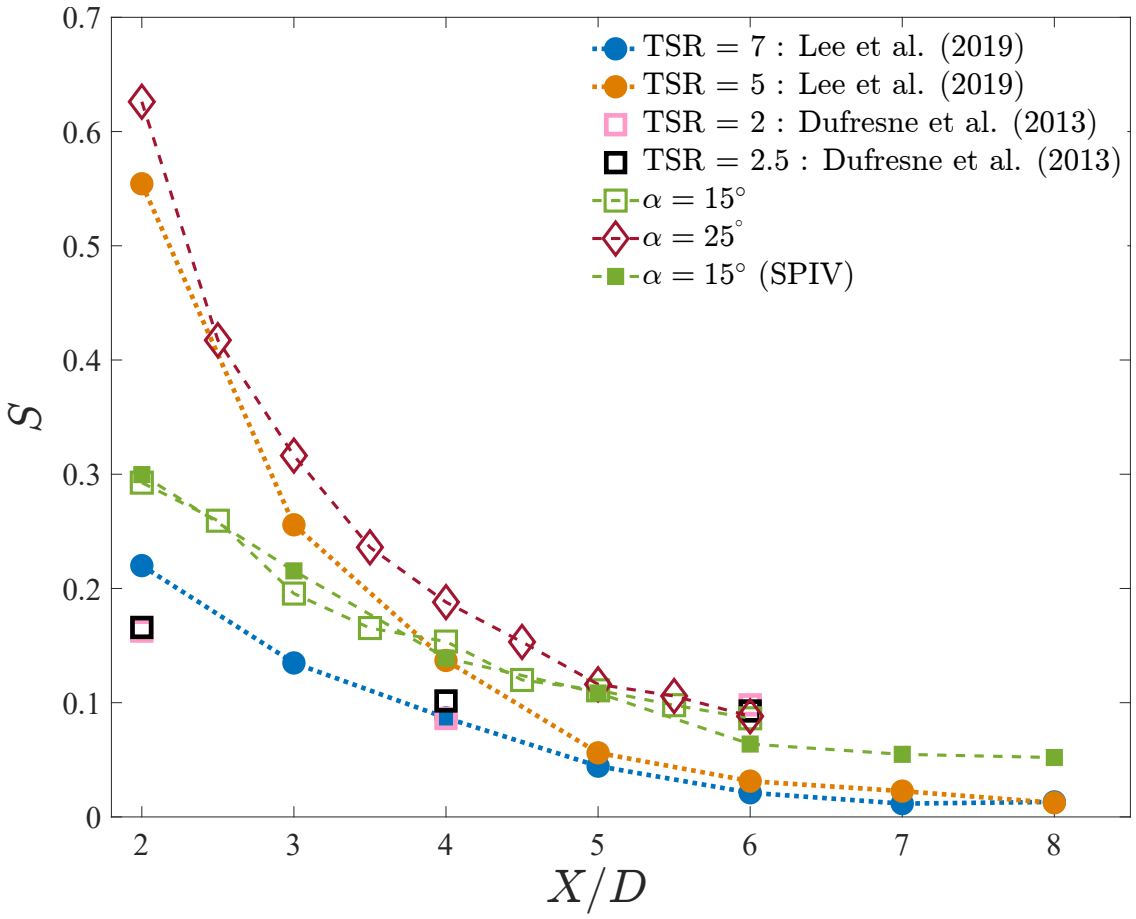

Figure 4.8: Velocity-based swirl number $S(x)$ as a function of the streamwise distance to the test rig for cases $\alpha = 15°$ and $\alpha = 25°$. The reference data was taken from Lee et al. (2020) and calculated for the data reported in Dufresne (2013). Marker sizes are adjusted to match the uncertainty.

was shown that C_D is not sensitive to the pitch angle, i.e $C_D \sim \alpha^0$. Additionally, the following trends were evidenced for swirl: $W_s \sim \alpha$ and $\delta_{swirl} \sim (\alpha - \alpha_0)$. Angular momentum conservation (equation 4.1.2) therefore predicts the swirl number to evolve as $\hat{S} \sim (\alpha - \alpha_0)^4$. Beyond α_c, it was shown that $C_D \sim \alpha$ to a first approximation and that swirl generation starts decreasing with α following an unknown law. In any case, it appears that $\hat{S}$ reaches a plateau at post-stall angles. Altogether, these arguments allow us to choose $\alpha = 15°$ as the case with maximum swirl generation at iso-porosity; and $\alpha = 25°$ as the case with decreased effective porosity with iso-swirl generation. In the following, an in-depth analysis will be conducted for cases $\alpha = 15°$ and $\alpha = 25°$ alongside with the reference case $\alpha = 0°$.

Another simpler definition for the swirl number was proposed in Gupta et al. (1984) and calculated in Lee et al. (2020) for hydrokinetic turbines. This swirl number noted $S(x)$ is defined as the ratio of the maximum mean swirling velocity $W_s(x)$ to the minimum mean axial velocity $U_{min}(x)$ such as:

$$S(x) = \frac{W_s(x)}{U_{min}(x)}. \tag{4.3.2}$$

Note that unlike $\hat{S}$, $S(x)$ depends on the streamwise location and can have negative values close enough from the object if a recirculation region is observed. From equation

(4.3.2) $S(x)$ can be computed at each streamwise location in the wake of the porous discs. Lee et al. (2020)'s experimental study calculated the swirl number, using ADV[2] measurements in the wake of a hydrokinetic turbine at different TSR. Dufresne (2013) measured the three components of velocity in the wake of a wind turbine using HWA but did not evaluate the evolution of the swirl number. However, S can be calculated from the available data.

Figure 4.8 shows the velocity-based swirl numbers $S(x)$ for cases $\alpha = 15°$ and $\alpha = 25°$ at different streamwise locations along with reference data points taken from the literature. In terms of order of magnitude, the porous disc with pitched blades generates levels of swirl comparable with those reported for lab-scale rotating turbines. The $\alpha = 15°$ case seems to follow the trend of the $TSR = 7$ case of Lee et al. (2020) fairly well, while the $\alpha = 25°$ matches the trend of the $TSR = 5$ case quite well. These results prove the effectiveness of our approach to produce swirl levels consistent with those observed in operational rotating turbines. In addition to the advantages underscored in chapter 3 (§3.1), this novel porous disc appears to be an inexpensive surrogate for rotating turbines, now incorporating the crucial element of swirl.

In the following, the topology of the swirling velocity is examined in the wake of the porous discs.

4.3.3 Distribution of swirl in the wake of the porous discs

The influence of the pitch angle α on the swirling motion is emphasised in figure 4.9 which shows normalised mean swirling velocity W/U_∞ fields at three key streamwise locations $X = 2D$, $X = 4D$ and $X = 6D$. For the porous disc with non-pitched blades ($\alpha = 0°$), the swirling motion is marginal aside from a small area where the wake of the disc merges with the mast's wake (figures 4.9a and 4.9b). This is probably due to 3D effects in this wake interaction region. The observed absence of swirl confirms that the porous disc is properly aligned with the direction normal to the incoming flow.

On the other hand, the swirling motion can be observed in the wake of the cases with pitched blades (figures 4.9c to 4.9h). At $X = 2D$, the swirl is mostly located within the disc boundaries independently of the pitch angle (figures 4.9c and 4.9f). Further downstream, the swirling wake expands outside the disc surface and its intensity decreases, following the conservation of angular momentum (equation 4.1.4). The $\alpha = 25°$ case (figures 4.9f-4.9h) generates about 3-4% more swirl than the $\alpha = 15°$ case. However, both cases show the same swirling velocity distribution and evolution in the streamwise direction. Swirl is shown to have a toroidal distribution around the centre of the porous disc at every streamwise location. The earlier observations of swirl decay and outwards spread with the streamwise direction are confirmed. The magnitude of swirl is higher closer to the porous disc, reaching 13% at $X = 2D$, and quickly decays to 2% at $X = 7D$.

There is a mild symmetry-breaking effect caused by the mast which is prominent in the near field but less visible as the streamwise direction increases. This is due to the tower shadow effect discussed in the work of Powles (1983), where the wake of the mast interacts with the rotor wake. In order to quantify the effect of the mast on the swirling motion, the azimuthally averaged fields for the $\alpha = 15°$ case are plotted in figure 4.10. The azimuthally averaged swirling velocity fields are defined as:

[2]Acoustic Doppler Velocimetry.

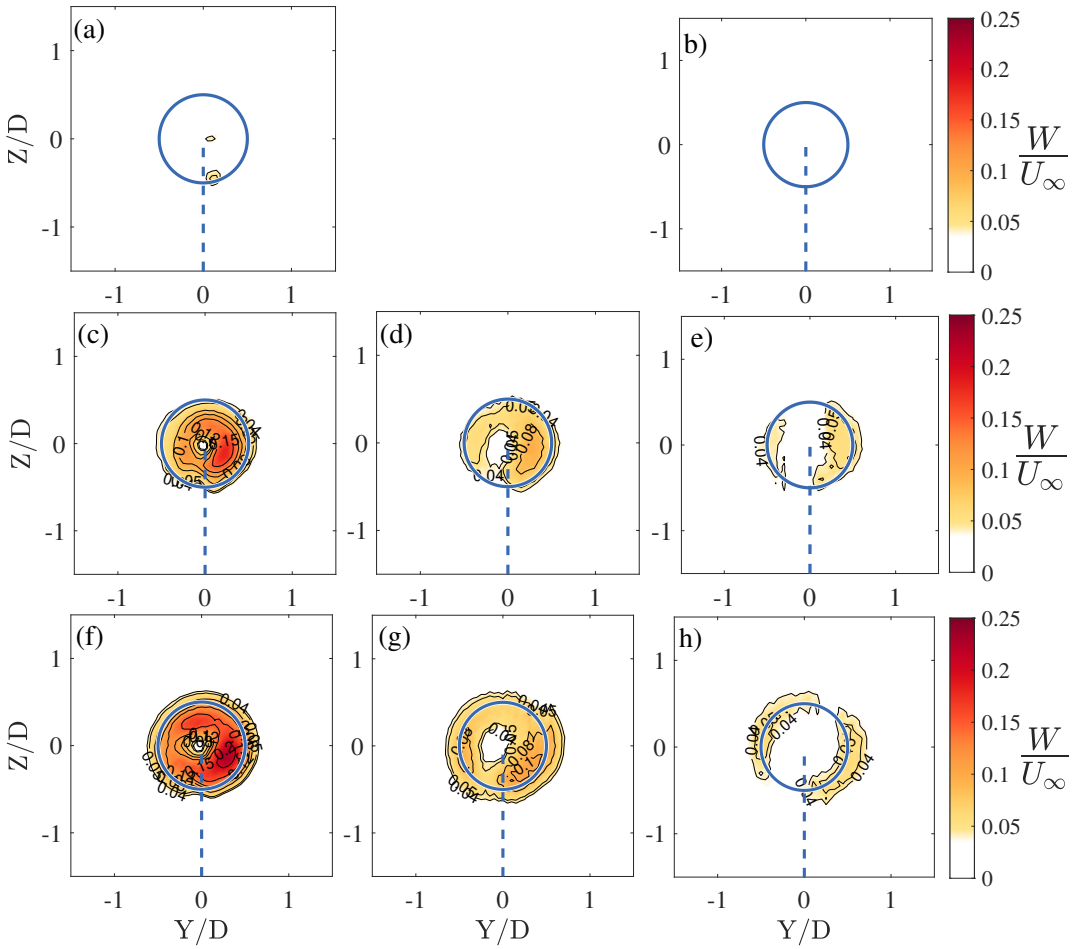

Figure 4.9: Normalised swirling velocity W/U_∞ 3CHWA cross-sectional maps for the (a, b) $\alpha = 0°$ case , (c, d, e) the $\alpha = 15°$ case and (f, g, h) the $\alpha = 25°$ case evaluated at $X = 2D$ (left), $X = 4D$ (middle) and at $X = 6D$ (right). Solid blue line: contour of the porous disc, dashed blue line: cylindrical mast.

$$\widehat{W}(x,r) = \frac{1}{2\pi}\int_0^{2\pi} W(x,r,\phi)d\phi. \tag{4.3.3}$$

The difference between the two fields defined as $\Delta_W(x,r,\phi) = ||W(x,r,\phi) - \widehat{W}(x,r)||$, directly quantifies the defect of axisymmetry of the swirling motion in the wake of the porous disc. The results show that the effect of the mast is weak. $||\Delta_W||/U_\infty$ reaches values of 2.5% near the mast, which are order of magnitude below the values of W. Therefore, the axisymmetric hypothesis for the swirling motion appears as a fair approximation even in the near wake.

As discussed in chapter 2, swirl is essentially balanced by a radial pressure gradient and is absent in the far wake approximation of streamwise momentum conservation. It is thus argued that swirl has a significant effect on the distribution of pressure in the wake of the porous discs. In the following, pressure is therefore reconstructed from the velocity measurements and a streamwise momentum budget is performed.

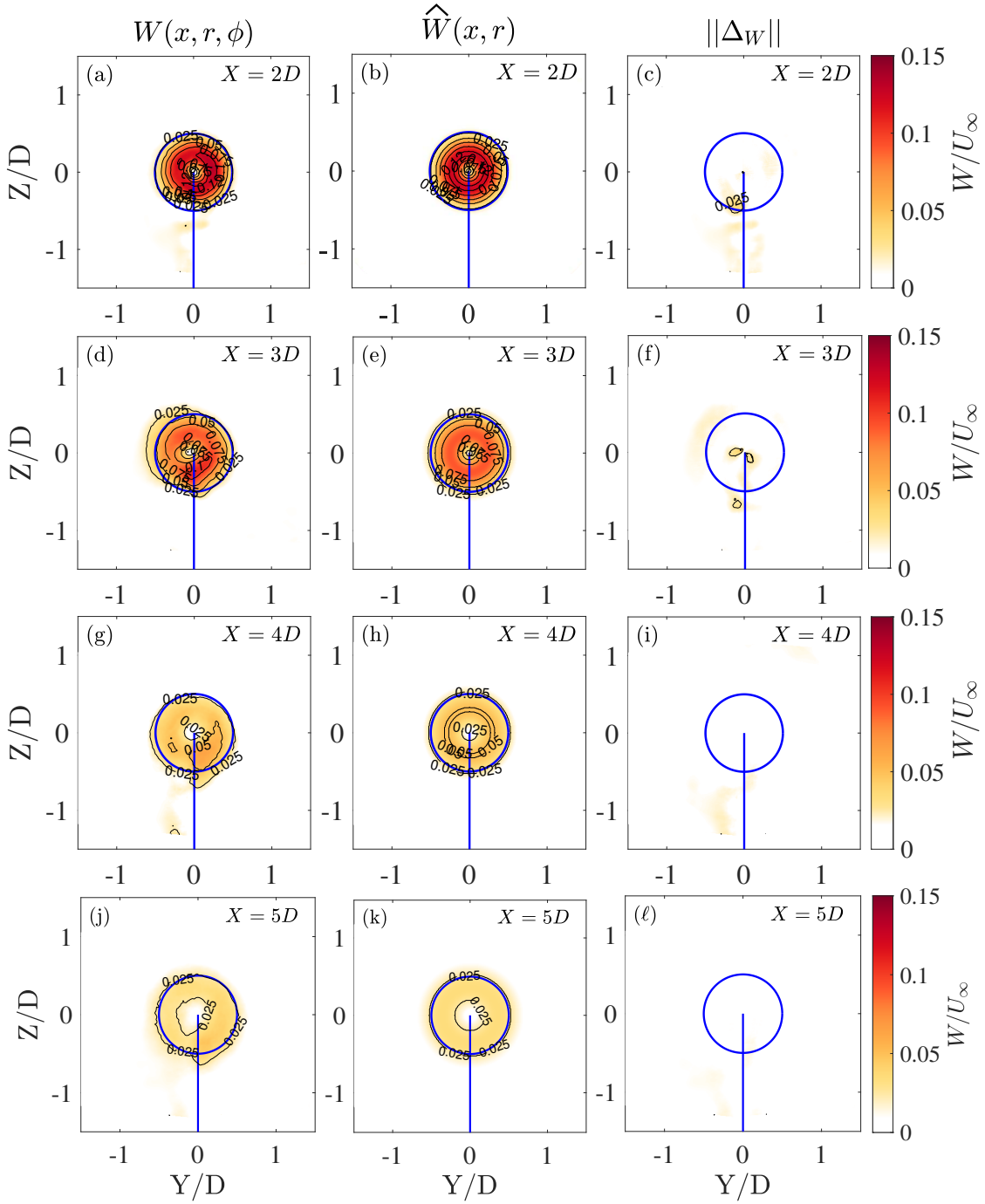

Figure 4.10: Cross-sectional maps showing the effect of the azimuthal averaging of the swirling velocity components for the $\alpha = 15°$ case. Different downstream locations are shown from $X = 2D$ to $X = 5D$ of the raw data $W(x,r,\phi)$ (left), the azimuthally averaged fields $\widehat{W}(x,r)$ (middle) and the difference $||\Delta_W||$. Solid blue line: contour of the porous disc and mast outline.

4.4 Pressure distribution on the swirling wake and mean momentum budget

4.4.1 Swirl: a pressure distributing term

The pressure reconstruction is carried out with a Poisson approach in cartesian coordinates in $Y-Z$ planes and neglecting viscosity. This method is detailed in the work of Shanmughan et al. (2020) and briefly summarised in the following. If a given x plane is considered, the horizontal and vertical RANS equations can give an expression for the in-plane mean pressure gradients such as:

$$\frac{\partial P}{\partial y} = -\rho(\underbrace{U_y\frac{\partial U_y}{\partial y} + U_z\frac{\partial U_y}{\partial z}}_{\text{Swirl}} + \underbrace{\frac{\partial \overline{u_y^2}}{\partial y} + \frac{\partial \overline{u_y u_z}}{\partial z}}_{\text{Turbulence}}), \tag{4.4.1}$$

and

$$\frac{\partial P}{\partial z} = -\rho(\underbrace{U_y\frac{\partial U_z}{\partial y} + U_z\frac{\partial U_z}{\partial z}}_{\text{Swirl}} + \underbrace{\frac{\partial \overline{u_y u_z}}{\partial y} + \frac{\partial \overline{u_z^2}}{\partial z}}_{\text{Turbulence}}), \tag{4.4.2}$$

where the out of plane gradients $\partial/\partial x$ are neglected following the thin shear layer approximation. There is a clear contribution coming from two sources: the mean flow gradients and the Reynolds stress gradients. The mean flow gradients are the terms which are expected to be modified by the additional swirl W. From the in-plane pressure gradients (4.4.1) and (4.4.2), the pressure coefficient $C_P(y,z)$ can be computed using a least squares surface reconstruction method as proposed by Harker and O'Leary (2008). The distribution of the scalar fields used to reconstruct pressure are shown in figure 4.11 at $X = 2D$, emphasising the effect of swirl.

As expected, the swirling motion induced by pitch increases the magnitude of the mean vertical and horizontal velocity. The $\alpha = 0°$ case generates very weak amounts of horizontal velocity (figure 4.11a), as only sparse patches can be found in the near field and around the edges of the test rig, as a result of 3D effects. In contrast, the $\alpha = 15°$ and $\alpha = 25°$ cases exhibit higher values of horizontal velocities in the top and bottom part of the wake because of the generated swirling motion. The horizontal velocity is similar for both cases and reaches 12-13% of U_∞ at $X = 2D$ (figures 4.11b and 4.11c). The mean vertical velocity shows symmetrical conclusions for the cases with swirl (figures 4.11e and 4.11f). However, this velocity component highlights the effect of the mast on the wake of the porous discs, regardless of swirl. For all cases, there is a lingering patch of low vertical velocity where the mast is located (figures 4.11 d,e,f). This downwards motion suggests that the wake of the cylindrical mast generates a downwash motion which will affect the near wake of the porous discs. This was already evidenced in the seminal round robin porous disc test reported in Aubrun et al. (2019) as a possible scenario depending on the test rig and experimental set-up (Pierella and Sætran, 2017). In our case however, the generated swirling velocity intensities are an order of magnitude larger than those induced by the downwash. Therefore, the in-plane mean flow gradients will be dominated by swirl, overcoming the downwash effect caused by the mast. The Reynolds normal stress terms $\overline{u_y^2}$ and $\overline{u_z^2}$

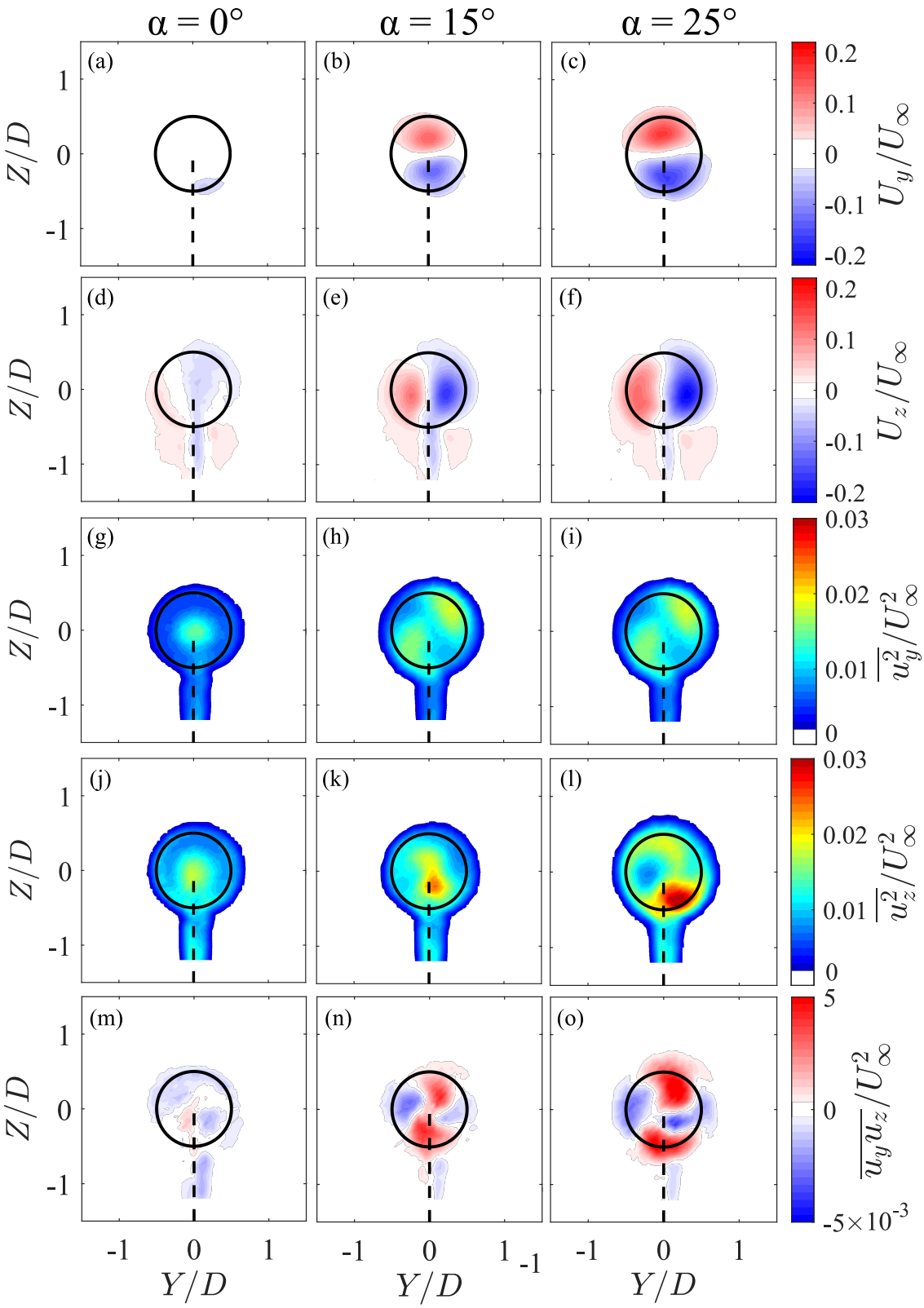

Figure 4.11: Maps for $\alpha = [0°, 15, 25°]$ at $X = 2D$ of the main scalars used in the pressure reconstruction algorithm showing (a,b,c) the mean horizontal velocity U_y, (d,e,f) the mean vertical velocity U_z, (g,h,i) the horizontal $\overline{u_y^2}$ and (j,k,l) vertical $\overline{u_z^2}$ Reynolds normal stress terms and (m,n,o) the $\overline{u_y u_z}$ in-plane Reynolds shear stress term, normalised using U_∞.

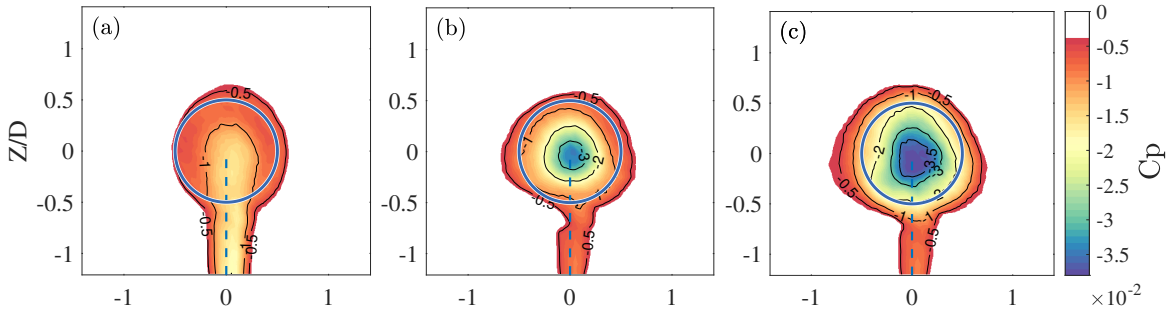

Figure 4.12: Reconstructed pressure coefficient C_P for (a) the $\alpha = 0°$ case, (b) the $\alpha = 15°$ case and for (c) the $\alpha = 25°$ case evaluated at $X = 2D$. Solid blue line: porous disc edges, dashed blue line: mast outline.

show a mild increase with swirl and marginal differences in their distribution (figures 4.11g-l). The Reynolds shear stress $\overline{u_y u_z}$ (figures 4.11 m,n,o) is increased by swirl by a factor 5 but remains an order of magnitude below the normal stress terms. Altogether, these results indicate that swirl will have an effect on the pressure distribution on the wake. The reconstructed pressure coefficient is reported in figure 4.12 at $X = 2D$ for cases $\alpha = 0°$, $\alpha = 15°$ and $\alpha = 25°$.

For the reference case (figures 4.12a) the low pressure area is mostly located around the mast where downwash is present and reaches values of $C_P = -1.5 \times 10^{-2}$. As expected, the introduction of a swirling motion (figures 4.12b and 4.12c) results in a decrease of C_P and in a spatial redistribution of the pressure coefficient in the wake. For both cases $\alpha = 15°$ and $\alpha = 25°$ (figures 4.12b and 4.12c) the lowest pressure area is now located at the centre of the porous disc's wake, near $(Y, Z) = (0, 0)$. The reconstructed pressure coefficient at the centre of the wake is $C_P = -3.46 \times 10^{-2}$ and $C_P = -3.87 \times 10^{-2}$ for cases $\alpha = 15°$ and $\alpha = 25°$, respectively, which represents a 12% difference between cases. This mild difference is explained by the increased blockage for case $\alpha = 25°$ due to stall. These values are comparable with those reported for rotating models and porous discs (Aubrun, 2013). These results prove that swirl governs the distribution of pressure in the wake of the porous discs and stabilises the flow. In contrast, the distribution of pressure in a non-swirling wake is particularly sensitive to asymmetries in the experimental apparatus such as the design of the porous disc itself and its implementation in the wind tunnel.

4.4.2 Mean momentum budget

As shown in section §4.2 the drag coefficient stays roughly constant with respect to α in the attached flow regime. Drag is driven by different terms coming mainly from the velocity deficit, swirl and turbulence (equation 4.1.1). To evaluate if the far wake approximation (4.1.3) is valid in our case, a momentum budget is prescribed. The terms in equation (4.1.1) can be individually computed and compared to the total drag. The streamwise momentum budget in dimensionless form can be rewritten as a sum of its parts such as:

$$C_D = C_D^{\Delta U} + C_D^{anis} + C_D^{swirl} \tag{4.4.3}$$

with

$$C_D^{\Delta U} = 16 \int_0^\infty [U^* \Delta U^*] r^* dr^* \tag{4.4.4}$$

$$C_D^{anis} = 16 \int_0^\infty \left[\frac{\overline{w^2}^* + \overline{v^2}^*}{2} - \overline{u^2}^* \right] r^* dr^* \tag{4.4.5}$$

$$C_D^{swirl} = 16 \int_0^\infty \left[\frac{W^{*2}}{2} \right] r^* dr^* \tag{4.4.6}$$

where the drag coefficient C_D is decomposed to emphasise the contributions of the velocity deficit $C_D^{\Delta U}$, turbulence anisotropy C_D^{anis} and mean swirl C_D^{swirl}, respectively.

Figure 4.13 shows the momentum budget result at three streamwise positions in percentage of C_D. For all cases the leading order term is by far the velocity deficit $C_D^{\Delta U}$ term. Aside from the $X = 2D$ position for case $\alpha = 25°$ where $C_D^{swirl} = 7\%$ of C_D, the anisotropy and swirl contributions to drag are marginal. This result points out that swirl has not significantly altered the momentum budget, especially beyond $X = 4D$. In other words, the first order expression for the streamwise momentum conservation law, i.e $C_D \sim \int U_\infty^* \Delta U^*$, can be used for both swirling and non-swirling wakes at the examined streamwise locations. In the very near wake ($0D < X \leq 2D$), the contribution of swirl to drag might be significant but given its rapid decay, it quickly becomes negligible with respect $C_D^{\Delta U}$. Moreover, the very near wake region of the wake is difficult to measure experimentally (with strong dynamics and 3D effects) and is not explored in this thesis.

In any case, the momentum budget proves that the swirling and the non-swirling wake are asymptotically identical; at least in terms of mean drag. The same result was found between swirling and non-swirling jets in the work of Shiri (2010). However, swirl plays an important role on the way pressure is distributed across the wake. The distribution of pressure dictates the topology of the mean wake and thus the shape of the velocity profiles. In the following section, the effect of swirl on the wake topology is therefore examined in detail.

4.5 Influence of swirl on the topology of the wake

4.5.1 Wake topology modifications

The mean streamwise velocity fields for cases $\alpha = [0°, 15°, 25°]$ on the streamwise ($Y = 0$) plane and spanwise planes at $X = 2D$ and $X = 6D$ are reported in figures 4.14 and 4.15, respectively. For all the cases, the position of the mean wake centre, assimilated to the location the minimum streamwise velocity, is plotted with dotted black lines or plus (+) markers. The reference case shown in figures 4.14a, 4.15a and 4.15d, exhibits a recirculation region in the very near wake ($X \leq 1D$), which is likely caused by the central solid disc at hub-height of each surrogate (see figure 3.1 in chapter 3: §3.1.1). The presence of the porous disc yields a velocity deficit area which is confined within the disc region until $X = 8D$. The cylindrical mast produces its own wake visible until around $X = 2D$ in figure 4.14 but with a lingering effect until further downstream in figure 4.15. More interestingly, the wake centre is deviated downwards

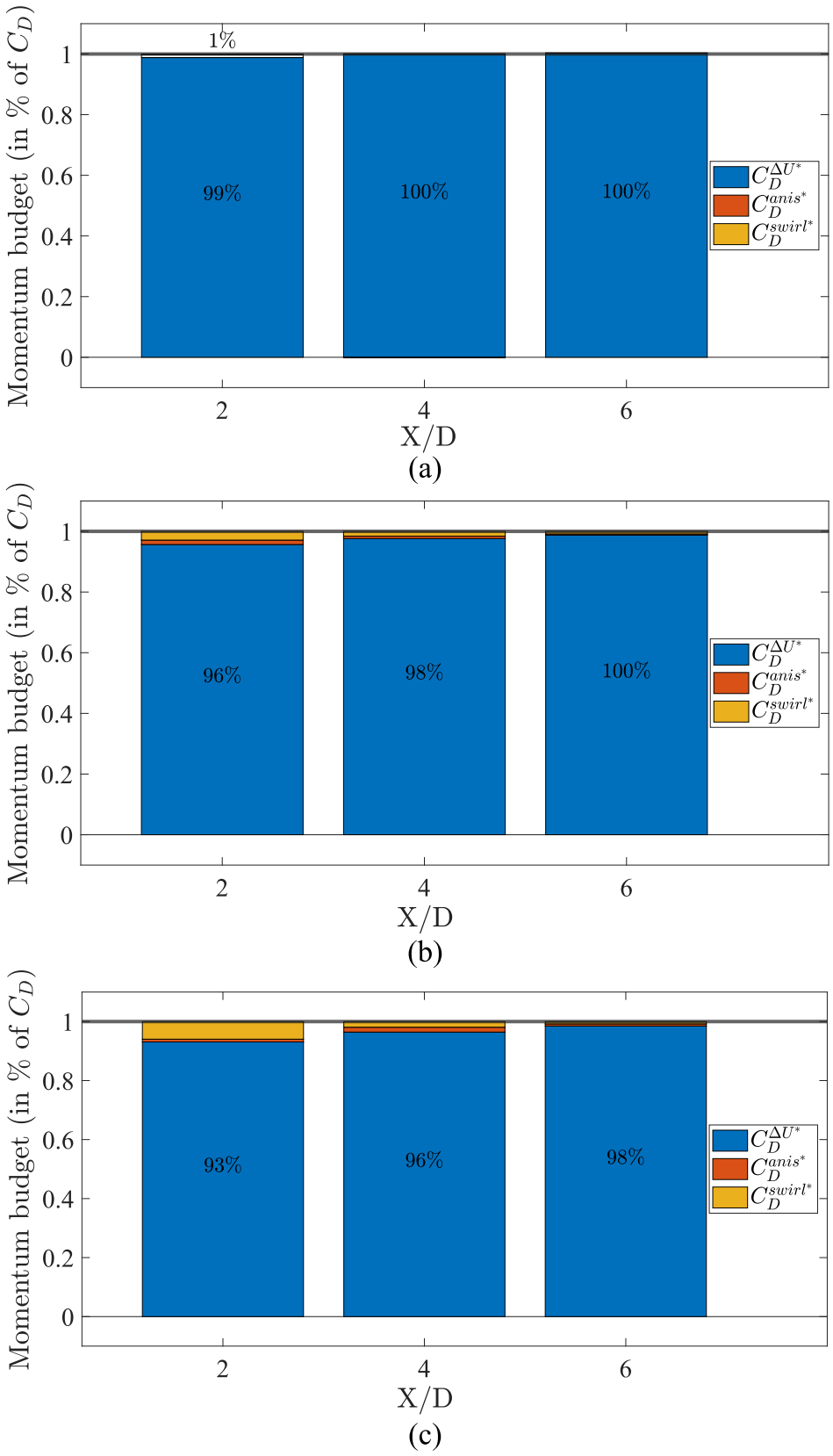

Figure 4.13: Normalised streamwise momentum budget for (a) the $\alpha = 0°$ case (b) the $\alpha = 15°$ case and (c) the $\alpha = 25°$ case at different streamwise locations.

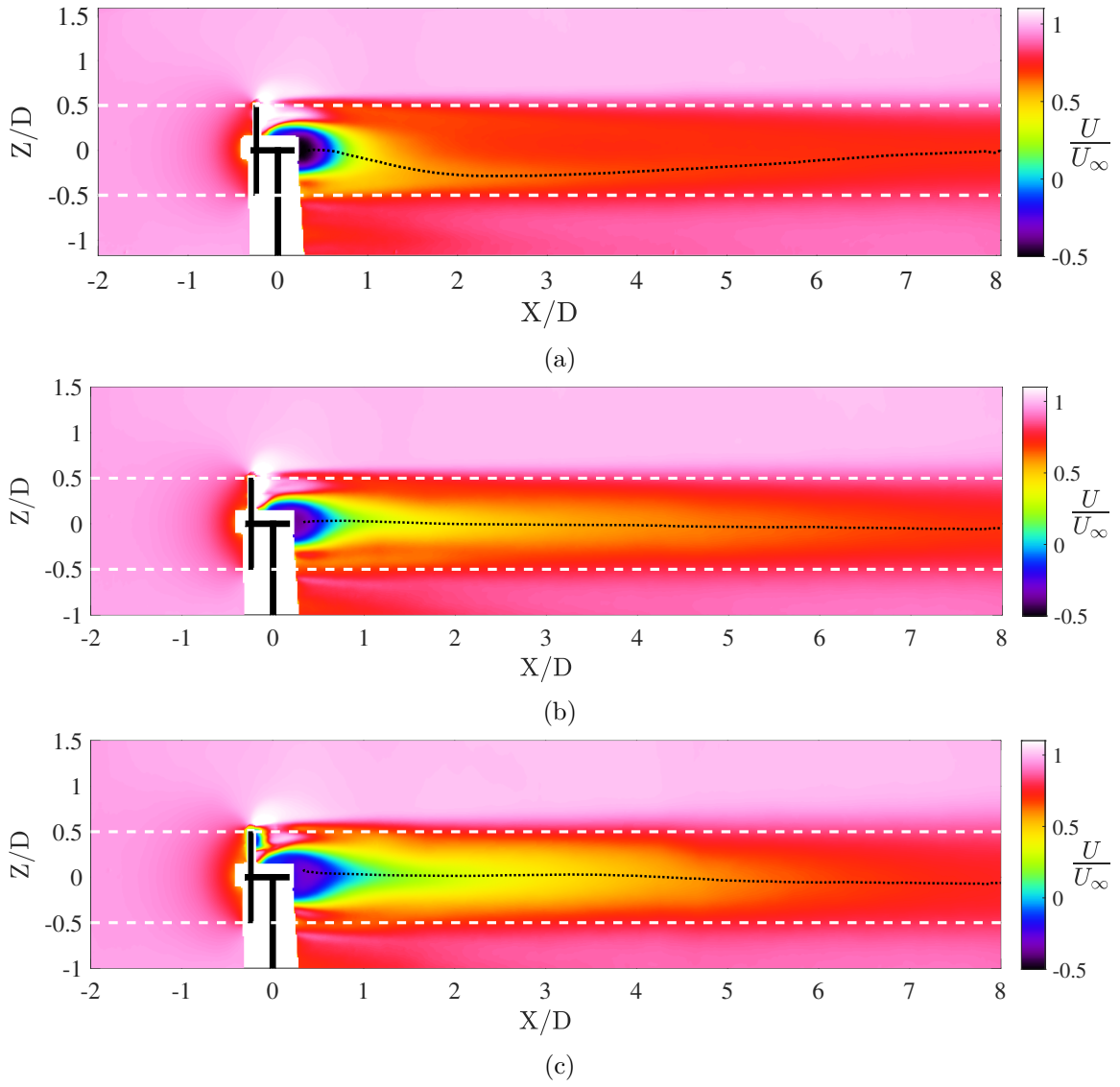

Figure 4.14: Normalised streamwise velocity $\overline{U}/U_\infty$ fields for the (a) $\alpha = 0°$ case, (b) the $\alpha = 15°$ case and for (c) the $\alpha = 25°$ case. The white area near $X = 0D$ is the masked zone where the test rig (black patched area) is located. Dashed white lines: edges of the porous disc, black dotted lines: coordinates of the wake centre.

until $X = 2D$, where it reaches a minimum height $Z/D = -0.3$, and then recovers towards hub-height further downwind ($X = 7D$). This downwash motion is caused by the previously evidenced lower pressure area in the turbulent wake of the mast. As the wake evolves downwind, the influence of the mast on the pressure distribution gradually diminishes, which explains the progressive recovery of the wake centre.

On the other hand, the introduction of a swirling motion has a very strong effect on the initial conditions of the generated wakes. The swirling wakes, have a larger velocity defect in the near wake ($X = [1.5D - 5D]$) compared to the non-swirling wake. This is even more pronounced with the case of stalled blades observed for $\alpha = 25°$. Further downstream, the differences between the non-swirling wake and the swirling wake vanishes. As mentioned in section §4.4.1, swirl creates a low pressure core at $Y = Z = 0$. By doing so, pressure stabilises the wake and resists to the downwash effect observed for the non-swirling wake (figure 4.14a). This is further evidenced by

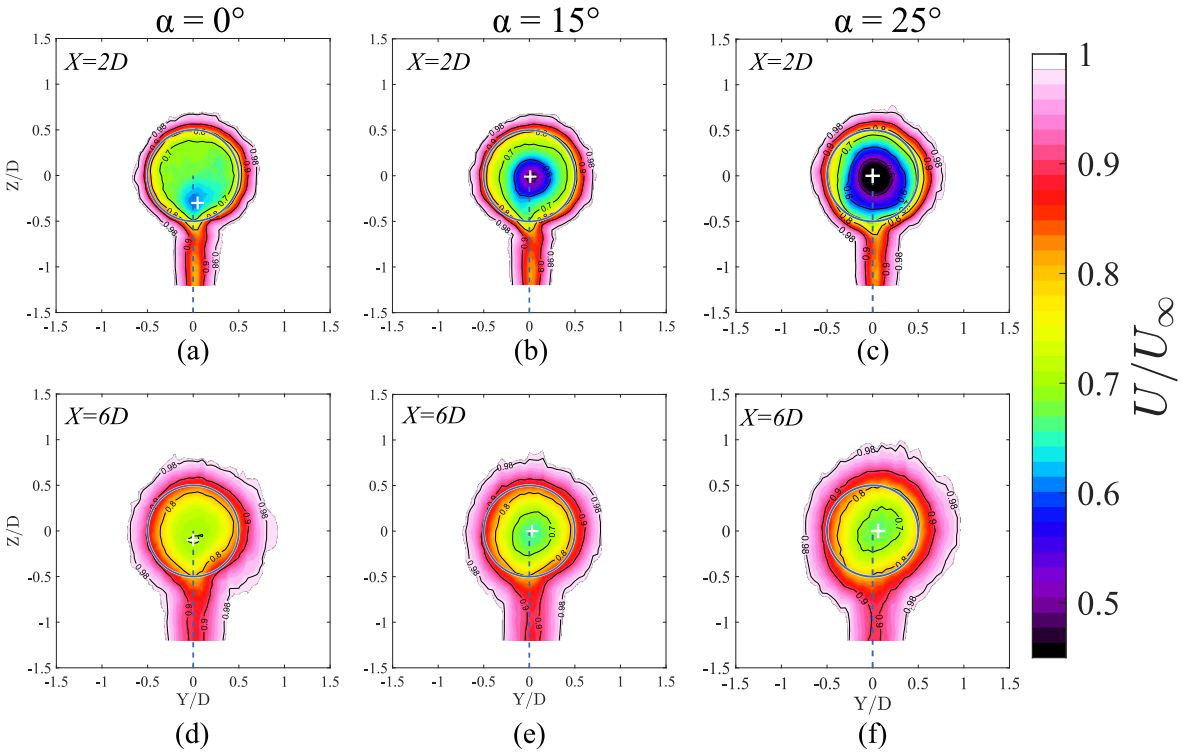

Figure 4.15: Normalised streamwise velocity $\overline{U}/U_\infty$ spanwise planes for the $\alpha = 0°$ case (left), the $\alpha = 15°$ case (middle) and for the $\alpha = 25°$ case (right) evaluated at $X = 2D$ (a,b,c) and at $X = 6D$ (d,e,f). Solid blue line: porous disc edges, dashed blue line: mast outline, white plus marker: wake centre.

the mean vertical velocity plots reported in figure 4.16. For all cases, as flow approaches the test rig, the positive and negative regions of U_z/U_∞, from either side of the hub-height, highlight the blockage effect of the porous disc. In this so-called induction zone (Jensen, 1983), there is no noticeable difference in U_z/U_∞ between cases $\alpha = 0°$ and $\alpha = 15°$, since the blockage (or equivalently the apparent porosity) remains unchanged in the attached flow regime. On the other hand, the stalled blades for case $\alpha = 25°$ (figure 4.16c) increase the effective blockage and thus decrease the bleed air of the porous disc (Castro, 1971; Steiros and Hultmark, 2018). Case $\alpha = 0°$ shows a clear downward motion of the mean wake at hub-height ($Z = 0D$) going from $X = 1D$ up to $X = 4D$. This negative vertical velocity patch highlights the evidenced downwash caused by the mast and changing the topology of the non-swirling wake. For cases $\alpha = 15°$ and $\alpha = 25°$, this region of downward velocity is completely absent confirming that downwash is mitigated by swirl. A direct consequence of the downwash observed for $\alpha = 0°$ is the failure of wake axisymmetry, unlike what is found for swirling wakes.

To quantify the downwash resistance effect of swirl, the vertical coordinates of the mean wake centre $\overline{Z_c}(x)/D$ are plotted in figure 4.17 for cases $\alpha = 0°$, $\alpha = 15°$ and $\alpha = 25°$. Streamwise planes allow to plot more points but are restricted to $Y = 0$ thus giving 2D information. However, as shown in figure 4.15, the centre of the mean wake stays fairly centred in the spanwise direction for all cases, except for a marginal deviation for case $\alpha = 25°$ at $X = 6D$. As presented in figure figure 4.17, for the $\alpha = 0°$ case, $\overline{Z_c}(x)/D$ quickly drops to a minimum of $-0.3D$ attained between $X = 2D$ and $X = 3D$ due to the strong downwash in the near wake. The streamwise slope of the wake centre downwash corresponds to an $-8.8°$ incline. After reaching a maximum downwash, the wake centre slowly recovers towards hub-height, i.e $Z = 0D$, and shows a slope of 3.1°.

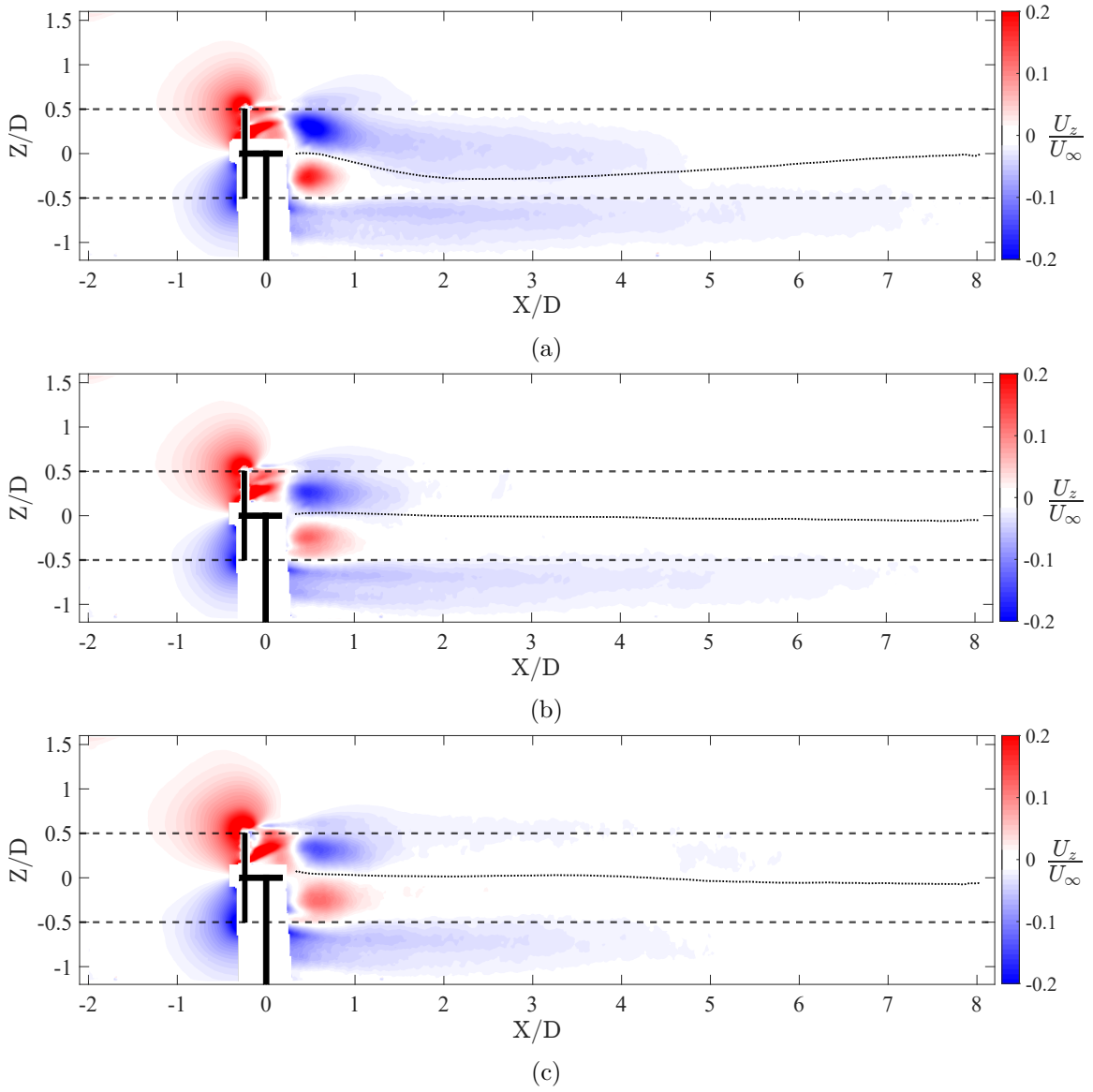

Figure 4.16: Mean vertical velocity U_z fields normalised by the free-stream velocity U_∞ for the (a) $\alpha = 0°$ case, (b) the $\alpha = 15°$ case and for (c) the $\alpha = 25°$ case. Dashed black lines: edges of the porous disc, black dotted lines: wake centre.

On the other hand, cases $\alpha = 15°$ and $\alpha = 25°$ have a completely different trend. As evidenced earlier, the downwash effect of the mast is not suppressed by swirl but rather counterbalanced by the strong effect of swirl which resists the downwash. Therefore, a weak downwash is still present for the swirling wakes. The wake centre $\overline{Z_c}(x)/D$ shows a light slope of $-0.7°$ for both cases which remains fairly constant all along the streamwise direction.

Figure 4.17 examined how swirl mitigated the downwash effect on the mean wake. To prove if such downwash resistance extends to the dynamics of the wake, a statistical analysis of $Z_c(x,t)$ at different streamwise positions for cases $\alpha = [0, 15, 25]°$ is reported in figure 4.18. The distribution of $Z_c(x,t)$ in the induction region $(X/D = -1)$ is identical for all cases, even for stalled blades. For case $\alpha = 0°$ (figure 4.18a), the distribution of $Z_c(x,t)$ shows signs of downwash as the probability distribution function (PDF) is skewed towards negative values of Z. Further downstream, the wake centre distribution gradually recovers the hub-height position, following the same trend as

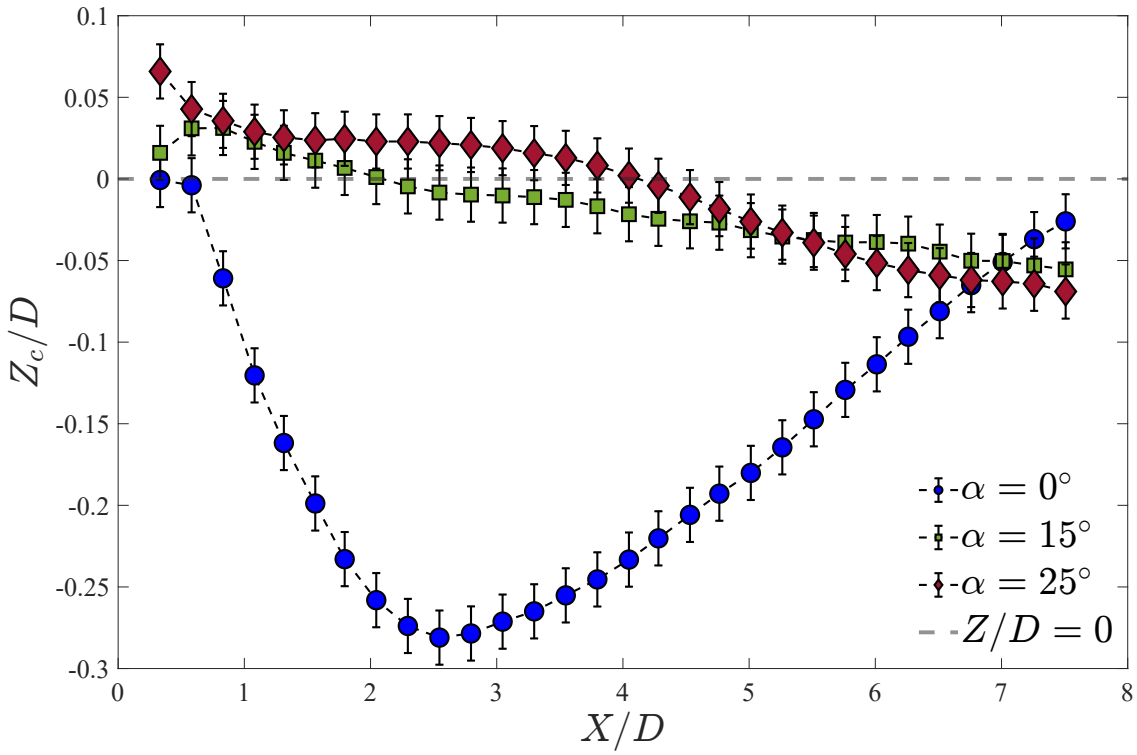

Figure 4.17: Streamwise evolution of the mean wake centre vertical coordinate $\overline{Z_c}(x)/D$ for $\alpha = [0°, 15°, 25°]$. Only 1/15 of the markers are plotted for visibility. The error-bars are the PIV spatial resolution (chapter 3 §3.5.3).

the mean wake. In contrast, for cases $\alpha = 15°$ and $\alpha = 25°$ (figures 4.18b and 4.18c), the distribution of $Z_c(x,t)$ is centred at all streamwise positions and no skewness is detected. Furthermore, the distributions for the swirling wakes show Gaussian characteristics even close to the rest rig ($X = 1D$) with tighter distributions than their non-swirling counterpart. This further proves the stabilising effect of swirl which keeps the wake centred and counterbalances the downwash effect.

To further confirm the downwash resistance of swirl and extend the analysis to the three-dimensional wake, the spanwise plane wake centre statistics for cases $\alpha = 0°$ and $\alpha = 15°$ are emphasised in figure 4.19. The $X = 3D$ spanwise plane is chosen as an example since it is the streamwise location at which downwash is most prominent. As shown in figure 4.19 swirl completely counterbalances the downwash effect suffered by the non-swirling wake. Moreover, the wake centre spanwise distribution for $\alpha = 15°$ has a more pronounced peak at the centre of the wake than the non-swirling case. This indicates that the low pressure core at the centre of wake caused by swirl, forces the wake centre to remain steadily centred. In contrast, the non-swirling wake centre has a broader distribution around its donwnwashed position. Altogether, these results prove that swirl stabilises the wake of the porous disc and keeps it fairly centred throughout its streamwise evolution.

The effect of swirl on the topology of the streamwise velocity component has been fully characterised in this section. However, swirl also has an impact on the generated turbulence since it generates an additional motion. In the following, the turbulence intensity of the swirling wakes is examined.

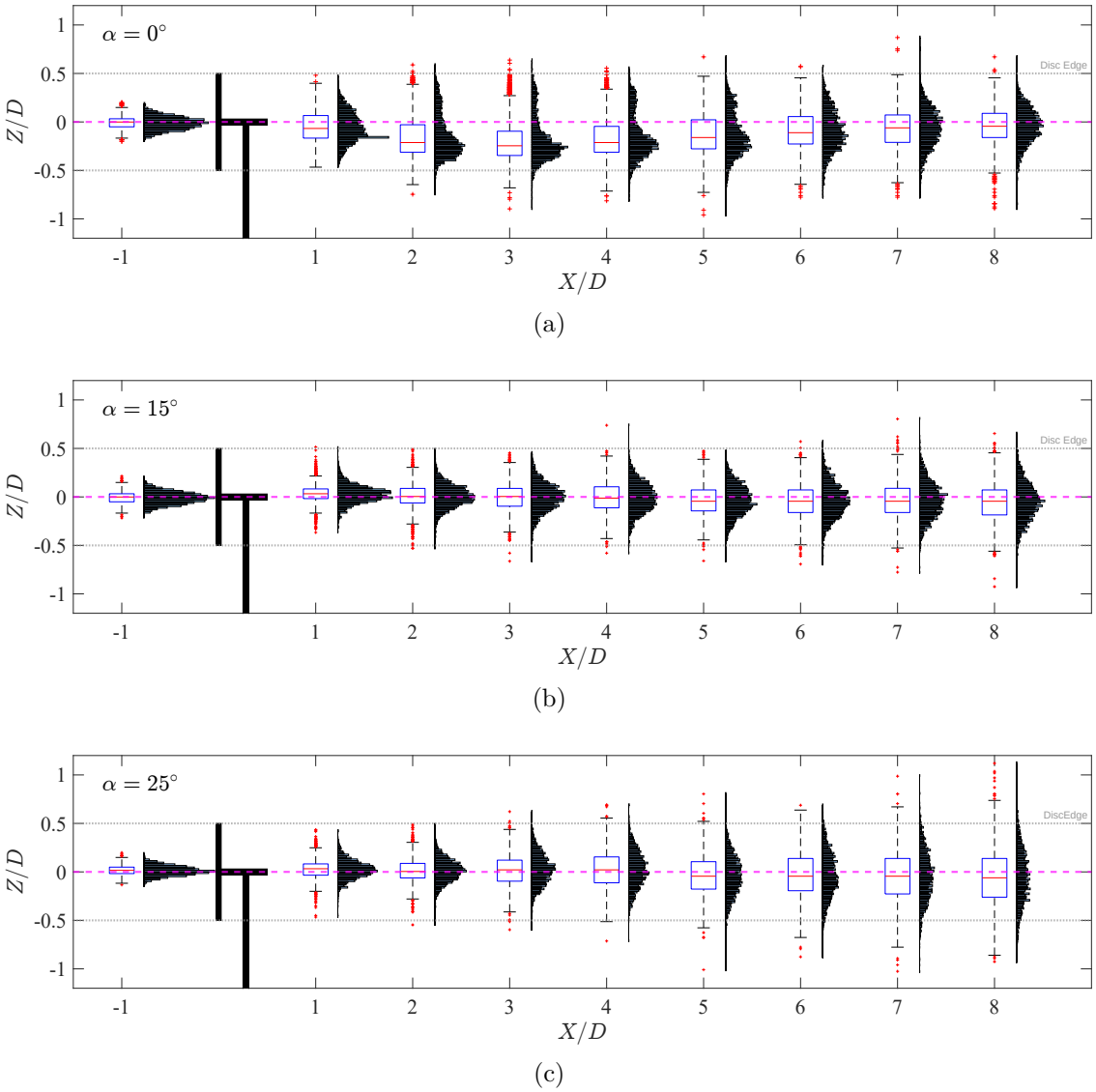

Figure 4.18: Statistics of the wake centre's vertical coordinate $Z_c(x,t)$ at different streamwise positions for case (a) $\alpha = 0°$, (b) $\alpha = 15°$ and (c) $\alpha = 25°$. Box-plots and normalised probability distribution histograms of $Z_c(x,t)$ are shown at each streamwise location. Black patched area: test rig, dashed magenta line: hub-height ($Z/D = 0$) iso-line, dotted grey lines: porous disc edges.

4.5.2 Effect of swirl on the turbulence intensity

Turbulence intensity is a fundamental part of the topology of a flow. Initial conditions change how turbulence is produced and distributed. Therefore, turbulence intensity is characterised in this section by evaluation the RMS velocity. In the streamwise plane ($Y = 0$) the vertical velocity corresponds to the radial velocity and their notations will be used interchangeably. The streamwise velocity $\sqrt{\overline{u^2}}/U_\infty$ and radial RMS velocity fields $\sqrt{\overline{v^2}}/U_\infty$ are reported in figures 4.20 and 4.21, respectively. For the $\alpha = 0°$ case (figure 4.20a), the streamwise RMS velocity shows a typical two-peak distribution for the wake of a porous bluff body immersed in a uniform flow (Aubrun (2013)). After $X = 3D$, two peaks are distinguished near the edges of the porous disc where the shear layers are located. For an axisymmetric bluff body these peaks would be symmetrical and have the same intensity. However, in this case the mast generates a high RMS

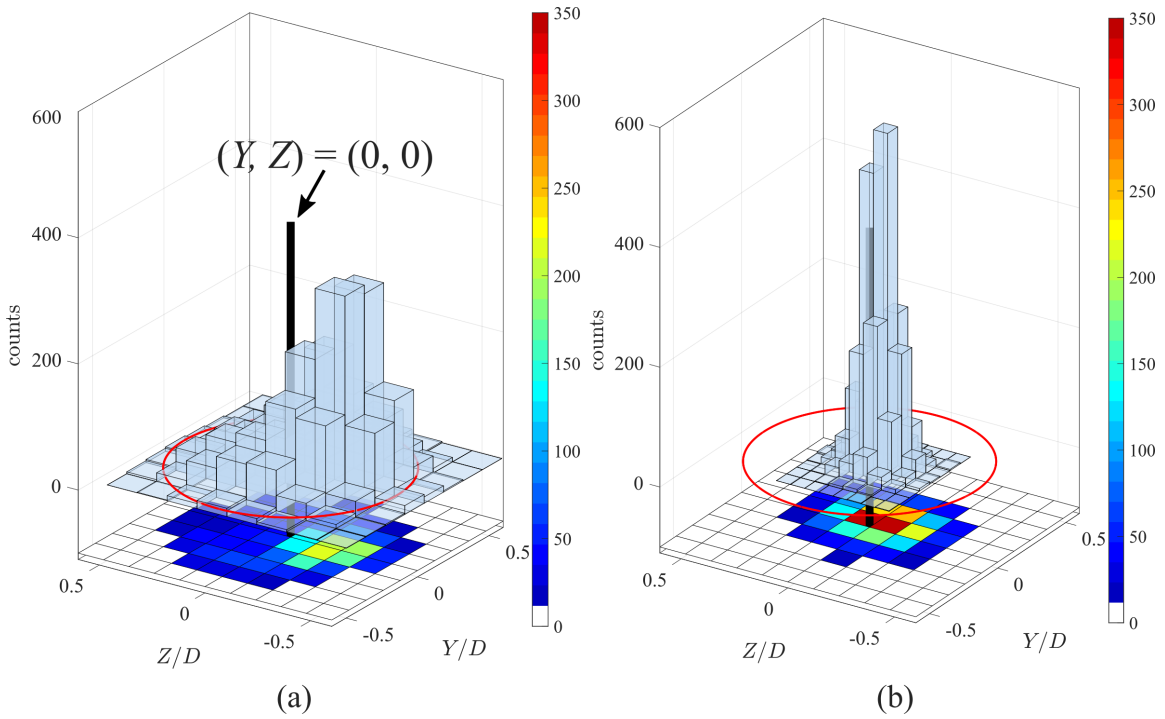

Figure 4.19: Wake centre spanwise plane statistics at $X = 3D$ for cases (a) $\alpha = 0°$ and (b) $\alpha = 15°$. Black line: $((Y, Z) = (0, 0))$ iso-line, red circle: porous disc outline

intensity zone near the test rig visible up until $X = 3D$ and with lingering values of around 4-5% up until $X = 8D$. The tower shadow effect consistently increases the intensity of the lower peak with respect to the top peak of around 1.7%. For the $\alpha = 15°$ case (figure 4.20b), the two-peak distribution is maintained and an overall intensity increase is observed. In particular, the intensity of the peaks have increased of around 1-2% as well as the thickness. More interestingly, the peaks are now symmetric with differences below 0.1% across the whole wake. Swirl's symmetrisation effect is not restricted to velocity deficit alone but extends to the turbulence quantities as well. For the $\alpha = 25°$ case (figure 4.20c), the sudden jump in effective blockage due to the stalled blades strongly increases the turbulence level in the wake of the porous disc. The intensity of $\sqrt{\overline{u^2}}/U_\infty$ increases of up to 4-5% with respect to the $\alpha = 15°$ case. However, the two-peak distribution is maintained despite the stalled blades and are also symmetric because swirl is still being generated with amplitudes similar to those reported for the $\alpha = 15°$ case. The vertical RMS velocity $\sqrt{\overline{v^2}}/U_\infty$ shows a similar range of values as $\sqrt{\overline{u^2}}/U_\infty$ going from 5% to 25% close to the test rig. As shown in figure 4.21a, case $\alpha = 0°$ shows a peculiar distribution for $\sqrt{\overline{v^2}}/U_\infty$ with a downwashed peak coinciding with the wake centre. On the other hand, case $\alpha = 15°$ (figure 4.21b) shows a more centred distribution of $\sqrt{\overline{v^2}}/U_\infty$ with an increased intensity of about 1-2%. Like with the streamwise RMS velocity, the stalled blades of case $\alpha = 25°$ generates a jump in the intensity of $\sqrt{\overline{v^2}}/U_\infty$ around 5-6% while remaining symmetric with respect to the hub height.

All in all, swirl moderately increases the overall turbulence level in the wake, especially when the pitch angle α exceeds the critical stall value. Most importantly, swirl enhances the symmetry in the distribution of turbulence inside the wake. This means that swirl gives back the important property of axisymmetry to the wake of the porous disc, an essential property of self-similarity which is addressed in the following.

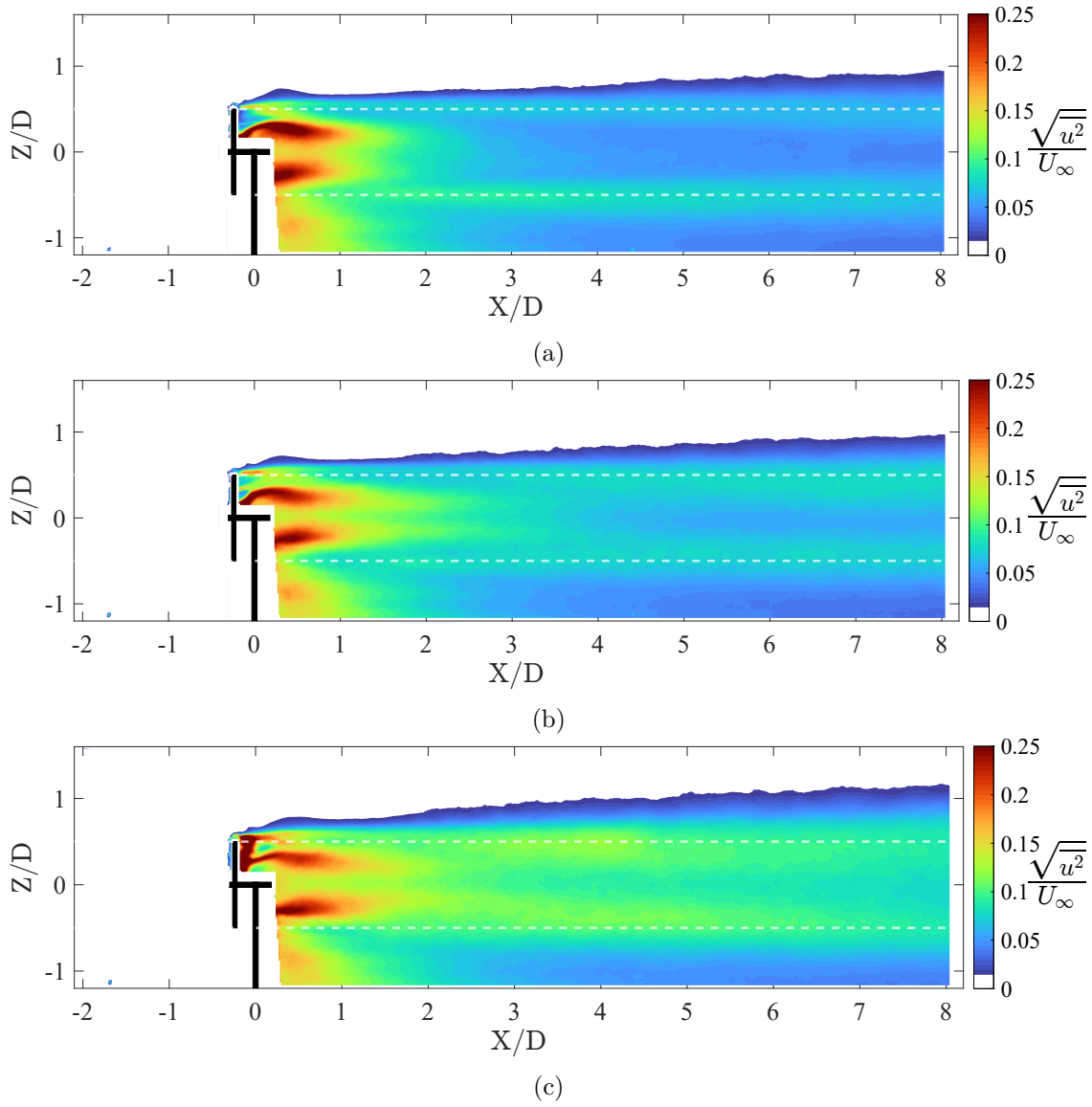

Figure 4.20: Streamwise RMS velocity $\sqrt{u^2}$ fields normalised by the free-stream velocity U_∞ for the (a) $\alpha = 0°$ case, (b) the $\alpha = 15°$ case and for (c) the $\alpha = 25°$ case. Dashed white lines: edges of the porous disc.

4.6 Similarity scalings of the swirling wake

4.6.1 Self-similarity of the wake properties

The characterisation of swirl and its effect on axisymmetry and drag being now established, the similarity properties of the mean flow can be explored. The reader is referred to chapter 2 (§2.3) for the complete similarity scaling laws derivations which are relevant to this section. In order to establish similarity, self-preserving solutions are considered for the wake properties, like the mean streamwise velocity which is recalled below:

$$U_\infty - U(x,r) \;=\; U_s(x) f(\eta), \tag{4.6.1}$$

where $\eta = r/\delta$ and $U_s(x) = U_\infty - U(r=0,x)$. In order to test for similarity, the mean

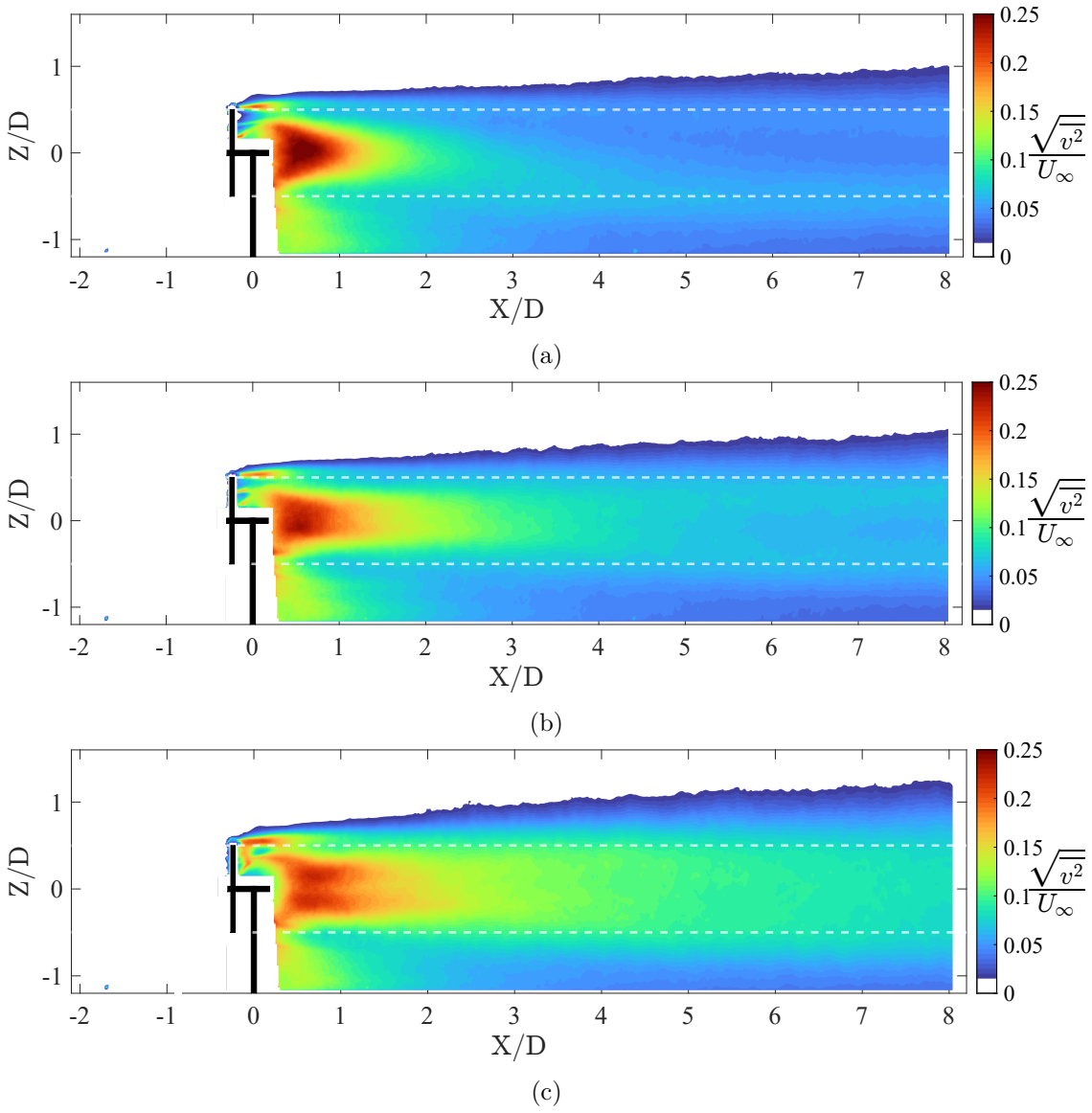

Figure 4.21: Vertical RMS velocity $\sqrt{\overline{v^2}}$ fields normalised by the free-stream velocity U_∞ for the (a) $\alpha = 0°$ case, (b) the $\alpha = 15°$ case and for (c) the $\alpha = 25°$ case. Dashed white lines: edges of the porous disc.

streamwise velocity deficit profiles (4.6.1) are reported in figure 4.22 using similarity scalings. The reference case (figure 4.22a), exhibits velocity profiles with a trilby hat shape up until $X/D = 6$ where the profiles only start to collapse towards a self-similar Gaussian shape. In contrast, the swirling wake streamwise velocity profiles (figures 4.22b and 4.22c) collapse and show self-similarity already at $X/D = 3$. Furthermore, the Gaussian profiles show good agreement with wind tunnel and numerical simulations reported in the literature for rotating wind turbines depicted as a shaded grey area in figure 4.22 (Bastankhah and Porté-Agel, 2014; Wu and Porté-Agel, 2012; Lignarolo et al., 2016a,b; Chamorro and Porté-Agel, 2010). This evidences that one of the main mechanisms governing self-similarity in the wakes of wind turbines is the swirling motion of the wake. Similarly to the case of a swirling jet shown in the work of Shiri et al. (2008), the mixing is enhanced and self-similarity is sped up by the swirling motion. Therefore, the proposed porous disc model better reproduces the physics in the near wake of a rotating wind turbine, in comparison to previous porous discs generating

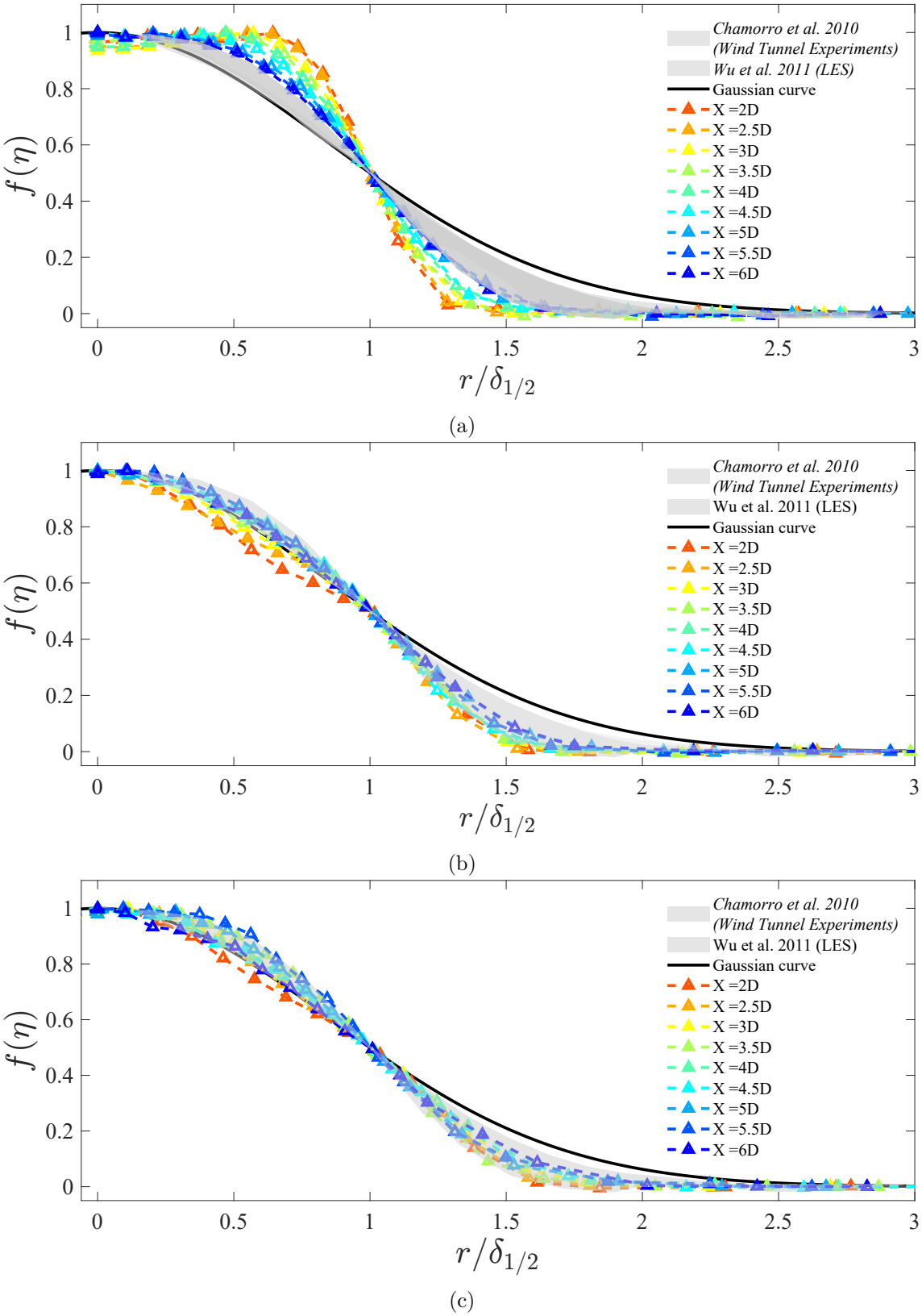

Figure 4.22: Self-similar streamwise velocity deficit profiles for (a) the $\alpha = 0°$ case, (b) the $\alpha = 15°$ case and for the (c) $\alpha = 25°$ case. Black solid line: theoretical self-similar Gaussian curve, grey shaded area: experimental and numerical data reported in the literature.

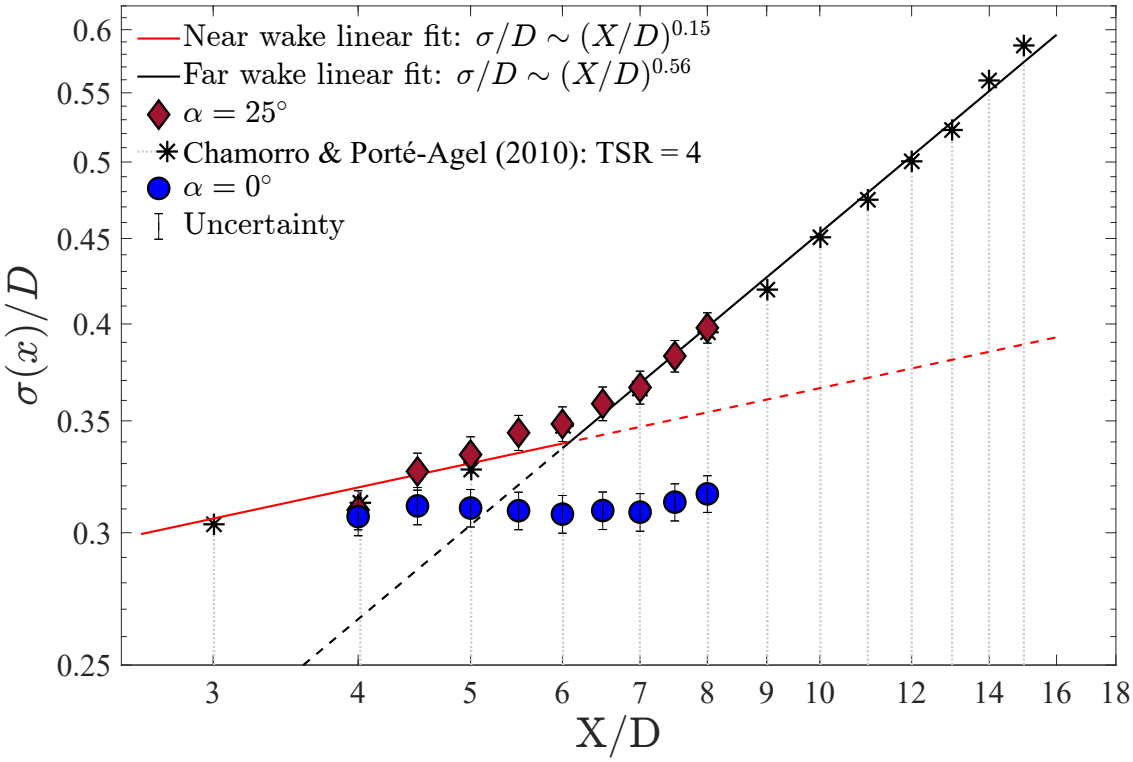

Figure 4.23: Normalised standard deviations of the streamwise velocity deficit profiles for cases $\alpha = 0°$ and $\alpha = 25°$ compared to the data reported in Chamorro and Porté-Agel (2010). Fitted linear trends are represented in solid lines.

non-swirling wakes.

In order to compare the wake's width to the reported trends for rotating turbines, the wake width can be calculated as an equivalent standard deviation $\sigma(x)$. In the work of Bastankhah and Porté-Agel (2014) for example, the proposed gaussian velocity deficit model was fitted to numerous data points also reported in this work. In particular, the data points reported in Chamorro and Porté-Agel (2010) are shown in figure 4.23, where the wake of a lab-scale three-bladed rotating wind turbine immersed in a boundary layer was investigated. For our data, $\sigma(x)$ can be directly calculated as the square root of the calculated variance from the streamwise velocity deficit profiles such as:

$$\sigma(x)^2 = \int_0^\infty \eta^2 f(\eta) d\eta. \tag{4.6.2}$$

Figure 4.23 compares the downwind evolution of $\sigma(x)$ along with the data reported in Chamorro and Porté-Agel (2010). The data points from the literature show a rupture in the trend of the wake expansion around $X = 6D$. From $X = 2D$ to $X = 6D$ a light slope ($\approx x^{0.15}$) is observed which does not correspond to any known scaling laws. Beyond this point however, the trend abruptly changes and endorses a wake expansion law closer to the non-equilibrium scaling $\sigma \sim x^{1/2}$ (Dairay et al., 2015) than to the classical equilibrium scaling $x^{1/3}$ (Johansson et al., 2003). Interestingly, the data obtained for $\alpha = 25°$ mimics this behaviour. In fact, as previously shown in figure 4.8, case $\alpha = 25°$ had a similar velocity-based swirl number streamwise evolution as a rotating turbine with a TSR=5, which is close to that used in the study of Chamorro and Porté-Agel (2010). In the near wake, the swirling velocity will be the driving factor admitting a length scale related to swirl. The velocity deficit will take over as swirl

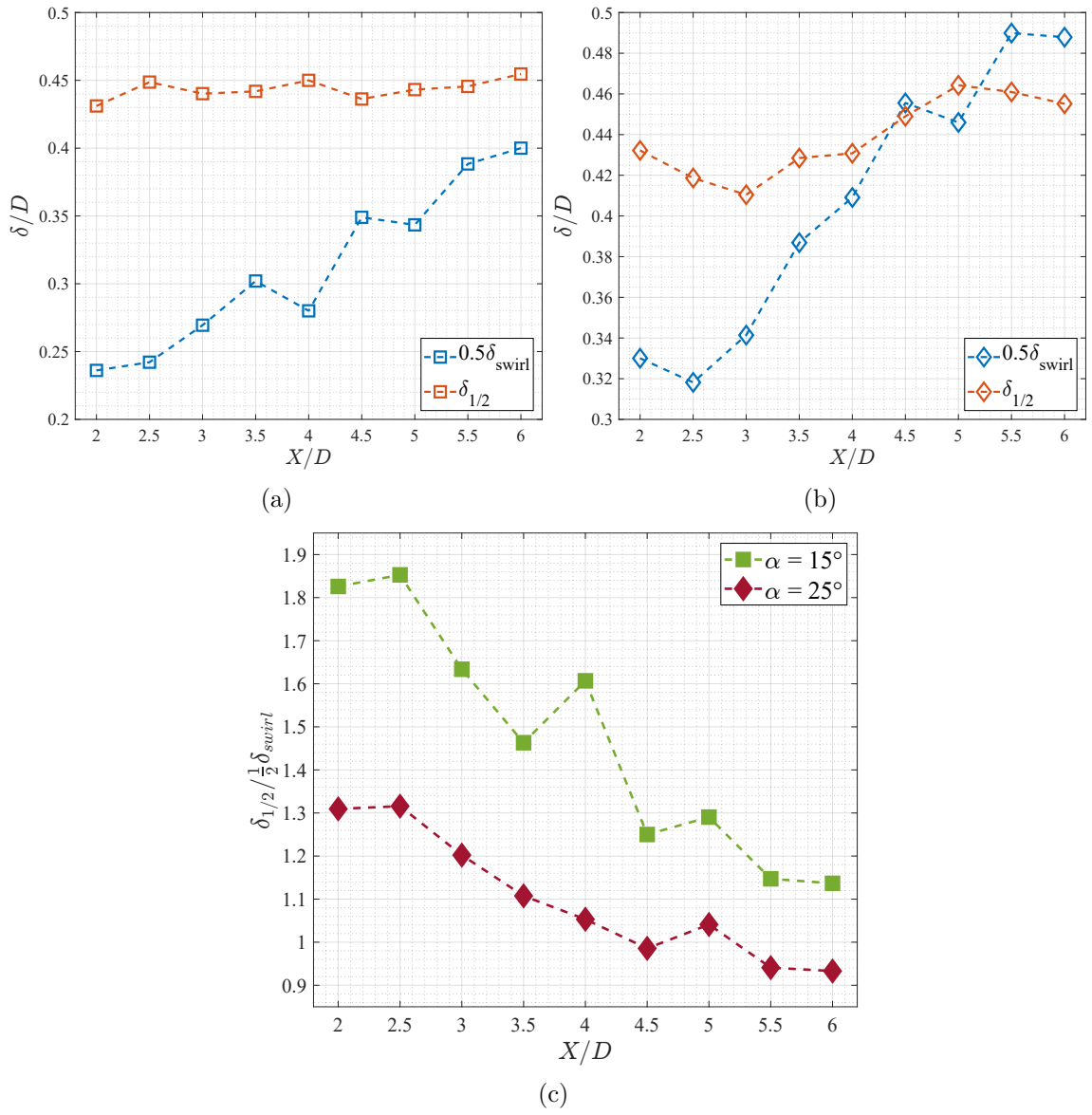

Figure 4.24: Streamwise evolution of the length scales profiles at different downwind locations of the wind-tunnel 3CHWA measurements for (a) the $\alpha = 15°$ case and for (b) the $\alpha = 25°$ case and (c) the length scale ratio $\delta_{1/2}/\delta_{swirl}$ downwind evolution

decays, imposing its length scale σ. This is inline with what was theorised in chapter 2 regarding the existence of two scales governing the streamwise evolution of the swirling wake when $\hat{S} = \mathcal{O}(1)$. On the other hand, the evolution of $\sigma(x)$ for case $\alpha = 0°$ appears to remain roughly constant at all streamwise positions as this case has not reached a self-preserving state yet.

The downwind evolution of δ_{swirl}, $\delta_{1/2}$ and their ratio is reported in figure 4.24. In the near wake, these two length scales appear to evolve independently (figures 4.24a and 4.24b). The wake half width $\delta_{1/2}$ shows minor variations for both cases $\alpha = 15°$ and $\alpha = 25°$. On the other hand, δ_{swirl} shows a clear trend in the near wake of the form $\delta_{swirl} \sim x^{\beta}$ with $\beta \approx 0.5$. Interestingly, as the $X = 6D$ location is approached, where the trend-break is expected, $\delta_{1/2}$ starts matching δ_{swirl} ($2\delta_{1/2} \sim \delta_{swirl}$).

The similarity profiles of the swirling velocity component are presented in figure 4.25 using δ_{swirl} and $\delta_{1/2}$ as length scales, respectively. Following figure (4.25) W_s scales the amplitude of the swirling velocity beyond $X = 3D$. The deficit length scale $\delta_{1/2}$ does

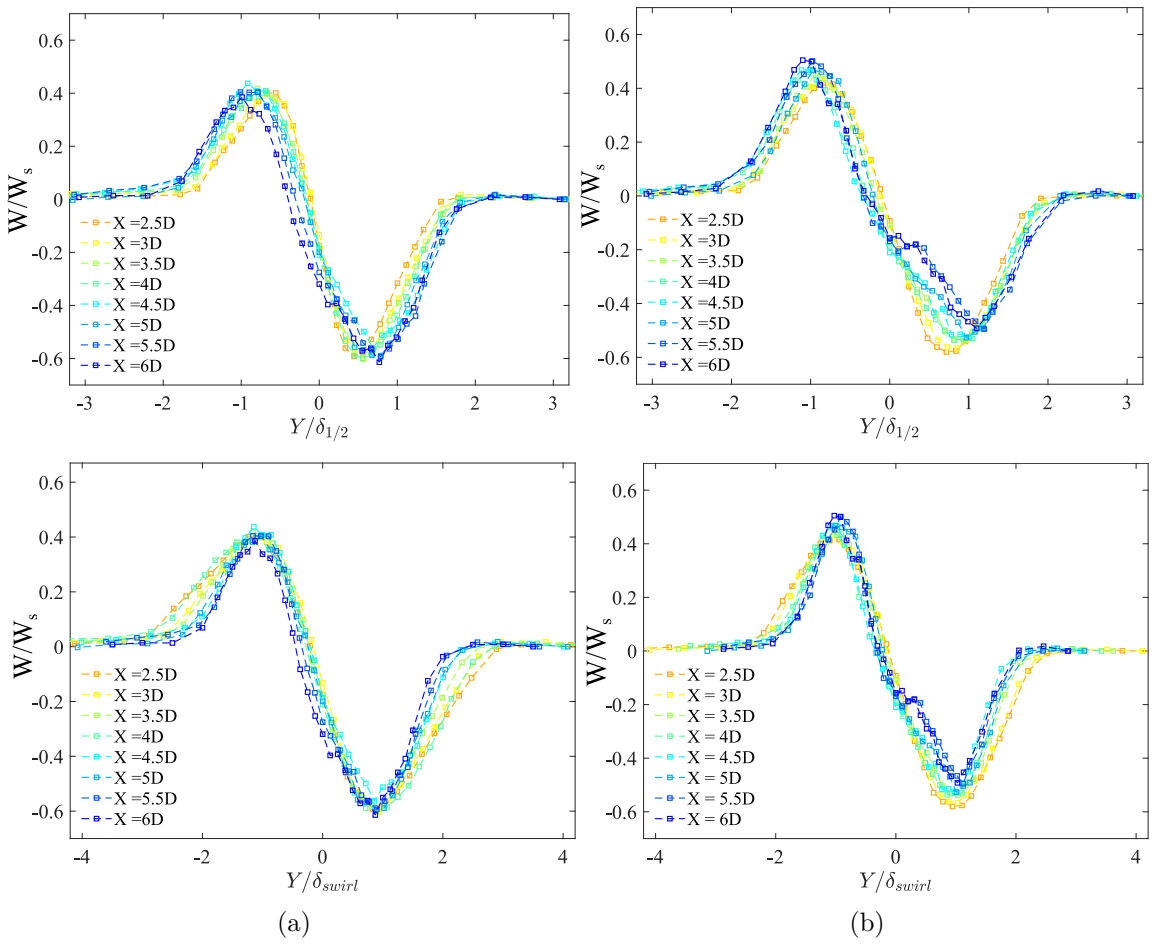

Figure 4.25: Self-similar swirling velocity profiles at different downwind locations for (a) the $\alpha = 15°$ case and (b) the $\alpha = 25°$ case using $\delta_{1/2}$ (top line) and δ_{swirl} as similarity length scales.

not seem to scale the data, especially in the near wake. However, further downwind ($X \geq 5D$), as $\delta_{1/2}$ approaches the trend of δ_{swirl} (figure 4.24), $\delta_{1/2}$ starts scaling the swirling velocity profiles. On the other hand, δ_{swirl} leads to a better data collapse and self-similarity can be approached for the swirling velocity profiles at $X = 3D$ and at $X = 4D$ for cases $\alpha = 15°$ and $\alpha = 25°$, respectively. This effect is more prominent at the centre of the wake near the low-pressure core but fails to achieve perfect self-similarity. This is likely due to an absence of complete self-similarity in the near wake. In any case, this result suggests that the length scale governing the near wake is the swirling length δ_{swirl}. This result further proves that the swirling wake is governed by (at least) two length scales which are in constant competition to fully represent the wake. In any case, in the examined streamwise locations, the swirling wake appears to be essentially governed by the swirling length δ_{swirl}. In the following, scaling laws for the wake properties are explored.

4.6.2 Scaling laws of the swirling wake's properties

Now that self similarity has been established for the streamwise velocity deficit and for the swirling velocity component, similarity scaling laws can be determined for the x-dependent wake properties such as wake expansion, recovery and swirl decay. As mentioned in chapter 2, the parameters of the scaling laws predicted from the similar-

Turbulence state	D_s	(δ/θ)	(U_s/U_∞)	(W_s/U_∞)	(W_s) vs. (U_s)
Equilibrium					
$(n=m=0)$	$\sim \frac{U_s^3}{\delta}$	$\sim \left(\frac{x}{\theta}\right)^{1/3}$	$\sim \left(\frac{x}{\theta}\right)^{-2/3}$	$\sim \left(\frac{x}{\theta}\right)^{-1}$	$\frac{W_s}{U_\infty} \sim \left(\frac{U_s}{U_\infty}\right)^{3/2}$
Non-equilibrium					
$(n=m=1)$	$\sim \frac{U_\infty U_s^2}{\delta}\left(\frac{D}{\delta}\right)$	$\sim \left(\frac{x}{\theta}\right)^{1/2}$	$\sim \left(\frac{x}{\theta}\right)^{-1}$	$\sim \left(\frac{x}{\theta}\right)^{-3/2}$	$\frac{W_s}{U_\infty} \sim \left(\frac{U_s}{U_\infty}\right)^{3/2}$

TABLE 4.1: Summary of the similarity scaling laws of the wake properties predicted by equilibrium and non-equilibrium turbulence (from chapter 2 §2.3.3).

ity analysis can be separated into two categories, depending on the nature of turbulence considered in the scaling of the dissipation rate in the energy equation. The methodology used to determine the best fit parameters for each function is similar to the non linear fit methods used by Nedic (2013) and later improved in the work of Dairay et al. (2015). The following functions are considered for the scaling laws:

$$\frac{U_s}{U_\infty} = A\left(\frac{x - x_{0_U}}{\theta}\right)^{\beta_U}, \tag{4.6.3}$$

$$\frac{\delta_{swirl}}{\theta} = B\left(\frac{x - x_{0_\delta}}{\theta}\right)^{\beta_\delta}, \tag{4.6.4}$$

$$\frac{W_s}{U_\infty} = C\left(\frac{x - x_{0_W}}{\theta}\right)^{\beta_W}, \tag{4.6.5}$$

where β_U, β_δ and β_W are the fit exponents of the power laws for the velocity deficit, the swirling length and the swirling velocity respectively. x_{0_U}, x_{0_δ} and x_{0_W} are the corresponding virtual origins and A, B and C are fit constants. The predicted values of the similarity exponents were derived in chapter 2 (§2.3.3) and a novel swirl decay scaling law was obtained based on non-equilibrium turbulence. For ease of reference, the different scaling laws stemming from similarity theory are recalled in table 4.1.

The first step of the fitting method consists in setting all virtual origins to 0 and performing initial linear fits of $(U_s/U_\infty)^{1/\beta_U}$, $(\delta_{swirl}/\theta)^{1/\beta_\delta}$ and $(W_s/U_\infty)^{1/\beta_W}$ in order to obtain a first approximation for the power law exponents. These values are then used in order to bound and initialise the nonlinear least-squares regression algorithm based on the work of Marquardt (1963). This algorithm is then used to simultaneously find the optimal values for the parameters. The resulting parameters from the fitting method are listed in table 4.2 for cases $\alpha = 15°$ and $\alpha = 25°$.

The downwind evolution of $U_s(x)/U_\infty$ with the resulting scaling laws for cases $\alpha = 15°$ and $\alpha = 25°$ is reported in figure 4.26. Additionally, the $\alpha = 0°$ case is also considered in figure 4.26a for reference. As expected, case $\alpha = 0°$ shows no signs of either similarity scaling law (equilibrium or non-equilibrium) for the considered streamwise distances and the fitted law has a light slope ($U_s(x) \sim x^{0.13}$). On the other hand, the swirling wakes recovery (figures 4.26b and 4.26c) is well predicted by the non-equilibrium predictions ($\beta_U \approx -1$).

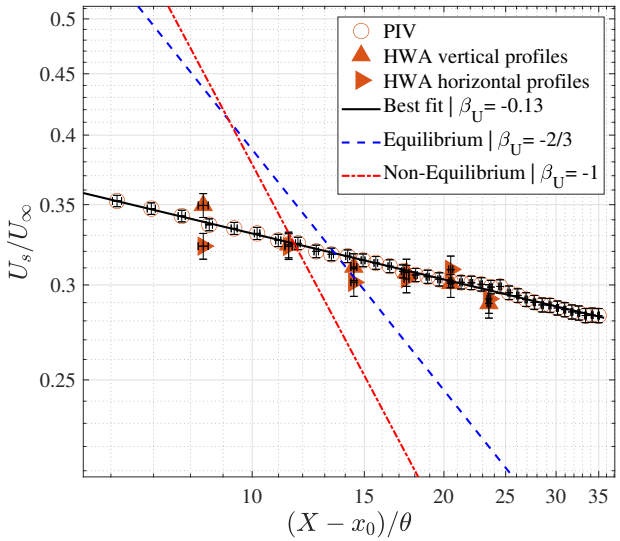

(a)

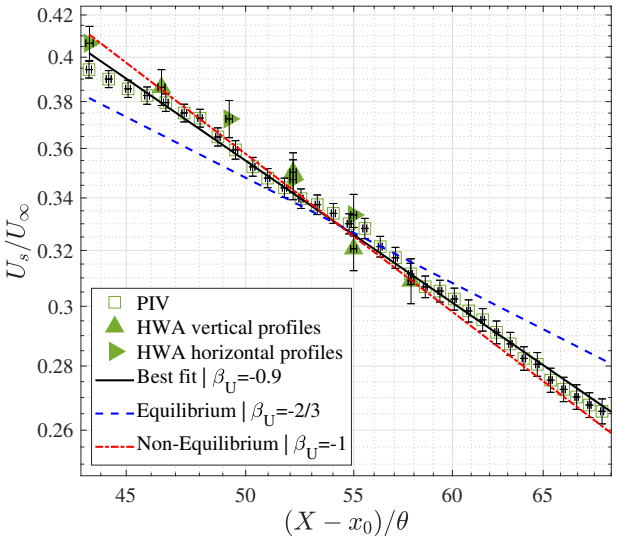

(b)

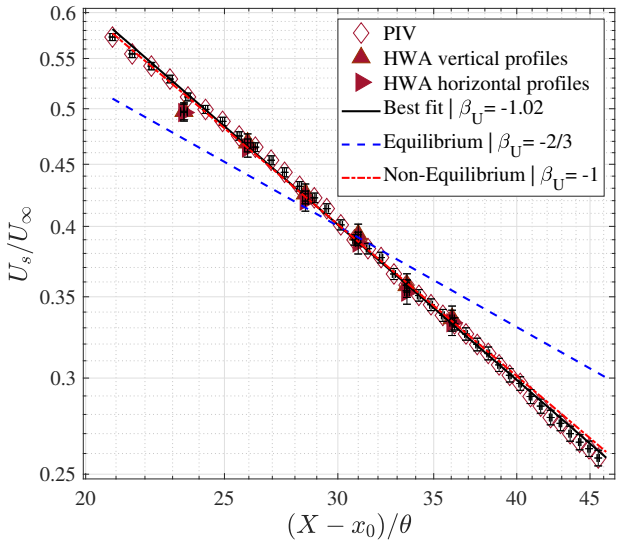

(c)

Figure 4.26: Scaling plots of the characteristic axial velocity deficit (U_s/U_∞) for (a) the $\alpha = 0°$ case, for (b) the $\alpha = 15°$ case and (c) the $\alpha = 25°$ case. Only one out of eight of the PIV data is plotted for clarity.

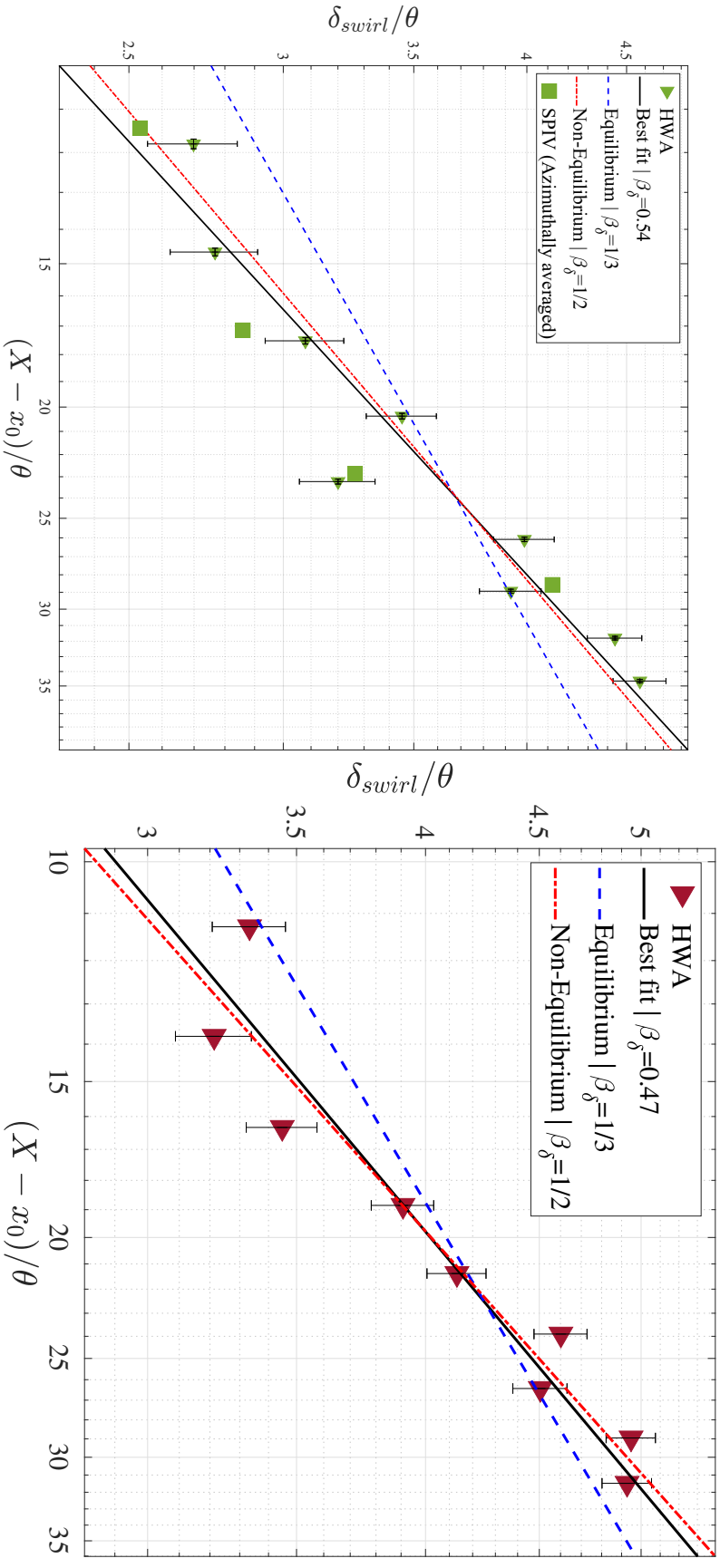

Figure 4.27: Scaling plots of the length scale δ_{swirl} for (a) the $\alpha = 15°$ case and for (b) the $\alpha = 25°$ case.

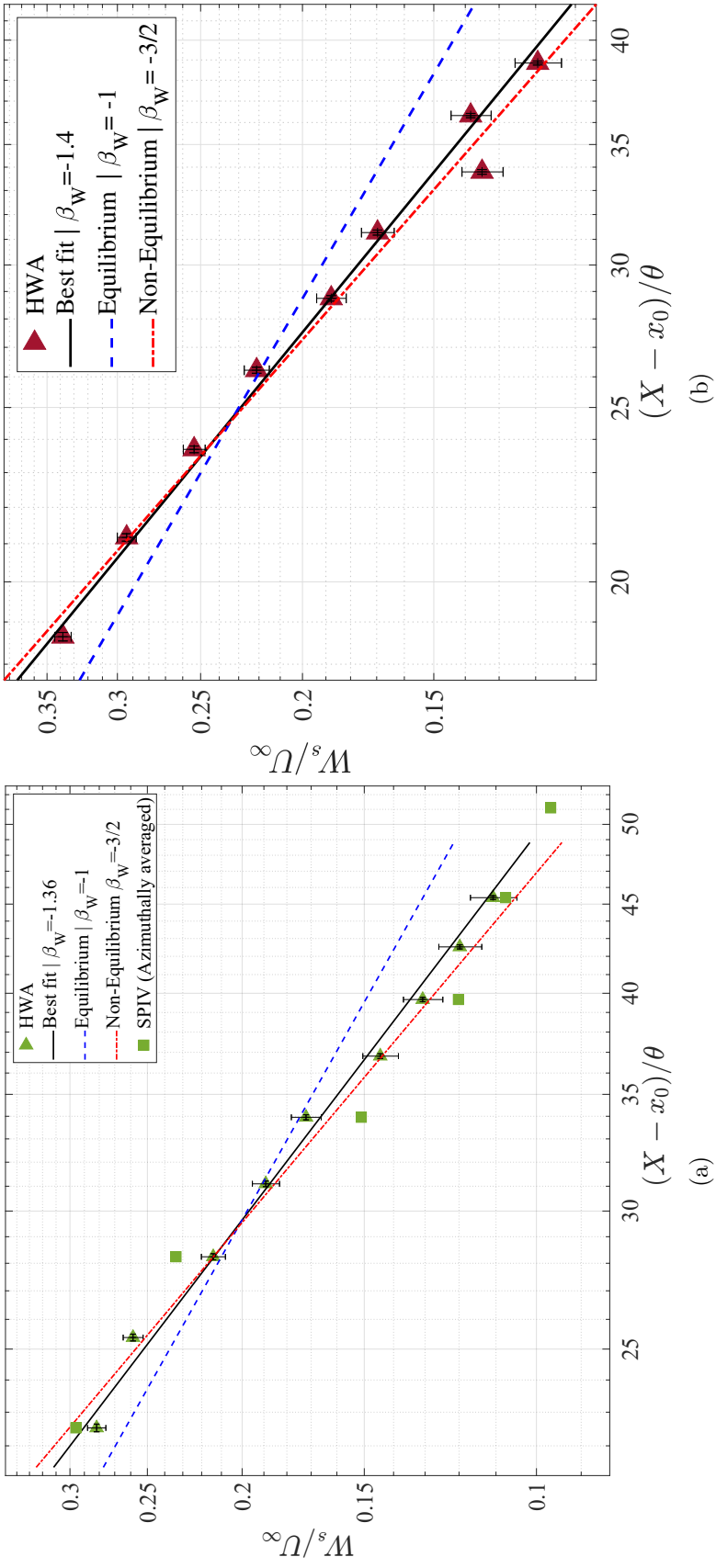

Figure 4.28: Scaling plots of the characteristic swirling velocity for (a) the $\alpha = 15°$ case and for (b) the $\alpha = 25°$ case.

Case	function	A, B, C	$\beta_{(U,\delta,W)}$	$x_{0_{(U,\delta,W)}}$
$\alpha = 15°$	U_s/U_∞	11.99	-0.9	-23.6
$\alpha = 15°$	δ_{swirl}/θ	0.65	0.54	-0.50
$\alpha = 15°$	W_s/U_∞	19.9	-1.36	-11.1
$\alpha = 25°$	U_s/U_∞	13.06	-1.02	-5.7
$\alpha = 25°$	δ_{swirl}/θ	0.96	0.47	-1.38
$\alpha = 25°$	W_s/U_∞	21.02	-1.40	-8.54

TABLE 4.2: Chosen parameters of the nonlinear fitting method for the scaling power laws (4.6.3)-(4.6.5).

As for the scaling of the wake's width in terms of swirling velocity spread, figure 4.27 shows the downwind evolution of the swirling length scale $\delta_{swirl}(x)/\theta$ for both swirling wakes ($\alpha = [15; 25]°$). The results show very good agreement with the non-equilibrium similarity predictions ($\beta_\delta \approx 1/2$) for both cases. As the wake evolves and swirl decays, the length scale $\delta_{1/2}$ is expected to exhibit a trend-shift and was shown to approach a similar trend as δ_{swirl}. Therefore, further downstream when swirl no longer drives the wake's behaviour, it is expected that $\delta_{1/2}$ will also scale as $x^{1/2}$ which was observed in the recent findings of Lingkan and Buxton (2023). Furthermore, as previously shown in figure 4.23, the $\alpha = 25°$ case showed the same non-equilibrium scaling for the wake width σ from $X = 6D$ onward.

The swirl decay for cases $\alpha = 15°$ and $\alpha = 25°$ is emphasised in figure 4.28 and shows the downwind evolution of $W_s(x)/U_\infty$ along with their respective fitted scaling law. Once again, the data matches the non-equilibrium predictions ($\beta_W \approx -3/2$). Furthermore, the data reported in Holmes and Naughton (2022) is treated using the the same non-linear method and the resulting scaling laws and fitting parameters are reported in table 4.3 and figure 4.29. The $\hat{S} = 0.30$ and $\hat{S} = 0.20$ cases are the ones comparable to this study as they have similar swirl numbers. The data reported in Holmes and Naughton (2022) also matches the non-equilibrium predictions of swirl decay developed in this thesis. Altogether, these results point out that the region of interest in the wake is well approximated by scaling laws based on non-equilibrium similarity. Moreover, the novel scaling laws for swirl decay is also found in our data and in the data reported in Holmes and Naughton (2022). The fact that the same conclusions are obtained for cases $\alpha = 15°$ $\alpha = 25°$ proves that porosity is not the dominant parameter in the development of the self-preserving swirling wake, it is swirl. Echoing the discussions made at the beginning of this thesis, swirl is therefore the dominant initial condition governing the development of the flow.

Moreover, as discussed in the beginning of this section, both similarity analyses result in the same scaling law between the swirl decay and the wake recovery such as $W_s/U_\infty \sim (U_s/U_\infty)^{3/2}$. The linear fit plots of these quantities is reported in figure 4.30 for cases $\alpha = 15°$ and $\alpha = 25°$. It is found that the data supports this scaling law, especially for the $\alpha = 25°$ case.

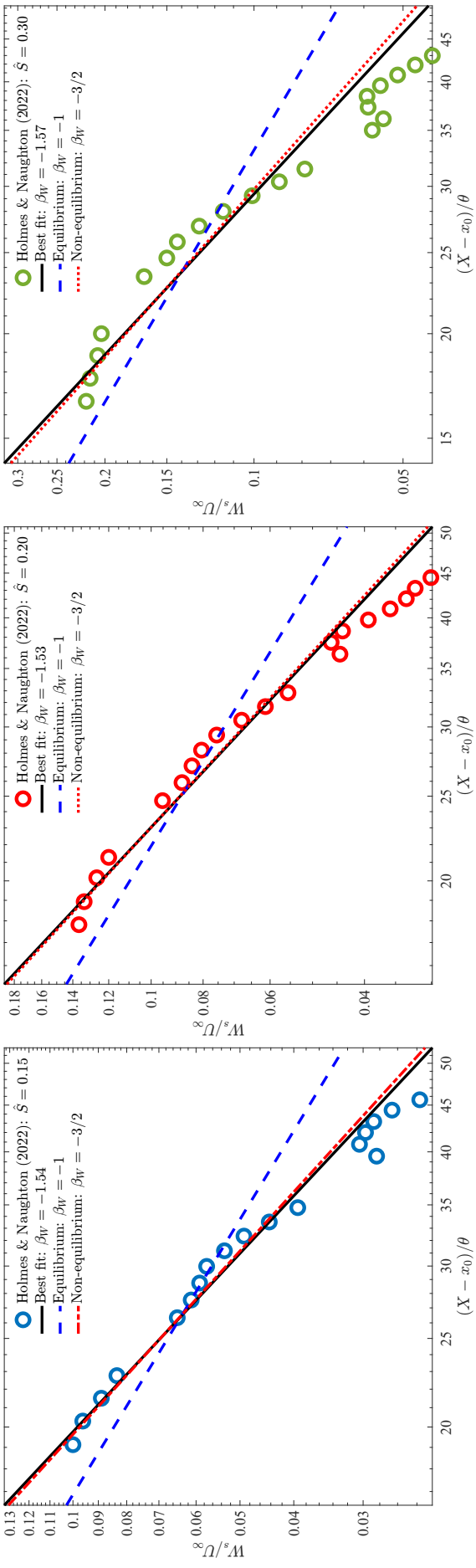

Figure 4.29: Scaling plots of the characteristic swirling velocity for (a) the $\hat{S} = 0.15$ case, (b) the $\hat{S} = 0.20$ and for (c) the $\hat{S} = 0.30$ cases from the data reported in Holmes and Naughton (2022).

$\hat{S}$	C	β_W	x_{0_W}
$\hat{S} = 0.15$	9.93	-1.54	-13.7
$\hat{S} = 0.20$	12	-1.53	-12.6
$\hat{S} = 0.30$	19.91	-1.57	-11.4

TABLE 4.3: Non-linear regression results from the swirling magnitude data reported in the rotating porous disc investigation of Holmes and Naughton (2022).

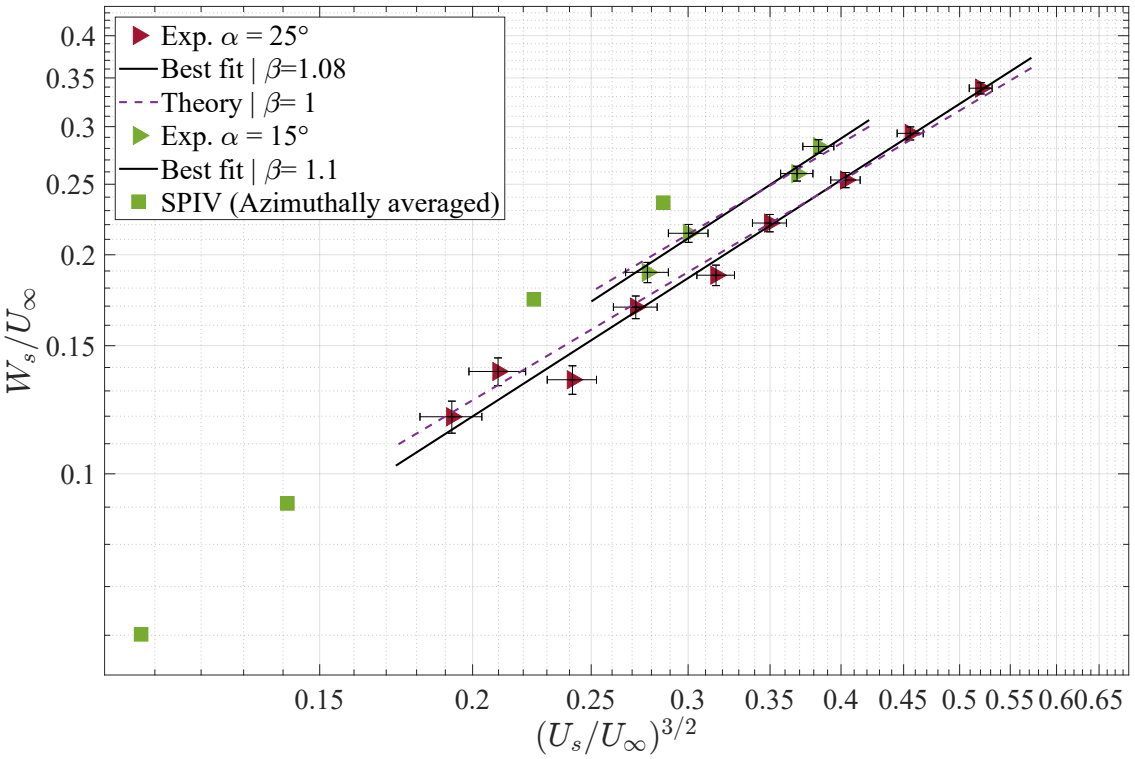

Figure 4.30: Scaling plots of $W_s(x)$ vs. $U_s(x)^{3/2}$ for cases $\alpha = 15°$ and $\alpha = 25°$.

4.7 Concluding remarks

This chapter demonstrated swirl's crucial role in shaping the wake of a porous disc. Swirl showed self-preserving characteristics and enhanced the self-similarity of the streamwise velocity deficit $U_s(x)/U_\infty$. The streamwise evolution of the swirling wake's characteristic deficit, swirl and length scale showed very good agreement with non-equilibrium similarity theory (Vassilicos, 2015; Dairay et al., 2015). In particular, the novel scaling law based on non-equilibrium similarity derived in chapter 2 (§2.3.3) was obtained for the swirl decay such as $x^{-3/2}$. The universal scaling law coupling the characteristic axial velocity deficit and the characteristic swirling velocity $(W_s(x)/U_\infty) \sim (U_s(x)/U_\infty)^{3/2}$ was also found in a restricted range of streamwise locations. Identical results were obtained for cases $\alpha = 15^\circ$ and $\alpha = 25^\circ$ which suggests that swirl might be the dominant initial condition for the near wake development relative to porosity. However, to firm up this conclusion, additional experiments need to be carried out with a lower porosity set of discs.

Since drag was not changed between cases $\alpha = 0^\circ$ and $\alpha = 15^\circ$ but the flow topology is completely changed as well as its streamwise development: what changed? Did the development mechanisms change or did just the virtual origin shift? The following chapter aims at answering these questions through the study of entrainment focusing on cases $\alpha = 0^\circ$ and $\alpha = 15^\circ$.

Résumé en français: Effet du swirl sur les propriétés du sillage tournant d'un disque poreux

Ce chapitre vise à caractériser l'influence du swirl sur les propriétés du sillage moyen. L'effet du calage des pâles d'un angle α sur la traînée est d'abord examiné. Ensuite, le swirl est évalué à différentes positions et deux échelles caractéristiques sont identifiées. L'effet du swirl sur la topologie de l'écoulement est évalué par le biais d'un bilan de quantité de mouvement et de la distribution de la pression à travers le sillage. Dans la dernière section, les lois d'échelle pilotant le développement du sillage tournant auto-similaire sont établies et comparées aux prédictions de la théorie de similarité.

En début de chapitre, les équations principales régissant le sillage tournant du disque poreux sont rappelées. D'après les prédictions établies dans le chapitre précédent, pour des angles de calage inférieurs à l'angle de décrochage, l'ajout de swirl dans le sillage devrait se faire sans altérer le coefficient de traînée. Conformément à nos prédictions, deux régimes sont mis en évidence en fonction de l'angle α : le régime d'écoulement attaché et le régime de décrochage. Dans le régime d'écoulement attaché, l'amplitude du swirl augmente linéairement et la traînée reste constante. Dans le régime de décrochage, le swirl commence à diminuer avec α et la traînée augmente linéairement en raison de la diminution de la porosité apparente (voir figures 4.1, 4.2 & 4.3). Un angle de calage critique est ensuite identifié $\alpha_c \in [16, 18°]$, au-delà duquel le décrochage se produit. En effet, au delà de cet angle, l'écoulement décolle sur l'extrados de chacune des pâles trapézoïdales du disque poreux. Ceci est à l'origine de l'augmentation du blocage effectif entraînant de facto une augmentation du coefficient de traînée. Les cas $\alpha = 0°$, $\alpha = 15°$ et $\alpha = 25°$ sont donc identifiés comme angles clés; le cas $\alpha = 15°$ générant une amplitude maximale de swirl à iso-porosité. Le cas $\alpha = 25°$ génère les mêmes niveaux de swirl que le cas $\alpha = 15°$ avec une porosité apparente réduite. Le swirl est ensuite caractérisé pour ces cas et montre des valeurs du nombre de swirl ($\hat{S} \approx 0.3$) comparables à celles rapportées pour des modèles rotatifs (Dufresne, 2013; Lee et al., 2020; Holmes and Naughton, 2022). Le swirl présente une distribution toroïdale axisymétrique autour du centre du sillage, avec une décroissance rapide dans la direction axiale ainsi qu'une propagation radiale vers l'extérieur pour conserver la quantité de mouvement angulaire.

Un bilan de quantité de mouvement, obtenu à partir de nos mesures, révèle que dans le régime d'écoulement attaché, le swirl n'affecte pas significativement la traînée du disque poreux, mais modifiait plutôt la distribution de la pression à travers le sillage. Pour évaluer la redistribution de la pression causée par le swirl, les champs de pression dans des plans orthogonaux au sens de l'écoulement ($X = 2D$, $X = 4D$ et $X = 6D$) ont été reconstruits à partir des mesures de vitesse suivant les travaux de Shanmughan et al. (2020) et Harker and O'Leary (2008). Il est montré que le swirl redistribue spatialement la zone de basse pression et crée un noyau de basse pression au centre du sillage près de $(Y, Z) = (0, 0)$. Pour le sillage sans swirl ($\alpha = 0°$), la zone de basse pression est plutôt située près de la région du mât où un fort effet d'aspiration verticale descendante ("*downwash*") est observé (Pierella and Sætran, 2017). Cette aspiration du sillage vers le bas à déjà été observée lors de l'étude menée par Aubrun et al. (2019).

Ensuite, l'effet du swirl sur la topologie de l'écoulement moyen est examiné, ainsi que la position du centre du sillage. Il est montré que le taux de rotation produit un effet stabilisant et d'axisymétrisation sur le sillage du disque poreux, contre-balançant ainsi l'aspiration causée par le mât. De plus, l'auto-similarité du déficit de vitesse

axiale $U_s(x)/U_\infty$ est renforcée grâce au swirl. Des profils Gaussiens auto-similaires sont obtenus à partir de $X = 3D$ pour les sillages avec swirl, contrairement au cas $\alpha = 0°$ pour lequel l'auto-similarité n'est pas établie. Ces profils sont ensuite comparés aux données rapportées dans la littérature et montrent une meilleure concordance avec les profils de déficit de vitesse provenant des données expérimentales en soufflerie d'une éolienne de laboratoire (Chamorro and Porté-Agel, 2010) et des résultats LES d'une éolienne de taille réelle (Wu and Porté-Agel, 2012). L'épaisseur du sillage en termes de déficit de vitesse axiale $\sigma(x)$ montre une rupture de tendance à environ $X = 6D$. Une nouvelle échelle de longueur δ_{swirl} est donc proposée dans cette étude, qui met à l'échelle la propagation du swirl dans le sillage et montre une évolution dans la direction axiale, contrairement à $\delta_{1/2}$. L'auto-similarité est également obtenue pour la composante azimutale de vitesse.

Avec les conditions d'auto-similarité remplies pour le déficit de vitesse axiale et pour le swirl, des lois d'échelle de similarité sont recherchées pour les propriétés du sillage (Nedic, 2013; Dairay et al., 2015). La procédure adoptée est une régression non linéaire d'optimisation de paramètres d'ajustement (Marquardt, 1963). Les résultats montrent une très bonne concordance avec les lois d'échelle de similarité basées sur une turbulence hors équilibre, dérivées dans le chapitre 2 (§2.3) (Vassilicos, 2015). Le déficit de vitesse moyen dans la direction axiale évolue comme x^{-1} et l'échelle caractéristique du sillage comme $x^{1/2}$. En particulier, la nouvelle loi d'échelle basée sur la similarité hors équilibre a été aussi obtenue pour la décroissance du swirl telle que $x^{-3/2}$. Les deux cas, $\alpha = 15°$ et $\alpha = 25°$, montrent un bon accord avec ces prédictions. La loi d'échelle couplant le déficit de vitesse axiale caractéristique et le swirl caractéristique $W_s(x)/U_\infty \sim (U_s(x)/U_\infty)^{3/2}$ est également trouvée dans une plage restreinte de positions dans le sillage. Des résultats identiques ont été obtenus pour les cas $\alpha = 15°$ et $\alpha = 25°$, ce qui montre que le taux de rotation injecté est la condition initiale dominante du sillage par rapport au taux de blocage. On démontre donc que le swirl déclenche l'auto-similarité dans le sillage du disque poreux à des distances plus proches de l'objet, et ce indépendamment de la porosité.

5

On the entrainment mechanisms of the swirling wake of a porous disc

Contents

The previous chapter established the role of swirl on the wake's mean properties and their evolution with the streamwise direction. It was shown that the swirling wake and the non-swirling wake of the porous discs are asymptotically identical in terms of the axial momentum integral (drag). The main difference relies in the pressure distribution across the wake, especially in the near field. Swirl creates a low pressure core at the centre of the wake enhancing its axisymmetry and promoting self-similarity. Furthermore, in presence of swirl, it was demonstrated that wake recovery, expansion and swirl decay evolve in the streamwise direction following the predictions of non-equilibrium turbulence (Nedic, 2013; Dairay et al., 2015; Vassilicos, 2015).

In summary, swirl changes how the wake evolves downstream without altering the drag coefficient, at least in the attached flow regime. In order to go further into the underlying mechanisms changed by swirl one has to ask the fundamental question: what causes a wake to expand and recover? An answer to this question can be found in the seminal works of Corrsin and Kistler (1955), Townsend (1966) and the comprehensive work of Turner (1986), where the entrainment notion was first introduced. In the case of a turbulent wake, entrainment is the process through which high momentum fluid featuring the free-stream is transported inside the wake, causing it to expand and recover. Swirl has thus changed how the wake interacts with its environment i.e the entrainment mechanisms. This poses the following questions: Was the entrainment velocity changed by swirl? Was the interface changed by swirl? Which scales of

entrainment were altered by swirl? How far is the reach of swirl's influence? This chapter aims at tackling these questions with the help of the experimental data collected during this investigation and a physical analysis of entrainment focusing on cases $\alpha = 0°$ and $\alpha = 15°$.

5.1 Introduction

Turbulent flows such as plumes, jets, wakes and boundary layers all share a common property: a sharp and irregular interface is drawn between the highly rotational turbulent flow and the quiescent ambient fluid (Townsend, 1976; Pope, 2000). Several experiments and numerical simulations reported in the literature support this fact, since the seminal work of Corrsin and Kistler (1955). In this critical investigation, the authors postulated the existence of a so-called *viscous superlayer* which demarcates the frontier between turbulent and non-turbulent regions of the flow. This tortuous[1] moving surface, is characterised by a high vorticity gradient and high intermittency (da Silva et al., 2014). Presently, it is established that there is a turbulent non-turbulent interface (TNTI) separating the irrotational ambient fluid and the turbulent, rotational flow. In this sense, the TNTI acts as a physical boundary between the external fluid and the turbulent wake which interact with each other through a process called entrainment.

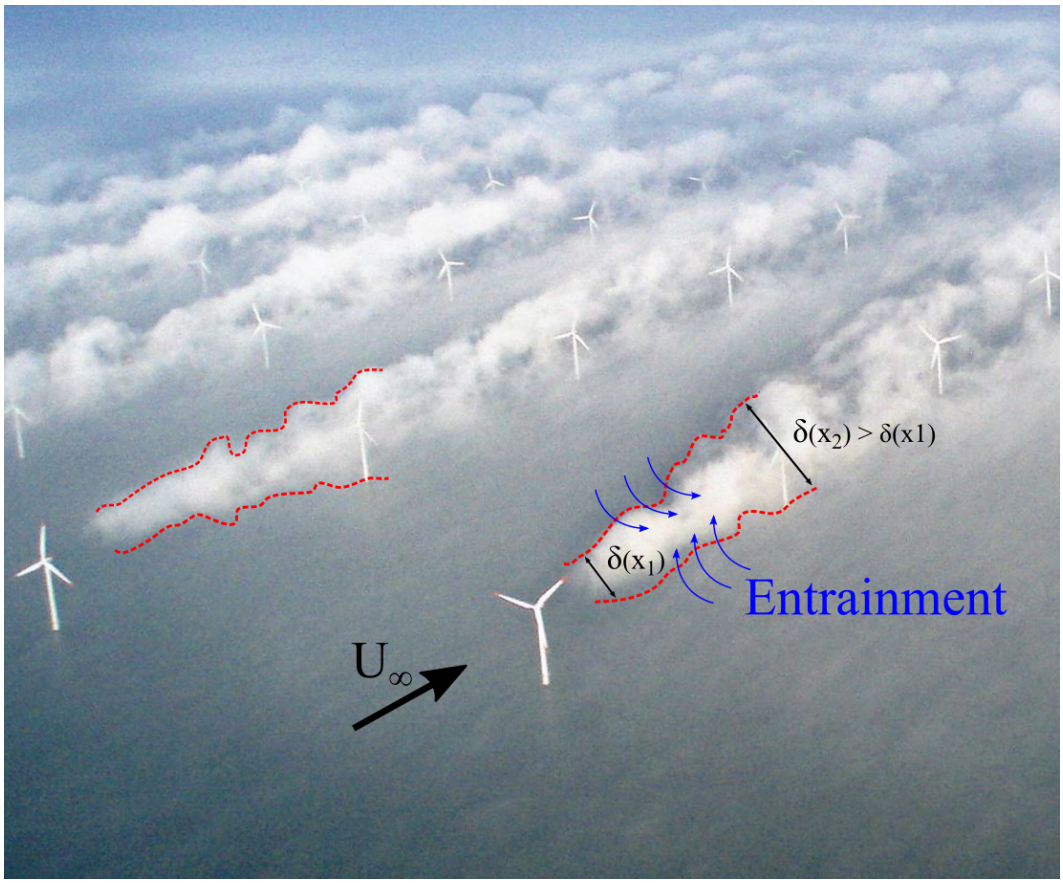

Figure 5.1: Horns Rev 1 wind farm located in the North Sea, near the Danish coastline. The particular meteorological conditions make the wind turbine wakes visible (red dashed outline). The wake width δ of a wind turbine is depicted at two arbitrary downstream locations x_1 and x_2 with $(x_2 > x_1)$. Photography taken by C. Steiness for Vattenfall.

In the case of wind turbine wakes, figure 5.1 shows the widely known photograph of the Horns Rev 1 wind farm located in the North Sea, close to the Danish coastline. This picture owes its popularity to the exceptionally rare meteorological conditions

[1]Tortuosity is a term adapted from porous media hydraulics used to characterise the degree of contortion of a line.

(humidity and temperature) causing water droplets to condense in the wake of the wind turbines and allowing a visualisation of these swirling flows. This natural seeding of the wake clearly shows an interface between the ambient air, characterised by a free-stream velocity U_∞, and the wind turbine wake outlined by the red dashed lines[2]. Since the historical observations of Corrsin and Kistler (1955) and of Phillips (1955), several other studies have concluded that the TNTI is the boundary at which several physical processes occur (Philip et al., 2014; Westerweel et al., 2009; Sreenivasan and Meneveau, 1986). In the case of wakes, the entrainment of mass, momentum and energy is the main mechanism which causes the wake to expand and recover (Bisset et al., 2002; Townsend, 1970).

5.2 What is "Entrainment"?

The first mention of the word "entrainment" found in scientific literature goes as early as the wartime (1945) reports of Sir Geoffrey Ingram Taylor and later reviewed in the work of Batchelor (1953). The notion of entrainment first started as a hypothesis, a consequence of self-similarity, used to explain physical processes at the interfaces of turbulent flows (Batchelor, 1954). Entrainment was thoroughly examined in later years by Morton et al. (1956) and especially by Turner (1986)'s seminal investigation. In this paper, Turner used many examples of naturally occurring turbulent flows to demonstrate the power of the entrainment hypothesis. The entrainment assumption, was used to explain how these shear flows evolved in their dominant direction and how mixing occurred. Particular attention was put into the study of axisymmetric jets and plumes, which are governed by simple conservation laws.

The entrainment mechanisms were already described back then as a transport of mass, momentum and energy by an "inflow velocity at the edges of the flow" (Turner, 1986). Even if no specific name was given to these "edges" they were describing what we now call: TNTI. Interestingly, when a flow exhibits mean recirculation regions, another interface can be defined by the recirculation bubble outline like in the work of Stella et al. (2018), for instance. More insight was given by Corrsin and Kistler (1955) on the nature of the interfaces which separate turbulent flows from a non-turbulent environment. A detailed summary of these aspects can be found in recent literature regarding entrainment on boundary layers and other shear flows such as da Silva et al. (2014); Chauhan et al. (2014) and Pope (2000). This interface was first referred to as the *viscous superlayer* (VSL) by Corrsin and Kistler (1955), having a thickness of the order of the Kolmogorov scale η. Following Townsend (1970) and later works of Bisset et al. (2002) and da Silva et al. (2014), the TNTI revealed to also contain a turbulent sublayer (TBSL) where enstrophy admitted a local maximum with a thickness of the order of the Taylor micro-scale λ. All in all, the TNTI is the interface separating a turbulent flow from a non-turbulent ambient fluid. The TNTI is characterised by a sharp jump in vorticity, turbulent kinetic energy and in velocity, as demonstrated in several studies like those of Chauhan et al. (2014); Westerweel et al. (2005, 2009); Fiscaletti et al. (2021) and Breda and Buxton (2019), and references therein. According to these definitions, entrainment is therefore an umbrella term which encompasses all mechanisms of transfer across a physical interface of a flow (Chauhan et al., 2014).

[2]The depicted interface is NOT the TNTI in a strict sense and is only shown for illustration purposes.

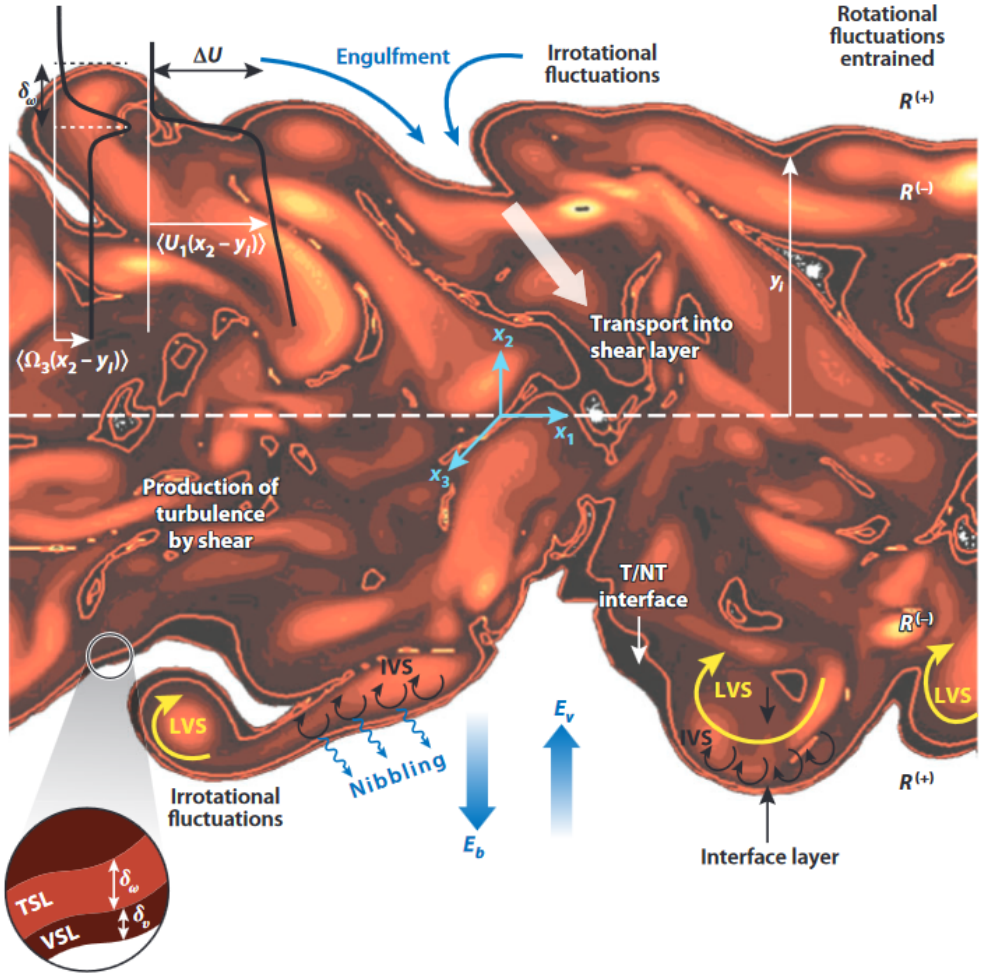

Figure 5.2: Schematic showcasing the different mechanisms, length scales and processes of entrainment for a shear layer. The TNTI coordinate y_i is shown, as well as the interface velocity E_b and the mean velocity of the flow in the direction of the interface E_v. IVS: intense vorticity structures, LVS: large-scale vortices, δ_ν: viscous superlayer thickness, δ_ω: turbulent sublayer thickness. Taken from da Silva et al. (2014)

As with all umbrella terms, in order to understand the meaning behind it, one has to examine its components. A graphical representation of the mechanisms involved in entrainment can be found in figure 5.2 which is extracted from the review paper of da Silva et al. (2014).

There seems to be a general consensus in scientific literature regarding the mechanisms of entrainment. Following Townsend (1966) and Turner (1986), there are two main mechanisms that operate the transfer of mass, momentum and energy across the TNTI: a large-scale process called "engulfment" and a small-scale process called "nibbling". Both of these processes are illustrated in figure 5.3. The engulfment process is a phenomenon occurring over large scales where a "blob" of turbulent fluid entraps pockets of irrotational fluid and "ingests"[3] it (Kovasznay, 1967; Chauhan et al., 2014). On the other side of the spectrum, nibbling is a viscous process of small scale interactions where the ambient irrotational fluid is converted into rotational fluid by vorticity diffusion (Fiscaletti et al., 2021).

[3]In the same manner through which phagocyte cells "eat" particles in biology.

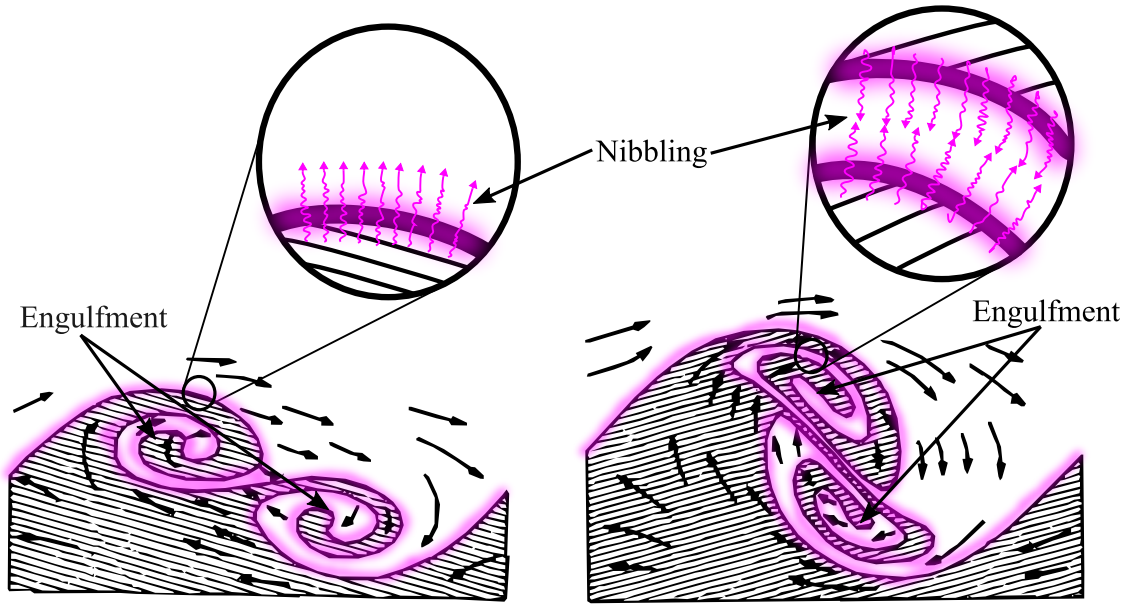

Figure 5.3: Schematic of two successive positions of the TNTI with a turbulent flow (hatched area) and a quiescent ambient fluid. Both engulfment and nibbling (pink shaded areas and pink arrows) are represented. Black arrows: segments of streamlines of arbitrary length. Adapted from Turner (1986).

Recently, Breda and Buxton (2019) reported on the open question regarding the dominant process of total entrainment. Whether the turbulent flow in question is a jet (Westerweel et al., 2005), a wake (Bisset et al., 2002), a plume (Morton et al., 1956) or a boundary layer (Stella et al., 2018), the dominant process of entrainment is not yet a settled matter. For example, if one is to examine the extensively documented case of the self-similar far field of a turbulent jet: some studies suggest that engulfment is the dominant process (Dahm and Dimotakis, 1987), while other studies (Westerweel et al., 2005) argued that the small scale interactions are the dominant process instead. In the case of the far field of an axisymmetric wake, Bisset et al. (2002) established that nibbling is the dominant process involved in entrainment. Following up on these considerations, it was initially thought that the large-scales of entrainment were completely decoupled from the small scales. However, recent studies have proven otherwise (Buxton, 2015; Fiscaletti et al., 2016; Baj and Buxton, 2017). Therefore, any action on the larger coherent structures will have a domino effect on the smaller scales. This strongly resonates with the work of Mazellier and Vassilicos (2008), where a close relationship was found between dissipative scales and energy-containing scales in turbulent flows. In other words, engulfment is expected to be intimately related to nibbling in such a way that any alteration of engulfment results in a modification of nibbling.

Entrainment can be characterised by the mass fluxes crossing the TNTI. Entrainment thus features a characteristic velocity $\boldsymbol{v_e}$, which is the velocity of the fluid at the interface, relative to the moving TNTI (Turner, 1986; Chauhan et al., 2014). The local instantaneous mass flux entrained across the TNTI is therefore expressed as:

$$d\dot{m} = \rho \boldsymbol{v_e} \cdot \mathbf{n} dS, \tag{5.2.1}$$

where dS is the interface surface element of the TNTI and $\boldsymbol{n}$ is the outward unit vector normal to the TNTI. The total mass flux across the TNTI at a given instant can be

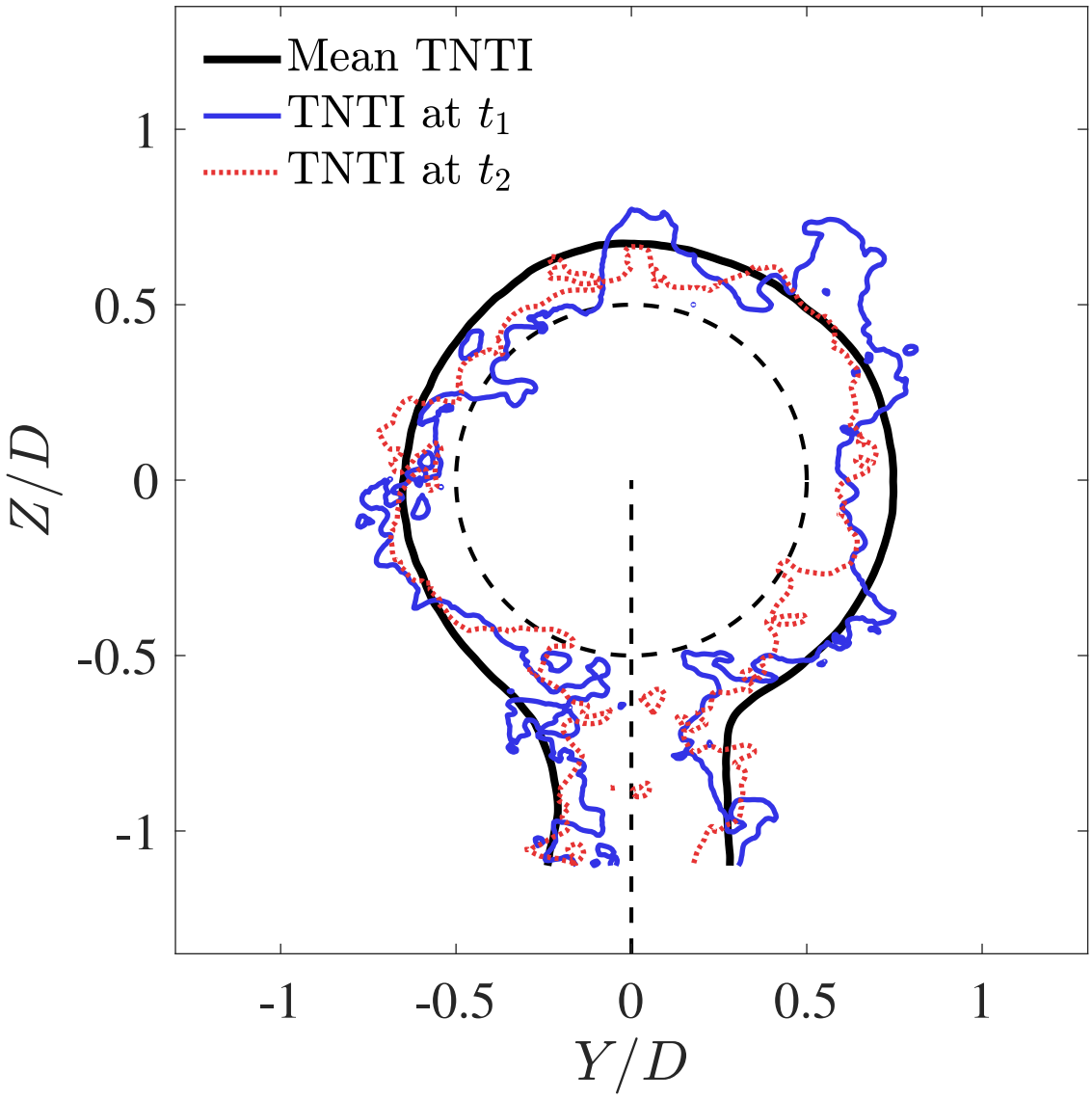

Figure 5.4: Example of the mean TNTI and two consecutive positions of the instantaneous TNTI of the swirling wake of a porous disc. The cross-section is chosen at $X = 6D$ and the instantaneous TNTIs where calculated at $t_1 > t_2$. The dashed black lines indicate the test rig outline.

then computed through integration over the curvilinear abscissa following the TNTI such as:

$$\dot{m} = \oint d\dot{m}. \tag{5.2.2}$$

However, measuring instantaneous entrainment velocities $\boldsymbol{v}_e$ across the moving TNTI demands not only high spatial resolution but also time-resolved data to track the TNTI position. Achieving these requirements poses a formidable challenge, especially for large fields of view. Presently, fulfilling these criteria remains unachievable, since the advancement of time-resolved PIV in air flows is still in early stages of development. Nonetheless, mean entrainment can be quantified and the scales at which entrainment occurs can still be assessed through the examination of the TNTI's geometrical properties.

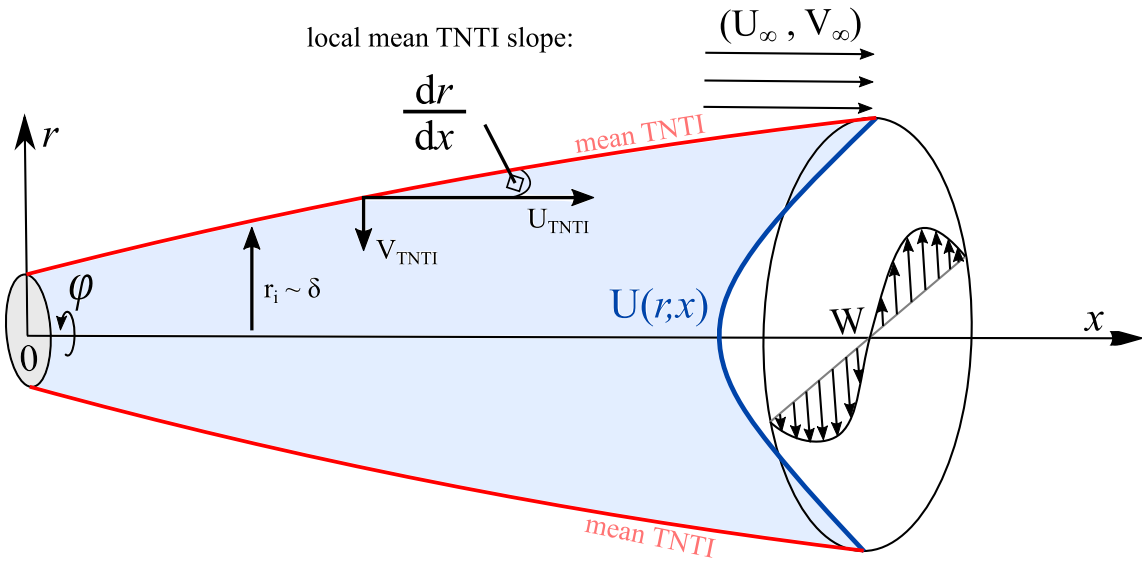

Figure 5.5: Schematic diagram of mean entrainment across the TNTI of an axisymmetric, swirling, turbulent wake.

As specified above, entrainment can be assessed by its mean, which is the average entrainment of mass, momentum and/or energy across the mean TNTI in a fixed frame of reference (Turner, 1986). The mean TNTI and two successive positions of the TNTI for case $\alpha = 15°$ is plotted in figure 5.4 for reference. The mean TNTI is the ensemble average of the instantaneous TNTIs calculated for each snapshot which is thereby a stationary frontier through which fluxes can be calculated. Following Maurice et al. (2016) the mean TNTI matches exactly the TNTI of the mean flow. Adapting the boundary layer work of Chauhan et al. (2014) to the case of a turbulent wake, the average mass flux across the TNTI can be defined as the mass transported by the mean flow velocity at the interface $\boldsymbol{U_{TNTI}} = (U_{TNTI}, V_{TNTI}, W_{TNTI})$ such as:

$$d\dot{M} = \rho \boldsymbol{U_{TNTI}} \cdot \boldsymbol{n} dS. \tag{5.2.3}$$

A representation of the mean entrainment across the mean TNTI of a swirling, axisymmetric wake is depicted in figure 5.5. In this configuration, equation (5.2.3) can be written as:

$$d\dot{M} = 2\pi r_i \rho [U_{TNTI} dr + V_{TNTI} dx], \tag{5.2.4}$$

where $r_i(x)$ is the radial coordinate of the mean TNTI and U_{TNTI} and V_{TNTI} are the mean streamwise and radial velocity components at the interface, respectively. Note that swirl is absent from this definition because of the axisymmetric hypothesis. Consequently, mean swirl does not entrain mass across the mean TNTI. Equation (5.2.4) can be divided by dx to obtain the following expression for the average mass flow rate per unit area across the mean TNTI:

$$\frac{d\dot{M}}{dx} = [U_{TNTI} K_z + V_{TNTI}] \cdot 2\pi r_i \rho, \tag{5.2.5}$$

where $K_z = dr/dx$ is the local mean TNTI slope which is intimately related to the wake expansion and recovery. The mean wake expansion will set the local mean TNTI slope which will in turn govern the surface through which U_{TNTI} entrains high momentum

free-stream into the wake. Equation (5.2.5) clearly shows that the local average mass flux across the TNTI has two main contributors: the axial mass flux $U_{TNTI}K$ weighted by the local mean TNTI slope and the radial inflow of mass V_{TNTI}, respectively. Since swirl was shown to modify the wake expansion and recovery (cf. chapter 4), mean entrainment must have been altered by swirl also. Following Bisset et al. (2002) and Chauhan et al. (2014), the velocity components at the TNTI will have values close to the free-stream values given their proximity to the ambient fluid. This makes $U_{TNTI} \sim U_\infty$ an order of magnitude above $V_{TNTI} \sim V_\infty$. However, since the term $U_{TNTI}K$ is weighted by the local mean TNTI slope it is difficult to predict which term drives the average mass flux across the TNTI envelope of the swirling wake. Altogether, these considerations pose the following questions for the study of the swirling wake: How was mean entrainment modified by swirl? What scales of entrainment were modified by swirl, the large scales, the small scales or both? In any case, the main requirement for answering these questions is an accurate detection of the TNTI. The following section will therefore focus on the detection methods used to capture the position of the TNTI.

5.3 TNTI detection methods

Since Corrsin and Kistler (1955)'s seminal work, several detection strategies of this interface have been proposed in scientific literature. In the early days of velocimetry techniques, only local measurement techniques such as HWA were available to detect the TNTI (Townsend, 1970). Following Pope (2000), these techniques exploited the intermittency property of the TNTI where the probe's signal alternated between low amplitude in the quiescent region and sharp bursts of turbulent fluctuations in the turbulent region. In this work, this technique is not used, as other spatially resolved techniques such as PIV are much more appropriate to detect the TNTI and were the preferred technique used here. However, the reader is referred to the excellent work of Corrsin and Kistler (1955) and of Pope (2000) for a comprehensive assessment on intermittency.

Since the TNTI is characterised by a region of sharp gradients in vorticity, velocity and turbulent kinetic energy, high resolution image-based techniques are well suited to detect this interface. This can be done directly by marking the rotational region of the flow with, for example, local seeding with fluorescent particles in a PIV/PLIF[4] combined metrology. This technique was used in the work of Prasad and Sreenivasan (1989) and of Westerweel et al. (2009), for instance. An example of the detected TNTI in Prasad and Sreenivasan (1989) is shown in figure 5.6, where a turbulent jet marked with fluorescent dye was studied. This type of method can provide very accurate results if certain conditions are met. Namely, if a fluorescent dye is used (like Rhodamine B), not only must this additional tracer respect the typical PIV criteria (cf. chapter 3 §3.5.2) but it must also have a high enough Schmidt number Sc. The Schmidt number is a dimensionless parameter comparing the viscous diffusion of a fluid and its mass diffusivity. A high Schmidt number ($Sc \gg 1$) ensures that the tracers do not diffuse into the irrotational parts of the flow. In water and other liquids, this is much more feasible than in air since these fluids have naturally high Schmidt numbers (Goldman and Marchello, 1969). Furthermore, a PIV/PLIF method increases the cost and complexity of the experimental set-up, since it involves more resources (laser units,

[4]Planar Laser-Induced Fluorescence (Imaging).

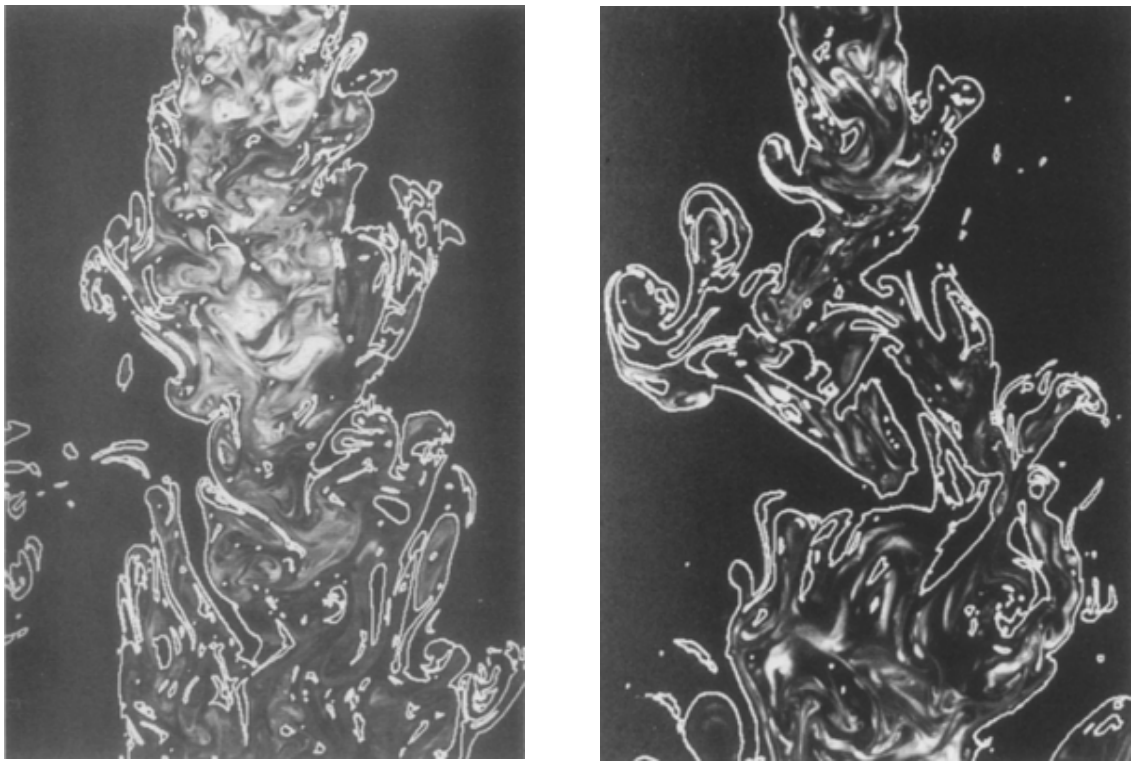

Figure 5.6: PLIF visualisation of the TNTI of a turbulent jet at two distinct regions and times. Taken from Prasad and Sreenivasan (1989).

cameras, filters) than regular PIV. An interesting alternative way to directly detect the TNTI using only PIV images is also found in Gan (2016) and further developed by Li et al. (2021b). This method uses different seeding densities in the ambient fluid and in the turbulent flow to obtain a sharp density contrast at the TNTI. This method has proven just as accurate as a PIV/PLIF combined method without increasing the experimental complexity and cost. However, in the case of the wake of a porous disc, differentiating seeding densities would involve changing the test rig in order to locally seed the wake of the porous disc. This method was tested during the thesis but proved highly challenging. This option is discussed in more detail in the perspectives of the manuscript.

5.3.1 Turbulent kinetic energy approach

For the reasons stated above, the scientific community has favoured TNTI detection techniques based on the flow properties at this interface from conventional PIV/SPIV data. As seen in the first section of this chapter, the TNTI is the frontier between an irrotational, quiescent free-stream and a highly rotational turbulent wake. Ideally, the TNTI can be hence detected from vorticity since it is by definition, the natural physical parameter with a sharp jump at the interface (irrotational vs. rotational regions) of the turbulent wake (Prasad and Sreenivasan, 1989). However, computing vorticity requires a very high spatial resolution and volumetric data of all three components of velocity. This is readily available in high fidelity numerical simulations like in the work of Bisset et al. (2002) or Zhou and Vassilicos (2017), but is much more difficult to obtain experimentally.

Recent investigations, such as those conducted by de Silva et al. (2013), Chauhan et al.

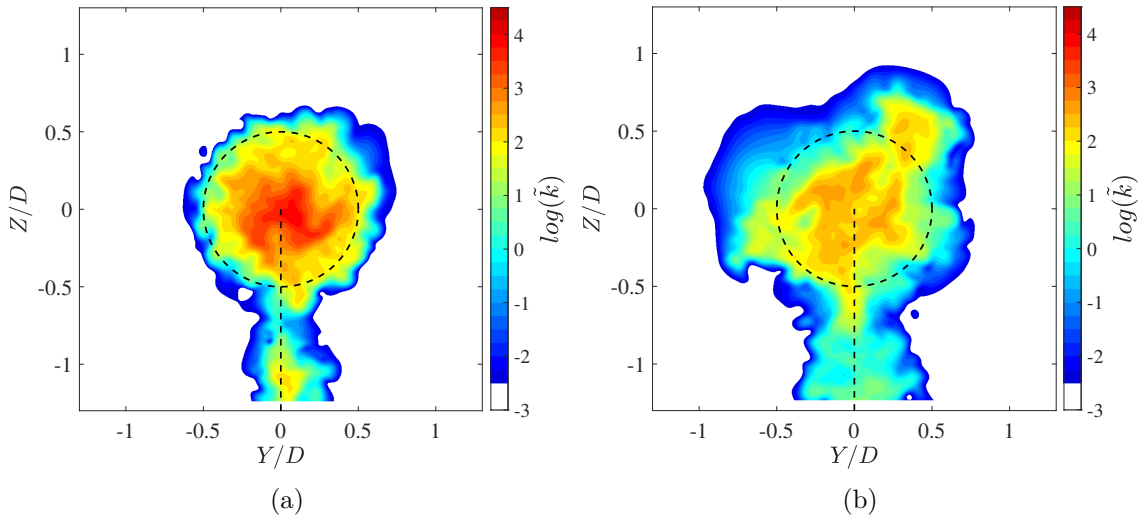

Figure 5.7: Example of a randomly chosen instantaneous field of $\log(\widetilde{k})$ for the $\alpha = 15°$ case at (a) $X = 2D$ and at (b) $X = 7D$.

(2014) and Stella et al. (2018) showed that another scalar can be used to accurately detect the TNTI: the turbulent kinetic energy $\tilde{k}$, averaged over a spatial kernel. In these studies, the TKE scalar is used to mark the turbulent flow by computing $\tilde{k}$ in percentage of the mean free-stream kinetic energy as follows:

$$\frac{\widetilde{k}}{100} = \frac{1}{U_\infty^2 + V_\infty^2 + W_\infty^2} \frac{1}{9} \sum_{m,n=-1}^{1} [(\widetilde{U}_{x_{m,n}} - U_\infty)^2 + (\widetilde{U}_{y_{m,n}} - V_\infty)^2 + (\widetilde{U}_{z_{m,n}} - W_\infty)^2], \quad (5.3.1)$$

where V_∞ and W_∞ are the free-stream spanwise and vertical velocity, respectively. Equation (5.3.1) implies an average over a 3×3 kernel to filter out possible measurement noise as advised in Chauhan et al. (2014) and Stella et al. (2018). Figure 5.7 depicts two examples of $\log(\widetilde{k})$ computed for the $\alpha = 15°$ case at two distinct streamwise locations $X = 2D$ and $X = 7D$. In the quiescent free-stream, $\widetilde{k}$ exhibits uniform values around the free-stream turbulence intensity 0.35% and increases rapidly as one enters the wake. This technique is an attractive alternative since it can be directly implemented to classic PIV data and does not require volumetric data. However, the TNTI detection from the $\widetilde{k}$ fields, is an iterative process in which a threshold $\widetilde{k}_{th}$ is empirically chosen (Chauhan et al., 2014). Therefore, irrotational velocity fluctuations in the background and in proximity to the TNTI are not discriminated by this technique. Moreover, the kernel averaging involved in equation (5.3.1) is a significant drawback when detecting the TNTI since it filters out the highly tortuous interface. This filtering implies that scales smaller than the size of the kernel will not be detected by this method and small-scale entrainment would be impossible to assess. This method therefore relies on the assumption that the total mass flux across the TNTI is invariant across scales (Meneveau and Sreenivasan, 1990).

5.3.2 Uniform momentum zones

A more robust alternative based on uniform momentum zones (UMZ) was also explored in recent works like those of Adrian et al. (2000b); Kwon et al. (2014); de Silva

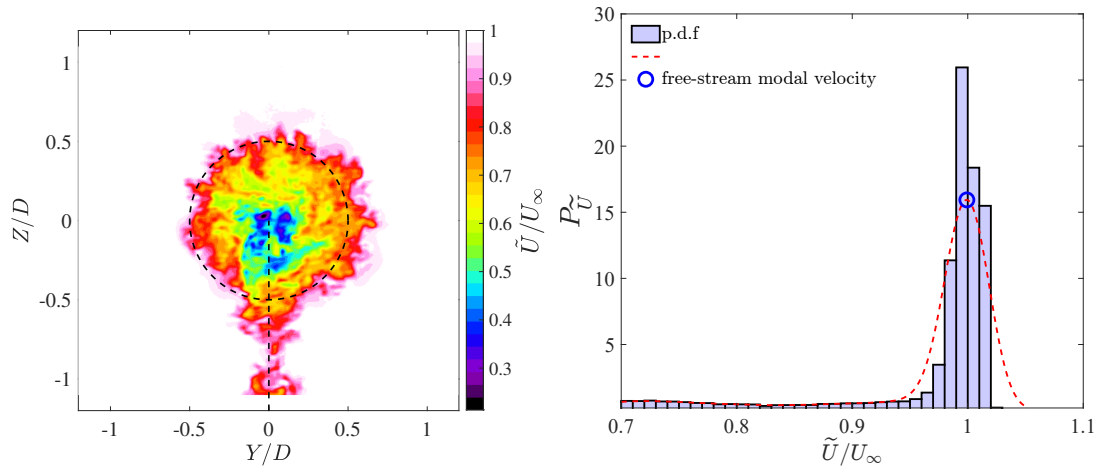

(a) (b)

Figure 5.8: Free-stream modal velocity example for the $\alpha = 15°$ case at $X = 2D$. (a) Example of an instantaneous normalised streamwise velocity field $\widetilde{U}/U_\infty$. (b) the corresponding probability distribution function $P_{\widetilde{U}}$.

et al. (2016); Stella et al. (2018). In these investigations, this method proved to be quite accurate, robust and much less sensitive to measurement noise than the $\widetilde{k}$-based approach. Following de Silva et al. (2016), uniform momentum zones, as the name implies, are regions of fluid with roughly uniform streamwise velocity magnitude. Their existence was first evidenced in the seminal work of Meinhart and Adrian (1995) and then thoroughly described in Adrian et al. (2000b). These UMZs, are separated by thin shear layers which show sharp jumps in vorticity, velocity and turbulent kinetic energy. According to the work of Adrian et al. (2000b), the uniformity of these regions is assessed through the peaks of the probability density function $P_{\widetilde{U}}$ (p.d.f) of the instantaneous streamwise velocity component called "probability modes" (Adrian et al., 2000b). These heaps of $P_{\widetilde{U}}$ are characteristic of UMZs and can be found throughout the interrogation region of the flow. Each local maxima of the streamwise p.d.f is referred to as a modal velocity and the local minimum of $P_{\widetilde{U}}$ between modes corresponds to a boundary between UMZs (Adrian et al., 2000a; Kwon et al., 2014).

For turbulent boundary layers without separation, at least two modes can be easily identified by inspecting $P_{\widetilde{U}}$ (Kwon et al., 2014). The interface detection then simply consists in finding the local minima of $P_{\widetilde{U}}$ between modes. These minima give the velocity level iso-sets which correspond to the boundaries between UMZs. In this manner, the TNTI can be assimilated to a velocity iso-contour equal to the local minimum between the free-stream mode and the nearest mode with a lower velocity value (de Silva et al., 2016). Note that a velocity iso-contour is not the same thing as the TNTI but allows us to give a definition of a physical interface relevant to the wake in proximity to the real TNTI. This approach proved effective in the work of de Silva et al. (2016) and Kwon et al. (2014) given that local minima were clearly defined. In the case of the wake of a porous disc, as reported in figure 5.8, a local minimum of $P_{\widetilde{U}}$ between modes is not always clearly defined. There is a clear mode corresponding to the quiescent free-stream at $\widetilde{U}/U_\infty \approx 1$ but secondary modes are difficult to define. In fact, like in the work of Stella et al. (2018) where the separation of a boundary layer above a ramp was studied, $P_{\widetilde{U}}$ shows a clear free-stream mode but then remains fairly uniform. Therefore, defining a local minimum is not straightforward, which complicates the detection of the interface. To tackle this issue, Stella et al. (2018)

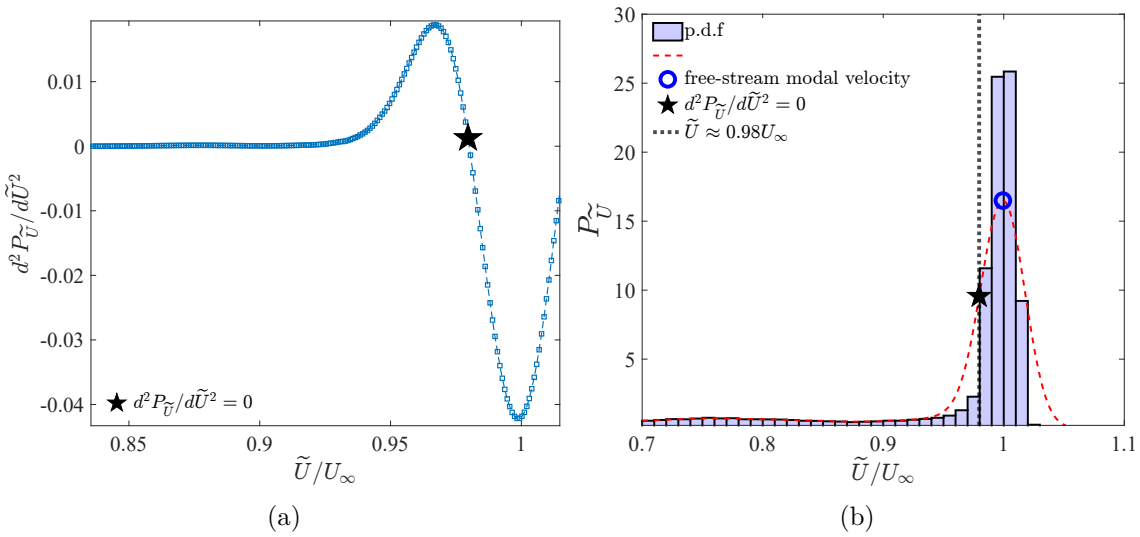

Figure 5.9: Example of the streamwise velocity p.d.f inflection point computation. (a) shows the first zero-crossing of $d^2P_{\widetilde{U}}/d\widetilde{U}^2$ and (b) the probability distribution function with the computed inflection point.

proposed to define the lower boundary of the free-stream mode as the inflection point of $P_{\widetilde{U}}$. This particular point can be computed by calculating the first zero-crossing of the second derivative of $P_{\widetilde{U}}$ such as:

$$\frac{d^2P_{\widetilde{U}}}{d\widetilde{U}^2} = 0. \tag{5.3.2}$$

The computation process of the velocity iso-set using this approach is illustrated in figure 5.9. As reported in figure 5.9a, the high spatial resolution of the SPIV data obtained in this particular case grants a low enough noise level so that the inflection point can be easily computed for each snapshot. However, the main drawback of this approach is that it deviates from the original definition of UMZs boundaries established by Adrian et al. (2000b). In fact, the boundary of the UMZ corresponds to a local minimum between modes or, the foot of the mode where momentum starts to show uniformity. As shown in figure 5.9b, the inflection point of $P_{\widetilde{U}}$ is located between the modal velocity and the foot of the mode. To address this issue an alternative method is proposed in this work with the aim to match closely the original definition of UMZs. The proposed approach is inspired from the work of Kovacs et al. (2022), where a Fourier self-deconvolution (FSD) based method was introduced to detect a shock-wave. A full description of FSD can be found in the works of Tooke (1988) and Kauppinen and Partanen (2001), as only a brief explanation is presented here. In Kovacs et al. (2022), the FSD method was used to capture the shock foot as well as the shock centre through the study of density variations across the shock. Adapting this technique to UMZs, one can define an interface near the TNTI as the foot of the free-stream mode, rather than the inflection point. This adaptation is mathematically sound since $P_{\widetilde{U}}$ is a continuous, monotonic function of $\mathbb{R} \rightarrow \mathbb{R}^+$ which admits a local maximum at the modal velocity (de Silva et al., 2016). These are necessary and sufficient conditions in order to carry out the FSD method which is explained in the following paragraph and illustrated in figure 5.10.

Let $f(\widetilde{U}) = P_{\widetilde{U}}$ be the probability density function of the normalised streamwise velocity field for any given snapshot. The Fourier transform of f is then defined as:

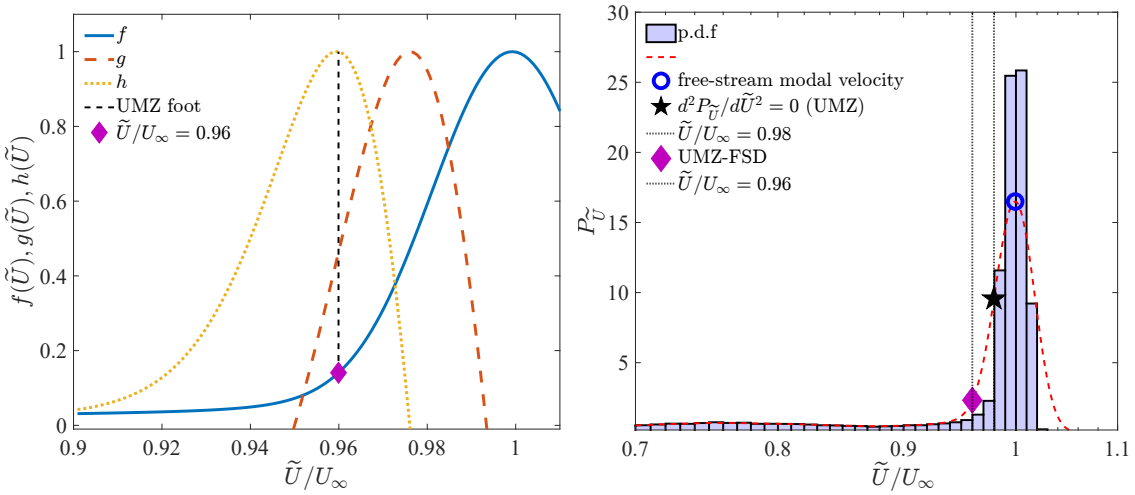

Figure 5.10: Fourier self-deconvolution methodology to capture the TNTI velocity iso-set compared to the inflection point method of Stella et al. (2018). (a) shows the detection methodology and (b) depicts the detected level in the probability histogram of the snapshot.

$$\mathscr{F}(f(\widetilde{U})) = \hat{f}(\xi) = \int_{-\infty}^{+\infty} f(\widetilde{U}) e^{-i\xi\widetilde{U}} d\widetilde{U}, \tag{5.3.3}$$

and the inverse Fourier transform is given by:

$$\mathscr{F}^{-1}(\hat{f}(\xi)) = f(\widetilde{U}) = \int_{-\infty}^{+\infty} \hat{f}(\xi) e^{+i\xi\widetilde{U}} d\xi, \tag{5.3.4}$$

Following Kovacs et al. (2022), the self-deconvolution function $g(\widetilde{U})$ can be computed as:

$$g(\widetilde{U}) = \mathscr{F}^{-1}(\hat{f}(\xi) \cdot \hat{f},(\xi)), \tag{5.3.5}$$

which is an operation requiring a so-called apodization window $A(\widetilde{U})$. Here, $A(\widetilde{U})$ corresponds to a simple truncating function between the free-stream mode and an empirical lower boundary $\widetilde{U}_b$ chosen far enough from the mode or the minimum streamwise velocity. Equation (5.3.5) can be written with the use of the apodization window yielding:

$$g(\widetilde{U}) = \mathscr{F}^{-1}(\mathscr{F}(A(\widetilde{U}) f(\widetilde{U})) \cdot \mathscr{F}(A(\widetilde{U}) f(\widetilde{U}))), \tag{5.3.6}$$

where $A(\widetilde{U})$ is defined to be $A = 1$ from $\widetilde{U}_b$ to the free-stream and $A = 0$ elsewhere. The resulting self-deconvolution function $g(\widetilde{U})$ can be then derived with respect to $\widetilde{U}$ to obtain:

$$h(\widetilde{U}) = \frac{dg(\widetilde{U})}{d\widetilde{U}}, \tag{5.3.7}$$

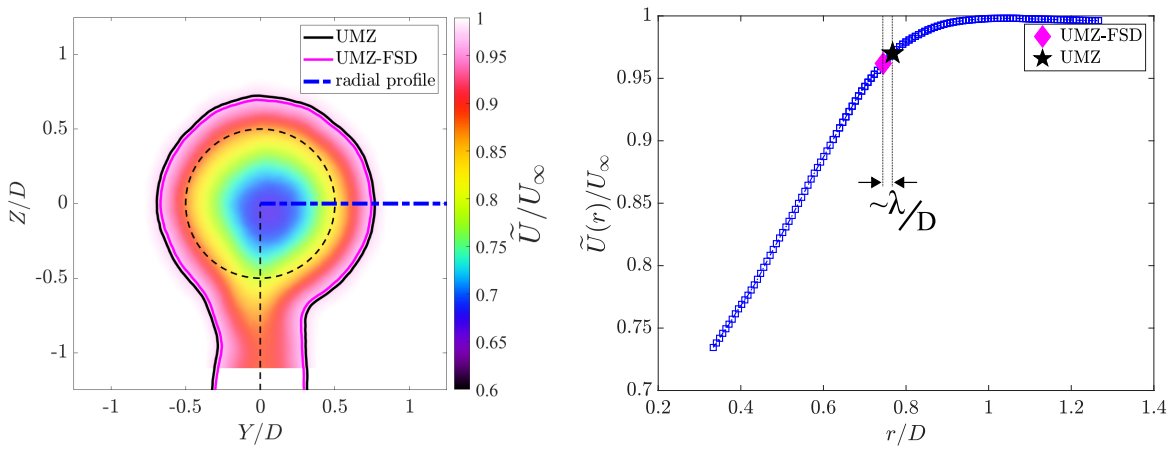

Figure 5.11: Example of the detected mean TNTI using the UMZ and UMZ-FSD methods for case $\alpha = 15°$ at $X = 7D$ showing (a) a spanwise mean streamwise velocity field and (b) a radial profile taken at $\phi = 0°$.

and finally, the maximum of $h(\widetilde{U})$ corresponds to the foot of the free-stream mode i.e the TNTI velocity iso-set. As shown in figure 5.10, the FSD method captures the foot of the free-stream mode without the need of setting a threshold. The detection of the mean TNTI using both approaches is exemplified in figure 5.11 for case $\alpha = 15°$ at $X = 7D$ but the results are identical at other streamwise locations and for $\alpha = 0°$. Both methods show almost identical results as the distance between the detected mean TNTIs is around the Taylor micro-scale λ for all azimuthal angles ϕ. Therefore, the UMZ and the UMZ-FSD methods yield the same result when detecting the mean TNTI. However, this is not the case for the instantaneous TNTI detection.

Figure 5.12 shows the TNTI of random snapshots taken for case $\alpha = 15°$ at $X = 2D$ and at $X = 7D$ using both UMZ detection methods. The normalised streamwise velocity fields are plotted as well as the available component of vorticity normalised using global parameters $\omega_x D/U_\infty$. In this example, it is clear that the differences between the TNTIs are subtle in some regions and quite evident in others. In some zones of the wake, both methods appear to collapse reasonably well but in some other areas, the differences are significant. In the example depicted in figure 5.12, the distance between the contours reaches 14 mm ($\sim \mathcal{L}_{int}$). In fact, the method proposed by Stella et al. (2018) overestimates the rotational regions of the flow as evidenced in figures 5.12c and 5.12d. Furthermore, in some regions of the flow the inflection point method shows unphysical excursions of the TNTI far from the rotational wake.

To quantify the difference between these methods and justify the TNTI detection improvement using FSD, an accuracy test was performed by examining radial profiles of streamwise velocity $\widetilde{U}(r)$, 2D enstrophy $\sqrt{\omega_x^2}(r)$ and $\widetilde{k}$. Many profiles were examined at different downstream locations and at different azimuthal angles ϕ. An example of such test at an angle where the methods collapse and where they differ the most is shown in figures 5.13 and 5.14, respectively. As shown in figure 5.13, when the methods collapse, the velocity iso-sets are the same but also the corresponding jump of enstrophy and TKE, as only marginal differences are observed. On the other hand, as presented in figure 5.14, at an angle where the methods differ, the gradient method overshoots the position of the TNTI and fails to catch the enstrophy jump. The overestimation of the gradient method reaches distances close to the integral length scale $\mathcal{L}_{int}$ depending

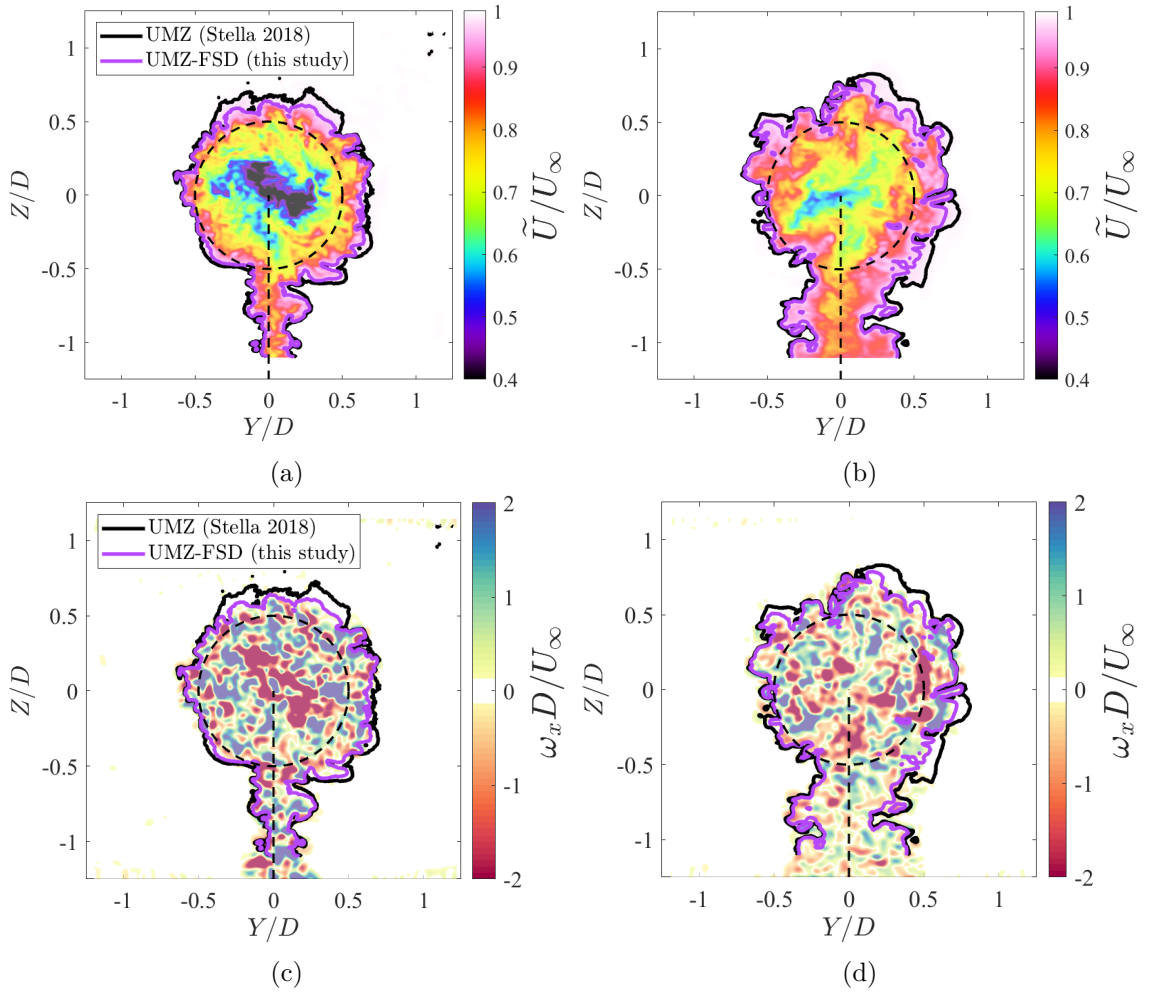

Figure 5.12: TNTI detection method based on uniform momentum zones. The figure compares the convention proposed in Stella et al. (2018) (black lines) to the one proposed in this investigation (purple lines). Normalised streamwise velocity fields at (a) $X = 2D$ and at (b) $X = 7D$ are presented as well as (c, d) normalised out-of-plane 2D-vorticity fields at the same locations.

on the examined angle. On the other hand, the FSD method shows a better detection of the enstrophy and TKE jumps. All in all, the FSD UMZ method, proposed in this work, appears as an improvement of the gradient approach proposed in Stella et al. (2018). The UMZ-FSD method thereby achieves a finer capturing of the instantaneous TNTI for several cases and shows higher robustness. This tackles the absence of a neighbouring mode in a way more akin to the original definition of the TNTI using UMZs (Adrian et al., 2000b; Kwon et al., 2014). For these reasons, this method was used to detect the TNTI for the bulk of the entrainment study.

5.4 Mean entrainment: average mass flux

The previous chapter has shown that swirl modified the way the wake of the porous disc expanded and recovered with the streamwise direction. This result already gives partial information on the effect of swirl regarding mean entrainment. In this section, the average mass entrainment is investigated.

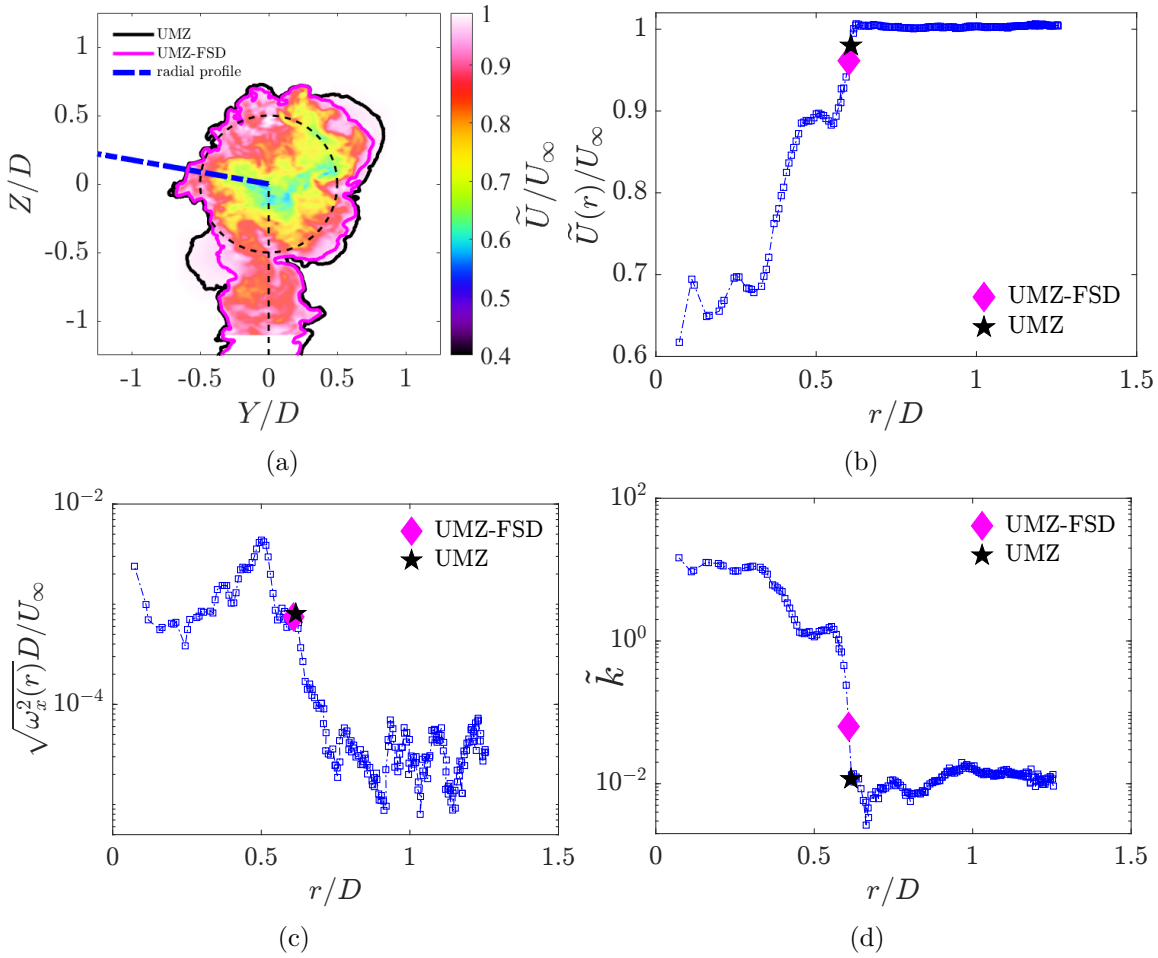

Figure 5.13: Example of the UMZ vs. UMZ-FSD TNTI detection method accuracy collapse showing (a) a random mean streamwise velocity field where radial profiles of (b) normalised mean streamwise velocity, (c) normalised enstrophy and (d) normalised TKE are plotted. Dashed black lines: test rig outline. The example radial profile is chosen at an azimuthal angle $\phi = 30°$.

Figure 5.15 depicts the mean swirling velocity cross-sections at different streamwise locations for the $\alpha = 15°$ case with particular attention to the $X = 3D$ location. It is clear that the TNTI does not describe a closed contour because of the mast, but can be closed through a horizontal segment at the lowest TNTI z-coordinate. In this plane, the TNTI has a tennis racket shape due to the presence of the mast. However, it has a roughly circular shape for the wake of the porous disc itself. This remains true for all streamwise positions as the wake expands and recovers. As detailed in the previous chapter, swirl expands radially and quickly decays. In terms of distribution with respect to the TNTI the swirling motion is always concentrated in a region below the TNTI without crossing it. Therefore, the azimuthal velocity vectors are expected to be tangential to the mean TNTI for the most part (figure 5.15). This leads to the conclusion that mean swirl is not expected to directly entrain mass across the TNTI. However, mean swirl has a direct influence on the pressure distribution across the wake. It was shown that swirl creates a core of low pressure at the centre of the wake. This will most likely indirectly change the total mass entrainment across the mean TNTI through other mechanisms.

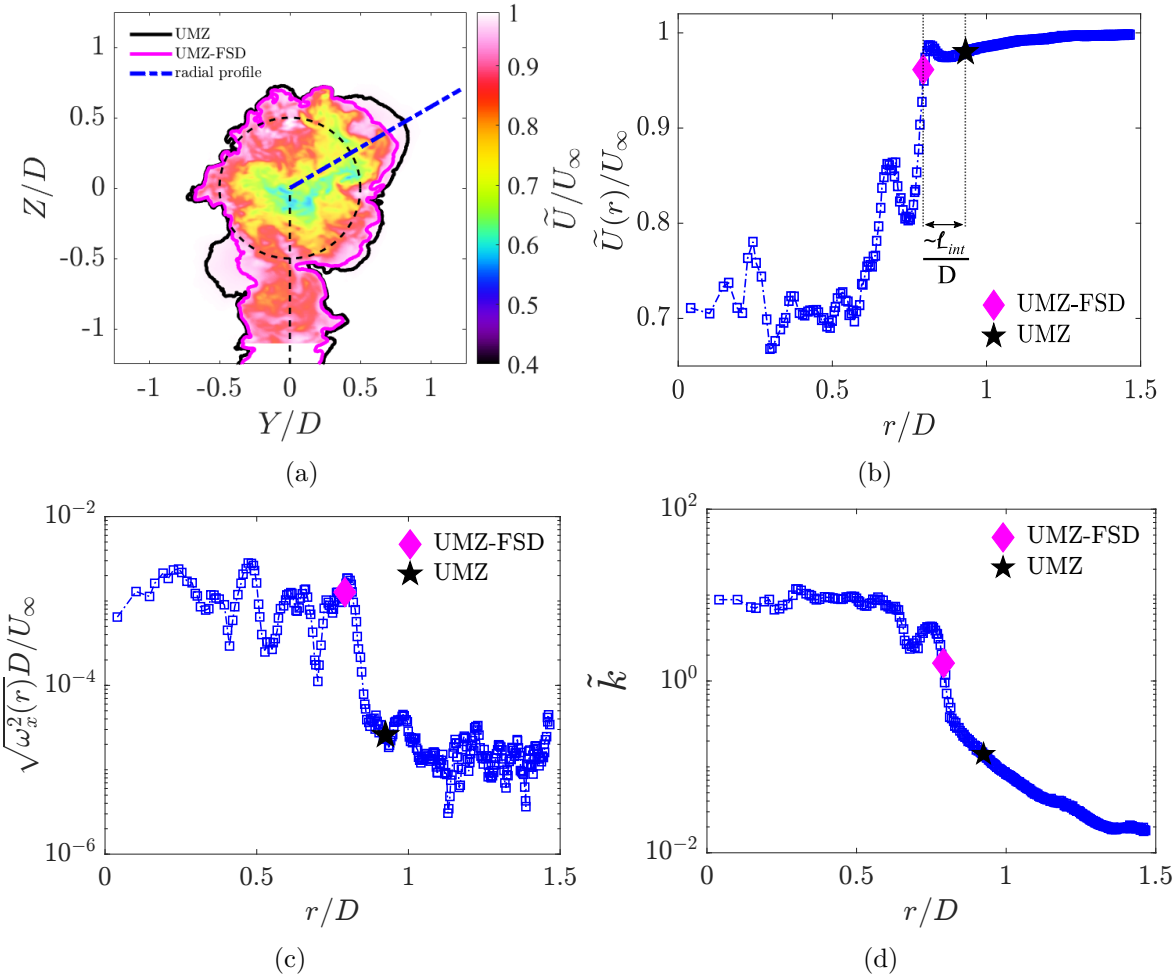

Figure 5.14: Example of the UMZ vs. UMZ-FSD TNTI detection method accuracy difference showing (a) a random mean streamwise velocity field where radial profiles of (b) normalised mean streamwise velocity, (c) normalised enstrophy and (d) normalised TKE are plotted. Dashed black lines: test rig outline. The example radial profile is chosen at an azimuthal angle $\phi = 170°$.

5.4.1 Mass entrainment between cross-sections

Mean entrainment can be evaluated through the average mass flux across the mean TNTI. Figure 5.16 explains how mean entrainment can be computed between the measured cross-sections of the wake. These figures show the mean normalised streamwise velocity cross-sections at different downwind locations for the $\alpha = 15°$ case as an example. For each cross-section, the TNTI can be detected using the UMZ-FSD method described in the previous section. Let's define a control volume $\mathcal{V}_c$ whose inlet and outlet surfaces are delimited by two consecutive cross-sections located at x_1 and x_2, respectively (see figure 5.16). Therefore, the defined control volume $\mathcal{V}_c$ encompasses the rotational region of the flow. Since the flow is incompressible, mass is conserved in $\mathcal{V}_c$ such as:

$$\rho \int_{\mathcal{V}_c} \frac{\partial U_i}{\partial x_i} dV = 0. \tag{5.4.1}$$

Equation 5.4.1 can be transformed into a sum of fluxes through the boundaries of $\mathcal{V}_c$ following the Green-Ostrogradsky theorem such as:

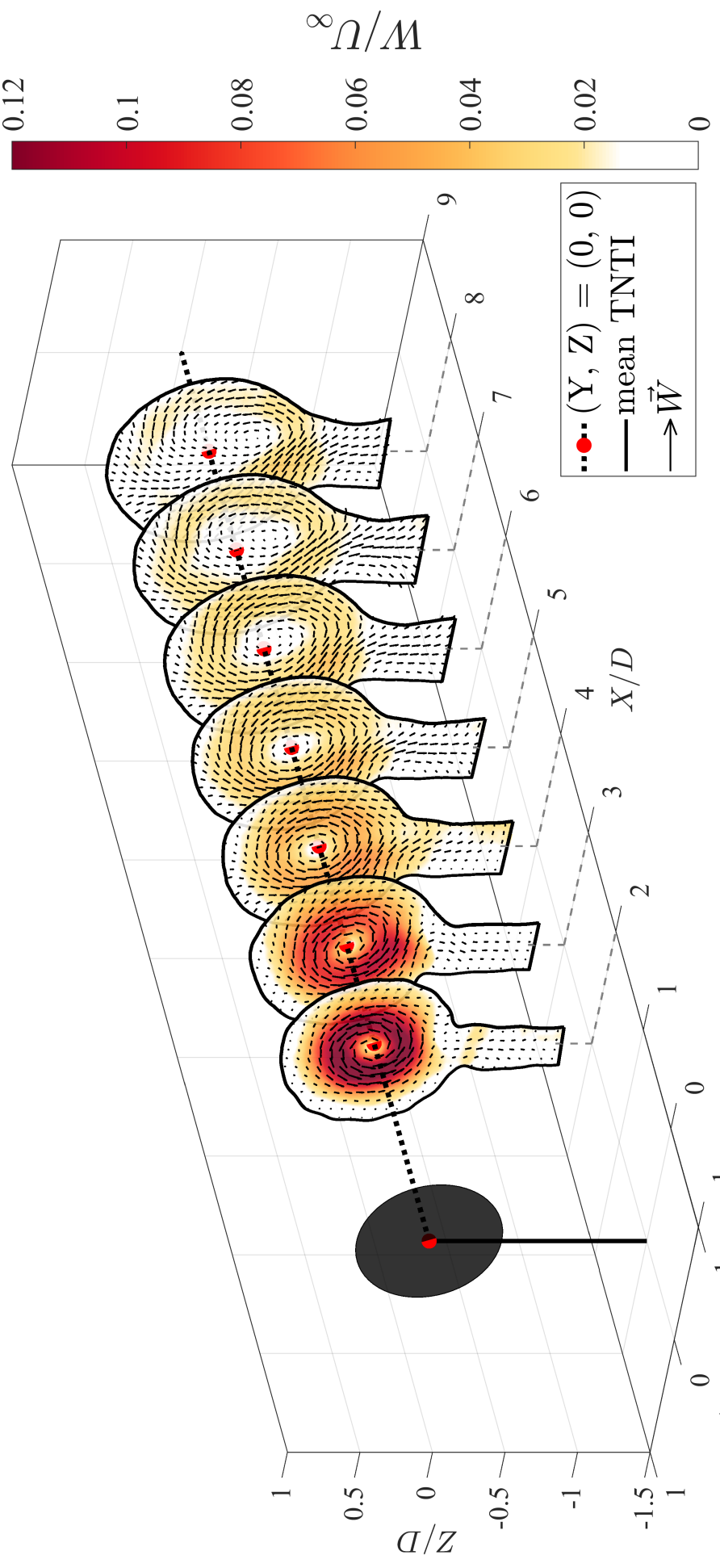

Figure 5.15: Mean normalised swirling velocity cross-sections for the $\alpha = 15°$ case at all measured downwind locations. Black patched area: porous disc location, black line: mast outline, arrows: swirling velocity vectors.

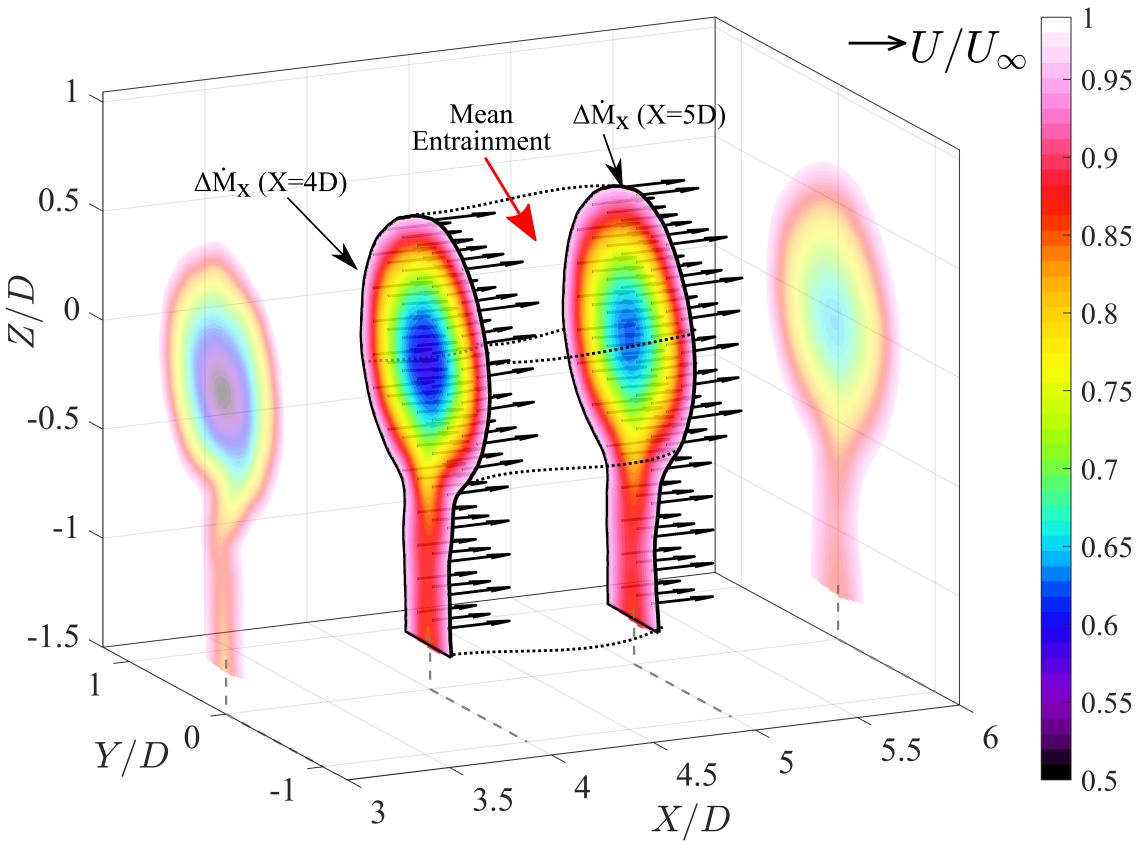

Figure 5.16: Diagram showing the computation of the inter-plane mean entrainment $\dot{M}_E$ between $X = 4D$ and $X = 5D$. The dotted black lines are a graphical representation of the two-dimensional TNTI between cross-sections.

$$\rho \oint_{\mathcal{S}_c} U_i n_i dS = 0, \tag{5.4.2}$$

where n_i is the outward local normal vector to $\mathcal{S}_c$, the surface delimiting $\mathcal{V}_c$. The essence of the mass conservation equation (5.4.2) is that all mass fluxes across $\mathcal{S}_c$ must balance out. Equation (5.4.2) can be rewritten in terms of mass deficit yielding:

$$\rho \oint_{\mathcal{S}_c} (U_\infty - U_i) n_i dS = 0, \tag{5.4.3}$$

where $\rho \oint_{\mathcal{S}_c} U_\infty n_i dS = \vec{0}$ by definition. Equation (5.4.3) can be decomposed into a sum of mean deficit mass fluxes across the following surfaces:

$$\underbrace{-\rho \oint_{\mathcal{S}_1} (U_\infty - U_i) n_i dS}_{\text{mass deficit inflow}} + \underbrace{\rho \oint_{\mathcal{S}_2} (U_\infty - U_i) n_i dS}_{\text{mass deficit outflow}} + \underbrace{\rho \oint_{\mathcal{S}_{TNTI}} (U_\infty - U_i) n_i dS}_{\text{mean entrainment}} = 0, \tag{5.4.4}$$

where S_1 and S_2 are the surfaces of the wake at two consecutive cross-sections and S_{TNTI} is the surface of the TNTI between S_1 and S_2. Figure 5.16 illustrates the fluxes through these surfaces taken between $X = 4D$ and $X = 5D$. The first two terms in equation (5.4.4) can be computed from the streamwise velocity measurements

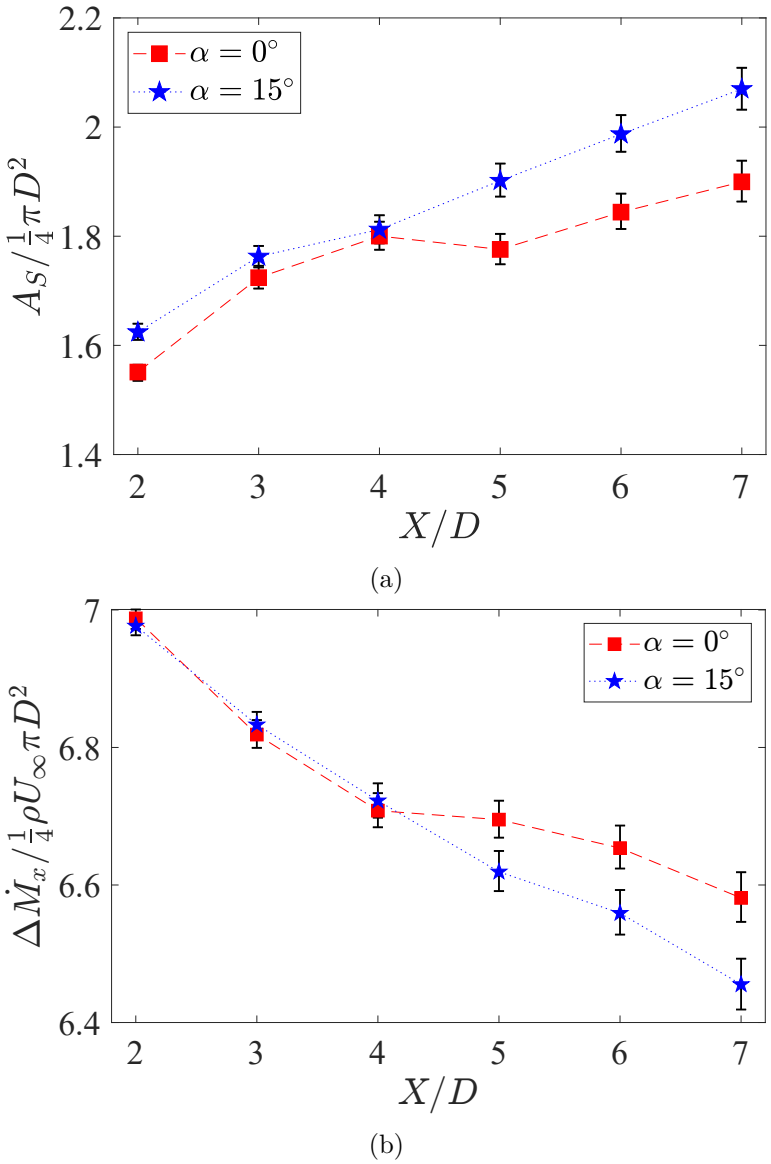

Figure 5.17: Mean entrainment evaluation at different cross-sections for cases $\alpha = 0°$ and $\alpha = 15°$. The streamwise evolution is reported for (a) the wake's area A_s and for (c) the average mass deficit flux $\Delta\dot{M}_x$.

at each downwind location yielding the mass deficit flux through S_1 : $\Delta\dot{M}_x(x_1) = \rho \oint_{S_1} (U_\infty - U_i) n_i dS$ and the same for S_2.

Figure 5.17 reports the streamwise evolution of the average mass fluxes across the different surfaces. In particular, the total area of the rotational region, noted A_S, can be calculated at each streamwise location. The mass fluxes are normalised by $\frac{1}{4}\rho U_\infty \pi D^2$. As evidenced in figure 5.17a, there is an overall increase in the size of the wake for the swirling case. The location $X = 4D$ marks a difference in trends due to the extent of the mast's influence and a change in wake expansion. Before $X = 4D$ the swirling wake is slightly bigger than the non-swirling wake. Beyond $X = 4D$ the difference is more distinguishable and shows an increase as the wake expands. Therefore, swirl increases the total area of the wake, which results in a bigger TNTI i.e a larger surface for entrainment to act. Despite the bigger integration surface for the swirling case, the mass deficit fluxes across S_c appear to be unchanged by swirl before $X = 4D$ (figure 5.17b). This is due to the increased velocity deficit in the near field of the swirling

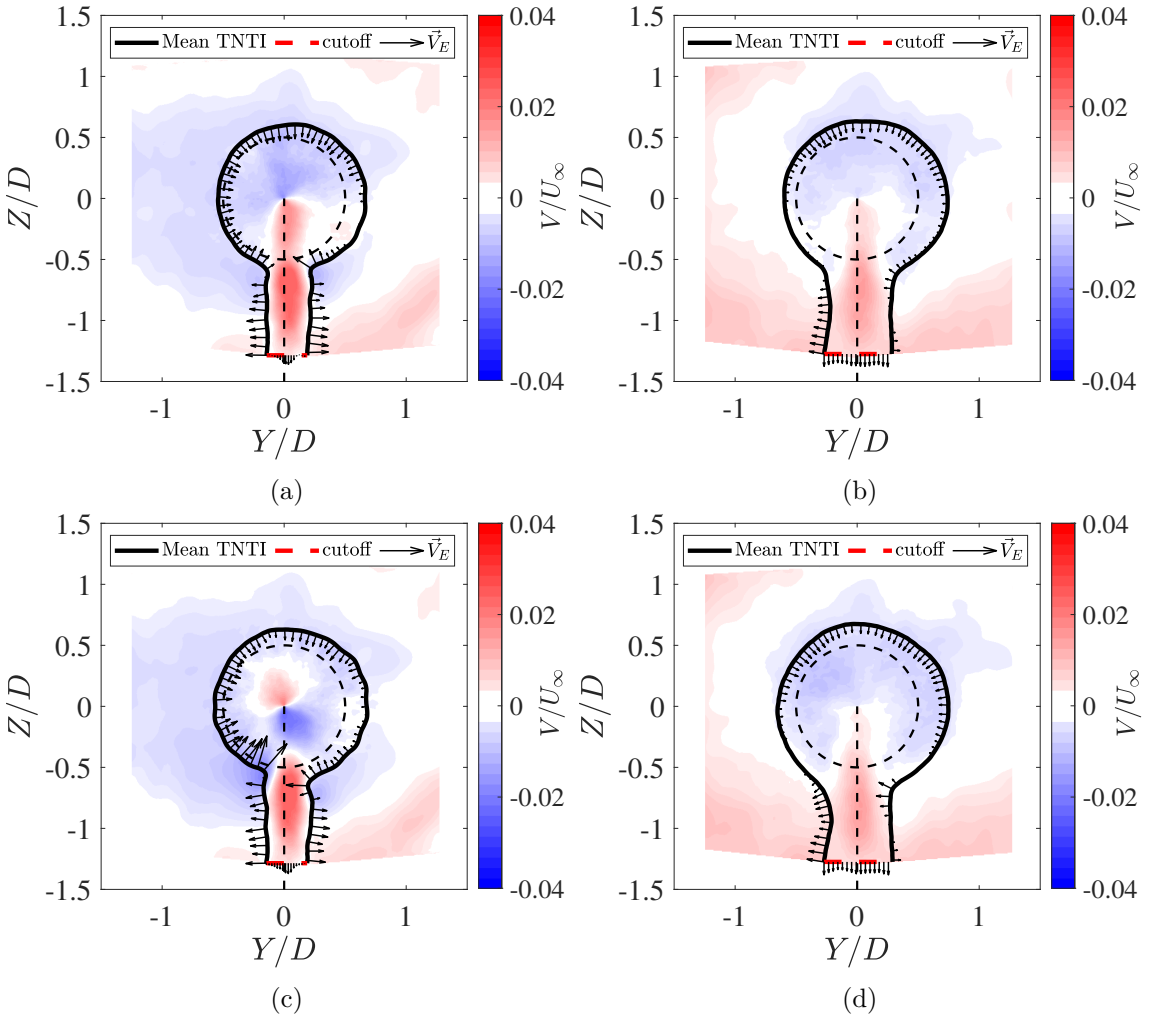

Figure 5.18: In-plane lateral entrainment maps showing the mean radial velocity component V/U_∞ and the velocity vectors normal to the TNTI ($\vec{V}_E$) for cases $\alpha = 0°$ (top) and $\alpha = 15°$ (bottom). Two streamwise locations are shown at (a, c) $X = 2D$ and (b, d) $X = 6D$. The vectors $\vec{V}_E$ are up-scaled of a factor 10 for visibility.

case discussed in chapter 4. Therefore, the bigger surface of the wake is compensated by the larger deficit to yield a similar mass deficit flux $\Delta\dot{M}_x$ in the near field. Beyond $X = 4D$ however, $\Delta\dot{M}_x$ decreases faster for the swirling wake. All in all, these results suggest that mean entrainment has been increased by swirl mainly by increasing the exchange surface. In the following section, the mean entrainment velocity is calculated to verify this hypothesis.

5.4.2 Lateral inflow of mass: mean entrainment velocity

The previous section established that swirl increases the mean effective surface where radial inflow of mass brings high momentum free-stream fluid into the wake (see figure 5.5). Figure 5.18 shows normalised mean radial velocity fields for cases $\alpha = 0°$ and $\alpha = 15°$ at $X = 2D$ and $X = 6D$, respectively. An in-plane control surface S_x is defined at each streamwise location x. The contours of S_x are delineated by the TNTI and closed at a cutoff vertical position $Z_{cut} = -1.25D$ (the border of the FoV). The total mass flux per unit depth through S_x is given by:

$$\dot{m}_{\text{lat}}(x) = -\rho \int_{L_{TNTI}} U_i n_i d\ell - \rho \int_{L_c} U_i n_i d\ell, \tag{5.4.5}$$

where L_{TNTI} is the length of the TNTI, L_c is the length of the cutoff segment and n_i is the unit normal to S_x. Here, the mean mass flux crossing L_c is an order of magnitude below the other term. Therefore, $\dot{m}_{\text{lat}}(x)$ is essentially the lateral mass flux through the TNTI. Figure 5.18 shows that the radial inflow of mass is indeed very small regardless of swirl. The main difference between cases is that, in the near field ($X = 2D$), the wake of the porous disc seems to be independant of the wake of the mast for the swirling case.

Figure 5.19 reports the streamwise evolution of the total lateral mass fluxes across L_{TNTI} for cases $\alpha = 0°$ and $\alpha = 15°$. Here, the lateral mass fluxes are normalised by $\rho D U_\infty$. As expected, the lateral mass inflow is higher for the swirling case. There appears to be a gradual increase in lateral mass flux up until $X = 4D$ where $\dot{m}_{\text{lat}}$ starts to drop. Interestingly, this position coincides with the location at which the mast's shadow effect fades. This could indicate that the downwash motion, which tends to pull down the wake of the disc, is compensated by an increase in lateral entrainment. The swirling wake shows consistently higher values of $\dot{m}_{\text{lat}}$ at each streamwise location with the exception of $X = 3D$. The values are overall quite similar between cases but an average increase of 15% in lateral mass flux is reported for the swirling case.

We introduced a mean entrainment velocity defined as:

$$V_E(x) = \frac{\dot{m}_{\text{lat}}}{L_{TNTI}}. \tag{5.4.6}$$

The streamwise evolution of the TNTI's perimeter $L_{TNTI}(x)$ and of $V_E(x)/U_\infty$ is reported in figure 5.19. On the other hand, as shown in figure 5.19b, the mean entrainment velocities $V_E(x)$ show almost identical values for both the swirling and the non-swirling case as only a marginal difference is observed at $X = 2D$. Hence, the introduction of swirl appears to have no significant impact on the mean entrainment velocity. Instead, it is the size of the TNTI that experiences an increase with swirl (3-4%) as well as its growth rate. This motivates to further examine the geometrical properties of the instantaneous TNTI and discern which scales of the TNTI were modified by swirl.

5.5 On the multi-scale aspects of entrainment

Since the seminal work of Mandelbrot (1982) and Sreenivasan and Meneveau (1986), turbulent entrainment is considered as a multi-scale phenomenon through a TNTI that appears to show fractal characteristics. This entails that the large scales of entrainment (engulfing motions) are intrinsically linked to the small scales related to viscous transfer (nibbling). This proposition has been backed up by a myriad of studies throughout the years and most recently studied in the work of Zhou and Vassilicos (2017) and Breda and Buxton (2019). Following Stella et al. (2017), this link can be expressed mathematically as:

$$v_E{}^\nu L^\nu = v_E(r)L(r) = v_E{}^\Lambda L^\Lambda \tag{5.5.1}$$

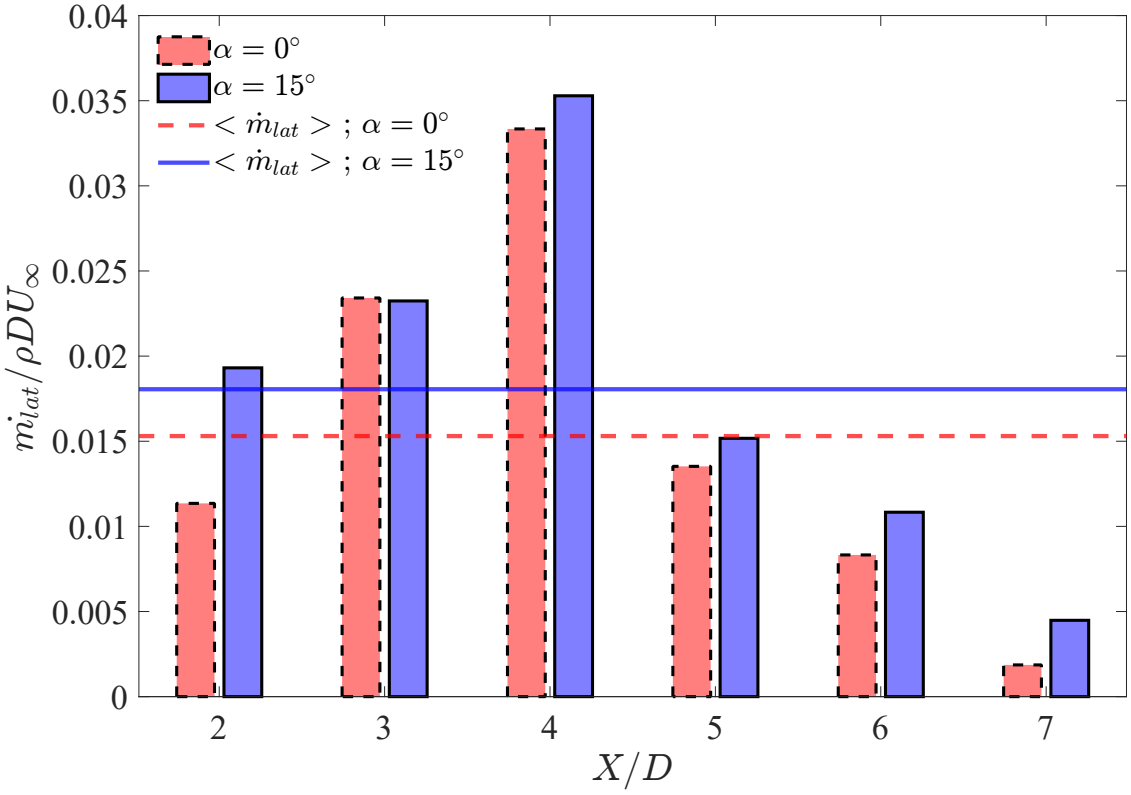

(a)

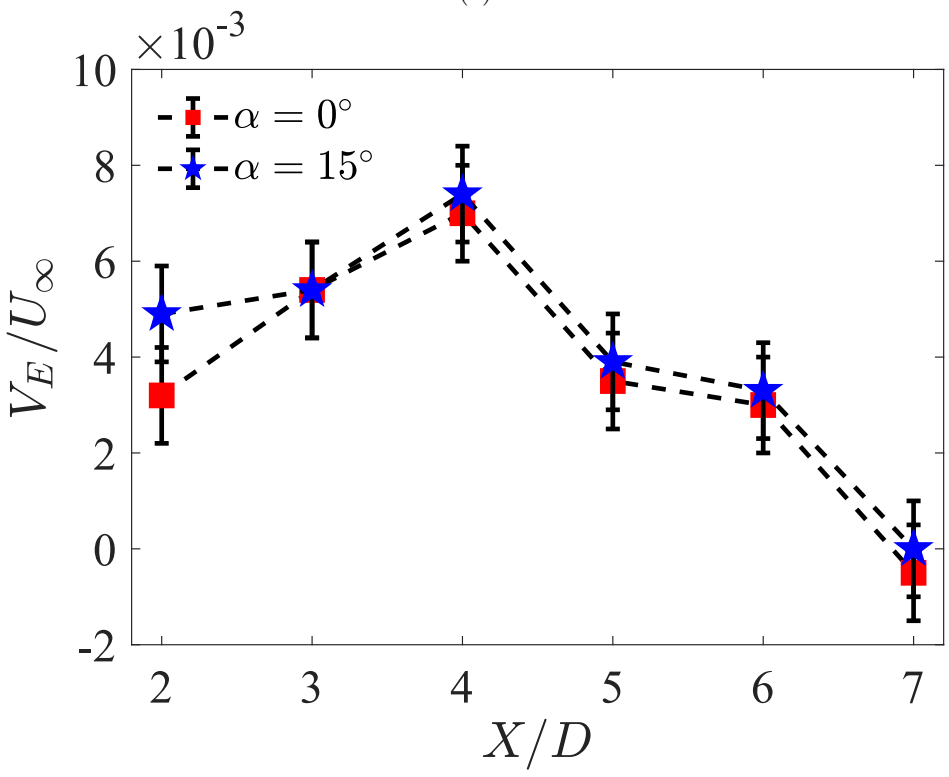

(b)

Figure 5.19: Streamwise evolution of (a) the lateral mass fluxes $\dot{m}_{\mathrm{lat}}(x)$ across the TNTI and (b) the mean entrainment velocity at the interface $V_E(x)/U_\infty$.

where the $^{\nu}$ and $^{\Lambda}$ superscripts denote small and large scales of entrainment, respectively and r represents a length scale of entrainment. This important finding motivates this study to pursue the implications of equation 5.5.1 in terms of a scale-by-scale analysis of entrainment. However, as clearly stated by Mistry et al. (2018), this is not achievable unless accurate information on the geometry and dynamics of the TNTI are accessible. Without proper interface tracking techniques, it is impossible to quantify local entrainment velocities. Nevertheless, the results presented in the last section showed that mean entrainment velocity was not particularly altered by swirl. Instead, the added swirl amplifies the size of the mean TNTI enveloping the wake. This motivates to further investigate the TNTI's geometrical properties which are quantified in the next section.

5.5.1 Geometrical properties of the TNTI: the importance of tortuosity

Recent work on the TNTI, like that of Zhou and Vassilicos (2017) and Breda and Buxton (2019), showed that the geometrical properties of the TNTI have a direct impact on the small scales of entrainment. Indeed, a longer or more tortuous interface leads to a larger surface where nibbling can act. In particular, Breda and Buxton (2019) showed that a change in the geometry of the exit orifice of a jet leads to a more tortuous TNTI in the $r-\phi$ plane, favouring the effective surface where entrainment can take place. Following up on equation (5.5.1), the local entrainment velocity v_E through the length of the instantaneous TNTI can be equated to an effective entrainment velocity V_E through the total length L_{TNTI} of the mean TNTI such as:

$$v_E{}^{\nu} L^{\nu} = V_E L_{TNTI}. \tag{5.5.2}$$

The local entrainment velocity for an axisymmetric wake is known to be mostly driven by the small scales (Bisset et al., 2002). Whether it is the Taylor micro-scale or the Kolmogorov scale is still a matter of debate. In any case, equation 5.5.2 can be written as:

$$v_E{}^{\nu} \tau_{\chi} = V_E, \tag{5.5.3}$$

where τ_{χ} is the tortuosity of the instantaneous TNTI defined as:

$$\tau_{\chi} = \frac{L^{\nu}}{L_{TNTI}}. \tag{5.5.4}$$

The previous section showed that swirl increased the $V_E L_{TNTI}$ term without changing V_E. In fact, as shown in chapter 3 (§3.5.1, table 3.2) the characteristic length scales of turbulence are not significantly modified by swirl as far as small scales are concerned. Therefore, if the hypothesis is made that the local entrainment velocity $v_E{}^{\nu}$ is not significantly changed by swirl then the enhanced entrainment would be solely explained by an increase in tortuosity τ_{χ}.

Figure 5.20 shows two extreme examples of the tortuous TNTI of the swirling wake of case $\alpha = 15°$. Figure 5.20a shows an occurrence of a wake with low TNTI tortuosity $\tau_{\chi} = 1.32$ and figure 5.20b shows an occurrence with high tortuosity $\tau_{\chi} = 2.83$. Both

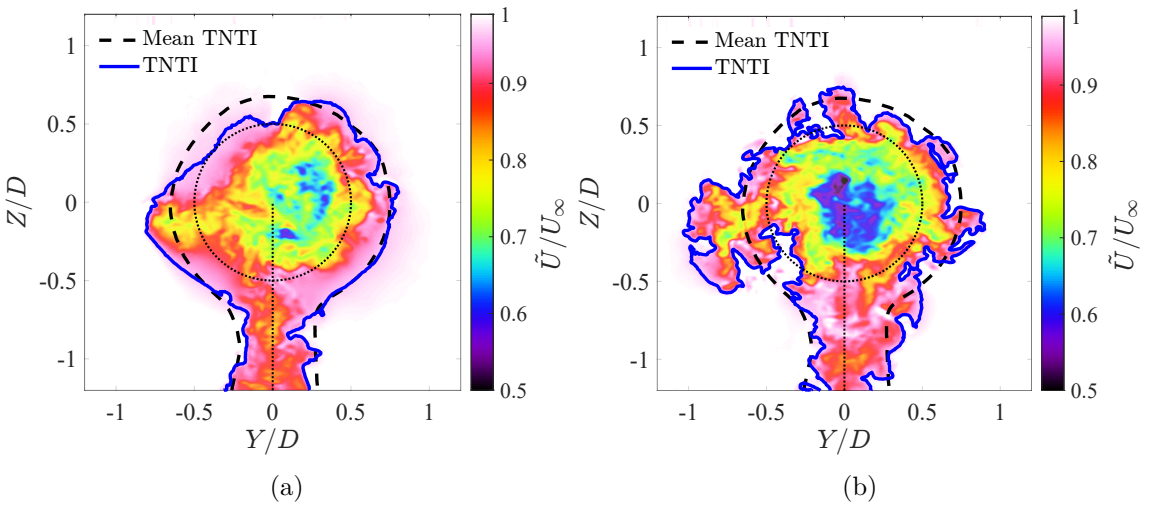

Figure 5.20: Examples of streamwise velocity fields for case $\alpha = 15°$ at $X = 6D$ with their respective mean and instantaneous TNTIs with (a) low tortuosity $\tau = 1.32$ and (b) high tortuosity $\tau = 2.83$.

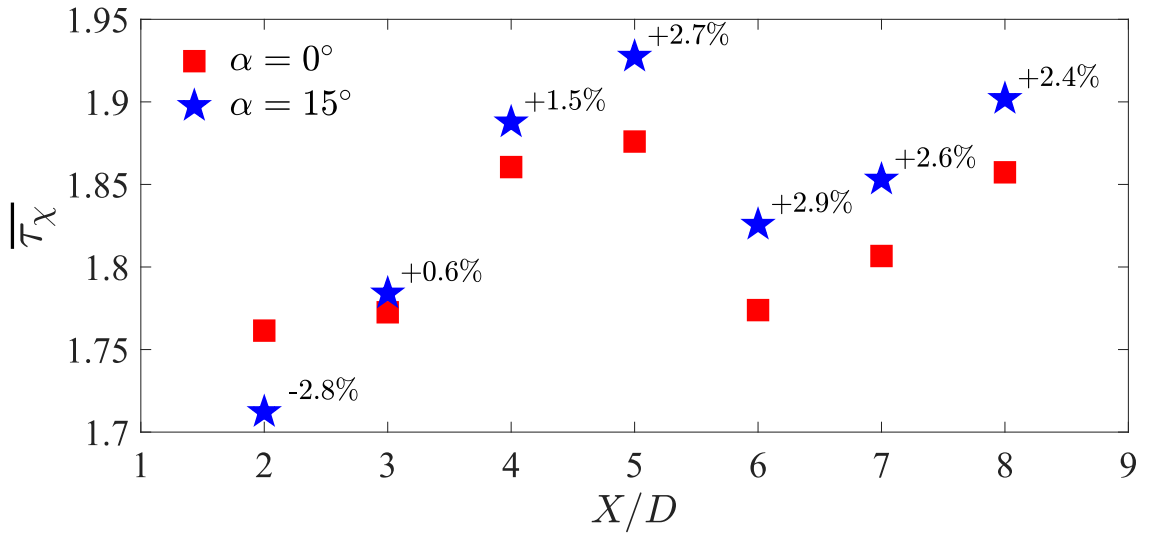

Figure 5.21: Streamwise evolution of the mean TNTI tortuosity $\overline{\tau_\chi}$ comparing the swirling (blue stars) and non-swirling (red squares) wakes

occurrences are rare events and are not statistically representative of the mean tortuosity. In any case, a highly tortuous TNTI will result in an increased surface area with more wrinkles and contortions. Naturally, this will grant a larger surface area to the TNTI where nibbling may act(Breda and Buxton, 2019). Furthermore, a high tortuosity (figure 5.20b) shows more medium-scale "bulges" and "valleys", hinting at longer TNTI excursions. These events may be linked to large scale engulfment events where big pockets of free-stream are likely to be engulfed by the wake. However, the dynamics of the interface remains the missing piece of the puzzle to confirm this hypothesis. In any case, a high tortuosity is very likely to be related to an enhanced entrainment.

The streamwise evolution of the mean tortuosity $\overline{\tau_\chi}$ is emphasised in figure 5.21. The mean tortuosity is consistently higher for the swirling wake, except for the nearest location $X = 2D$. At this location, swirl has the highest intensity and is concentrated near the centre of the wake, creating a low pressure core (chapter 4 §4.4.1). This is also the location where downwash is most prominent for case $\alpha = 0°$ which could have

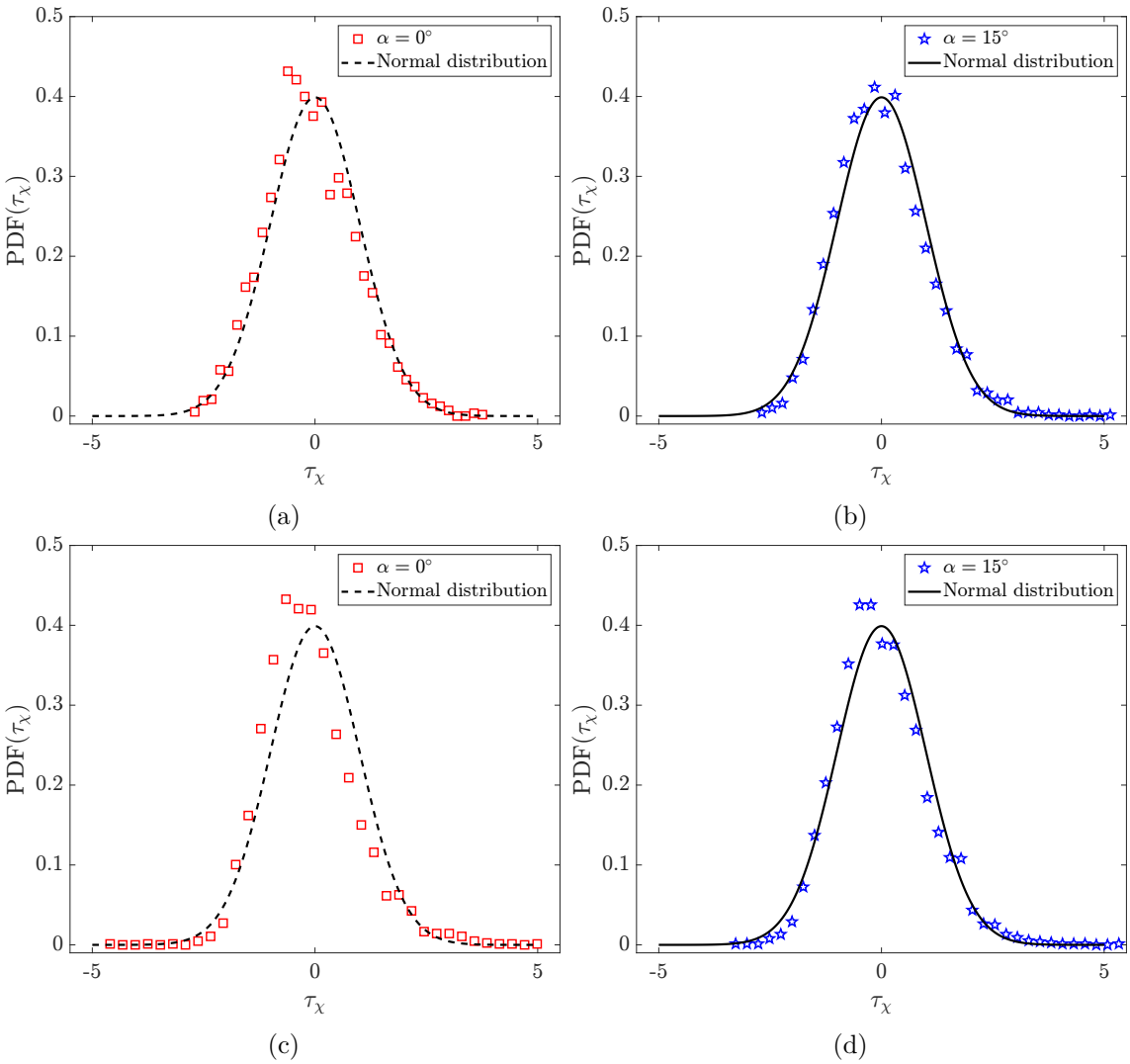

Figure 5.22: Centred and reduced distribution of tortuosity τ_χ at $X = 3D$ (left) and $X = 6D$ (right) for the $\alpha = 0°$ case (a, c) and the $\alpha = 15°$ case (b, d).

an effect on mean tortuosity. Beyond $X = 3D$, the swirling case shows consistently higher values of mean tortuosity around $2 - 3\%$ which corroborates the increase in mean entrainment showed in section §5.4 (figure 5.19). This slight increase appears to be fairly small but consistent, which suggests a more tortuous TNTI in the whole wake envelope.

The statistical distribution of τ_χ for the swirling and non swirling wakes at different streamwise locations is reported in figure 5.22. The centred and reduced tortuosity seems to be well fitted by a gaussian distribution which is characterised by a standard deviation σ_{τ_χ}. All other streamwise locations show similar results and only $X = 3D$ and $X = 6D$ are plotted. Some deviations from the normal law are present which are especially noticeable for the $\alpha = 0°$ case at $X = 6D$. The streamwise evolution of the standard deviation of τ_χ is therefore reported in figure 5.23. σ_{τ_χ} is higher for the swirling wake, especially after the previously evidenced regime change at around $X = 4D$. A higher standard deviation is related to more common high tortuosity events for the swirling case since the mean is also increased by swirl. It is hypothesised that, as the wake evolves, the interface will show more ample excursions at farther distances from the wake centre due to swirl. This means that, the swirling wake has a statistically more

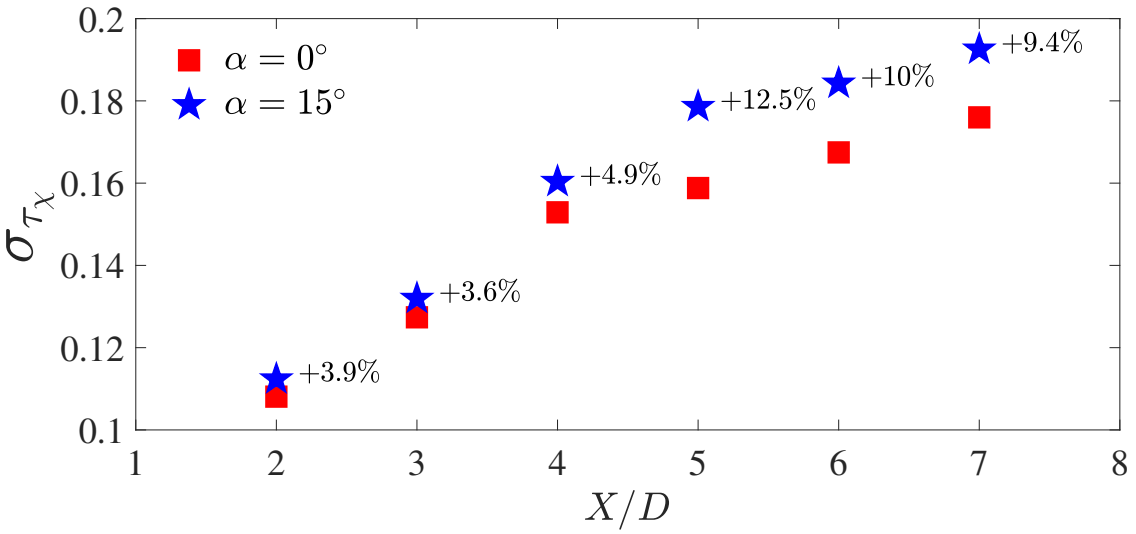

Figure 5.23: Streamwise evolution of the standard deviation of the TNTI tortuosity σ_{τ_χ}.

tortuous TNTI, favouring local entrainment possibly at all scales. These conclusions in combination with equation (5.5.1) motivate a deeper analysis of the geometrical properties of the TNTI through the term $L(r)$. The influential work of Sreenivasan and Meneveau (1986) and Mandelbrot (1982) provided the turbulence scientific community with a very useful tool to investigate the geometrical characteristics of the TNTI: the fractal analysis. This technique gives information on the different scales that describe the convoluted surface of the TNTI and its fractality[5].

5.5.2 Fractal analysis of the TNTI

Following Sreenivasan and Meneveau (1986), it has been believed that turbulence exhibits fractal-like properties and in particular their interfaces. The TNTI of different turbulent flows has proven to be a fractal surface following a self-similar law of type $S_{TNTI} \sim r^{2-D_f}$ where D_f is the fractal dimension. As stated in Breda and Buxton (2019) and shown in Mistry et al. (2018), despite many computational and experimental efforts, accurately capturing a full TNTI envelope with enough spatial resolution has posed a significant limitation to the determination of the fractal dimension of this interface. Therefore, instead of evaluating the surface of the TNTI, the fractality of its length is assessed in the spanwise planes and confronted to the power laws that stem from the similarity analysis (Zhou and Vassilicos, 2017). In this sense, the length of the TNTI is believed to follow the similarity law:

$$L(r) \sim r^{-\beta} \tag{5.5.5}$$

where r is a scale at which the interface is analysed and β is the fractal codimension. The fractal codimension is related to the fractal dimension as $D_f = 1 + \beta$. Following Sreenivasan et al. (1989) and Thiesset et al. (2016), the scales of this corrugated surface can admit a fractal dimension but not in an infinite range of scales. For a turbulent interface, fractality can be found between an inner scale η_i and an outer scale η_o. The inner scale is related to the smaller scales of the wrinkles in the TNTI and the outer scale is related to the large bulges and valleys. In the case of an axisymmetric

[5]Geometrical property of a shape admitting a fractal dimension over a non-null range of scales.

wake, the higher β is, the more tortuous the TNTI is. Conversely, low values of β are linked to a smooth surface roughly following the path of the mean TNTI L_{TNTI}. For a surface with $\beta = 0$ the fractal dimension would be unity, an integer. In this hypothetical case, fractality would be broken and the fractal dimension would approach the Euclidean dimension of a circle. These scalings can be conveniently matched into the same expression following Thiesset et al. (2016):

$$\frac{L(r)}{L_{TNTI}} = \left(\frac{\eta_o}{\eta_i}\right)^{\beta} \left[\frac{1+\left(\frac{r}{\eta_o}\right)^2}{1+\left(\frac{r}{\eta_i}\right)^2}\right]^{\beta/2} . \tag{5.5.6}$$

The fractal dimension of the TNTI can be related to the self-similarity scalings (George, 1989; Nedic, 2013), developed in chapter 2, to yield theoretical predictions for the fractal dimension of the TNTI. Following Mistry et al. (2018), if one is to take the historical similarity hypothesis of Reynolds and Kolomorogv's equilibrium similarity scalings, a prediction of $D_f = 1 + 1/3 = 4/3$ or $\beta = 1/3$ would be obtained. The recent work on the self-similar statistics of the TNTI of an axisymmetric wake (Zhou and Vassilicos, 2017) have expanded on the work of non-equilibrium turbulence and its consequences on the fractal dimension predictions. It was shown that non-equilibrium similarity scalings lead to a different fractal dimension of $D_f = 1 + 1/5 = 6/5$ or $\beta = 1/5$. This non-equilibrium fractal dimension has been previously reported in jets and plumes (Lane-Serff et al., 1993; Breda and Buxton, 2019) and in Zhou and Vassilicos (2017). In this last reference, the authors conducted a highly resolved DNS of an axisymmetric wake where this non-equilibrium scaling was observed in the TNTI fractal dimension at several spanwise planes of the wake.

To test which scaling is present in the experimental data set of this study, a few methods exist. There is the well known "box-counting" method algorithm proposed in Mandelbrot (1982) and in Sreenivasan and Meneveau (1986) which counts the number of squares of different sizes required to cover the whole TNTI. However, an alternative algorithm called the calliper technique was used here following the methodology described in Cintosun et al. (2007). This method proved reliable and robust when assessing the fractal characteristics of flame fronts and TNTIs in the recent work of Stella et al. (2018). In this technique, for each instantaneous TNTI, a scale r is associated with the developed length $N \times r$, where N is the number of callipers needed to complete the total path of the TNTI. This process is iterated for a wide enough range of r so that the cutoff scales are properly captured. Then, the ensemble average (thus obtaining the detailed field) of the r and $N \times r$ values are plotted in a log-log space known as the Richardson plot. The slope of the Richardson plot gives the fractal codimension of the interface.

The Richardson plots of the detailed fields for the swirling and non-swirling wakes at $X = 3D$ and $X = 7D$ are reported in figure 5.24. Figures 5.24a and 5.24b show pre-multiplied Richardson plots with the equilibrium scalings and the non-equilibrium scalings, respectively. As evidenced by figure 5.24a, none of the interfaces follow the Kolmogorov equilibrium scaling. Instead, figure 5.24b shows that the interfaces appear to follow a power law scaling in agreement with non-equilibrium dissipation (Zhou and Vassilicos, 2017; Breda and Buxton, 2019; Dairay et al., 2015) at least for a specific range of scales roughly going from $r/D = [3-4] \times 10^{-2}$ to $r/D = [2-4] \times 10^{-1}$. These cutoff scales coincide with the Taylor micro-scale λ of the flow and the integral

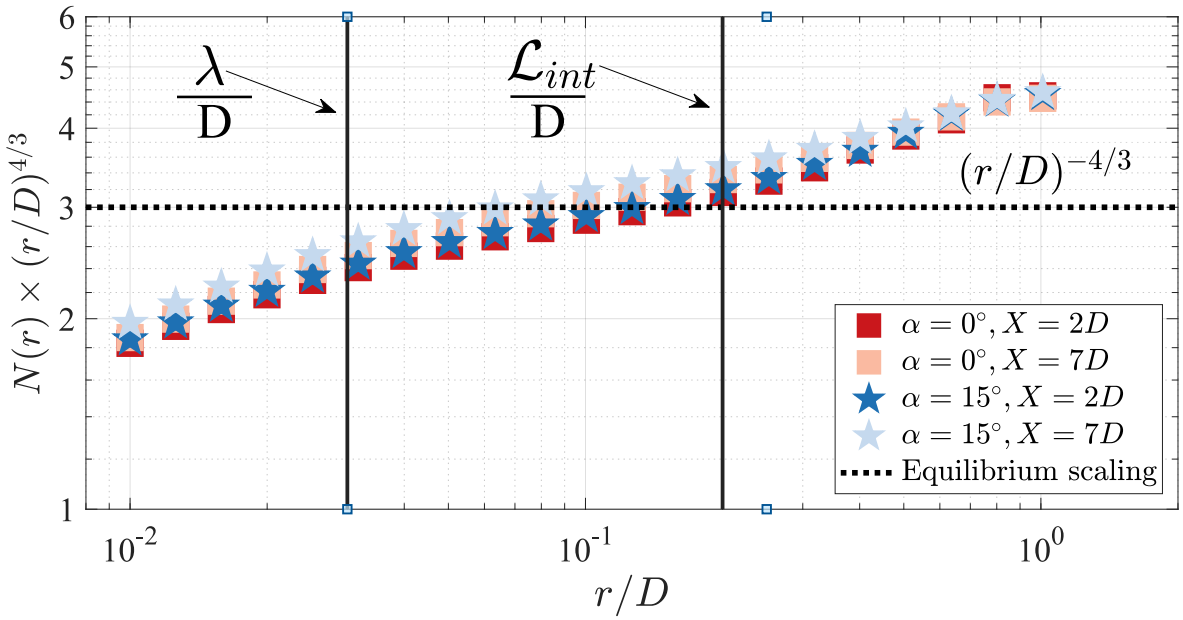

(a)

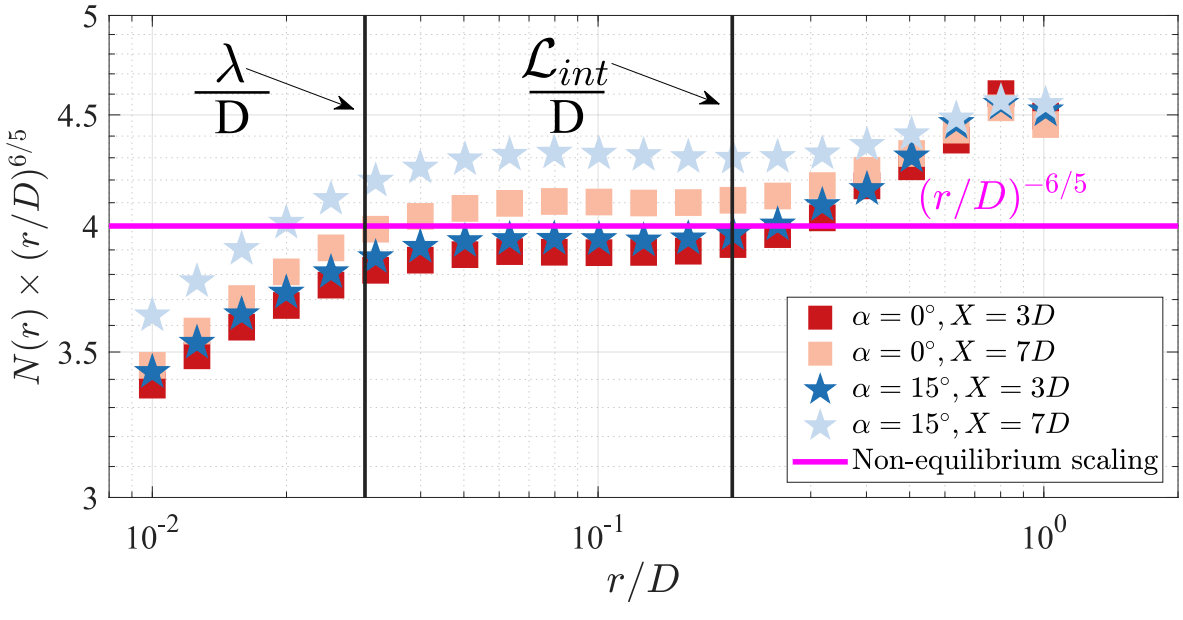

(b)

Figure 5.24: Richardson plots using the calliper method for cases $\alpha = 0°$ (red shades squares) and $\alpha = 15°$ (blue shades stars) at $X = 2D$ and. Two pre-multiplied Richardson plots are shown here using (a) the Kolmogorov equilibrium scaling and (b) the non-equilibrium scaling. Only one tenth of the markers are plotted for clarity.

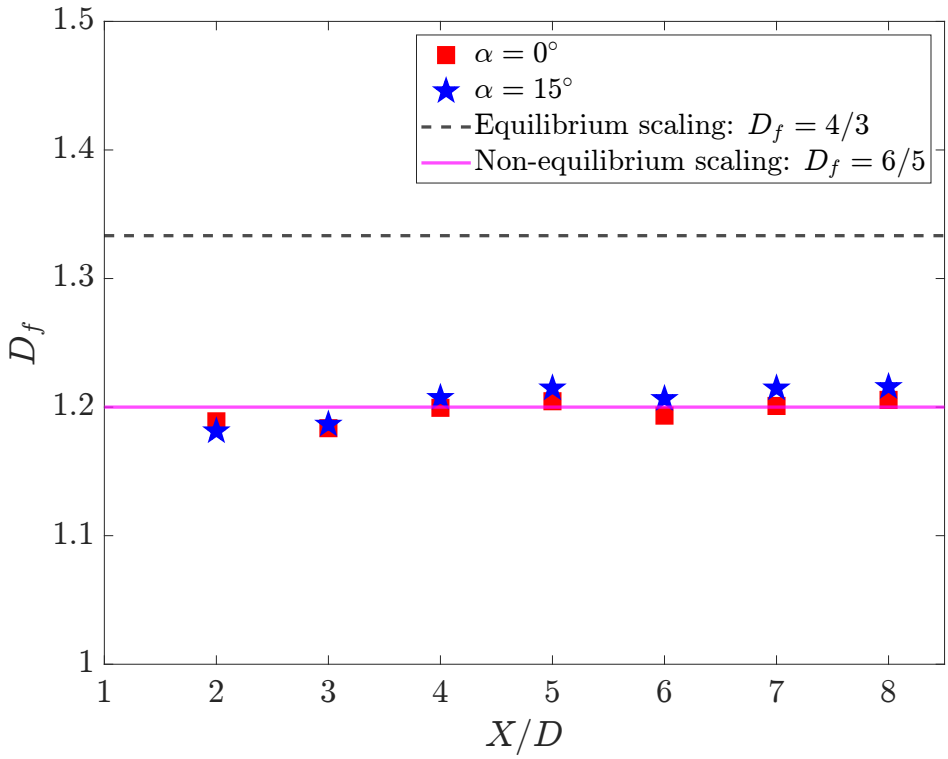

Figure 5.25: Streamwise evolution of the fractal dimension D_f of the TNTI in spanwise planes for cases $\alpha = 0°$ and $\alpha = 15°$.

length scale $\mathcal{L}_{int}$ reported in chapter 3 (§3.5.1). This suggests that the TNTI admits a fractal dimension linked to non-equilibrium dissipation for a range of scales that encompass the inertial range of the flow and captures most scales of motion relevant to entrainment. Interestingly, swirl does not appear to change the fractal dimension of the TNTI. The only observable difference with the non-swirling case, is the positive offset towards higher values of N due to the naturally longer (i.e more tortuous) interface for the swirling wake.

Furthermore, the streamwise evolution of the fractal dimension D_f for both cases is emphasised in figure 5.25. The computed fractal dimensions show excellent agreement with non-equilibrium predictions at all streamwise locations and appear unchanged by swirl. Altogether, these results suggest that non-equilibrium dissipation is present in the near to intermediate field of the axisymmetric wake, regardless of its initial conditions. The same conclusion was reached for the near field of two jets with different initial conditions in Breda and Buxton (2019). In chapters 2 and 4, the swirling and non-swirling wake were predicted and shown to evolve towards the same asymptotic state, with the swirling wake becoming self-similar quicker than the non-swirling counterpart. The self-similar swirling wake properties evolved following the power laws predicted by non-equilibrium dissipation scalings. These findings now also confirm the presence of non-equilibrium scalings in the fractal dimension of the TNTI where entrainment takes place. The fact that this fractal dimension is unchanged by swirl is further evidence that, as theorised by George (1989), a multiplicity of self-preserving states exist where a hierarchy of similarity might be established as concluded in Bevilaqua and Lykoudis (1971). In this framework, it is argued that local self-preservation is achieved by both wakes, where non-equilibrium dissipation dictates the internal readjustments of the flow to reach a full self-preserving state. The additional swirling aspect of the wake, only accelerates the process of readjustment through an enhanced entrainment, which

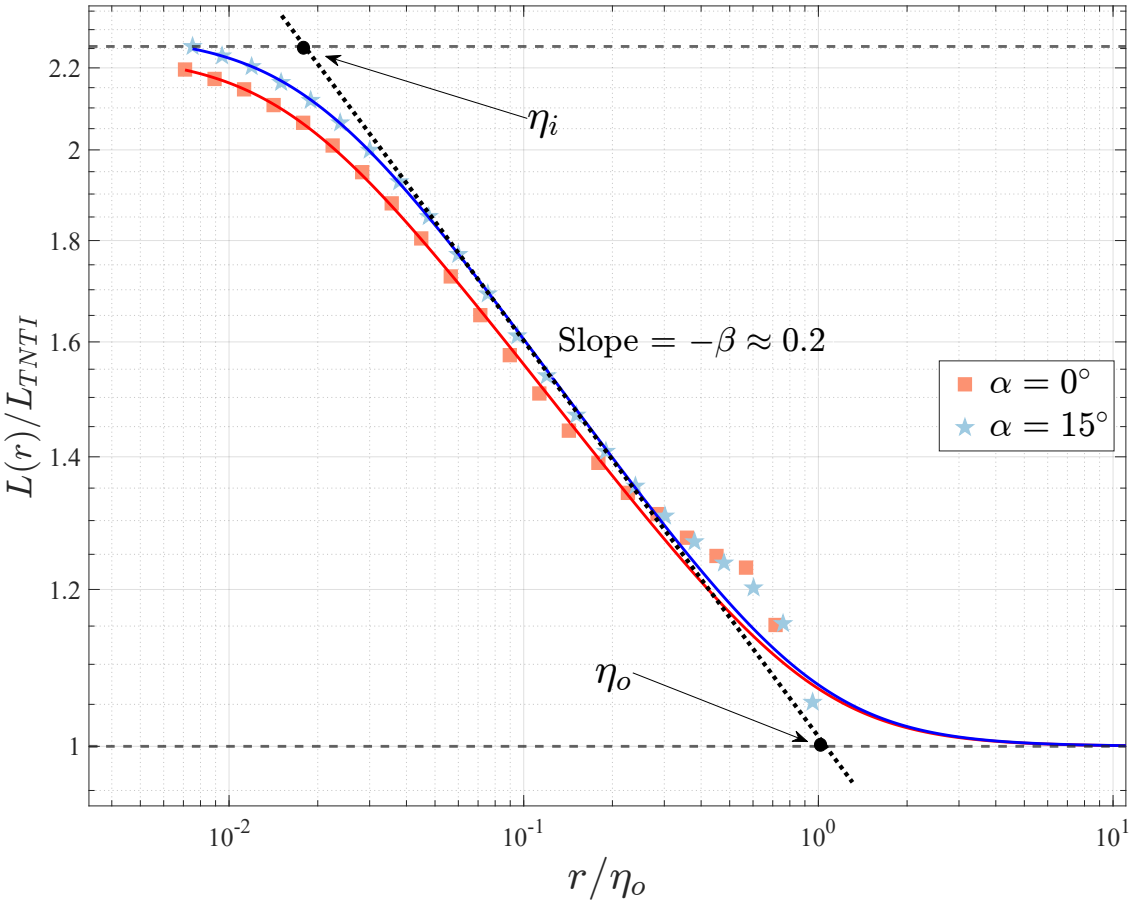

Figure 5.26: $L(r)$ vs. r Richardson plot of the TNTI at $X = 6D$ for the swirling and non-swirling wake with their respective best fits of equation (5.5.6). The codimension β and inner (η_i) and outer (η_o) cutoff length scales are depicted for the swirling case. Only one tenth of the markers are plotted for clarity.

leads to a self-similar wake at shorter distances than the non-swirling case. Furthermore, since entrainment takes place at the edges of the turbulent flow, the fractal dimension is expected to reach equilibrium at much longer distances than macroscopic characteristic scales like velocity deficit, swirl magnitude and length scales $\delta_{1/2}$ and δ_{swirl}. Expanding on the ideas put forward by Bevilaqua and Lykoudis (1971) and George (1989), it is hypothesised that, the rate at which local self-preservation evolves towards a fully self-preserving state, is entirely determined by the initial conditions of the flow as well as its virtual origin.

The Richardson plot can also be plotted using the developed length of the interface $L(r)$ instead of the number of callipers following the definition $L(r) = N(r) \times r$. In this type of plot the slope is the fractal codimension β instead of the fractal dimension D_f. However, in this representation, equation (5.5.6) can be fitted (in a mean least squares sense) onto the Richardson plot. From this fit, values for β, η_i, η_o can be computed in a self-constrained manner as discussed in Stella et al. (2017) and Thiesset et al. (2016). Figure 5.26 shows the aforementioned representation of the Richardson plot normalised by the mean TNTI length L_{TNTI} and by the outer cutoff length scale η_o. The Richardson plot is very similar at all streamwise locations which suggests that fractality in the near wake is independant of the probed streamwise location. For this reason only the position $X = 6D$ is represented in figure 5.26. The complete summary of the fractal parameters obtained using the calliper method (Cintosun et al., 2007) on

the detailed fields is reported in table 5.1.

$\alpha = 0°$						
X/D	$D_f \pm \sigma_{D_f}$	β	$L_{TNTI}/\pi D$	η_0/D	η_i/D	η_o/η_i
2	1.189 ± 0.012	0.189	1.21	1.13	0.0140	80
3	1.183 ± 0.013	0.183	1.23	1.37	0.0156	88
4	1.199 ± 0.015	0.199	1.24	1.29	0.0167	76
5	1.205 ± 0.015	0.205	1.24	1.20	0.0179	67
6	1.193 ± 0.015	0.193	1.23	1.41	0.0221	64
7	1.201 ± 0.016	0.201	1.23	1.38	0.0230	60
8	1.206 ± 0.017	0.206	1.21	1.49	0.0253	59

$\alpha = 15°$						
X/D	$D_f \pm \sigma_{D_f}$	β	$L_{TNTI}/\pi D$	η_0/D	η_i/D	η_o/η_i
2	1.181 ± 0.015	0.181 (-4%)	1.23 (+1.7%)	1.25 (+10.6%)	0.0147 (+5%)	85 (+6.3%)
3	1.187 ± 0.015	0.187 (+2%)	1.25 (+1.6%)	1.29 (-5.8%)	0.0161 (+3.2%)	80 (-9.1%)
4	1.208 ± 0.017	0.208 (+4.5%)	1.25 (+0.8%)	1.19 (-7.8%)	0.0178 (+6.6%)	67 (-11.8%)
5	1.215 ± 0.017	0.215 (+4.9%)	1.26 (+1.6%)	1.20 (-0%)	0.0197 (+10%)	61 (-9%)
6	1.206 ± 0.018	0.206 (+6.7%)	1.26 (+2.4%)	1.33 (-5.7%)	0.0242 (+9.5%)	55 (-14.1%)
7	1.215 ± 0.017	0.215 (+7%)	1.27 (+3.3%)	1.30 (-5.8%)	0.0254 (+10.4%)	51 (-15%)
8	1.216 ± 0.018	0.216 (+4.9%)	1.23 (+1.6%)	1.44 (-3.4%)	0.0273 (+7.9%)	53 (-10.2%)

TABLE 5.1: Fractal parameters, computed on the detailed fields, of the spanwise TNTIs for all available streamwise locations and both cases $\alpha = 0°$ and $\alpha = 15°$. D_f is the fractal dimension, β is the fractal codimension, L_{TNTI} is the length of the mean TNTI and η_i and η_o are the inner and outer scales, respectively. As a reminder the Kolmogorov scalings predict: $D_f = 4/3 \approx 1.33$ and the non-equilibrium scalings predict: $D_f = 6/5 = 1.2$.

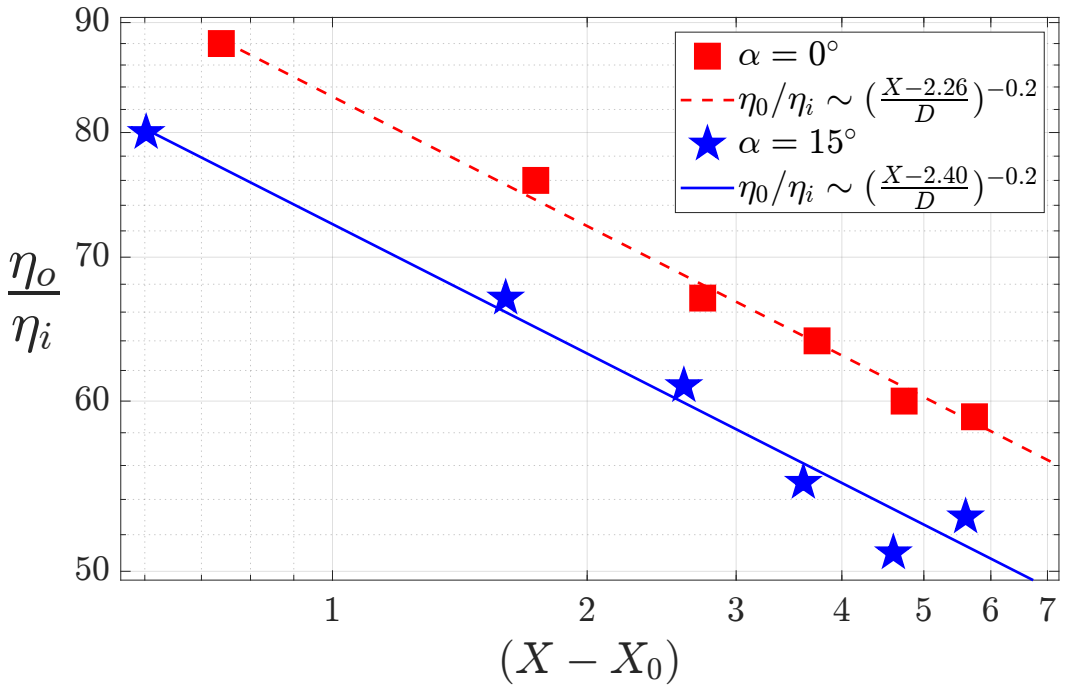

Figure 5.27: Power law streamwise evolution of the fractality cutoff scales ratio for cases $\alpha = 0°$ and $\alpha = 15°$.

The fitting of equation (5.5.6) confirms our previous observations in figure 5.24 of the fractal dimension of the TNTI. Regardless of swirl, the TNTIs show a strikingly good agreement with the non-equilibrium predictions. The points of the Richardson plot appear to be well approximated by equation (5.5.6) for the small scales especially but show some deviation for the bigger scales between the integral scale and the outer scale η_o. This could be due to the mast which breaks the assumed axisymmetry of the wake and is common for both cases. In terms of scales, for $X \geq 3D$, the swirling wake shows consistently smaller outer scales and larger inner scales. However, the differences in the outer scales are only around 3-4% contrary to an 8% shift in the inner scales.

Interestingly, it appears that the outer to inner cutoff scales ratio evolves in the streamwise direction as a self-similar variable following a power law such as:

$$\frac{\eta_o}{\eta_i} \sim \left(\frac{X - X_0}{D}\right)^{-\beta} \tag{5.5.7}$$

where x_0 is the virtual origin of the wake in terms of entrainment. Figure 5.27 emphasises the power law scalings (5.5.7) for both cases. The non-linear least squares-based algorithm confirms that the exponent β is indeed the fractal co-dimension and that the main difference between cases is the virtual origin X_0. The virtual origin is 14 mm ($\sim \mathcal{L}_{int}$) larger for the swirling wake. This suggests that swirl has not fundamentally altered the mechanisms of entrainment but rather shifted the virtual origin of the wake closer to the porous disc both in terms of self-similarity and entrainment.

5.6 Concluding remarks

In this chapter, it was shown that swirl increased entrainment through the TNTI by increasing the tortuosity of the TNTI and the size of the mean TNTI. This resulted in a

bigger effective surface available for entrainment to act. A more in-depth examination of the fractal characteristics of the TNTI revealed that the fractal dimension D_f of this interface shows very good agreement with the non-equilibrium scalings, irrespective of the presence of swirl. Moreover, the cutoff scales of fractality η_0/η_i appeared to follow a self-similar power law evolution in the streamwise direction for both wakes. A non linear fit revealed that swirl only shifts the virtual origin of entrainment, moving it closer to the porous disc. Altogether, along with the results presented in chapter 4, it is concluded that swirl does not change the mechanisms of wake expansion and recovery but rather shifts the virtual origin of the self-preserving wake.

Résumé en français: Les mécanismes d'entraînement du sillage tournant d'un disque poreux

Le chapitre précédent a établi le rôle du swirl sur les propriétés moyennes du sillage et leur évolution dans la direction axiale. Il a été démontré que le sillage tournant et le sillage non tournant des disques poreux sont asymptotiquement identiques en termes de quantité de mouvement linéaire (traînée). La principale différence réside dans la distribution de pression à travers le sillage, en particulier dans le champ proche. Le swirl crée un noyau de basse pression au centre du sillage, renforçant ainsi son axisymétrie et favorisant l'auto-similarité. De plus, en présence de swirl, il a été démontré que la récupération du sillage, son expansion et la décroissance du swirl évoluent dans la direction axiale suivant les prédictions de la turbulence hors équilibre (Nedic, 2013; Vassilicos, 2015; Dairay et al., 2015). En résumé, le swirl modifie la façon dont le sillage évolue dans l'espace sans altérer le coefficient de traînée, du moins dans le régime d'écoulement attaché. Pour aller plus loin dans les mécanismes sous-jacents modifiés par le swirl, il faut poser la question fondamentale : qu'est-ce qui provoque l'expansion et la récupération d'un sillage ? Une réponse à cette question peut être trouvée dans les travaux de Corrsin and Kistler (1955), Townsend (1966) et l'impressionnant travail de Turner (1986), où la notion d'entraînement a été introduite pour la première fois. Dans le cas d'un sillage turbulent, l'entraînement est le processus par lequel une parcelle de fluide porteuse de quantité de mouvement, caractéristique de l'écoulement incident ("*free-stream*"), est transportée à l'intérieur du sillage, provoquant ainsi son expansion et sa récupération. Le swirl a donc modifié la manière dont le sillage interagit avec son environnement, c'est-à-dire les mécanismes d'entraînement. Cela soulève les questions suivantes : la vitesse d'entraînement a-t-elle été modifiée par le swirl ? L'interface a-t-elle été modifiée ? Quelles échelles d'entraînement ont été altérées par le swirl ? Quelle est l'étendue de l'influence du swirl ? Ce chapitre vise à aborder ces questions à l'aide des données expérimentales collectées au cours de cette étude et d'une analyse physique de l'entraînement. Cette analyse est conduite sur les cas $\alpha = 0°$ et $\alpha = 15°$ car les deux disques ont des coefficients de traînée identiques.

Le chapitre débute par une revue de la littérature sur le phénomène d'entraînement turbulent. L'entraînement est un processus de transport de quantités physiques (masse, quantité de mouvement, énergie cinétique) contenues dans une parcelle d'air du "*free-stream*" vers ou depuis le sillage turbulent. Deux mécanismes prédominants sont distingués: "*L'engulfment et le nibbling*". Le premier est associé aux grandes échelles de l'écoulement turbulent où des parcelles de fluide à l'extérieur du sillage sont englouties par des excursions du sillage à grande amplitude. Le second mécanisme, davantage associé aux petites échelles, brasse l'écoulement irrotationnel pour le convertir en écoulement rotationnel par diffusion visqueuse de la vorticité (da Silva et al., 2014). Pour quantifier l'entraînement, il est donc impératif de détecter l'interface turbulente/non-turbulente (TNTI) ainsi que de mesurer la vitesse de l'écoulement avec une résolution temporelle suffisante pour suivre la trajectoire de la TNTI.

En raison des limitations expérimentales et de temps, l'entraînement a été caractérisé uniquement par l'entraînement de masse moyen et par les propriétés géométriques de l'interface. Une amélioration de la détection de la TNTI en utilisant l'auto-déconvolution de Fourier (FSD) est proposée et permet de capturer plus précisément la TNTI. Cette méthode est prometteuse puisqu'elle détecte l'interface en utilisant uniquement les propriétés de l'écoulement sans avoir besoin de fixer un seuil de dépassement (Kovacs

et al., 2022). Cette approche est basée sur les zones de quantité de mouvement uniforme proposée dans les travaux de Adrian et al. (2000b) et de Silva et al. (2016).

On observe que l'introduction du swirl augmente l'entraînement de masse moyen à travers la TNTI, en élargissant la surface de la TNTI. Malgré la présence du swirl, la vitesse d'entraînement moyenne reste inchangée. En revanche, la tortuosité de la TNTI instantanée corrobore le fait que le swirl augmente principalement la surface à travers laquelle l'entraînement se produit. De plus, La TNTI montre des caractéristiques fractales dans les plans $r - \phi$ à tous les emplacements examinés. Indépendamment du swirl, la dimension fractale montre une très bonne concordance avec les prédictions de la turbulence hors équilibre $D_f = -6/5$ (Zhou and Vassilicos, 2017). Cette découverte suggère que la dissipation hors équilibre est présente aux bords de ces deux écoulements, mais que l'écoulement tournant atteint un état auto-similaire à des distances plus courtes. Ainsi, le swirl est une condition initiale à grande échelle, mais avec un effet à toutes les échelles pertinentes pour l'entraînement (augmentation de la surface et de la tortuosité). Cela est en accord avec la relation intime entre les échelles dissipatives et les grandes échelles contenant de l'énergie, telle que trouvée dans Mazellier and Vassilicos (2008). Par ailleurs, les échelles de coupure de la fractalité η_0/η_i semblent suivre une évolution auto-similaire selon une loi de puissance dans la direction axiale pour les deux sillages. Un ajustement non linéaire (Thiesset et al., 2016) révèle que le swirl ne fait que déplacer l'origine virtuelle de l'entraînement, la rapprochant du disque poreux. Dans l'ensemble, avec les résultats présentés au chapitre 4, on en conclut que le swirl ne modifie pas les mécanismes d'expansion et de récupération du sillage, mais déplace plutôt l'origine virtuelle du sillage auto-similaire.

6

Conclusions and future work

I Conclusions

In this study, the absence of swirl in the wake of a porous disc wind turbine surrogate was tackled. An extensive experimental investigation was conducted on the swirling turbulent wake generated by a modified porous disc now including swirl. The primary objective was therefore to thoroughly characterise and quantify the effect of swirl on the streamwise evolution of the wake.

The theoretical framework of a swirling wake was first established in chapter 2 where the governing RANS equations were given along with the relevant simplifications and corresponding hypotheses. Swirl was shown to be governed by both the streamwise and angular momentum conservation laws. The far wake approximations of these conservation laws revealed that the drag coefficient of a swirling wake and of a non-swirling wake are identical. A similarity analysis was conducted following the framework established in the seminal work of George (1989). The conservation of angular momentum added an extra similarity constraint thereby introducing an additional degree of freedom to the similarity analysis. It was remarked that two parameters could prescribe the characteristic length scale of a swirling wake, depending on which constraint was used first. This resonated with the work of Reynolds (1962) where theoretical scaling laws were derived based on the asymptotic values of the momentum-based swirl number $\hat{S}$. However, at that time, equilibrium similarity theory only permitted the derivation of scaling laws for either $\hat{S} \ll 1$ or $\hat{S} \gg 1$. Following the work of Mazellier and Vassilicos (2008); Nedic (2013); Vassilicos (2015) and Dairay et al. (2015), non-equilibrium similarity theory was used to tackle the $\hat{S} = \mathcal{O}(1)$ case, which is likely to exist in the wake of a HAWT. Unlike equilibrium turbulence, it was shown that non-equilibrium turbulence does not require the use of a similarity constraint to obtain a scaling law for the characteristic length scale of the swirling wake. In fact, when $\hat{S} = \mathcal{O}(1)$, two characteristic length scales $\delta_{1/2}$ and δ_{swirl} can be defined linked to the velocity deficit U_s and swirl magnitude W_s, respectively. For the first time, non-equilibrium similarity theory was extended to the streamwise evolution of swirl magnitude. The novel scaling law predicted a swirl decay such as $W_s \sim x^{-3/2}$. Interestingly, the same link between wake recovery and swirl decay was found such as $W_s/U_\infty \sim (U_s/U_\infty)^{3/2}$ regardless of

the turbulence state.

A porous disc featuring non-uniform porosity β was designed taking inspiration from the work of Camp and Cal (2016) and Helvig et al. (2021). To passively generate swirl, the blades of the porous disc were pitched of an angle α. This approach allowed us to separate the parameters β and α and predict some trends using thin airfoil theory (Batchelor, 1953; Anderson, 2011). Then, the swirling wake and drag coefficient C_D of this surrogate was measured in the S2 wind tunnel of the PRISME laboratory using a combination of force measurements, 3CHWA and (S)PIV. The redundancy of some velocity measurements was leveraged to corroborate each other and estimate uncertainties.

In accordance to our predictions, two regimes were underscored based on the pitch angle α of the blades: the attached flow regime and the stall regime. In the attached flow regime, swirl magnitude increases linearly and drag is constant. In the stall regime, the swirl starts to decrease with α and drag increases linearly due to the decreased apparent porosity. A critical pitch angle was evidenced $\alpha_c \in [16, 18°]$ beyond which stall occurs. Cases $\alpha = 0°$, $\alpha = 15°$ and $\alpha = 25°$ were chosen as key pitch angles since the $\alpha = 15°$ case generated a maximum amplitude of swirl at iso-porosity. The $\alpha = 25°$ case generated the same levels of swirl with a decreased apparent porosity. Swirl was fully characterised for these cases and showed swirl number values ($\hat{S} \approx 0.3$) comparable to what is reported for rotating models (Dufresne, 2013; Lee et al., 2020; Holmes and Naughton, 2022). Swirl showed an axisymmetric toroidal distribution around the centre of the wake and a quick decay in the streamwise direction with a radial outward spread to conserve angular momentum.

A momentum budget confirmed that in the attached flow regime, swirl did not affect the porous disc drag significantly but rather change the distribution of pressure across the wake. To assess the redistribution of pressure caused by swirl, the pressure fields in the spanwise planes were reconstructed from velocity measurements following the work of Shanmughan et al. (2020) and Harker and O'Leary (2008). It was shown that swirl spatially redistributed the low pressure area and generated a low pressure core at the centre of the wake near $(Y, Z) = (0, 0)$. For the non-swirling wake ($\alpha = 0°$), the low pressure area was located near the mast region where a strong downwash effect was observed (Pierella and Sætran, 2017; Aubrun et al., 2019). The effect of swirl on the mean flow topology was further examined as well as the dynamic position of the wake centre. The swirling motion was shown to have a stabilising and axisymmetrisation effect on the wake of the porous disc thereby resisting the downwash caused by the mast.

Moreover, the self-similarity of the axial velocity deficit $U_s(x)/U_\infty$ was enhanced as swirl increased. Self-similar gaussian profiles were obtained starting at $X = 3D$ for the swirling wakes, as opposed to the $\alpha = 0°$ case for which self-similarity was not obtained. These profiles were compared to the data reported in the literature and were shown to better match the velocity deficit profiles from experimental wind tunnel data of a lab-scale wind turbine of Chamorro and Porté-Agel (2010) and numerical LES results of a real-size wind turbine found in Wu and Porté-Agel (2012). The wake's width in terms of axial velocity deficit $\sigma(x)$ was shown to exhibit a trend break at around $X = 6D$. A new length scale δ_{swirl} was proposed in this study which scaled the swirl spread in the near wake and showed a streamwise evolution, as opposed to $\delta_{1/2}$. Self-similarity was also obtained for the swirling velocity.

With the self-similarity conditions met for the axial velocity deficit and for the swirling

velocity component, similarity scalings laws were fitted to the wake's properties (Nedic, 2013; Dairay et al., 2015). The results showed very good agreement with the similarity scalings based on the non-equilibrium similarity analysis conducted in chapter 2 (§2.3) (Vassilicos, 2015). The mean streamwise velocity deficit is shown to evolve as x^{-1} and the wake characteristic length scale as $x^{1/2}$. In particular, the novel scaling law based on non-equilibrium similarity derived in chapter 2 (§2.3.3) was obtained for the swirl decay such as $x^{-3/2}$. Both cases showed very good agreement with the predicted scaling law. The universal scaling law coupling the characteristic axial velocity deficit and the characteristic swirling velocity $W_s(x)/U_\infty \sim (U_s(x)/U_\infty)^{3/2}$ was also found in a restricted range of streamwise locations. Identical results were obtained for cases $\alpha = 15°$ and $\alpha = 25°$ which proves that swirl is the dominant initial condition of the wake relative to porosity. It is thus argued that swirl triggers self-preservation in the wake of the porous disc regardless of porosity.

Finally, since the wake recovery and expansion were proven to be altered by swirl at iso-porosity, the effect of swirl on the entrainment mechanisms were further quantified. Due to experimental limitations, entrainment was only characterised by mean mass entrainment and by the geometrical properties of the TNTI. An improved uniform momentum zones TNTI detection using FSD was proposed and showed a more accurate capture of the instantaneous TNTI. It was found that the introduction of swirl increased mean mass entrainment through the TNTI, achieving this by expanding the surface area of the TNTI. Interestingly, despite the presence of swirl, the entrainment velocity remained unaffected. The tortuosity of the instantaneous TNTI corroborated that swirl mainly increases the surface area through which entrainment takes place. The TNTI showed fractal characteristics in the $r - \phi$ planes at all examined streamwise locations. Regardless of swirl, the fractal dimension showed very good agreement with non-equilibrium turbulence predictions $D_f = -6/5$ (Zhou and Vassilicos, 2017). This finding suggested that non-equilibrium dissipation is present at the edges of both flows but the swirling flow reaches a fully self-preserving state at shorter distances. Therefore, swirl is a large scale initial condition but with an effect at all scales relevant to entrainment (increased surface and tortuosity). This is inline with the intimate relation between the dissipative scales and the large energy-containing scales found in Mazellier and Vassilicos (2008).

All in all, these findings resulted in the proposition of a novel porous disc wind turbine surrogate now passively and inexpensively including swirl. This approach allows to generate an axisymmetric, self-preserving, turbulent wake with swirl levels ranging from $\hat{S} = 0$ to $\hat{S} \approx 0.3$. This is achieved using a single extra parameter α without altering the drag coefficient of the disc. These findings therefore open the door to many other investigations of the swirling wake of a HAWT using a porous disc surrogate (swirling wake meandering, external turbulence, inertial particles in a swirling wake, yaw and tilt rotor angles angles etc...). For example, Bossuyt et al. (2021) showed that the yaw and tilt angles of a HAWT rotor were shown to change the topology of the wake. With the new porous disc proposed in this work, several yawed and tilted rotor configurations in a wind farm layout could be experimentally tested in a simple and inexpensive fashion. Moreover, the actuator disc model in numerical simulations could also benefit from the addition of angular momentum since it was already shown to be sensitive to the initial conditions of the actuator disc (Stevens et al., 2018). This was already pointed out by Okulov et al. (2015) in their review paper of Professor Joukowsky's rotor theories. In particular, according to Okulov et al. (2015), Professor Georgy Bothezat (1917) had already theorised that including angular momentum to

the actuator disc concept would yield a more accurate version of the generated wake.

II Future work

To exemplify potential future research directions arising from this study, this section presents some perspectives and discusses certain aspects that were contemplated in this study but ultimately omitted from the main manuscript.

II.1 Uniform helicity zones: a new TNTI detection approach?

Another TNTI detection method was also explored at later stages of this thesis which revealed an interesting property of the TNTI. This method was not chosen as the main detection method since it still needs proper testing and confrontation with either highly resolved numerical simulations or direct interface measurements. However, this methodology extends the concepts introduced by Corrsin and Kistler (1955), Pope (2000) and by Adrian et al. (2000b) regarding the properties of the TNTI and uniform regions of the flow. As explained in chapter 5, the natural scalar field to detect the TNTI is vorticity $\boldsymbol{\omega}$ (or enstrophy). However, computing vorticity requires volumetric data with sufficient spatial resolution to accurately calculate velocity gradients. For the study of wakes, the axial component of vorticity ω_x is accessible with stereoscopic data acquired in the cross-section. Following the review paper of Hunt and Hussain (1991), helicity density is a particularly interesting quantity to consider when it comes to turbulent boundaries definitions. In fact, one of the main conclusions in Hunt and Hussain (1991) is that helicity is intimately related to entrainment at the TNTI. Helicity is a notion taken from particle physics and adapted to fluid mechanics by Moffatt (1969). Helicity density in a reference frame moving with the free-stream velocity U_∞ is given by:

$$\hat{h}(x,t) = (\boldsymbol{u}(x,t) - U_\infty) \cdot \boldsymbol{\omega}(x,t), \tag{II.1}$$

and the helicity integral is defined as:

$$\mathscr{H} = \int_{\mathcal{V}} \hat{h} dV, \tag{II.2}$$

where $\mathcal{V}$ is an enclosed domain of the flow. This particular quantity is conserved in inviscid flows and constitutes the second invariant of the Euler equations (Rosa, 2020). Following Meinhart and Adrian (1995)'s work on boundary layers, the authors revealed the canonical properties of uniform momentum zones in turbulent flows. Their first, and well known observation, was that these so-called uniform momentum zones exist in turbulent flows scattered throughout the flow. This observation gave rise in later years (Adrian et al., 2000b; Kwon et al., 2014) to the previously described UMZ-based TNTI detection method. However, there is a second observation in the seminal work of Meinhart and Adrian (1995): these UMZs are also characterised by "concentrated vortical" regions of mainly spanwise vorticity. Combining these observations with the notions introduced by Moffatt (1969) regarding helicity, one can also expect that turbulent flows may be populated by regions of uniform helicity density.

Figures 6.1 and 6.2 shows the detection method using regions of uniform helicity density for the swirling wake of the $\alpha = 15°$ porous disc. The helicity density is shown in a logarithmic scale for clarity as it jumps from nearly zero in the irrotational free-stream, to several orders of magnitude above unity in the wake. As shown in figures 6.1a and

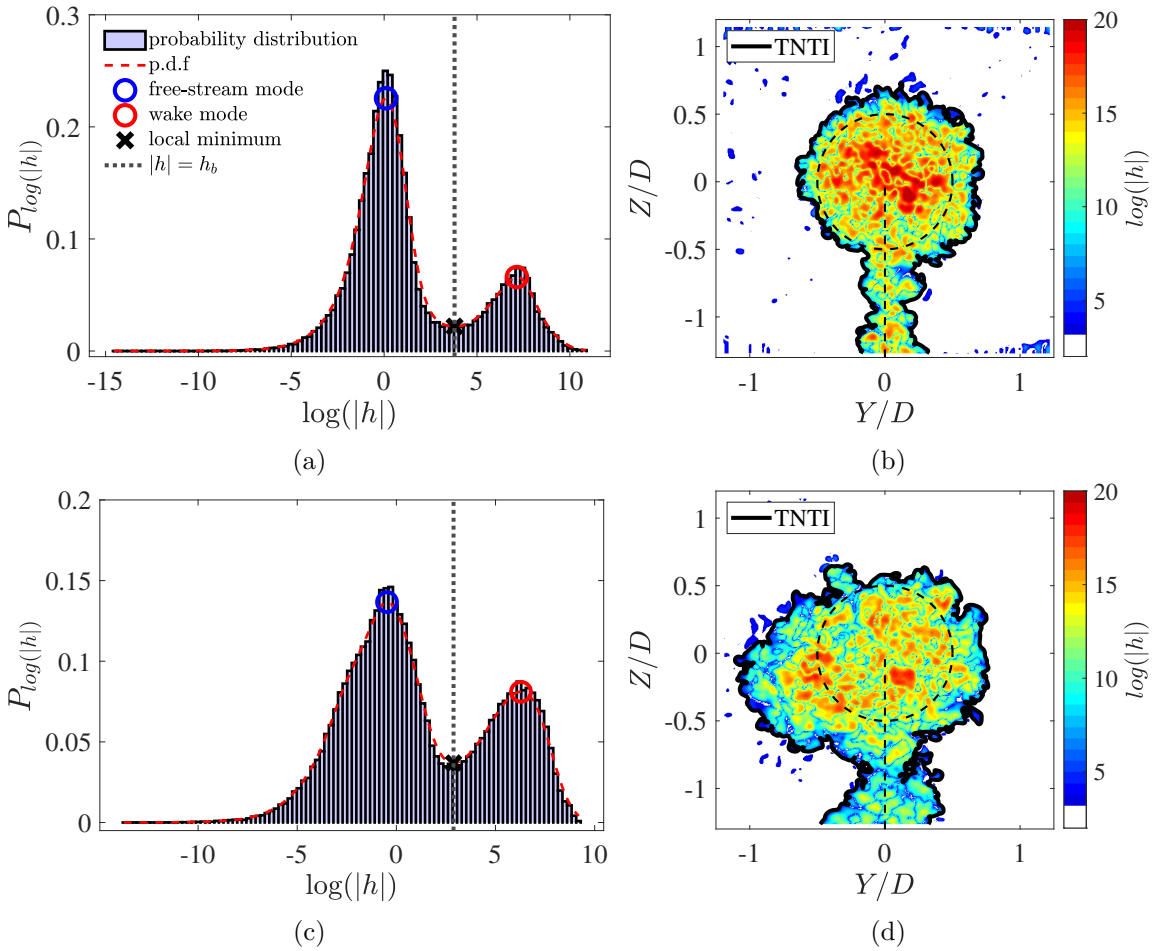

Figure 6.1: Example of the TNTI detection method based on regions of uniform helicity for random snapshots of the swirling wake of $\alpha = 15°$ at $X = 2D$ (top) and $X = 7D$ (bottom). (a, c) show the probability log-distribution functions of the norm of helicity. (b, d) show the corresponding helicity density field with the detected TNTI.

6.1c, the free-stream is characterised by uniformly low values of helicity, lumped into what can be defined as a helicity mode following Adrian et al. (2000b)'s terminology. Interestingly, as opposed to the momentum p.d.f, there is another mode clearly defined at high helicity density values around $h = 500$ m.s^{-2}. This other mode corresponds to the turbulent wake of the porous disc. Following the same principles of uniform momentum zones, these two regions of uniform helicity can be used to define a local minimum between the two helicity modes noted h_b. The corresponding contour of iso-helicity at this minimum acts as the boundary between the irrotational free-stream and the rotational wake. As can be seen in figure 6.1, the detected helicity boundary values for both examples are $h_b = 44.3$ m.s^{-2} and $h_b = 17.9$ m.s^{-2}, respectively.

The detected TNTI manages to capture the rotational parts of the wake with a remarkable accuracy for both examples and does not show unphysical excursions into irrotational regions of the free-stream. Interestingly, as the wake evolves downstream, the helicity modes appear to spread and the free-stream peak decreases in amplitude (figures 6.1a and 6.1c). This is due to the finite extent of the field of view which is gradually filled by the rotational wake as it expands with the downstream distance. This observation was already pointed out by Adrian et al. (2000b) for momentum histograms in boundary layers. In our case, this limitation does not hinder the method

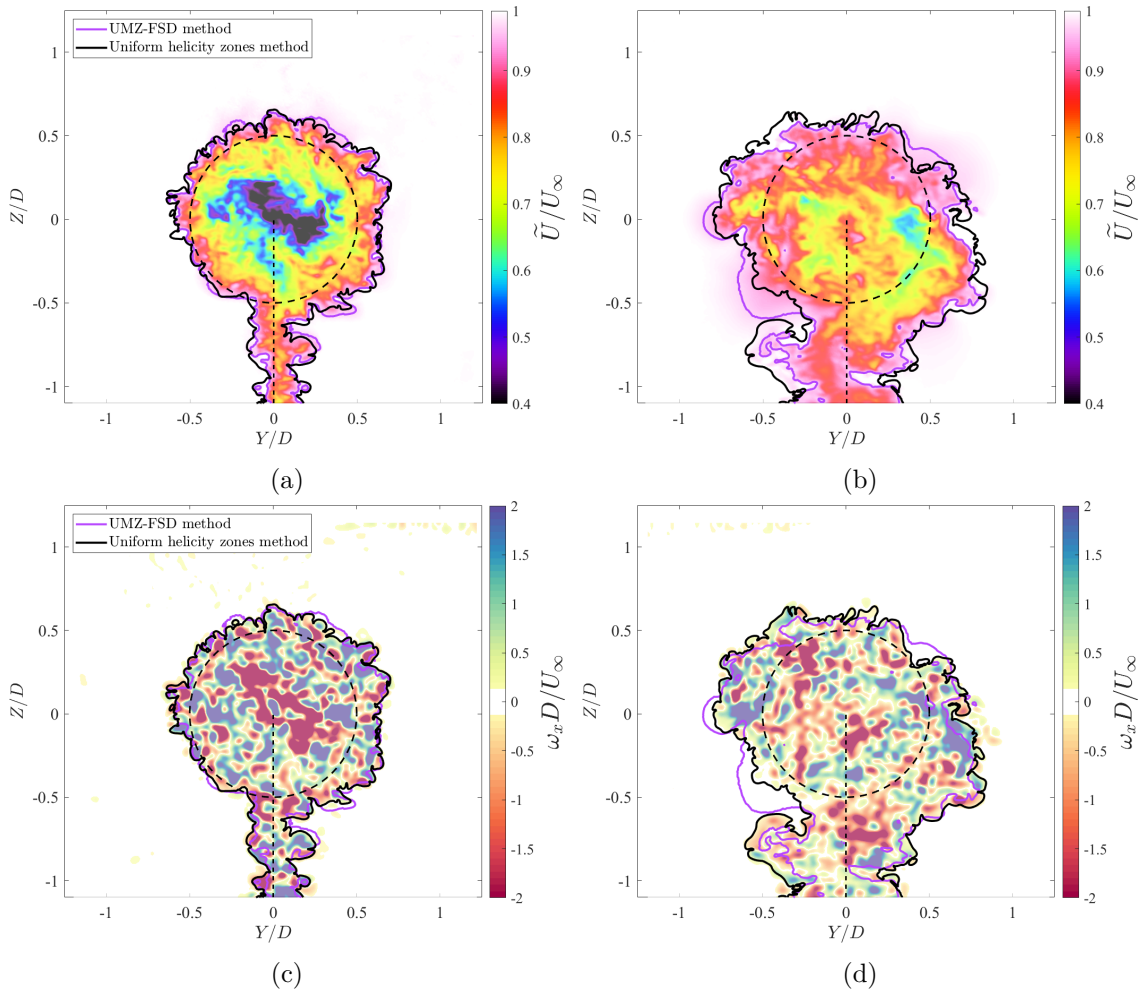

Figure 6.2: Comparison of the helicity-based TNTI detection method with the UMZ-FSD detection method. Normalised streamwise velocity fields at (a) $X = 2D$ and at (b) $X = 7D$ are presented as well as (c, d) normalised out-of-plane 2D-vorticity fields at the same locations. Black dashed lines: test rig outline

since the free-stream mode remains detectable even in the farthest measured downwind locations. As evidenced in figures 6.2a and 6.2c, the UMZ-FSD method appears to collapse with the helicity-based approach in the near wake ($X = 2D$). Both TNTIs only show small discrepancies in some regions where the rotational regions of the flow are highly contorted. Further downstream however, there are some differences between methods. In particular, the UMZ-FSD method sometimes overestimates or underestimates the detection of the rotational parts of the flow as evidenced in figures 6.2b and 6.2d. This reveals some limitations of the use of an iso-contour of streamwise momentum as a detection criteria. In fact, when the TNTI describes a highly contorted surface, some parts of the free-stream trapped in a valley of rotational flow will locally accelerate according to mass conservation. This can lead to a local offset in the free-stream momentum mode provoking a detection bias.

The helicity-based method shows promising results as an alternative criteria used to capture the turbulent/non-turbulent interface. Since helicity is directly calculated from velocity data, using it as a TNTI detection method does not require techniques involving additional resources like PIV/PLIF or a seeding density differentiation. Furthermore, this particular scalar combines both the sharp velocity and vorticity change at the TNTI, making it a naturally adapted transition marker. This section only proposes

this methodology and tests it in a specific case where: the spatial resolution is good enough to compute vorticity and large enough to obtain uniform helicity zones. Furthermore, an important limitation to mention is that only one term of helicity density can be computed in this configuration. In fact, since in-plane gradients are accessible from planar measurements, only the out-of-plane component of vorticity can be computed. In order to fully prove the accuracy of this method, more validation is needed with numerical simulations or access to volumetric data of the wake. This method is therefore only proposed as a starting point of an alternative detection method of the TNTI in turbulent flows.

II.2 Effect of the nacelle. Application to other types of turbine.

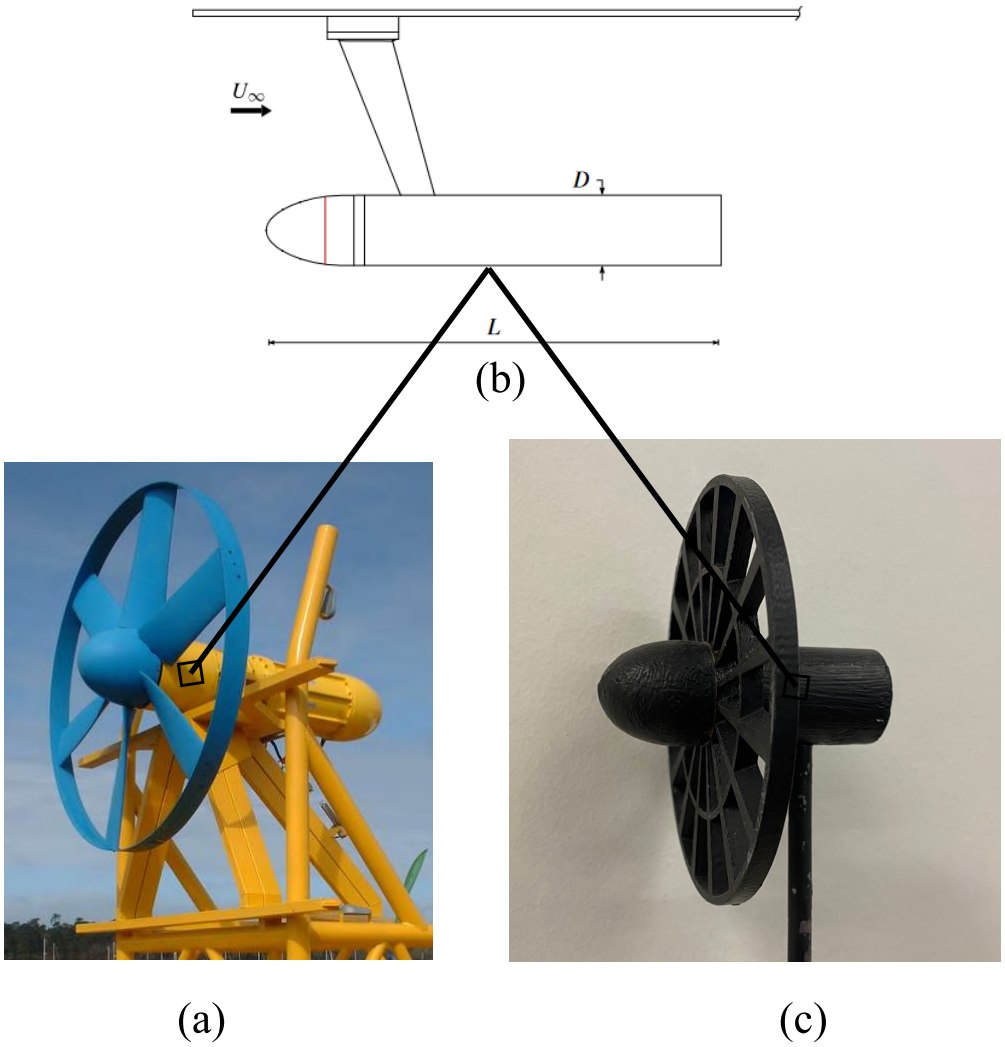

Figure 6.3: Schematic diagram showing (a) a photography of the Sabella^{TM} D03 30kW tidal turbine and of (c) a porous disc test rig with a similar nacelle having a (b) bluff body shape comparable to that reported in Rigas et al. (2014).

Following up on the importance of initial conditions in determining the virtual origin of the wake, accounting for a more realistic geometry in the design of the porous disc surrogate is an interesting research topic. In fact, as shown in Stevens et al. (2018) and in Foti et al. (2019), the nacelle has a non-negligible impact in both the mean

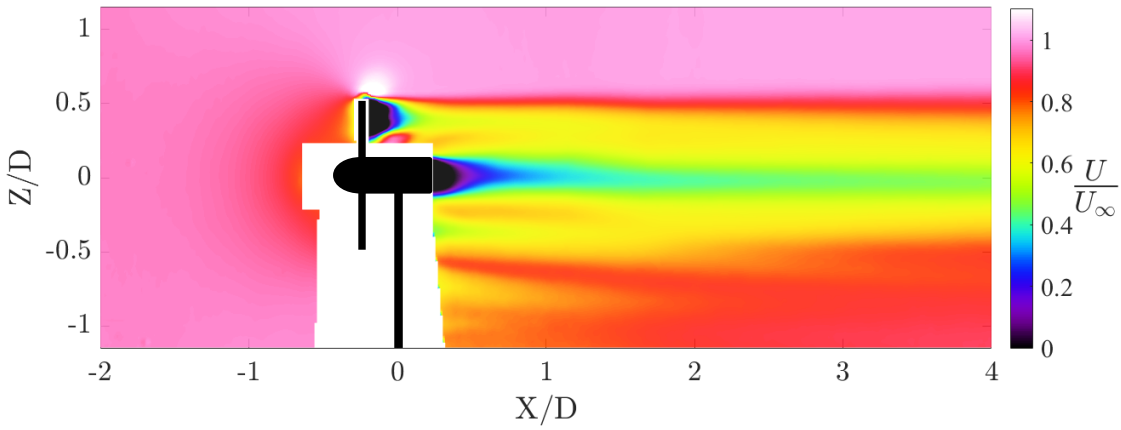

Figure 6.4: Normalised mean streamwise velocity fields U/U_∞ of the test rig with a bluff body-like nacelle.

and the wake dynamics. For HAWT the nacelle has a very small aspect ratio when compared to the rotor diameter (3-5%). However, other types of turbine have a bigger aspect ratio depending on the fluid from which we seek to harness kinematic energy. This is the case for tidal turbines like the Sabella^{TM} D03 30kW turbine shown in figure 6.3a. Its operating conditions warrants the use of a bigger structure with a particularly big nacelle (25% aspect ratio). This nacelle is similar in shape to the bluff body studied in Rigas et al. (2014) (figure 6.3b). This inspired the design of another test rig with a similar nacelle depicted in figure 6.3c. Since the geometry of the test rig and swirl are both initial conditions of the wake, it is likely the flow around the nacelle will have an effect on the swirling wake. To quickly illustrate this point, the normalised streamwise velocity fields of the flow over this test rig with swirl is shown in figure 6.4. Clearly, the nacelle has its own wake inside of the porous disc wake. This research topic is indeed very rich since more nacelle shapes can be tested as well as different aspect ratios. A turbulent flow inside of another turbulent flow naturally gives rise to questions regarding entrainment across the interface separating both flows (Kankanwadi and Buxton, 2022).

II.3 External free-stream turbulence

Another topic which naturally stems from this work is the effect of adding external free-stream turbulence (FST) to the swirling wake of the porous disc which has already shown to have an effect on the wake and drag of other bluff bodies (Bearman and Morel, 1983; Passaggia et al., 2021). To provide a starting block to this topic, SPIV measurements were performed at $X = 7D$ of the swirling wake of case $\alpha = 15°$ with external turbulence. FST was achieved with the help of a regular bi-planar grid of square-mesh arrays featuring square bars. This grid was designed and built based on the work of Roach (1987). The external turbulence intensity reached 4% at $X = 7D$ which is 10 times higher than the case without external turbulence. The FST on the swirling wake is emphasised in figure 6.5. A main characteristic underscored here is that the interface of the turbulent wake is more difficult to discern as now both the wake and the ambient flow are rotational. A sharp jump in enstrophy is now absent and makes the turbulent/turbulent interface (TTI) a more challenging interface to detect (Kankanwadi and Buxton, 2022). The following scientific questions can be asked regarding the addition of external turbulence:

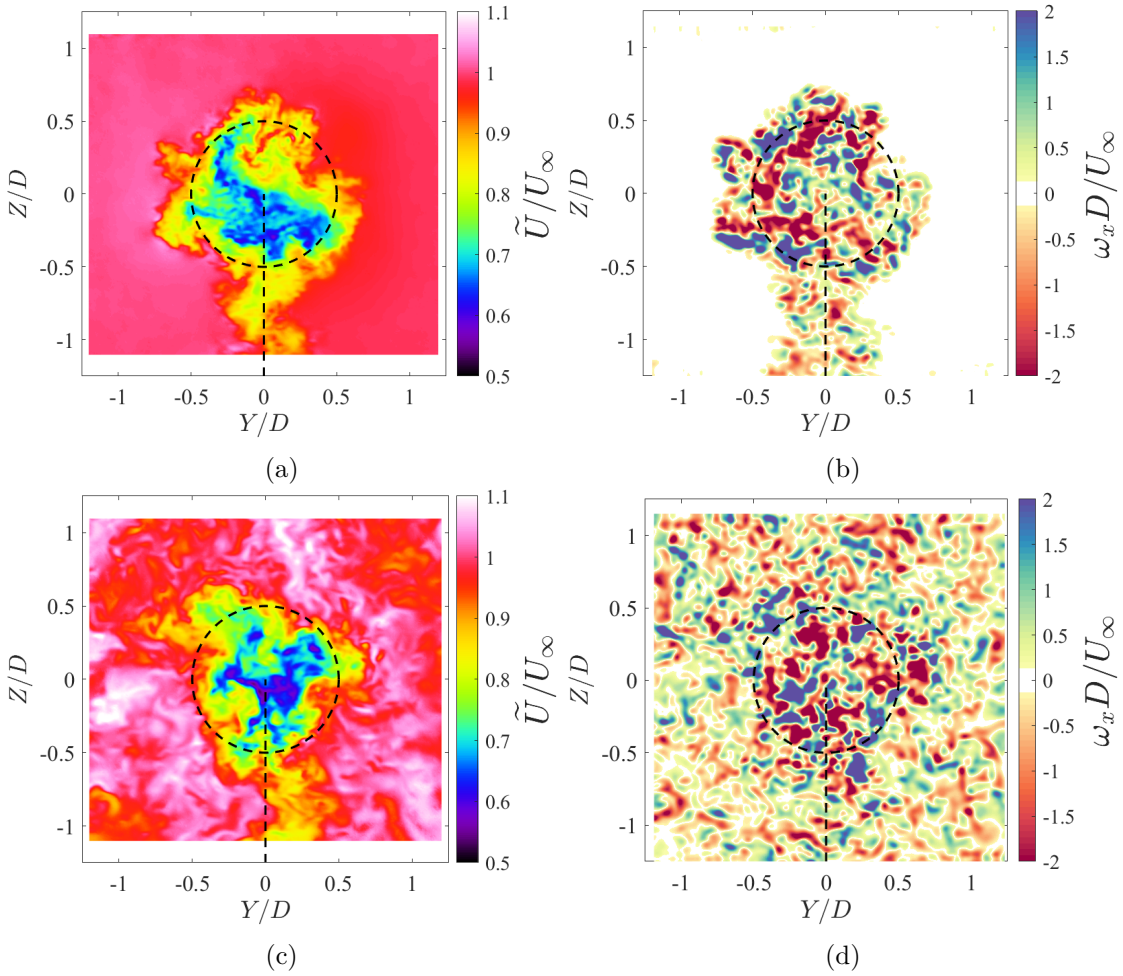

Figure 6.5: Effect of external free-stream turbulence of a randomly chosen SPIV snapshot at $X = 7D$ for case $\alpha = 15°$. The (a, c) normalised instantaneous streamwise velocity fields and streamwise vorticity (b, d) are shown without (a,b) and (c, d) with FST. Dashed black lines: test rig outline.

- Is the drag coefficient of a porous disc modified by FST?
- Was the virtual origin of the wake shifted by FST or the entrainment mechanisms?
- What scaling laws can be found in a swirling wake with FST?
- How can we detect a TTI in turbulent air flows?

This topic is currently being investigated at the PRISME laboratory as a direct continuation of this work. Moreover if external turbulence is generated to mimic a turbulent ABL, wake meandering could be triggered (Espana et al., 2011; Aubrun, 2013). In this configuration, the effect of swirl on wake meandering could be investigated. In any event, with external turbulence, the TTI needs to be properly detected.

Evidence on the existence of the TTI was recently presented in the work of Kankanwadi and Buxton (2022) and measured in water with the means of PIV/PLIF. In this study a fluorescent high-Schmidt number dye was used to mark the wake of a cylinder in a turbulent flow. For our case, the type of flow (turbulent air flow) and test rig configuration increased the challenge of locally seeding the wake. A test rig prototype

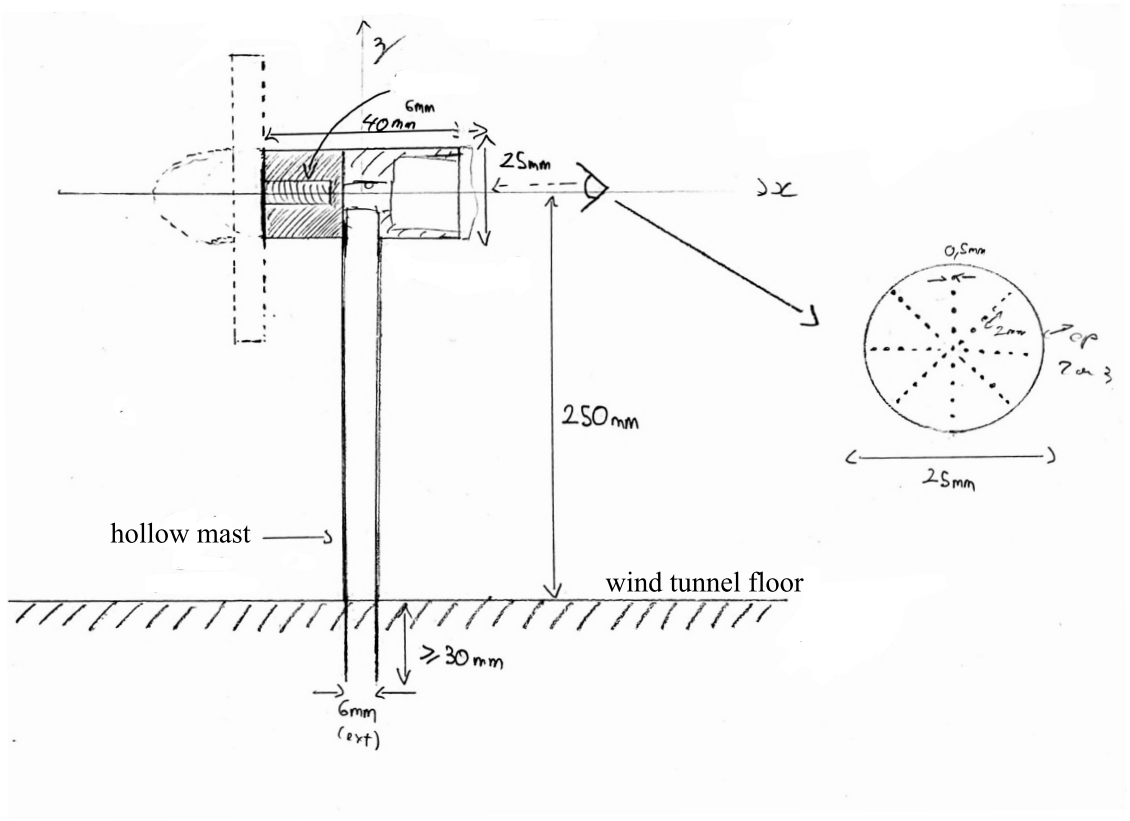

Figure 6.6: Porous disc test rig prototype with a hollow mast and partially hollow nacelle capable of locally seeding the wake of the rig.

using the nacelle shown in §II.2 was built and its schematic is shown in figure 6.6. The prototype featured a hollow mast where tracer particles can be locally injected. The end of the mast is connected to a 3D printed partially hollowed nacelle with a porous back. The prototype was successful in locally injecting olive oil droplets in the back of the nacelle. Figure 6.7 shows a visualisation of the obtained seeding. The visualisation was achieved using a commercially available laser and a cylindrical lens to generate a blue laser sheet. Since swirl was chosen as the main topic of this work, this prototype was not further developed. Nevertheless, it could prove useful when marking the wake of the porous disc, especially if external turbulence is considered in future work. Local seeding would grant the ability to perform a PIV/PLIF combined metrology or a seeding density differentiation to detect the TTI (Prasad and Sreenivasan, 1989; Westerweel et al., 2009; Gan, 2016).

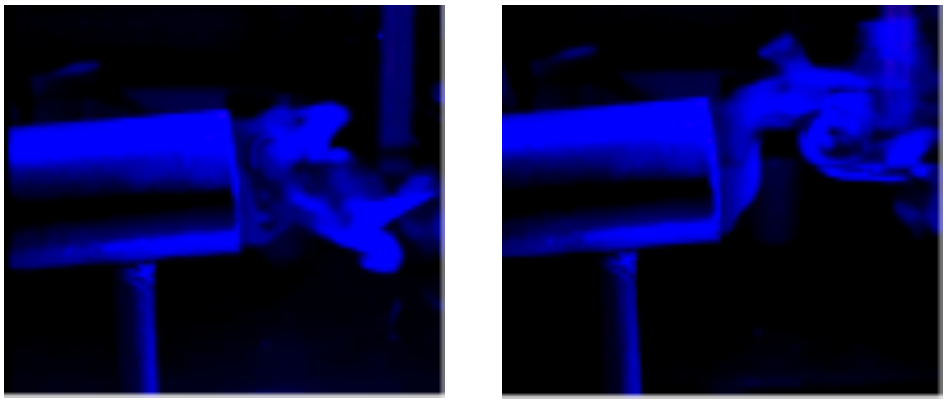

Figure 6.7: Olive oil droplets visualisation of the local seeding injected at the back of the nacelle of a porous disc test rig at two instants (a) and (b).

Résumé en français: Conclusions et perspectives

Ce chapitre final synthétise les résultats les plus saillants issus de cette étude. De plus, quelques perspectives sont esquissées, incluant des éléments préliminaires explorés au cours de cette thèse. Cette étude se penche sur l'absence de swirl dans le sillage d'un ersatz d'éolienne du type disque poreux. Une investigation expérimentale approfondie a été menée sur le sillage turbulent et tournant généré par un disque poreux modifié, intégrant désormais le swirl. L'objectif principal était donc de caractériser et quantifier de manière approfondie l'effet du swirl sur l'évolution du sillage.

Le cadre théorique du sillage turbulent tournant a été établi au chapitre 2, où les équations RANS régissant cet écoulement ont été exposées, avec les simplifications correspondantes. En particulier, la composante azimutale de vitesse ajoute la conservation de la quantité de mouvement angulaire aux lois fondamentales qui régissent l'écoulement. Une analyse de similarité a révélé que le coefficient de traînée d'un sillage tournant et non tournant est identique dans l'approximation du sillage lointain. La théorie de similarité hors équilibre a été utilisée pour aborder le cas $\hat{S} = \mathcal{O}(1)$, montrant que deux longueurs caractéristiques peuvent être définies, l'une liée au déficit de vitesse U_s et l'autre à l'amplitude de swirl W_s. Une nouvelle loi d'échelle a été proposée pour la décroissance du swirl moyen, $W_s \sim x^{-3/2}$.

Un disque poreux avec une porosité non uniforme a été conçu afin de générer passivement un sillage tournant en inclinant les pales du disque d'un angle $\alpha > 0°$. Deux régimes distincts ont été identifiés en fonction de l'angle de calage : le régime d'écoulement attaché et le régime de décrochage. Le swirl a ensuite été caractérisé pour différents angles α, montrant une distribution du swirl autour du centre du sillage. Un bilan de quantité de mouvement a confirmé que, dans le régime d'écoulement attaché, le swirl ne change pas le coefficient de traînée du disque mais modifie la distribution de pression dans le sillage. En outre, l'axisymétrie et l'auto-similarité du déficit de vitesse axiale $U_s(x)/U_\infty$ ont été renforcées avec le swirl, démontrant des profils Gaussiens auto-similaires à partir de $X = 3D$. Une nouvelle échelle δ_{swirl} a été proposée pour mesurer la propagation du swirl dans le sillage proche. Des lois d'échelle de similarité ont été ajustées pour les propriétés du sillage, montrant une excellente concordance avec les prédictions de la turbulence hors équilibre dérivées dans le chapitre 2.

Enfin, l'impact du swirl sur les mécanismes d'entraînement a été quantifié, montrant une augmentation de l'entraînement moyen malgré une vitesse d'entraînement constante. Une nouvelle méthode de détection de la TNTI à été proposée en nous basant sur les zones de quantité de mouvement uniforme. En outre, La fractalité de la TNTI a été étudiée, montrant une dimension fractale conforme avec les prédictions de la turbulence hors équilibre.

En conclusion, cette étude a conduit à la proposition d'un nouveau modèle de disque poreux, générant passivement et pour un coût de fabrication modeste un sillage turbulent auto-similaire avec des niveaux de swirl comparables à ceux trouvés dans des éoliennes de taille réelle. L'approche choisie, permet de générer ces nombres de swirl sans changer le blocage effectif du disque et génère un sillage tournant à l'aide d'un paramètre ajustable α. Ces résultats ouvrent la voie à de nombreuses investigations sur le sillage tournant d'une éolienne en utilisant un disque poreux (méandrement du sillage tournant, interactions entre sillages tournants, turbulence externe, particules inertielles, angles d'inclinaison des rotors, etc.).

La dernière partie de ce chapitre concerne quelques perspectives de ce travail et des

résultats préliminaires menés pour chacun des éléments. Nous nous sommes par exemple intéressés à l'étude de l'hélicité dans le sillage généré en l'utilisant comme un critère supplémentaire de détection de la TNTI. Cette quantité, invariante des équations d'Euler, peut en effet être utilisée pour mieux caractériser l'entraînement sur la TNTI. En outre, les conditions initiales du substitut de l'éolienne peuvent être encore améliorés pour prendre en compte la géométrie complexe d'une éolienne. Par exemple, une nacelle de dimensions plus grandes peut être étudiée (voir figure 6.3) pour mieux représenter le caractère multi-échelle d'une hydrolienne. A ce sujet, un autre dispositif à été fabriqué et caractérisé afin d'étudier l'effet d'une nacelle de plus grandes dimensions. Cependant, nous avons fait le choix de nous concentrer sur la rotation du sillage dans ce manuscrit. Finalement, un sujet qui découle naturellement de ce travail est l'effet de l'ajout d'une turbulence externe au sillage tournant du disque poreux ce qui a déjà montré avoir un effet sur le sillage et la traînée d'autres corps épais (Bearman and Morel, 1983; Passaggia et al., 2021). Afin d'esquisser ce sujet, des mesures SPIV ont été effectuées à $X = 7D$ du sillage tournant ($\alpha = 15°$) avec une turbulence externe. La turbulence externe a été générée à l'aide d'une grille bi-planaire régulière de mailles carrées avec des barreaux de section carrée. Cette grille a été conçue et construite selon les indications formulées dans le travail de Roach (1987). L'intensité de la turbulence externe atteint 4% à X = 7D, soit 10 fois plus élevée que dans le cas sans turbulence externe. Une caractéristique principale soulignée ici est que l'interface du sillage turbulent est plus difficile à discerner, car à présent, le sillage ainsi que l'écoulement ambiant sont rotationnels. Un saut brusque d'enstrophie est désormais absent, rendant l'interface turbulente/turbulente (TTI) plus difficile à détecter (Kankanwadi and Buxton, 2022). Afin de détecter une telle interface dans le cas d'un disque poreux, un prototype utilisant la nacelle présentée dans la §II.2 a été construit, et son schéma est illustré dans la figure 6. Le prototype comprend un mât creux où des particules peuvent être injectées localement. L'extrémité du mât est reliée à une nacelle partiellement creuse imprimée en 3D avec un culot poreux. Le prototype nous a permis d'ensemencer localement l'arrière de la nacelle. La figure 7 montre une visualisation de l'ensemencement obtenu. Toutes ces perspectives ont été considérées dans ce travail mais n'ont pas été incluses dans ce manuscrit. Néanmoins, ces études préliminaires montrent la pertinence de ces sujets ainsi que des résultats encourageants.

Bibliography

M. S. Adaramola and P. Krogstad. Experimental investigation of wake effects on wind turbine performance. *Renewable energy*, 36(8):2078–2086, 2011.

R. J. Adrian, K. T. Christensen, and Z. C. Liu. Analysis and interpretation of instantaneous turbulent velocity fields. *Experiments in Fluids*, 29:275–290, 2000a.

R. J. Adrian, C. D. Meinhart, and C. D. Tomkins. Vortex organization in the outer region of the turbulent boundary layer. *Journal of Fluid Mechanics*, 422:1–54, 2000b.

S. V. Alekseenko, P. A. Kuibin, V. Okulov S. Leonidovich, and S. I. Shtork. Helical vortices in swirl flow. *Journal of Fluid Mechanics*, 382:195–243, 1999.

D. Allaerts and J. Meyers. Gravity waves and wind-farm efficiency in neutral and stable conditions. *Boundary-layer meteorology*, 166(2):269–299, 2018.

J. D. Anderson. *Fundamentals of aerodynamics*. McGraw-Hill, 2011.

R. A. Antonia and S. Rajagopalan. Determination of drag of a circular cylinder. *AIAA journal*, 28(10):1833–1834, 1990.

S. Aubrun. Wind turbine wake properties: Comparison between a non-rotating simplified wind turbine model and a rotating model. *J. Wind Eng. Ind. Aerodyn.*, 2013.

S. Aubrun, M. Bastankhah, R. B. Cal, B. Conan, R.J Hearst, D. Hoek, and A. Zasso et al. Round-robin tests of porous disc models. *Journal of Physics: Conference Series*, 47, 2019.

B. Baj and O. Buxton. Interscale energy transfer in the merger of wakes of a multiscale array of rectangular cylinders. *Physical Review Fluids*, 2(11):114607, 2017.

R. W. Baker and S. N. Walker. Wake measurements behind a large horizontal axis wind turbine generator. *Solar Energy*, 33(1):5–12, 1984.

J. B. Barlow, W. H. Rae, and A. Pope. *Low-speed wind tunnel testing*. John wiley & sons, 1999.

D. B. Barrie and D. B. Kirk-Davidoff. Weather response to a large wind turbine array. *Atmospheric Chemistry and Physics*, 10(2):769–775, 2010.

R. J. Barthelmie and L. E. Jensen. Evaluation of wind farm efficiency and wind turbine wakes at the nysted offshore wind farm. *Wind Energy*, 13(6):573–586, 2010.

R. J. Barthelmie, G. C. Larsen, S. T. Frandsen, L. Folkerts, K. Rados, S. C. Pryor, B. Lange, and G. Schepers. Comparison of wake model simulations with offshore wind turbine wake profiles measured by sodar. *Journal of atmospheric and oceanic technology*, 23(7):888–901, 2006.

M. Bastankhah and F. Porté-Agel. Wind tunnel study of the wind turbine interaction with a boundary-layer flow: Upwind region, turbine performance, and wake region. *Physics of Fluids*, 29(6), 2017.

M. Bastankhah and F. Porté-Agel. A new analytical model for wind-turbine wakes. *Renewable Energy*, 70, 2014.

C. K. Batchelor. *An introduction to fluid dynamics*. Cambridge university press, 1967.

G. K. Batchelor. *The theory of homogeneous turbulence*. Cambridge university press, 1953.

G. K. Batchelor. Heat convection and buoyancy effects in fluids. *Quarterly journal of the royal meteorological society*, 80(345):339–358, 1954.

P. W. Bearman and T. Morel. Effect of free stream turbulence on the flow around bluff bodies. *Progress in aerospace sciences*, 20(2-3):97–123, 1983.

P. Bénard, A. Viré, V. Moureau, G. Lartigue, L. Beaudet, P. Deglaire, and L. Bricteux. Large-eddy simulation of wind turbines wakes including geometrical effects. *Computers & Fluids*, 173:133–139, 2018.

C. Bendicks, D. Tarlet, C. Roloff, R. Bordás, B. Wunderlich, B. Michaelis, and D. Thévenin et al. Improved 3-d particle tracking velocimetry with colored particles. *Journal of Signal and Information Processing*, 2(02):59, 2011.

F. Berger, L. Kröger, D. Onnen, V. Petrović, and M. Kühn. Scaled wind turbine setup in a turbulent wind tunnel. In *Journal of Physics: Conference Series*, volume 1104, page 012026. IOP Publishing, 2018.

T. Berk, T. Medjnoun, and B. Ganapathisubramani. Entrainment effects in periodic forcing of the flow over a backward-facing step. *Physical Review Fluids*, 2(7):074605, 2017.

A. Betz. Schraubenpropeller mit geringstem energieverlust dissertation. *Göttingen Nachrichten, Göttinge*, 1919.

P. M. Bevilaqua and P. S. Lykoudis. Mechanism of entrainment in turbulent wakes. *AIAA Journal*, 9(8), 1971.

P. M. Bevilaqua and P. S. Lykoudis. Turbulence memory in self-preserving wakes. *Journal of Fluid Mechanics*, 89(3):589–606, 1978.

D. K. Bisset, J. C. R. Hunt, M. Rogers, and M. Michael. The turbulent/non-turbulent interface bounding a far wake. *Journal of Fluid Mechanics*, 451:383–410, 2002.

J. Bleeg, M. Purcell, R. Ruisi, and E. Traiger. Wind farm blockage and the consequences of neglecting its impact on energy production. *Energies*, 11(6):1609, 2018.

J. Bossuyt, R. Scottand N. Ali, and R. B. Cal. Quantification of wake shape modulation and deflection for tilt and yaw misaligned wind turbines. *Journal of Fluid Mechanics*, 917, 2021.

C. L. Bottasso, F. Campagnolo, and V. Petrović. Wind tunnel testing of scaled wind turbine models: Beyond aerodynamics. *Journal of wind engineering and industrial aerodynamics*, 127:11–28, 2014.

M. Breda and O. Buxton. Behaviour of small-scale turbulence in the turbulent/non-turbulent interface region of developing turbulent jets. *Journal of Fluid Mechanics*, 879:187–216, 2019.

H. H. Bruun. *Hot-wire anemometry: principles and signal analysis*. Oxford University Press, 1996.

T. Burton, N. Jenkins, D. Sharpe, and E. Bossanyi. *Wind energy handbook*. John Wiley & Sons, 2011.

N. Butt, H. L. Beyer, J. R. Bennett, D. Biggs, R. Maggini, M. Mills, A. R. Renwick, L. M. Seabrook, and H. P. Possingham. Biodiversity risks from fossil fuel extraction. *Science*, 342(6157):425–426, 2013.

O. Buxton. Modulation of the velocity gradient tensor by concurrent large-scale velocity fluctuations in a turbulent mixing layer. *Journal of Fluid Mechanics*, 777:R1, 2015.

E. H. Camp and R. B. Cal. Mean kinetic energy transport and event classification in a model wind turbine array versus an array of porous disks: Energy budget and octant analysis. *Physical Review Fluids*, 1, 2016.

F. Campagnolo, V. Petrović, J. Schreiber, E. Nanos, A. Croce, and C. L. Bottasso. Wind tunnel testing of a closed-loop wake deflection controller for wind farm power maximization. In *Journal of Physics: Conference Series*, volume 753. IOP Publishing, 2016.

H. Canet, P. Bortolotti, and C. L. Bottasso. On the scaling of wind turbine rotors. *Wind Energy Science*, 6(3):601–626, 2021.

S. Cannon, F. Champagne, and A. Glezer. Observations of large-scale structures in wakes behind axisymmetric bodies. *Experiments in Fluids*, 14(6):447–450, 1993.

I. P. Castro. Wake characteristics of two-dimensional perforated plates normal to an air-stream. *Journal of Fluid Mechanics*, 46:599–609, 1971.

L. P. Chamorro and F. Porte-Agel. Turbulent flow inside and above a wind farm: a wind-tunnel study. *Energies*, 4(11):1916–1936, 2011.

L. P. Chamorro and F. Porté-Agel. Effects of thermal stability and incoming boundary-layer flow characteristics on wind-turbine wakes: A wind-tunnel study. *Boundary-Layer Meteorology*, 136, 2010.

F. H. Champagne. The fine-scale structure of the turbulent velocity field. *Journal of Fluid Mechanics*, 86(1):67–108, 1978.

K. Chauhan, J. Philip, C. M. de Silva, N. Hutchins, and I. Marusic. The turbulent/non-turbulent interface and entrainment in a boundary layer. *Journal of Fluid Mechanics*, 742:119–151, 2014.

Y. T. Chew et al. The directional sensitivities of crossed and triple hot-wire probes. *Journal of Physics E: Scientific Instruments*, 21(6):613, 1988.

E. Cintosun, G. J. Smallwood, and Ö. L/ Gülder. Flame surface fractal characteristics in premixed turbulent combustion at high turbulence intensities. *AIAA journal*, 45 (11):2785–2789, 2007.

G. Comte-Bellot. Hot-wire anemometry. *Annual review of fluid mechanics*, 8(1):209–231, 1976.

S. Corrsin and A. L. Kistler. Free-stream boundaries of turbulent flows. Technical report, National Aeronautics and Space Administration (NASA), 1955.

G. Crasto, A. R. Gravdahl, F. Castellani, and E. Piccioni. Wake modeling with the actuator disc concept. *Energy Procedia*, 24:385–392, 2012.

A. Crespo, J. Hernandez, and S. Frandsen. Survey of modelling methods for wind turbine wakes and wind farms. *Wind Energy: An International Journal for Progress and Applications in Wind Power Conversion Technology*, 2(1):1–24, 1999.

C. B. da Silva, J. C. R. Hunt, I. Eames, and J. Westerweel. Interfacial layers between regions of different turbulence intensity. *Annual review of fluid mechanics*, 46:567–590, 2014.

W. J. A. Dahm and P. E. Dimotakis. Measurements of entrainment and mixing in turbulent jets. *AIAA journal*, 25(9):1216–1223, 1987.

T. Dairay, M. Obligado, and J. C. Vassilicos. Non-equilibrium scaling laws in axisymmetric turbulent wakes. *J. Fluid Mech.*, 781:166–195, 2015.

C. M. de Silva, J. Philip, K. Chauhan, C. Meneveau, and I. Marusic. Multiscale geometry and scaling of the turbulent-nonturbulent interface in high reynolds number boundary layers. *Physical review letters*, 111(4):044501, 2013.

C. M. de Silva, N. Hutchins, and I. Marusic. Uniform momentum zones in turbulent boundary layers. *Journal of Fluid Mechanics*, 786:309–331, 2016.

I. Dincer. Renewable energy and sustainable development: a crucial review. *Renewable and sustainable energy reviews*, 4(2):157–175, 2000.

G. D. Duffman. Calibration of triaxial hot-wire probes using a numerical search algorithm. *Journal of Physics E: Scientific Instruments*, 13(11):1177, 1980.

N. P. Dufresne. *Experimental investigation of the turbulent axisymmetric wake with rotation generated by a wind turbine*. PhD thesis, University of New Hampshire, 2013.

G. Espana, S. Aubrun, S. Loyer, and P. Devinant. Spatial study of the wake meandering using modelled wind turbines in a wind tunnel. *Wind Energy*, 14(7):923–937, 2011.

J. Finn. How to measure turbulence with hot-wire anemometers - a practical guide. In *How to measure turbulence with hot-wire anemometers - a practical guide*, 2002.

D. Fiscaletti, A. Attili, F. Bisetti, and G. E. Elsinga. Scale interactions in a mixing layer–the role of the large-scale gradients. *Journal of Fluid Mechanics*, 791:154–173, 2016.

D. Fiscaletti, O. Buxton, and A. Attili. Internal layers in turbulent free-shear flows. *Physical Review Fluids*, 6(3):034612, 2021.

D. Foti, X. Yang, L. Shen, and F. Sotiropoulos. Effect of wind turbine nacelle on turbine wake dynamics in large wind farms. *Journal of Fluid Mechanics*, 869:1–26, 2019.

S. Frandsen, R. J. Barthelmie, S. Pryor, O. Rathmann, S. Larsen, J. Højstrup, and M. Thøgersen. Analytical modelling of wind speed deficit in large offshore wind farms. *Wind Energy: An International Journal for Progress and Applications in Wind Power Conversion Technology*, 9(1-2):39–53, 2006.

A. Fuchs, S. Kharche, M. Wächter, and J. Peinke. An open source matlab package to perform basic and advanced statistical analysis of turbulence data and other complex systems. *arXiv preprint arXiv:2106.13042*, 2021.

L. Gan. Detection of passive scalar interface directly from PIV particle images in inhomogeneous turbulent flows. *Flow, Turbulence and Combustion*, 97:141–170, 2016.

W. K. George. The self-preservation of turbulent flows and its relation to initial conditions and coherent structures. *Advances in Turbulence*, 1989.

J. H. Gerrard. The mechanics of the formation region of vortices behind bluff bodies. *Journal of fluid mechanics*, 25(2):401–413, 1966.

T. Göçmen, P. Van der Laan, P. E. Réthoré, A. P. Diaz, G. Larsen, and S. Ott. Wind turbine wake models developed at the technical university of denmark: A review. *Renewable and Sustainable Energy Reviews*, 60:752–769, 2016.

I. B. Goldman and J. M. Marchello. Turbulent schmidt numbers. *International Journal of Heat and Mass Transfer*, 12(7):797–802, 1969.

J. M. R. Graham. Turbulent flow past a porous plate. *Journal of Fluid Mechanics*, 73 (3):565–591, 1976.

A. Gupta, D. G. Lilley, and N. Syred. Swirl flows. *Tunbridge Wells*, 1984.

M. Hamdi, M. Havet, O. Rouaud, and D. Tarlet. Comparison of different tracers for PIV measurements in ehd airflow. *Experiments in Fluids*, 55, 2014.

J. T. Hardy. *Climate change: causes, effects, and solutions*. John Wiley & Sons, 2003.

M. Harker and P. O'Leary. Least squares surface reconstruction from measured gradient fields. In *2008 IEEE conference on computer vision and pattern recognition*, pages 1–7. IEEE, 2008.

C. B. Hasager, L. Rasmussen, A. Peña, L. E. Jensen, and P. E. Réthoré. Wind farm wake: The horns rev photo case. *Energies*, 6(2):696–716, 2013.

S. J. Helvig, K. M. Vinnes, A. Segalini, A. N. Worth, and R. J. Hearst. A comparison of lab-scale free rotating wind turbines and actuator disks. *Journal of Wind Engineering and Industrial Aerodynamics, American Society of Mechanical Engineers ASME*, 209, 2021.

S. Herpin, C. Y. Wong, M. Stanislas, and J. Soria. Stereoscopic piv measurements of a turbulent boundary layer with a large spatial dynamic range. *Experiments in fluids*, 45:745–763, 2008.

U. Högström, D. N. Asimakopoulos, H. Kambezidis, C. G. Helmis, and A. Smedman. A field study of the wake behind a 2 mw wind turbine. *Atmospheric Environment (1967)*, 22(4):803–820, 1988.

M. J. Holmes and J. M. Naughton. The impact of swirl and wake strength on turbulent axisymmetric wake evolution. *Physics of Fluids*, 34(9):095101, 2022.

M. Howland, J. Bossuyt, L. A. Martinez-Tossas, J. Meyers, and C. Maneveau. Wake structure in actuator disk models of wind turbines in yaw under uniform inflow conditions. *Journal of Renewable and Sustainable Energy*, 8, 2016.

J. C. R Hunt and F. Hussain. A note on velocity, vorticity and helicity of inviscid fluid elements. *Journal of Fluid Mechanics*, 229:569–587, 1991.

IEA. Wind power capacity in the net zero scenario, 2015-2030, 2023. URL `https://www.iea.org/data-and-statistics/charts/wind-power-capacity-in-the-net-zero-scenario-2015-2030`. Licence: CC BY 4.0.

T. Ishihara and G. W. Qian. A new gaussian-based analytical wake model for wind turbines considering ambient turbulence intensities and thrust coefficient effects. *Journal of Wind Engineering and Industrial Aerodynamics*, 177:275–292, 2018.

T. Ishihara, A. Yamaguchi, and Y. Fujino. Development of a new wake model based on a wind tunnel experiment. *Global wind power*, 6, 2004.

G. V. Iungo, Y. Wu, and F. Porté-Agel. Field measurements of wind turbine wakes with lidars. *Journal of Atmospheric and Oceanic Technology*, 30(2):274–287, 2013.

N. O. Jensen. A note on wind turbine interaction. *Riso-M-2411, Risoe National Laboratory, Roskilde, Denmark*, page 16, 1983.

P. B. V. Johansson, W. K. George, and M. J. Gourlay. Equilibrium similarity, effects of initial conditions and local reynolds number on the axisymmetric wake. *Phys. Fluids*, 15, 2003.

J. Jonkman, S. Butterfield, W. Musial, and G. Scott. Definition of a 5-mw reference wind turbine for offshore system development. Technical report, National Renewable Energy Lab.(NREL), Golden, CO (United States), 2009.

N. E. Joukowsky. Vortex theory of screw propeller. *Trudy Otdeleniya Fizicheskikh Nauk Obshchestva Lubitelei Estestvoznaniya (in Russian)*, 16(1):1–31, 1912.

J. K. Kaldellis, P. Triantafyllou, and P. Stinis. Critical evaluation of wind turbines analytical wake models. *Renewable and Sustainable Energy Reviews*, 144:110991, 2021.

G. A. Kallio and D. E. Stock. Interaction of electrostatic and fluid dynamic fields in wireplate electrostatic precipitators. *Journal of Fluid Mechanics*, 240:133–166, 1992.

K. S. Kankanwadi and O. Buxton. On the physical nature of the turbulent/turbulent interface. *Journal of Fluid Mechanics*, 942:A31, 2022.

Y. Käsler, S. Rahm, R. Simmet, and M. Kühn. Wake measurements of a multi-mw wind turbine with coherent long-range pulsed doppler wind lidar. *Journal of Atmospheric and Oceanic Technology*, 27(9):1529–1532, 2010.

J. Kauppinen and J. Partanen. *Fourier transforms in spectroscopy*. John Wiley & Sons, 2001.

L. V. King. On the convection of heat from small cylinders in a stream of fluid: Determination of the convection constants of small platinum wires with applications to hot-wire anemometry. *Philosophical transactions of the royal society of London. series A, containing papers of a mathematical or physical character*, 214(509-522): 373–432, 1914.

A. N. Kolmogorov. Dissipation of energy in the locally isotropic turbulence. In *Dissipation of energy in the locally isotropic turbulence*, volume 32, pages 19–21, 1941.

L. Kovacs, P. Y. Passaggia, N. Mazellier, and V. Lago. Detection method for shock-waves in viscous flows. *Experiments in Fluids*, 63(1):11, 2022.

L. Kovasznay. Structure of the turbulent boundary layer. *The Physics of Fluids*, 10 (9):S25–S30, 1967.

Y. S. Kwon, J. Philip, C. M. de Silva, N. Hutchins, and J. P. Monty. The quiescent core of turbulent channel flow. *Journal of Fluid Mechanics*, 751:228–254, 2014.

S. Laizet, J. C. Vassilicos, and C. Cambon. Interscale energy transfer in decaying turbulence and vorticity–strain-rate dynamics in grid-generated turbulence. *Fluid Dynamics Research*, 45(6):061408, 2013.

G. F. Lane-Serff, P. F. Linden, and M. Hillel. Forced, angled plumes. *Journal of hazardous materials*, 33(1):75–99, 1993.

G. C. Larsen, H. Madsen, K. Thomsen, and T. J. Larsen. Wake meandering: a pragmatic approach. *Wind Energy: An International Journal for Progress and Applications in Wind Power Conversion Technology*, 11(4):377–395, 2008.

P. Lavoie, L. Djenidi, and R. A. Antonia. Effects of initial conditions in decaying turbulence generated by passive grids. *Journal of Fluid Mechanics*, 585:395–420, 2007.

G. Lee and C. Smith. Distortion of the vortex core during blade-vortex interaction. In *19th AIAA, Fluid Dynamics, Plasma Dynamics, and Lasers Conference*, page 1243, 1987.

J. Lee, Y. Kim, A. Khosronejad, and S. Kang. Experimental study of the wake characteristics of an axial flow hydrokinetic turbine at different tip speed ratios. *Ocean Engineering*, 196:106777, 2020.

H. Li, Y. Zhao, J. Liu, and J. Carmeliet. Physics-based stitching of multi-fov PIV measurements for urban wind fields. *Building and Environment*, 205, 2021a.

Y. Li, G. Blois, F. Kazemifar, and K. T. Christensen. A particle-based image segmentation method for phase separation and interface detection in PIV images of immiscible multiphase flow. *Measurement Science and Technology*, 32(9):095208, 2021b.

L. E. M. Lignarolo, D. Mehta, R. J. A. M. Stevens, and A. E. Yilmaz et al. Validation of four LES and a vortex model against stereo-PIV measurements in the near wake of an actuator disc and a wind turbine. *Renewable Energy*, 94, 2016a.

L. E. M. Lignarolo, D. Ragni, and C. J. Ferreira. Experimental comparison of a wind-turbine and of an actuator-disc near wake. *J. Renewable Sustainable Energy*, 2016b.

E. Lingkan and O. Buxton. An assessment of the scalings for the streamwise evolution of turbulent quantities in wakes produced by porous objects. *Renewable Energy*, 209: 1–9, 2023.

M. Magnusson and A. S. Smedman. Air flow behind wind turbines. *Journal of Wind Engineering and Industrial Aerodynamics*, 80(1-2):169–189, 1999.

B. B. Mandelbrot. *The fractal geometry of nature*, volume 1. WH freeman New York, 1982.

M. E. Mann, R. S. Bradley, and M. K. Hughes. Northern hemisphere temperatures during the past millennium: Inferences, uncertainties, and limitations. *Geophysical research letters*, 26(6):759–762, 1999.

J. F. Manwell, J. G. McGowan, and A. L. Rogers. *Wind energy explained: theory, design and application*. John Wiley & Sons, 2010.

D. W. Marquardt. An algorithm for least-squares estimation of nonlinear parameters. *Journal of the society for Industrial and Applied Mathematics*, 11(2):431–441, 1963.

A. R. Masri, P. Kalt, and R. S. Barlow. The compositional structure of swirl-stabilised turbulent nonpremixed flames. *Combustion and Flame*, 137(1-2):1–37, 2004.

G. Maurice, F. Thiesset, F. Halter, N. Mazellier, C. C. Chauveau, I. Gökalp, and A. Kourta. Scale analysis of the flame front in premixed combustion using Proper Orthogonal Decomposition. *Experimental Thermal and Fluid Science*, 73:109–114, 2016.

N. Mazellier and J. C. Vassilicos. The turbulence dissipation constant is not universal because of its universal dependence on large-scale flow topology. *Physics of Fluids*, 20(1), 2008.

N. Mazellier and J. C. Vassilicos. Turbulence without richardson–kolmogorov cascade. *Physics of fluids*, 22(7):075101, 2010.

G. B. McCullough and D. E. Gault. Boundary-layer and stalling characteristics of the naca 64a006 airfoil section. Technical report, National Aeronautics and Space Administration (NASA), 1949.

C. D. Meinhart and R. J. Adrian. On the existence of uniform momentum zones in a turbulent boundary layer. *Physics of Fluids*, 7:694–696, 1995.

C. Meneveau and K. R. Sreenivasan. Interface dimension in intermittent turbulence. *Physical Review A*, 41(4):2246, 1990.

D. Mistry, J. R. Dawson, and A. R. Kerstein. The multi-scale geometry of the near field in an axisymmetric jet. *Journal of Fluid Mechanics*, 838:501–515, 2018.

H. K. Moffatt. The degree of knottedness of tangled vortex lines. *Journal of Fluid Mechanics*, 35(1):117–129, 1969.

M. Mohebi, D. Wood, and R. J. Martinuzzi. The turbulence structure of the wake of a thin flat plate at post-stall angles of attack. *Experiments in Fluids*, 58:1–18, 2017.

F. Moisy, C. Morize, M. Rabaud, and J. Sommeria. Decay laws, anisotropy and cyclone–anticyclone asymmetry in decaying rotating turbulence. *Journal of Fluid Mechanics*, 666:5–35, 2011.

D. O. Mora, E. M. Pladellorens, P. R. Turró, M. Lagauzere, and M. Obligado. Energy cascades in active-grid-generated turbulent flows. *Physical Review Fluids*, 4(10): 104601, 2019.

C. E. Morris, D. M. Odoherty, A. Mason-Jones, and T. ODoherty. Evaluation of the swirl characteristics of a tidal stream turbine wake. *International Journal of Marine Energy*, 14:198–214, 2016.

B. R. Morton, G. I. Taylor, and J. S. Turner. Turbulent gravitational convection from maintained and instantaneous sources. *Proceedings of the Royal Society of London. Series A. Mathematical and Physical Sciences*, 234(1196):1–23, 1956.

K. Nagata, Y. Sakai, T. Inaba, H. Suzuki, O. Terashima, and H. Suzuki. Turbulence structure and turbulence kinetic energy transport in multiscale/fractal-generated turbulence. *Physics of Fluids*, 25(6), 2013.

K. Nagata, T. Saiki, Y. Sakai, Y. Ito, and K. Iwano. Effects of grid geometry on non-equilibrium dissipation in grid turbulence. *Physics of Fluids*, 29(1), 2017.

Y. Nakayama. *Visualized flow: fluid motion in basic and engineering situations revealed by flow visualization*. Pergamon Press, 1988.

J. Nedic. *Fractal-generated wakes*. PhD thesis, Imperial College of London, 2013.

I. Neunaber, M. Obligado, J. Peinke, and S. Aubrun. Application of the townsend-george wake theory to field measurements of wind turbine wakes. In *Journal of Physics: Conference Series*, volume 1934. IOP Publishing, 2021.

V. L. Okulov, I. V. Naumov, R. F. Mikkelsen, I. K. Kabardin, and J. N. Sørensen. A regular strouhal number for large-scale instability in the far wake of a rotor. *Journal of Fluid Mechanics*, 747:369–380, 2014.

V. L. Okulov, J. N. Sørensen, and D. H. Wood. The rotor theories by professor joukowsky: Vortex theories. *Progress in aerospace sciences*, 73:19–46, 2015.

J. G. J. Olivier, G. Janssens-Maenhout, and J. Peters. Trends in global co2 emissions. *PBL Netherlands Environmental Assessment Agency*, 500114022:6–39, 2012.

B. Öztürk, A. Hassanein, M. T. Akpolat, A. Abdulrahim, M. Perçin, and O. Uzol. On the wake characteristics of a model wind turbine and a porous disc: Effects of freestream turbulence intensity. *Renewable Energy*, 212:238–250, 2023.

P. Y. Passaggia, N. Mazellier, and A. Kourta. Aerodynamic drag modification induced by free-stream turbulence effects on a simplified road vehicle. *Physics of Fluids*, 33 (10), 2021.

J. Philip, C. Meneveau, C. M. de Silva, and I. Marusic. Multiscale analysis of fluxes at the turbulent/non-turbulent interface in high Reynolds number boundary layers. *Physics of Fluids*, 26(1), 2014.

O. M. Phillips. The irrotational motion outside a free turbulent boundary. In *Mathematical Proceedings of the Cambridge Philosophical Society*, volume 51, pages 220–229. Cambridge University Press, 1955.

F. Pierella and Lars Sætran. Wind tunnel investigation on the effect of the turbine tower on wind turbines wake symmetry. *Wind Energy*, 20(10):1753–1769, 2017.

F. Pisanò. Input of advanced geotechnical modelling to the design of offshore wind turbine foundations. *Proceedings of the XVII ECSMGE-2019: Geotechnical Engineering foundation of the future*, pages 1–6, 2019.

S. B. Pope. *Turbulent flows*. Cambridge University Press, 2000.

F. Porté-Agel, Y. Wu, H. Lu, and R. J. Conzemius. Large-eddy simulation of atmospheric boundary layer flow through wind turbines and wind farms. *Journal of Wind Engineering and Industrial Aerodynamics*, 99(4):154–168, 2011.

H. Pörtner, D. C. Roberts, H. Adams, C. Adler, P. Aldunce, E. Ali, R. Begum, R. Betts, and R. Kerr. *Climate change 2022: Impacts, adaptation and vulnerability*. IPCC Geneva, Switzerland, 2022.

F. Porté-Agel. Wind-turbine and wind-farm flows: A review. *Springer*, 2019.

S. R. J. Powles. The effects of tower shadow on the dynamics of a horizontal-axis wind turbine. *Wind Engineering*, pages 26–42, 1983.

R. R. Prasad and K. R. Sreenivasan. Scalar interfaces in digital images of turbulent flows. *Experiments in fluids*, 7(4):259–264, 1989.

M. Raffel, C. E. Willert, and J. Kompenhans. *Particle image velocimetry: a practical guide*. Springer Science & Business Media, 2007.

M. Ragheb. Wind turbines theory-the betz equation and optimal rotor tip speed ratio. *Fundamental and advanced topics in wind power*, 1(1):19–38, 2011.

J. Redford, I. P. Castro, and G. N. Coleman. On the universality of turbulent axisymmetric wakes. *Journal of fluid mechanics*, 710:419–452, 2012.

PRS REN21. Renewables 2022 global status report, 2022.

A. J. Reynolds. Similarity in swirling wakes and jets. *Journal of Fluid Mechanics*, 14 (2):241–243, 1962.

G. Rigas, A. R. Oxlade, A. S. Morgans, and J. F. Morrison. Low-dimensional dynamics of a turbulent axisymmetric wake. *Journal of Fluid Mechanics*, 755:R5, 2014.

H. Ritchie, P. Rosado, and M. Roser. Energy production and consumption. *Our World in Data*, 2020. https://ourworldindata.org/energy-production-consumption.

P. E. Roach. The generation of nearly isotropic turbulence by means of grids. *International journal of heat and fluid flow*, 8(2):82–92, 1987.

L. De Rosa. On the helicity conservation for the incompressible euler equations. *Proceedings of the American Mathematical Society*, 148(7):2969–2979, 2020.

CF. Schleussner, J. Rogelj, M. Schaeffer, T. Lissner, R. Licker, E. M. Fischer, R. Knutti, A. Levermann, K. Frieler, and W. Hare. Science and policy characteristics of the paris agreement temperature goal. *Nature Climate Change*, 6:827–835, 2016.

H. Schlichting and J. Kestin. *Boundary layer theory*, volume 121. Springer, 1961.

B. Schliffke. *Experimental Characterisation of the Far Wake of a Modelled Floating Wind Turbine as a Function of Incoming Swell*. PhD thesis, École centrale de Nantes, 2022.

A. Sciacchitano and B. Wieneke. PIV uncertainty propagation. *Measurement Science and Technology*, 27(8):084006, 2016.

R. E. Seoud and J. C. Vassilicos. Dissipation and decay of fractal-generated turbulence. *Physics of fluids*, 19(10), 2007.

P. M. Sforza, P. Sheerin, and M. Smorto. Three-dimensional wakes of simulated wind turbines. *AIAA journal*, 19(9):1101–1107, 1981.

M. Shademan and A. Naghib-Lahouti. Effects of aspect ratio and inclination angle on aerodynamic loads of a flat plate. *Advances in Aerodynamics*, 2(1):1–23, 2020.

R. Shanmughan, P. Y. Passaggia, N. Mazellier, and A. Kourta. Optimal pressure reconstruction based on planar particle image velocimetry and sparse sensor measurements. *Experiments in Fluids*, 61:1–19, 2020.

M. Sherry, A. Nemes, D. Lo-Jacono, H. M. Blackburn, and J. Sheridan. The interaction of helical tip and root vortices in a wind turbine wake. *Physics of fluids*, 25(11), 2013.

A. Shiri. *Turbulence Measurements in a Natural Convection Boundary Layer and a Swirling Jet*. PhD thesis, Chalmers University of Technology, Göteborg, Sweden, 2010.

A. Shiri, W. K. George, and J. W. Naughton. Experimental study of the far field of incompressible swirling jets. *AIAA Journal*, 46, 2008.

E. P. Soares-Ramos, L. de Oliveira-Assis, R. Sarrias-Mena, and L. M. Fernández-Ramírez. Current status and future trends of offshore wind power in europe. *Energy*, 202:117787, 2020.

A. Sommer. Burning fossil fuels: impact of climate change on health. *International Journal of Health Services*, 46(1):48–52, 2016.

D. A. Spera. *Wind turbine technology*. Fairfield, NJ (United States); American Society of Mechanical Engineers, 1994.

K. R. Sreenivasan and C. Meneveau. The fractal facets of turbulence. *Journal of Fluid Mechanics*, 173:357–386, 1986.

K. R. Sreenivasan, A. Prabhu, and R. Narasimha. Zero-crossings in turbulent signals. *Journal of Fluid Mechanics*, 137:251–272, 1983.

K. R. Sreenivasan, R. R. Prasad, C. Meneveau, and R. Ramshankar. The fractal geometry of interfaces and the multifractal distribution of dissipation in fully turbulent flows. *Fractals in Geophysics*, pages 43–60, 1989.

K. Steiros and M. Hultmark. Drag on flat plates of arbitrary porosity. *Journal of Fluid Mechanics*, 853:R3, 2018.

F. Stella, N. Mazellier, and A. Kourta. Scaling of separated shear layers: an investigation of mass entrainment. *Journal of Fluid Mechanics*, 826:851–887, 2017.

F. Stella, N. Mazellier, P. Joseph, and A. Kourta. Mass entrainment-based model for separating flows. *Physical Review Fluids*, 3:114702, 2018.

R. J. A. M. Stevens and C. Meneveau. Flow structure and turbulence in wind farms. *Annual Review of Fluid Mechanics*, 49:31–39, 2016.

R. J. A. M. Stevens, L. A. Martínez-Tossas, and C. Meneveau. Comparison of wind farm large eddy simulations using actuator disk and actuator line models with wind tunnel experiments. *Renewable energy*, 116:470–478, 2018.

H. Tennekes and J. L. Lumley. *A first course in turbulence*. MIT press, 1972.

F. Thiesset, G. Maurice, F. Halter, N. Mazellier, C. Chauveau, and I. Gökalp. Geometrical properties of turbulent premixed flames and other corrugated interfaces. *Physical Review E*, 93(1):013116, 2016.

K. Thomsen and P. Sørensen. Fatigue loads for wind turbines operating in wakes. *Journal of Wind Engineering and Industrial Aerodynamics*, 80(1-2):121–136, 1999.

R. S. J. Tol. The economic effects of climate change. *Journal of economic perspectives*, 23(2):29–51, 2009.

P. B. Tooke. Fourier self-deconvolution in IR spectroscopy. *Trends in Analytical Chemistry*, 7(4):130–136, 1988.

A. A. Townsend. The mechanism of entrainment in free turbulent flows. *Journal of Fluid Mechanics*, 26:689–715, 1966.

A. A. Townsend. Entrainment and the structure of turbulent flow. *Journal of Fluid Mechanics*, 41:13–46, 1970.

A. A. Townsend. *The Structure of Turbulent shear flow, 2nd ed.* Cambridge University Press, 1976.

K. N. Travis, S. E. Smith, L. Vignal, H. Djeridi, M. Bourgoin, R. B. Cal, and M. Obligado. Characterization of coupling between inertial particles and turbulent wakes from porous disk generators. *Journal of Fluid Mechanics*, 933, 2022.

N. Troldborg, G. C. Larsen, H. A. Madsen, K. S. Hansen, J. Sørensen, and R. Mikkelsen. Numerical simulations of wake interaction between two wind turbines at various inflow conditions. *Wind Energy*, 14(7):859–876, 2011.

J. S. Turner. Turbulent entrainment: the development of the entrainment assumption, and its application to geophysical flows. *Journal of Fluid Mechanics*, 173:431–471, 1986.

J. C. Vassilicos. Dissipation in turbulent flows. *Annual review of fluid mechanics*, 47: 95–114, 2015.

L. J. Vermeer, J. Sørensen, and A. Crespo. Wind turbine wake aerodynamics. *Progress in aerospace sciences*, 39(6-7):467–510, 2003.

VP Vetchinkin. Calculation of screw propeller, part i. *Trudy Avia Raschetno-Ispytatelnogo Byuro*, 4:1–129, 1913.

J. H. Vincent. *Aerosol sampling: science, standards, instrumentation and applications*. John Wiley & Sons, 2007.

M. K. Vinnes. *The actuator disk as a wind turbine model: An experimental assessment of the fluid dynamics*. PhD thesis, Norwegian University of Science and Technology, 2023.

M. K. Vinnes, S. Gambuzza, B. Ganapathisubramani, and R. J. Hearst. The far wake of porous disks and a model wind turbine: Similarities and differences assessed by hot-wire anemometry. *Journal of Renewable and Sustainable Energy*, 14, 2022.

Q. R. Wald. The aerodynamics of propellers. *Progress in Aerospace Sciences*, 42(2): 85–128, 2006.

J. Westerweel, C. Fukushima, J. M. Pedersen, and J. C. R. Hunt. Mechanics of the turbulent-nonturbulent interface of a jet. *Physical review letters*, 95(17):174501, 2005.

J. Westerweel, C. Fukushima, J. M. Pedersen, and J. C. R. Hunt. Momentum and scalar transport at the turbulent/non-turbulent interface of a jet. *Journal of Fluid Mechanics*, 631:199–230, 2009.

F. M. White. *Fluid mechanics*. McGraw Hill, 1990.

B. Wieneke. PIV uncertainty quantification from correlation statistics. *Measurement Science and Technology*, 26, 2015.

M. Wosnik and N. Dufresne. Experimental investigation and similarity solution of the axisymmetric turbulent wake with rotation. *Fundamental Issues and Perspectives in Fluid Mechanics, ASME 2013 Fluids Engineering Division Summer Meeting*, 1B, 2013.

Y. T. Wu and F. Porté-Agel. Atmospheric turbulence effects on wind-turbine wakes: An LES study. *Energies*, 5, 2012.

Y. T. Wu and F. Porté-Agel. Simulation of turbulent flow inside and above wind farms: model validation and layout effects. *Boundary-layer meteorology*, 146:181–205, 2013.

Y. Zhou and J. C. Vassilicos. Related self-similar statistics of the turbulent/non-turbulent interface and the turbulence dissipation. *Journal of Fluid Mechanics*, 821: 440–457, 2017.

List of Figures

List of Tables

Ernesto FUENTES NORIEGA

Analyse physique du sillage tournant d'un disque poreux : application aux éoliennes

La production d'énergie éolienne, élément fondamental du portefeuille d'énergies renouvelables, a connu une croissance exponentielle ces dernières années. À cause de la limitation des sites dits à fort potentiel éolien, les turbines sont généralement regroupées dans des parcs éoliens, dont la production d'énergie est entravée par les interactions entre sillages. Par conséquent, prédire l'évolution du sillage éolien est d'une importance cruciale. À cette fin, des études fondamentales sont nécessaires pour apporter une compréhension fine de la physique sous-jacente des sillages d'éoliennes. Les disques poreux sont des dispositifs populaires utilisés pour imiter le sillage des éoliennes à l'échelle du laboratoire. Jusqu'à présent, les disques poreux ont été conçus en ajustant un seul paramètre physique, leur porosité, dans le but de reproduire le déficit de vitesse d'une éolienne cible. Cependant, cette approche simpliste exclut une caractéristique clé des sillages éoliens : le taux de rotation (swirl). Ce travail aborde cette problématique en étudiant en profondeur le rôle du taux de rotation sur le développement d'un sillage généré par un disque poreux. Pour ce faire, des expériences en soufflerie ont été menées pour mesurer le sillage d'un disque poreux modifié de telle sorte à intégrer passivement un taux de rotation. Il s'avère que le taux de rotation est un ingrédient clé pour atteindre l'auto-similarité du déficit de vitesse dans la région intermédiaire du sillage et correspond très bien aux données rapportées dans la littérature sur les éoliennes. Sur la base de la théorie de la turbulence hors-équilibre, une nouvelle loi d'échelle pour la décroissance du taux de rotation est dérivée et montre une très bonne concordance avec les données collectées. Enfin, l'entraînement turbulent à l'interface turbulent/non-turbulent (TNTI) est analysé en utilisant des données PIV hautement résolues. Une technique de détection améliorée basée sur les zones de quantité de mouvement uniforme est développée pour détecter avec précision la TNTI, dont la dimension fractale ne semble pas être modifiée par la rotation. Cependant, nos résultats soulignent que le taux de rotation augmente à la fois l'entraînement moyen et la tortuosité de la TNTI. Ces observations révèlent la nécessité d'incorporer désormais le taux de rotation dans le modèle de disque actuateur pour reproduire fidèlement le sillage d'une éolienne, aussi bien sur le plan expérimental que numérique.

Mots clés : éolienne, sillage, disque poreux, autosimilarité, turbulence hors-équilibre, entrainement

Physical analysis of the swirling wake of a porous disc: application to wind turbines

Wind energy stands out as a capital component of the renewable energy portfolio and has accordingly shown an exponential growth in recent years. Due to the limited regions with high wind energy potential, wind turbines are usually clustered in wind farms, whose power output will be impacted by wake interactions. Therefore, predicting the wake's evolution is of critical importance. To this end, fundamental studies are required to bring a comprehensive understanding of the underlying physics of wind turbine wakes. Porous discs are popular devices used to mimic the wake of wind turbines at the laboratory scale. So far, porous discs have been designed by adjusting a single physical parameter, its porosity, with the aim to match the velocity deficit of a target wind turbine. However, this simplistic approach excludes a key feature of wind turbine wakes: swirl. The present work tackles this issue by investigating in depth the role of swirl on the development of a wake generated by a porous disc. To do so, extensive wind tunnel experiments were conducted to measure the wake of a porous disc modified to passively incorporate swirl. It is found that swirl is a key ingredient to achieve self-similarity of the wake deficit in the intermediate wake region and matches very well the data reported in the literature of wind turbines. Based on non-equilibrium similarity theory, a novel scaling law for the decay of swirl is derived and shows very good agreement with the collected data. Finally, the turbulent entrainment at the turbulent/non-turbulent interface (TNTI) is analysed using highly resolved PIV data. An improved uniform momentum zones-based detection technique is developed to accurately detect the TNTI, whose fractal dimension appears to be unaffected by swirl. However, our results emphasise that swirl increases both the mean entrainment and the TNTI tortuosity. Altogether, these observations reveal the need to incorporate swirl to the actuator disc model to faithfully reproduce the wake of a wind turbine, both experimentally and numerically.

Keywords: Wind turbine, wake, porous disc, swirl, self-similarity, non-equilibrium turbulence, entrainment

Laboratoire PRISME
8 Rue Léonard de Vinci
45072 Orléans, France